ISSN 1983-4195

YEARS IBRACON

IBRACON Structures and Materials Journal

Revista IBRACON de Estruturas e Materiais

Volume 15, Number 1
February 2022

ISSN 1983-4195
Volume 15, Number 1
February 2022

IBRACON

Editorial

IBRACON and Scientific and Technological Research in Brazil

With the arrival of the date of commemoration of the Golden Jubilee of the Brazilian Concrete Institute, to take place in June 2022, the Editor-in-Chief of RIEM Journal, Prof. Dr. Guilherme Parsekian, decided along with the Executive Board that the editorials of the journals published in this period should tell the history and contribution of the Institute to the development of concrete engineering in Brazil. It was up to me, honorably, to write this first editorial.

The Institute was founded in 1972 by visionaries who realized the importance of creating a space for valuing the exchange and technical discussion among professionals in the area. In the early 1970s Brazil was already living in the period known as an "economic miracle", under the management of the military dictatorship that obtained many resources and investments from abroad. The Central Bank, BNH, Embratel and more than 270 other state-owned companies were created, reaching the peak of national GDP growth of 11.1%.

As a result, there was a lot of investment in general, and specially in infrastructure construction putting the country's civil engineering in new construction challenges, for example sanitation and underground metropolitan train, durable, watertight, and resistant. Frequent accidents and even tragedies such as the collapses of the traffic bridge Paulo de Frontin in RJ, Gameleira in Belo Horizonte and even the Rio-Niterói bridge that victimized IPT engineers from São Paulo, among other minor accidents, contributed to demonstrate that without knowledge and in-depth expertise in design and experience in construction technology, the challenges would not succeed.

IBRACON then started from a congress whose main theme was the concrete permeability. The voluntary contributions of IPT, USP and ABCP professionals, among others, had a decisive role in this beginning. The correct understanding that Congresses is one of the most important resources for knowledge development lasted for several years and is still one of the noble alternatives of IBRACON in fulfilling its Institutional mission.

It should be registered here that it was also at this time that the country began, modestly, *its strictu sensu graduate programs,* first with master's degrees and later with doctorates, including at the Polytechnic School of USP, because CNPq and CAPES, founded in 1951, only began to have the current attributions in 1974 determined by a presidential law.

The first IBRACON's congresses cannot be called scientific because in fact they were organized from inviting distinguished professionals to participate and share their knowledge. Also, the few graduate programs in the country in the concrete area, had no sufficient students, professors, and critical mass to demand local scientific congresses.

Little by little a process of paper calls was created, embryonic scientific committees were formed, and the congresses were molded to the international standards. Nowadays they are recognized as highest level of excellence. They receive contributions from more than a hundred research centers recognized and registered in CNPq and CAPES, and more than seven hundred new articles are submitted annually.

In the 1990s it became clear that another tool needed to be created and the CONCRETO & Construções Magazine was then launched. However, this Magazine does not intend to meet international protocols of scientific journals, although it includes scientific papers in its content. It was then at the beginning of the century/millennium, in its first decade, that the need to constitute a scientific journal of international scope and standard became evident.

International entities, such as ISI, SCOPUS, ELSEVIER, and many others, during this period, organized to create a database and to classify journal publications in the world, theoretically separating chaff from wheat, that is, distinguishing what should be considered science and innovative technology from what is about practicing engineering and applied science.

Aware of the need to expand its scope and follow the international movement, in the early 2000s IBRACON invested heavily in the creation of initially two scientific journals, “IBRACON Materials Journal” and “IBRACON Structural Journal”. Those journals provided a vehicle of quality and international standard to the entire Brazilian community, from research centers, universities, and public agencies, allowing them to publish their research and thus to be properly evaluated, promoting their academic and professional careers.

In a short time, it was clear that the ideal would be to join the two journals, since many of the articles’ topics overlap. It was the begging of the current IBRACON Structures and Materials Journal or RIEM from its Brazilian Portuguese name “Revista IBRACON de Estruturas e Materiais” in 2008. One cannot fail to quote the outstanding voluntarism and competence of Prof. Dr. Tulio Bittencourt and Prof. Dr. José Luiz Antunes de Oliveira e Sousa, who led the process and “*carried the piano*” in the early days of this journal, now recognized and established nationally and internationally.

Nor we can omit the huge concern of the Brazilian community with the future of science and technology in the country, at this time when it is reported that the Ministry of Science and Technology will receive only 13% of its budget for 2022. Scientific and technological knowledge, its generation, dissemination, transference, absorption, and application, is one of the main and indispensable factors for the development of any country.

In the modern world, the relations between knowledge and power, knowledge and development, knowledge and technology mark economic differences, trade positions, regional leaders, and even military power. Negligent countries are punished with an unwanted technology dependence.

Conscious Brazilians aspire to independence, sovereignty, and technological autonomy, dependable on an adequate research structure. The ability to organize, produce and articulate knowledge, to create development and improves the quality of life of society. This requires the incentive to scientific research that is born in research centers and universities.

IBRACON will not refrain from its original role, envisioned by visionaries, which is to support research in Brazil, being a strong instrument for the dissemination and valorization of knowledge. Supporting research centers and universities is critical to the healthy development of a strong and autonomous nation.

Paulo Helene
President
2019-2021 Biennium

ISSN 1983-4195
Volume 15, Number 1
February 2022

IBRACON Structures and Materials Journal
Revista IBRACON de Estruturas e Materiais

Contents

Cover: Parametric Tower

Courtesy: Marcela Noronha P. de O. e Sousa

IBRACON

Ibracon Structures and Materials Journal is published bimonthly
(February, April, June, August, October, and December) by IBRACON.

IBRACON
Instituto Brasileiro do Concreto Founded in 1972

Av. Queiroz Filho, nº 1700 — sala 407/408
Torre D — Villa Lobos Office Park
CEP 05319-000 — São Paulo, SP — Brazil
Phone: +55 11 3735-0202
Fax: +55 11 3733-2190
E-mail: riem@ibracon.org.br
Website: http://www.ibracon.org.br

Cover design & Layout: Editora Cubo
www.editoracubo.com.br

Aims and Scope

Aims and Scope

The IBRACON Structures and Materials Journal (in Portuguese: Revista IBRACON de Estruturas e Materiais) is a technical and scientific divulgation vehicle of IBRACON (Brazilian Concrete Institute), published every two months. Each issue has 12 to 15 articles and, possibly, a technical note and/or a technical discussion regarding a previously published paper. All contributions are reviewed and approved by professionals with recognized scientific competence in the area. The IBRACON Structures and Materials Journal is an open access Journal, free of charges for authors and readers.

Objectives

The IBRACON Structures and Materials Journal´s main objectives are:

- Present current developments and advances in concrete structures and materials.
- Make possible the better understanding of structural concrete behavior, supplying subsidies for a continuous interaction among researchers, producers, and users.
- Stimulate the development of scientific and technological research in the areas of concrete structures and materials, through papers peer-reviewed by a qualified Editorial Board.
- Promote the interaction among researchers, constructors and users of concrete structures and materials and the development of Civil Construction.
- Provide a vehicle of communication of high technical level for researchers and designers in the areas of concrete structures and materials.

Submission Procedure

The procedure to submit and revise the contributions, as well as the formats, are detailed in the Journal Website (ismj.org).

The papers and the technical notes are revised by at least two reviewers indicated by the editors. Discussions and replies are accepted for publication after a review by the editors and at least one member of the Editorial Board. In case of disagreement between the reviewer and the authors, the contribution will be sent to a specialist in the area, not necessarily linked to the Editorial Board. Conflict of interests is carefully handled by the Editors.

Contribution Types

The Journal will publish original papers, short technical notes, and paper discussions. Original papers will be accepted if they are in accordance with the objectives of the Journal and present quality of information and presentation. A technical note is a brief manuscript. It may present a new feature of research, development, or technological application in the areas of Concrete Structures and Materials, and Civil Construction. This is an opportunity to be used by industries, companies, universities, institutions of research, researchers, and professionals willing to promote their works and products under development.

A discussion is received no later than 3 months after the publication of the paper or technical note. The discussion must be limited to the topic addressed in the published paper and must not be offensive. The right of reply is granted to the Authors. The discussions and the replies are published in the subsequent issues of the Journal.

The submission file should be in accordance with the paper template available at the Journal Website. It is recommended that the length of the papers does not exceed 25 pages. Where available, URLs for the references should be provided.

The IBRACON Structures and Materials Journal will conduct the review process for manuscripts submitted in English. Titles, abstracts, and keywords are presented in English, and in Portuguese or Spanish. Articles and technical notes are peer-reviewed and only published after approval of the reviewers and the Editorial Board.

Once accepted, an article is typeset according to the journal layout. The author will be required to review and approve the galleys before publishing. At this stage only typesetting errors will be considered.

Internet Access

The IBRACON Structures and Materials Journal Webpage is available at http://ismj.org.

Sponsors

The funds for the maintenance of the Journal are currently obtained from the IBRACON. The Journal is not supposed to be maintained with funds from private sponsorship, which could diminish the credit of the publications.

Photocopying

Photocopying in Brazil. Brazilian Copyright Law is applicable to users in Brazil. IBRACON holds the copyright of contributions in the journal unless stated otherwise at the bottom of the first page of any contribution. Where IBRACON holds the copyright, authorization to photocopy items for internal or personal use, or the internal or personal use of specific clients, is granted for libraries and other users registered at IBRACON.

Copyright

IBRACON

Av. Queiroz Filho, 1700 – sala 407/408 – Torre D
Villa Lobos Office Park
05319-000 – Vila Hamburguesa
São Paulo – SP
Phone: +55 (11) 3735-0202
E-mail: riem@ibracon.org.br

Disclaimer

Papers and other contributions and the statements made, or opinions expressed therein are published on the understanding that the authors of the contribution are the only responsible for the opinions expressed in them and that their publication does not necessarily reflect the views of IBRACON or of the Journal Editorial Board.

Editorial Board

IBRACON

Direction

IBRACON Structures and Materials Journal
Revista IBRACON de Estruturas e Materiais
ISSN 1983-4195 ismj.org

ORIGINAL ARTICLE

Comparison between exact and approximate methods for geometrically nonlinear analysis prescribed in design standards for steel and reinforced concrete structures

Comparação entre métodos exato e aproximados de análise geometricamente não linear prescritos em normas de estruturas de aço e de concreto armado

Laís De Bortoli Lecchi[a]
Walnório Graça Ferreira[b]
Paulo Manuel Mendes Pinheiro da Providência e Costa[c]
Arlene Maria Cunha Sarmanho[a]

[a]Universidade Federal de Ouro Preto – UFOP, Departamento de Engenharia Civil, Ouro Preto, MG, Brasil
[b]Universidade Federal do Espírito Santo, UFES, Departamento de Engenharia Civil, Vitória, ES, Brasil
[c]Universidade de Coimbra, Instituto de Engenharia de Sistemas e Computadores de Coimbra – INESC Coimbra, Departamento de Engenharia Civil, Coimbra, Portugal

Received 28 December 2020
Accepted 13 April 2021

Abstract: Current practices in structural engineering demand ever-increasing knowledge and expertise concerning stability of structures from professionals in this field. This paper implements standardized procedures for geometrically nonlinear analysis of steel and reinforced concrete structures, with the objective of comparing methodologies with one another and with a geometrically exact finite element analysis performed with Ansys 14.0. The following methods are presented in this research: Load Amplification Method, from NBR 8800:2008; the γ_z coefficient method, from NBR 6118:2014; the P-Delta iterative method and the α_{cr} coefficient method, prescribed in EN 1993-1-1:2005. A bibliographic review focused on standardized approximate methods and models for consideration of material and geometric nonlinearities is presented. Numerical examples are included, from which information is gathered to ensure a valid comparison between methodologies. In summary, the presented methods show a good correlation of results when applied within their respective recommended applicability limits, of which, Eurocode 3 seems to present the major applicability range. The treated approximate methods show to be more suitable for regular framed structures subjected to regular load distributions.

Keywords: global stability analysis, approximate nonlinear analysis, P-Delta iterative method, α_{cr} coefficient, ANSYS.

Resumo: As práticas atuais em engenharia estrutural exigem cada vez mais conhecimento e expertise, em relação à estabilidade de estruturas, por parte dos profissionais da área. Este artigo implementa procedimentos normativos de análise de segunda ordem aproximada de estruturas de aço e concreto armado, com o objetivo de comparar as metodologias aproximadas entre si e com uma análise de elementos finitos geometricamente exata realizada no Ansys 14.0. Os seguintes métodos são tratados nesse trabalho: Método da Amplificação dos Esforços Solicitantes, da NBR 8800:2008; o método do Coeficiente γ_z, da NBR 6118:2014; o método P-Delta iterativo e o método do Coeficiente α_{cr}, da EN 1993-1-1:2005. É apresentada uma revisão bibliográfica a respeito dos métodos normativos e como são tratadas as não linearidades de materiais e geométricas. Exemplos numéricos estão incluídos, de onde são extraídas as informações para a comparação entre as metodologias. Em resumo, os métodos apresentados mostram boa correlação de resultados quando aplicados dentro dos respectivos limites de aplicabilidade recomendados, dos quais, o Eurocódigo 3 aparenta ter a maior faixa de aplicabilidade. Os métodos aproximados tratados mostram ser mais adequados para estruturas aporticadas regulares e sujeitas à carregamentos regulares.

Corresponding author: Laís De Bortoli Lecchi. E-mail: laislecchi@gmail.com
Financial support: None.
Conflict of interest: Nothing to declare.

Palavras-chave: análise de estabilidade global, análise não linear aproximada, método P-Delta iterativo, coeficiente α_{cr}, ANSYS.

How to cite: L. B. Lecchi, W. G. Ferreira, P. M. M. P. Providência e Costa, and A. M. C. Sarmanho, "Comparison between exact and approximate methods for geometrically nonlinear analysis prescribed in design standards for steel and reinforced concrete structures," *Rev. IBRACON Estrut. Mater.*, vol. 15, no. 1, e15101, 2022, https://doi.org/10.1590/S1983-41952022000100001

1 INTRODUCTION

1.1 Initial considerations

In recent decades, structural engineering and civil construction underwent significant technological advancements, which resulted in the reduction of weight and overall improvement of structural systems, in turn allowing the construction of buildings with heights previously deemed impossible. As such, the development of methods and analysis software to ensure the safety of these buildings became a necessity.

Engineering design standards include procedures for first and second order structural analyses. A first order analysis is characterized by determining the equilibrium equations of structures in their undeformed condition. In this type of analysis, structures are assumed to undergo small displacements that bear no effect on the developed internal forces. Alternatively, in a second order geometric analysis (or nonlinear), the equilibrium equations refer to the structure in the deformed configuration, resulting in a system of nonlinear equations. This approach is required when the applied loads interact with the resulting displacements inducing significant additional internal forces [1]. It is worth noting that nonlinear analyses may be performed considering either small or large strains theories – the former case is considered in this paper. To evaluate second order effects, it is necessary to consider the different types of nonlinearity, namely, geometric and material nonlinearities. The nonlinear behavior of a structure significantly affects displacements and internal forces.

Publications by Horne [2], Wood et al. [3] and LeMessurier [4], [5] were fundamental for the development of practical design methods for multi-story buildings, namely by introducing an approximate method for considering the $P-\Delta$ effect. In Brazil, studies conducted by Franco [6], Franco and Vasconcelos [7] and Vasconcelos [8], focused on the assessment of second order effects in reinforced concrete buildings, culminated in the γ_z coefficient method, currently detailed in NBR 6118:2014 [9] for the structural design of reinforced concrete structures.

This paper presents four approximate methods: the Load Amplification Method (MAES, in Portuguese), originally presented in ANSI/AISC 360-16 [10], and subsequently adopted by NBR 8800:2008 [11] for the structural design of steel buildings; the γ_z coefficient prescribed in NBR 6118:2014 [9] and used for the classification of the structure and also as a design factor for the horizontal loads; the equivalent lateral force method (iterative *P-Delta*), adopted by NBR 8800:1986 [12], which adds fictitious lateral loads to the horizontal loads; and the method prescribed in the European standard EN 1993-1-1:2005 [13] for the design of steel structures, that uses the α_{cr} coefficient to classify a structure according to its sensitivity to second order effects.

1.2 Material nonlinearity

Material nonlinearity is defined as a nonlinear relationship between stress and strain on a given material. This issue can come from: partial yielding of steel sections, also accentuated by the presence of residual stresses; the influence of semirigid connections; creep and cracking on reinforced concrete elements, for example.

The standards NBR 8800:2008 [11], NBR 6118:2014 [9] and ANSI/AISC 360-16 [10], allow the approximate treatment of material nonlinearities, characterized by a reduction of the axial and flexural stiffnesses of structural elements.

1.3 Geometric nonlinearities

An effect of geometric nonlinearity is the lack of proportionality between applied loads and resulting displacements [14]. This type of nonlinear behavior results from the interaction between the load and the displacements. In frames, two different types of displacement are relevant: the inter-story drift, which causes the $P-\Delta$ effect, and the curvature of the elements, which causes the $P-\delta$ effect. However, the global imperfections (initial drift) and the local imperfections (initial curvature) are not nonlinear effects.

Design standards commonly include simplified methods for modelling geometric nonlinearities. The Brazilian standard NBR 8800:2008 [11], for instance, determines that, in structures subjected to load combinations composed exclusively of vertical forces, initial geometric imperfections are considered by introducing notional forces equivalent to 0.3% of the value of dead loads. Alternatively, ANSI/AISC 360-16 [10] also allow the use of notional forces, but with a magnitude of 0.42% for first order analyses and 0.2% for the direct analysis method, a method for assessment of overall system structural stability (it also includes initial material imperfections, by adjustments in stiffness).

The method prescribed in NBR 6118:2014 [9] accounts for the misalignment of structural elements, and, for cases with a load amplification factor $\gamma_z > 1.1$, such a factor is taken as $0.95\gamma_z$. For the design of frames, Eurocode 3 [13] allows the amplification of horizontal loads if $\alpha_{cr} \geq 3$, along with the inclusion of theoretical lateral loads even in cases with horizontal load combinations. However, the inclusion of notional forces when horizontal external loads are present is only applicable if these forces are inferior to 15% of the loads attributed to the weight of structural elements.

1.4 Approximate methods for second order analysis

The inelastic second order analysis can properly describe the actual behavior of a structure, since it includes the plastic behavior of materials [15]. However, the relatively complex formulation of this refined approach is a complicating factor. As such, simplified procedures may be used to perform second order analyses. Computational alternatives for $P-\Delta$ analyses were being developed since the 1980s, such as the procedure introduced by Rutenberg [16]. Wilson and Habibullah [17] also presented an approximate computational method for determining second order effects in frames subjected to horizontal loads.

LeMessurier [5] presented an interesting formulation for approximate nonlinear analysis that relies on the amplification of first order effects, which eventually served as a base for the development of other methods such as MAES ($B_1 - B_2$).

As stated by Ziemian [15], approximate methods must be used with caution since they may be inadequate for amplifying bending moments in regions connecting beams and columns. It is worth noting that these methodologies are only recommended for framed structures with uniform loads [18].

Dória et al. [19] assert that the ratio of first to second order displacements (Δ_2 / Δ_1) may not be the best approach for quantifying second order effects in structures. Additionally, the B_2 coefficient, used to approximate Δ_2 / Δ_1, might lead to incorrect results when analyzing second order effects. As an alternative, the above authors recommend the use of the α_{cr} coefficient adopted by Eurocode 3 [13], as a more adequate indicator of the importance of second order effects in structures.

2 APPROXIMATE METHODS FOR GEOMETRICALLY NONLINEAR ANALYSIS

2.1 Method prescribed in NBR 8800:2008

2.1.1 Introduction

The Load Amplification Method implements the amplification factors B_1 and B_2. This approach was first introduced by SSRC (Structural Stability Research Council) and subsequently adopted by AISC in 1986 [20].

B_1 amplifies the loads to account for the $P-\delta$ effect (local), while B_2 treats the $P-\Delta$ effect (global). These coefficients may be used for the analysis of reticulated structures consisting of structural elements with uniform geometry and stiffness, provided $B_2 \leq 1.4$ [21]. The B_2 coefficient must be determined for each pavement, and it is not adequate for analyzing structures with split story levels [15].

The $B_1 - B_2$ method consists in decomposing the structural model in two parts, as shown in Figure 1. The first submodel, traditionally referred to as *nt*, meaning *"no translation"* – maintains the original load configuration, but is now subjected to fictitious horizontal restraints in each pavement to prevent horizontal translation. The second submodel – named *lt*, for *"lateral translation"* – is exclusively subjected to the aforementioned horizontal restraints reactions, but with opposite direction. After the subdivision, both models are subjected to an elastic first-order analysis.

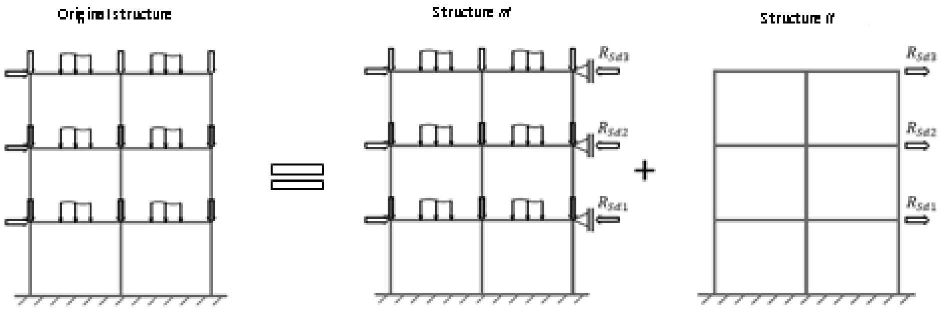

Figure 1 – Original structure divided into two models. Source: Badke-Neto and Ferreira [22].

2.1.2 Adjustments to stiffness

According to NBR 8800:2008 [11] the flexural and axial stiffnesses of structures with high sensitivity to second order effects must be reduced to $0.8EI$ and $0.8EA$, respectively. ANSI/AISC-360-16 [10] includes an additional reduction factor τ_b, and stipulates that the reduced stiffnesses must be used to determine strength and stability limits only. In other words, the reduced properties are not used to obtain displacements, deflections or periods of vibration.

2.1.3 Initial Geometric imperfections

NBR 8800:2008 [11] determines that the initial global geometric imperfections may be accounted for by either considering an inter-story drift equal to $h/333$, where h is the story height, or by imposing notional forces equivalent to 0.3% of the gravitational loads acting on a given story subjected to combinations without lateral loads, in other words, it provides a minimum destabilizing effect [23].

2.1.4 Classification of the structure

The Brazilian standard [11] classifies a structure according to its susceptibility to displacements. If the ratio between the second-order displacement Δ_2 and first-order displacement Δ_1 is less than or equal to 1.1, the structure is defined as having small susceptibility. Alternatively, if the condition $1.1 < \Delta_2 / \Delta_1 \leq 1.4$ is satisfied, the structure is of medium susceptibility. If neither of these conditions are met, a high susceptibility to displacements is attributed to the structure. The B_2 coefficient is considered an acceptable approximation of the ratio Δ_2 / Δ_1, if $\Delta_2 / \Delta_1 \leq 1.4$ [11], or $\Delta_2 / \Delta_1 \leq 1.5$, in ANSI/AISC-360-16 [10] case. It is worth noting that ANSI/AISC-360-16 [10] does not include this classification (small, medium, or high susceptibility).

2.1.5 Methodology from annex D of NBR 8800:2008

Given an adequately defined load combination, the axial load N_{sd} and the bending moment M_{sd} acting on each floor are given by Equations 1 and 2, respectively.

$$M_{sd} = B_1 M_{nt} + B_2 M_{lt} \tag{1}$$

$$N_{sd} = N_{nt} + B_2 N_{lt} \tag{2}$$

where M_{nt} and N_{nt} are the design bending moment and axial force, respectively, obtained via elastic first-order analysis of submodel *nt*. Similarly, M_{lt} and N_{lt} are the design bending moment and axial force obtained from an elastic first-order analysis of submodel *lt*. The shear force is determined with an elastic first-order analysis of the original model (which is equivalent to the sum of submodels *nt* and *lt*).

2.1.6 The B_1 coefficient

For an unbraced member in the plane of bending under consideration, NBR 8800:2008 [11] defines B_1 as:

$$B_1 = \frac{C_m}{1 - \frac{|N_{Sd1}|}{N_e}} \geq 1.0 \tag{3}$$

C_m is an equivalent moment factor given by $C_m = 0.60 - 0.40(M_1 / M_2)$, where M_1 and M_2, calculated from a first-order analysis, are the smaller and larger moments, respectively, at the ends of that member. M_1 / M_2 is positive when the member is bent in reverse curvature and negative when bent in single curvature. N_{Sd1} is the design axial force on the member, obtained from a first-order analysis, $N_{Sd1} = N_{nt} + N_{lt}$. N_e is the critical elastic buckling load of the member in the direction of bending, given by Euler's critical load $N_e = \pi^2 EI / L^2$, where E is the modulus of elasticity, I is the moment of inertia of the cross-section and L is the length of the member.

2.1.7 The B_2 coefficient

A detailed deduction of B_2 is given e.g. in Souza et al. [24]. NBR 8800:2008 [11] defines B_2 as:

$$B_2 = \frac{1}{1 - \frac{1}{R_S} \frac{\Delta_h}{h} \frac{\Sigma N_{Sd}}{\Sigma H_{Sd}}} \tag{4}$$

where ΣN_{Sd} is the total dead load acting on the analyzed story. ΣH_{Sd} is the total shear force on this story, obtained from the original structure or from submodel *lt* (Figure 1). Δ_h is the relative displacement between the top and bottom pavements of the story, obtained from the original structure or submodel *lt*. h is the ceiling height of the story. R_S is an adjustment coefficient, associated to the type of present bracing and it values $0,85$, for frame bracing systems and $1,0$, for all others.

2.2 Method prescribed in NBR 6118:2014: The γ_Z coefficient

2.2.1 Introduction

NBR 6118:2014 [9] classifies framed structures as either fixed nodes or movable nodes. When ratio of second-order to first-order internal forces is larger than 10%, i.e. $\gamma_z > 1.1$, the structure is sensitive to second order effects. Otherwise, fixed nodes are considered. The γ_z coefficient serves two purposes: Classification of the structure and second order amplification of horizontal loads, determining the total horizontal load acting on the system.

2.2.2 Material nonlinearity according to NBR 6118:2014

Material nonlinearities, commonly present in reinforced concrete structures and having a significant influence on second order effects, must always be accounted for [25], by means of reducing the stiffness of each structural element.

2.2.3 Initial geometric imperfections according to NBR 6118:2014

Initial global geometric imperfections are included in the form of an initial out of plumbness of the columns, or the corresponding angle θ_a, as shown in Figure 2 (Eurocode 3 [13] provides similar expressions):

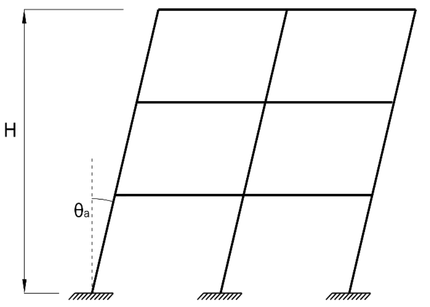

Figure 2 – Initial out of plumbness. Source: Adapted from NBR 6118-2014 [9].

where:

$$\theta_1 = \frac{1}{100\sqrt{H}} \tag{5}$$

$$\theta_a = \theta_1 \sqrt{\frac{1+1/n}{2}} \tag{6}$$

in which:

$\theta_{1,min} = 1/300$; $\theta_{1,max} = 1/200$;

H is the total height; n is the total number of columns lines of the frame.

The drift in angular form (θ_a) can be converted into an equivalent force $H_i = \theta_a F_{vi}$, in which F_{vi} is the load acting on a given floor [26].

According to NBR 6118-2014 [9], if 30% of the tipping moment caused by the incidence of wind is larger than the tipping moment caused by horizontal out of plumbness, the latter is neglected. Alternatively, if the moment caused by wind is less than 30% of the horizontal out of plumbness moment, the former is neglected. In any other scenario, the two types of tipping moment are considered in the load combination, not necessarily respecting the condition imposed by $\theta_{1,min}$.

Initial local geometric imperfections in reinforced concrete structures are included during structural design procedures for each column, using either the method of approximate curvature or the method of approximate stiffness.

2.2.4 The γ_Z coefficient

In 1991, Franco and Vasconcelos presented the γ_z coefficient for the first time, in the paper "Practical Assessment of Second Order Effects in Tall Buildings" [7]. The complete deduction of γ_z is detailed in Souza et al. [24], and it is ultimately determined by:

$$\gamma_z = \frac{1}{1 - \frac{\Delta M_{tot,d}}{M_{1,tot,d}}} \tag{7}$$

where $M_{1,tot,d}$ is the tipping moment and $\Delta M_{tot,d}$ is the sum of the products between vertical forces acting on the structure and the respective horizontal displacements.

In essence, the only difference between γ_z and B_2 is the factor $1/R_s$, present in the formula for B_2, and attributed to the type of bracing on the structure. According to section 15.7.2 of NBR 6118:2014 [9], if $\gamma_z > 1.1$, the horizontal loads must be multiplied by the factor $0.95\gamma_z$. This procedure is valid only for $\gamma_z \leq 1.3$.

The fact that γ_z is defined only once for the entire structure is an interesting practical advantage, especially if compared to other methods such as MAES. However, as stated by Avakian [27], the γ_z coefficient does not yield acceptable results when implemented in frames with non-rigid connections. Additionally, Silva [14] concluded that the γ_z method gives poor results for frames with lateral bracing.

2.3 The lateral equivalent force method or iterative P-Delta method

NBR 8800:1986 [12] prescribes in, Annex L, an approximate method for performing elastic second-order analyses, designated as iterative P-Delta method. This method, also adopted by AISC and by the Canadian standard CSA-S16.1 [28], consists of adding the actual horizontal loads of the structure to fictitious lateral loads obtained iteratively (see Figure 3). At the end of this process, the total load on the structure is obtained, since the fictitious lateral loads induce a behavior similar to second-order effects.

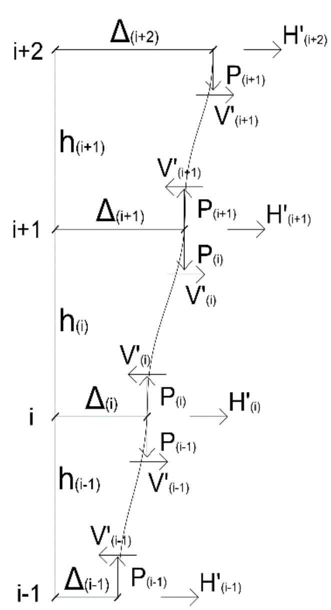

Figure 3 – Displacements and fictitious loads in multi-story buildings. Source: Adapted from NBR 8800:1986 [12].

Every analysis in this method is first-order. Initially, horizontal displacements are calculated for each floor. This step is followed by determining the fictitious shear force in each story *i* using Equation 8:

$$V'_i = \frac{\sum P_i}{h_i}\left(\Delta_{i+1} - \Delta_i\right) \tag{8}$$

where V'_i is the fictitious shear force in floor *i*; $\sum P_i$ represents the summation of axial forces acting on the columns of floor *i*; h_i is the height of the floor under analysis and Δ_{i+1}, Δ_i indicate the horizontal displacement of floors *i+1* and *i*, respectively. Since displacements differ in each floor, the shear forces V'_i are not in equilibrium. This unbalanced equation induces the fictitious lateral force H'_i, as shown in Figure 3, calculated with Equation 9.

$$H'_i = V'_{i-1} - V'_i \tag{9}$$

On the next iteration, initial loads must be once again applied to the structure, including the obtained forces H'_i, resulting in new displacements. Consequently, a new lateral force H'_i must be added to the initial loading in the following iteration. This procedure is repeated until the difference between displacements in two consecutive iterations is smaller than a convergence criterion established beforehand.

Bernuzzi and Cordova [29] affirm that, if convergence is slow, demanding six or seven iterations, it indicates that the loading configuration is considerably close to the elastic limit or that the structure is excessively flexible. Moreover, the process may be interrupted when the convergence factor is equal to 5%. The NBR 8800:1986 [12] does not mention reductions of axial and flexural stiffnesses to account for material nonlinearity.

2.4 Methodology from the European standard for steel structures EN 1993-1-1: 2005

2.4.1 Initial considerations

The standard EN 1993-1-1:2005 [13], Eurocode 3 in this paper, indicates that first-order analyses may be used if the effect of the displacements is not relevant, i.e. provided Equations 10 and 11 are met.

$$\alpha_{cr} = \frac{\mathrm{F}_{cr}}{\mathrm{F}_{ed}} \geq 10, \textit{ for elastic analysis} \tag{10}$$

$$\alpha_{cr} = \frac{\mathrm{F}_{cr}}{\mathrm{F}_{ed}} \geq 15, \textit{ for plastic analysis} \tag{11}$$

where α_{cr} is a factor by which design loads would have to be increased to result in elastic instability; F_{ed} is the vertical design load acting on the structure and F_{cr} is the critical elastic buckling load. If $\alpha_{cr} \geq 10$, the structure is considered to have low sensitivity to second order effects, which is equivalent to the fixed node classification of NBR 6118:2014 [9].

It is important to note that this method is only applicable if the framed structure under analysis is subjected to equally spaced gravitational and destabilizing loads and is composed of uniform structural elements. Since the method is based on a linear elastic analysis, second-order effects are induced by amplifying horizontal loads. This procedure is executed by applying a β coefficient (Equation 12), which is a function of α_{cr}.

$$\beta = \frac{1}{1 - \frac{1}{\alpha_{cr}}} \tag{12}$$

An alternative for determining α_{cr} via elastic buckling analysis is given in Equation 13, which is based on a method for standard framed systems proposed by Horne [2]. It is worth noting that this proportionality relation is valid for small displacement theory. For multi-story structures, the factor must be calculated for each story, but only the smallest value is ultimately used. This method is applicable if $\alpha_{cr} \geq 3$.

$$\alpha_{cr} = \frac{\mathrm{H}_{ed}}{\mathrm{V}_{ed}} \cdot \frac{h}{\delta_{H,ed}} \tag{13}$$

In which H_{ed}: is the total horizontal force; V_{ed}: is the total vertical load applied on the horizontal surface of a given story under analysis; h: is the height of the building and $\delta_{H,ed}$: is the displacement of the level above, calculated for a structure subjected only to the horizontal loads H_{ed}.

It is possible to note similarity between β, γ_z and B_2. β, as well as γ_z, does not depend on the factor $1/R_s$. In essence, the difference among the procedures for determining each of these coefficients lays in how each method accounts for initial material and geometric imperfections.

2.4.2 Initial geometric imperfections

2.4.2.1 Initial global geometric imperfections

Initial global geometric imperfections are included in the analysis by applying a global initial sway imperfection angle φ to the structure, which may be neglected if $H_{ed} \geq 0.15V_{ed}$ (clause 5.3.2(4) of Eurocode 3 [13]). In Eurocode 3, the angle φ is given by: $\varphi = \varphi_0 \alpha_h \alpha_m$, where φ_0 is the basic value ($\varphi_0 = 1/200$); α_h is a reduction coefficient related to the height h of the structure in meters ($\alpha_h = 2/\sqrt{h}$, with $2/3 \leq \alpha_h \leq 1$) and α_m is a reduction coefficient related to the number of columns, $\alpha_m = \sqrt{0.5(1+1/m)}$ and m is the number of columns on a given row. It is easy to notice that these expressions are identical to those prescribed by in NBR 6118-2014 [9].

Alternatively, the horizontal drift may be replaced by the equivalent lateral force shown in Figure 4 [30], given by:

$$F' = \varphi V_{ed} \tag{14}$$

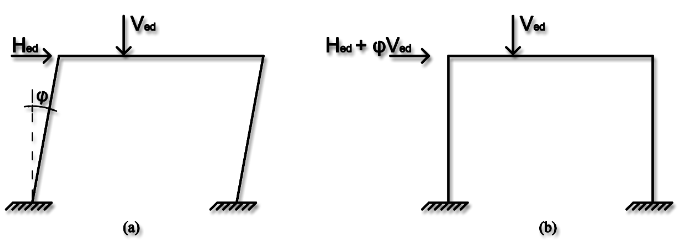

Figure 4 – Consideration of initial global imperfection by (a) initial sway; (b) equivalent lateral force (notional force). Source: Adapted from [30].

2.4.2.2 Initial local geometric imperfections

Clause 5.3.2(6) of Eurocode 3 stipulates that the global analysis of structures sensitive to second-order effects must include initial local imperfections in members subjected to compression in which a) at least one end is not free to rotate and b) $N_{ed} > (F_{cr}/4)$. Initial local imperfections may also be replaced by equivalent forces.

2.4.3 Adjustments to stiffness associated to material nonlinearity

Eurocode 3 does not require a reduction of the modulus of elasticity E, as other standards do.

3 NUMERICAL EXAMPLES

3.1 Example 1: Single span single story frame

Figure 5a shows a single span single story plane frame (adapted from [30]), along with its dimensions and the numbering of nodes and bars (underlined). The structure is subjected to the loads shown in Figure 5b. The load magnitudes displayed already represent the least favorable load combination. All columns are composed of the profile HEA280, while beams feature section IPE500. The modulus of elasticity of steel is taken as $E = 200GPa$.

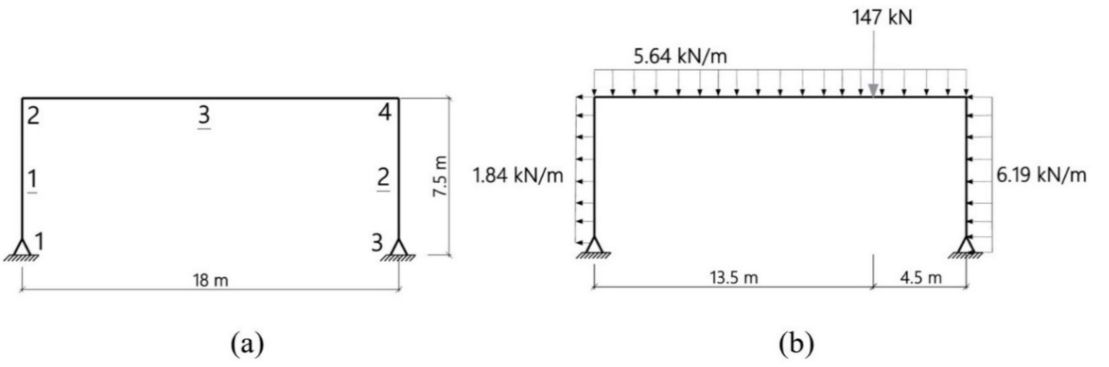

Figure 5 - Single-span single-story frame: (a) dimensions and numbering (b) design loads. Source: Authors (2020).

A first-order elastic analysis was performed to determine the displacements and internal forces, on Ftool 4.0 program. The structure was also modeled in a finite-element based analysis software (Ansys 14.0), in order to perform an exact geometrically nonlinear analysis. Each bar was modelled with a mesh of 10 elements BEAM188 (a two-node linear finite strain beam based on Timoshenko beam theory). Initial geometric imperfections (notional forces) were not included on this model with the least favorable load combination, according to the rules and recommendations of each standard. Material nonlinearity was considered by adjusting the members stiffness by means of a reduction of the modulus of elasticity ($0.8E$), for the case of MAES, the γ_z coefficient and on Ansys. The Newton-Raphson method was used to perform the nonlinear analysis.

Summary of results

Table 1 summarizes the results obtained with each method:

Table 1 – Summary of results. Source: Authors (2020).

	Elastic analysis	**$B_1 - B_2$ Method**	**γ_Z coefficient**	**P-Delta method**	**Eurocode method**	**Ansys**
Amplification coefficients	-	$B_1 = 1.00$ $B_2 = 1.20$	$\gamma_Z = 1.20$	$\frac{\Delta_2}{\Delta_1} = 1.13$	$\beta = 1.13$	$\Delta_2 / \Delta_1 = 1.21$
Δ_4 . node 4 [cm]	15.22	18.96	22.11	17.18	20.40	24.3
Bending moment Column 2 [kNm]	96.8	63.9	75.7	75.4	75.6	64.2
Axial force Column 2 [kN]	−148.5	−144.8	−145.9	−146.1	−146.0	−146.3
Shear force Column 2 [kN]	36.1	36.1	38.0	33.3	36.3	31.4

3.2 Example 2: Eleven story two span frame

Figure 6 shows a steel frame with eleven stories and two spans (adapted from [14]), along with its dimensions and numbering of nodes and bars (underlined). The columns feature welded profiles and the beams rolled profiles, as shown in Table 2. The modulus of elasticity of steel is taken as $E = 200\,GPa$.

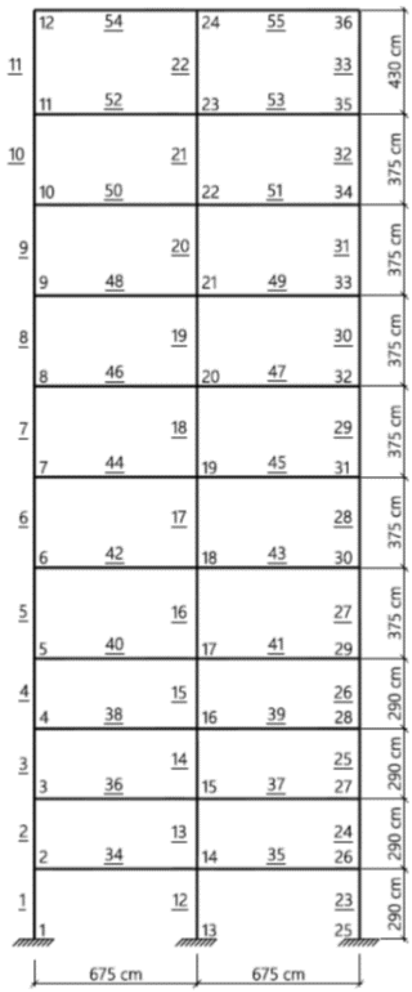

Figure 6 – Frame with eleven stories and two spans: Dimensions and numbering. Source: Authors (2020)

Table 2 – Profiles used for columns and beams (dimensions in mm). Source: Authors (2020)

Bar number	Profile
1 - 4; 23 - 26	PS 500 x 300 x 16 x 8
12 - 15	PS 500 x 300 x 19 x 9,5
5 - 7; 16 - 18; 27 - 29	PS 500 x 300 x 12,5 x 8
8 - 11; 19 - 22; 30 - 33	PS 500 x 300 x 9,5 x 6,5
34 - 55	W 530 x 66

Figure 7a and 7b illustrates the design horizontal and vertical loads, respectively. The values displayed correspond to the least favorable load combination of the structure. The group of loads shown in Figure 7 is designated as $\boldsymbol{Q_R}$ (set of reference loads).

An exact geometrically nonlinear analysis of the structure was performed using a finite element analysis program (Ansys 14.0). Each bar was modelled with a mesh of 20 elements BEAM188 (a two-node linear finite strain beam based on Timoshenko beam theory). Initial geometric imperfections (notional forces) were included on this model (with the least favorable load combination) only for the Eurocode 3 method, according to the rules and recommendations of each standard.

Material nonlinearity was again considered by adjusting the members stiffness by means of their reduction ($0.8EI; 0.8EA$), for the case of MAES, the γ_z coefficient and on Ansys, when the related amplification factors were greater than 1.1. Five simulations were performed, progressively increasing the reference load Q_R by a factor $.n$. Tables 3, 4, 5 and 6 present the obtained results.

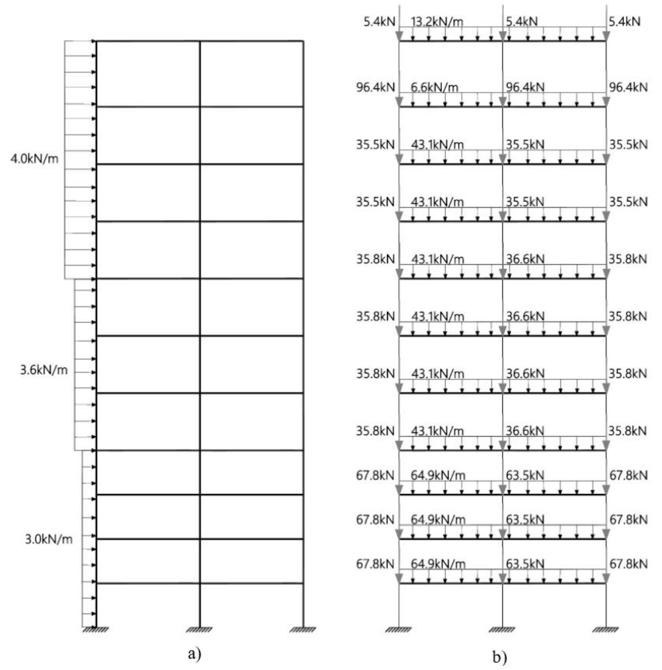

Figure 7 – Design loads applied to the structure: a) horizontal loads and b) vertical loads. Source: Authors (2020)

Table 3 – Final multiplier B_2. (bold font values exceed the applicability limit of the method). Source: Authors (2020).

n	**Coefficient B_2**										
	1º floor	**2º floor**	**3º floor**	**4º floor**	**5º floor**	**6º floor**	**7º floor**	**8º floor**	**9º floor**	**10º floor**	**11º floor**
1	1.06	1.10	1.10	1.09	1.10	1.09	1.07	1.05	1.03	1.02	1.01
2	1.16	1.30	1.30	1.26	1.30	1.25	1.20	1.15	1.10	1.05	1.03
3	1.27	**1.52**	**1.52**	**1.44**	**1.52**	**1.43**	1.33	1.25	1.15	1.08	1.04
4	1.40	**1.83**	**1.84**	**1.70**	**1.84**	**1.67**	**1.49**	1.36	1.21	1.10	1.06
5	**1.55**	**2.31**	**2.34**	**2.04**	**2.33**	**2.00**	**1.70**	**1.50**	1.28	1.13	1.07

Table 4 – Multiplier coefficients γ_Z, α_{cr} and β. (bold font values exceed the applicability limit of the methods) Source: Authors (2020).

n	**B_1 .**	**γ_Z**	**α_{cr} .**	**β**
1	1.0	1.08	12.68	1.09
2	1.0	1.18	6.19	1.19
3	1.0	1.29	4.23	1.31
4	1.0	**1.43**	3.17	1.46
5	1.0	**1.61**	**2.54**	**1.65**

Table 5 – Ratio of initial to final displacements (Δ_2 / Δ_1). obtained with the P-Delta method. Source: Authors (2020).

n	**(Δ_2 / Δ_1) - P-Delta method.**										
	1º floor	**2º floor**	**3º floor**	**4º floor**	**5º floor**	**6º floor**	**7º floor**	**8º floor**	**9º floor**	**10º floor**	**11º floor**
1	1.10	1.12	1.13	1.13	1.14	1.15	1.16	1.17	1.18	1.20	1.22
2	1.20	1.18	1.18	1.18	1.18	1.18	1.18	1.18	1.17	1.17	1.17
3	1.27	1.29	1.29	1.29	1.28	1.27	1.27	1.25	1.24	1.23	1.23
4	1.41	1.43	1.42	1.42	1.41	1.40	1.38	1.36	1.35	1.34	1.33
5	1.56	1.59	1.59	1.59	1.57	1.55	1.53	1.51	1.49	1.47	1.46

Table 6 - Ratio of initial to final displacements (Δ_2 / Δ_1) obtained with Ansys. Source: Authors (2020).

n	(Δ_2 / Δ_1) **- Ansys.**										
	1º floor	**2º floor**	**3º floor**	**4º floor**	**5º floor**	**6º floor**	**7º floor**	**8º floor**	**9º floor**	**10º floor**	**11º floor**
1	1.07	1.08	1.08	1.08	1.08	1.08	1.08	1.07	1.07	1.07	1.07
2	1.15	1.17	1.18	1.18	1.18	1.17	1.17	1.16	1.15	1.15	1.14
3	1.27	1.28	1.29	1.29	1.29	1.28	1.27	1.26	1.25	1.24	1.23
4	1.39	1.42	1.43	1.43	1.43	1.42	1.40	1.38	1.36	1.35	1.39
5	1.54	1.58	1.60	1.60	1.60	1.59	1.56	1.53	1.51	1.49	1.48

The horizontal top floor displacement (node 36) is shown in Figure 8. The geometrically exact analysis performed with Ansys gives the larger displacement values, followed by γ_Z , Eurocode method, P-Delta and MAES.

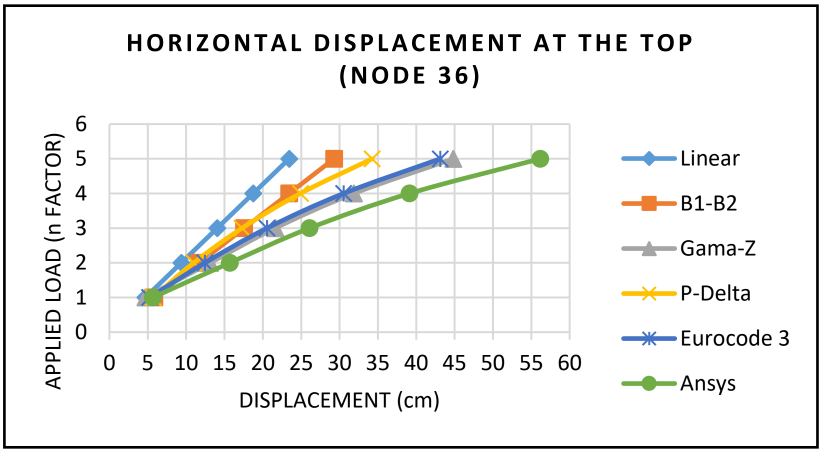

Figure 8 – Top floor displacement at node 36. Source: Authors (2020)

For each method, internal forces were analyzed on column 27 (5th floor), where the highest values of load multipliers are observed, and column 33 (11th floor), which presents the smallest values. Figures 9 through 14 show the obtained results.

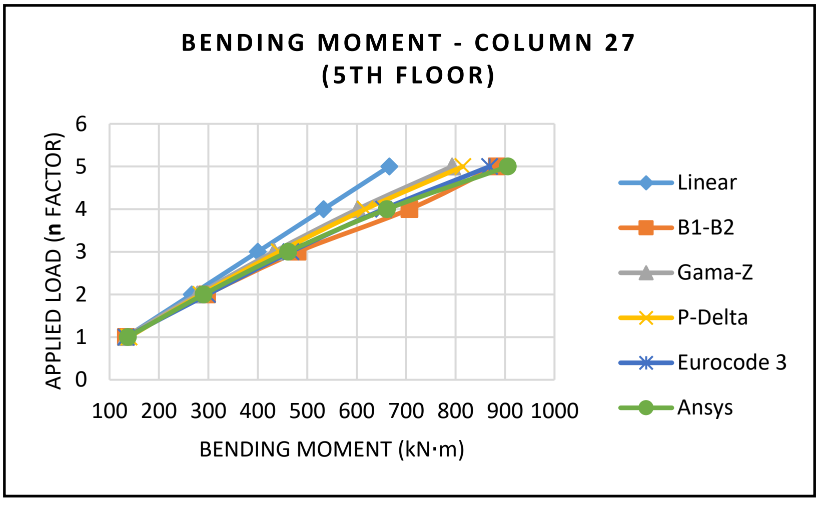

Figure 9 – Load - bending moment relationship for column 27. Source: Authors (2020).

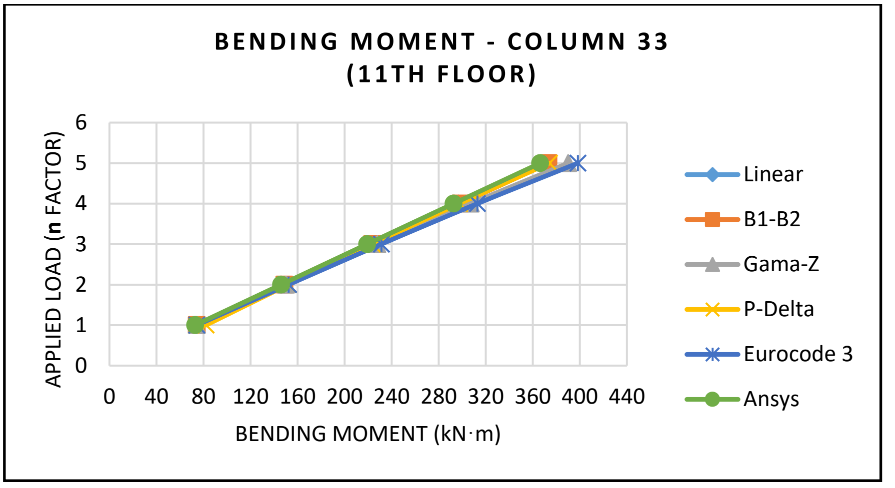

Figure 10 - Load - bending moment relationship for column 33. Source: Authors (2020).

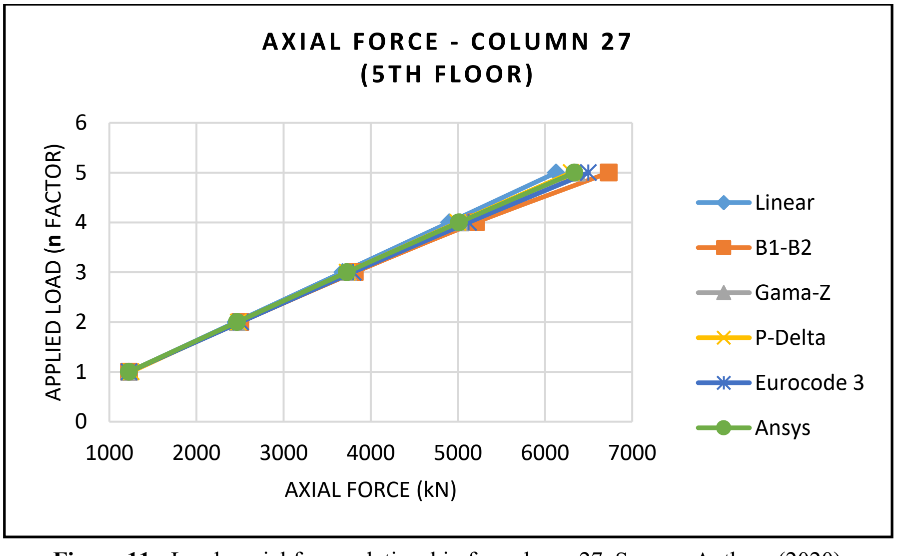

Figure 11 - Load - axial force relationship for column 27. Source: Authors (2020).

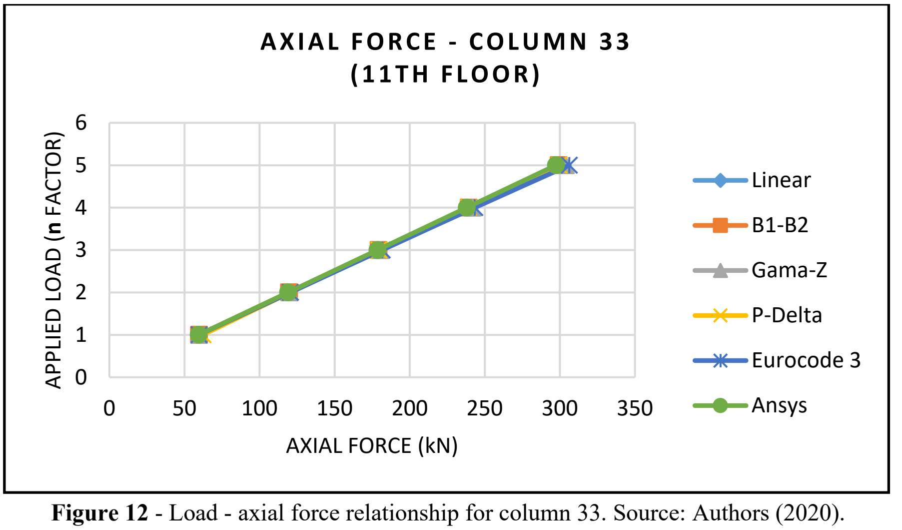

Figure 12 - Load - axial force relationship for column 33. Source: Authors (2020).

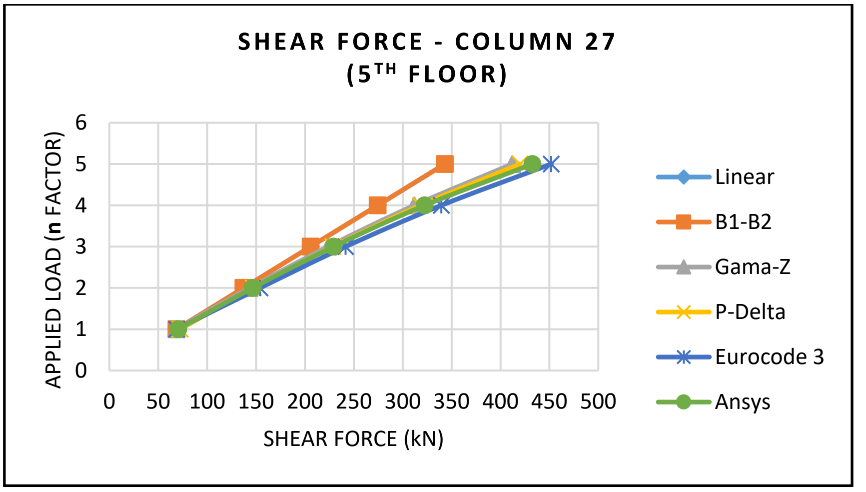

Figure 13 - Load - shear force relationship for column 27. Source: Authors (2020).

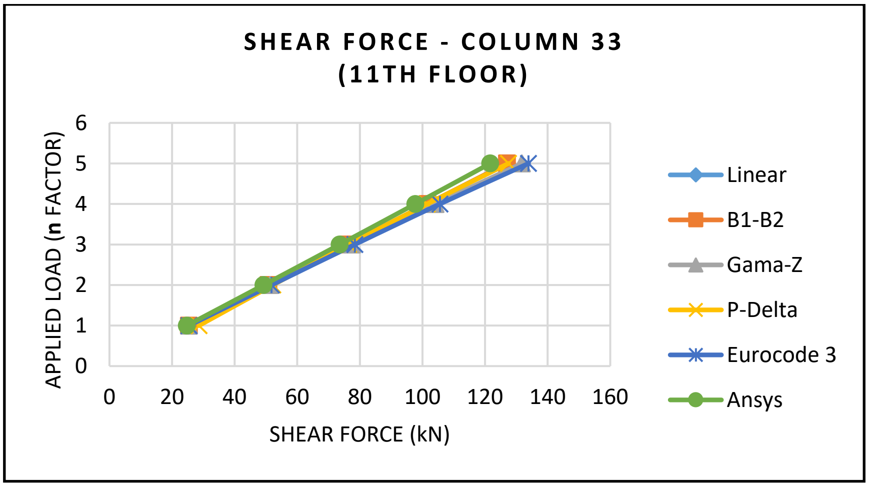

Figure 14 - Load - shear force relationship for column 33. Source: Authors (2020).

4 RESULTS AND DISCUSSIONS

4.1 Example 1: Single span single story frame

Concerning the analysis of displacements, the exact analysis performed with Ansys presents the most conservative results, followed by γ_Z coefficient and the Eurocode method, known for overestimating horizontal loads. However, according to ANSI/AISC-360-16 [10], the amplified displacements should not be taken as an accurate depiction of reality, and here they only serve as a parameter for qualitative analysis.

Results for bending moments obtained via the $B_1 - B_2$ method are the closest to Ansys. Remaining methods yielded similar results between them and differ from the exact analysis by approximately 17.5%.

All methods present similar results for axial forces, with a maximum observed difference of 1%. This is not the case for the values of shear force, which show significant difference between the exact analysis and the other methods, the γ_Z method presenting the largest value of maximum shear force acting on the structure.

4.2 Example 2: Frame with eleven stories and two spans

Figure 9 (Load - bending moment relationship), for column 27, indicates that the approximate methods show good correlation among them up to $n = 2$, with a mean percentage deviation of 3.0%, being the $B_1 - B_2$ method and the γ_z

coefficient the ones performing the major percentual difference (about 7.0%) among them. For larger values of factor n, methods P-delta and γ_z coefficient show similar behavior (less than 2% of percentage difference) and become less conservative than the other implemented methods.

It is worth noting that for $n=3$, the γ_z coefficient method practically reaches the applicability limit ($\gamma_z \leq 1.3$) recommended by NBR 6118-2014 [9], as well as, the $B_1 - B_2$ method, that also reaches the applicability limit ($B_2 \leq 1.4$) recommended by NBR 8800:2008 [11], for columns 2 to 6. The Eurocode method only reaches its applicability limit ($3 \leq \alpha_{cr} < 10$) for $n=5$, with $\alpha_{cr} = 2.54$.

Figure 10 (Load - bending moment relationship) shows overall similarity of results between methods up to $n=4$. For $n=5$, the γ_z method and the Eurocode method yield the largest results, this is so because the value of the coefficients used in these methods (determined only once for the entire structural system) is also larger than that used in the other approaches.

Figure 11 (column 27) reveals that the axial force values determined by the methods diverge for $n \geq 4$. On the other hand, Figure 12 (column 33) presents similar results for all methods. This result shows that second order effects have a lower influence on axial forces than on the bending moment behavior, for example.

The shear force analysis of column 27 shows that MAES diverges from the other methods for $n \geq 2$. This can be explained by the fact that MAES does not amplify the shear forces. For column 33, however, the degree of agreement of the results of all methods is acceptable.

5 CONCLUSIONS

The subject studied herein has been extensively researched since the 1970s and, considering its relevance, especially for the design of tall and slender structures, it is still challenging for structural engineers and researchers. As such, this paper presented, in a complete and yet simple manner, a comparison between numerous approximate methods with the objective of enriching discussions about this important field of study.

In summary, the presented approximate methods for elastic second-order analysis of structures show a good degree of agreement of results when applied within their recommended applicability limits, in the case of the $B_1 - B_2$ method ($B_2 \leq 1.4$), the γ_z coefficient ($\gamma_z \leq 1.3$) and the Eurocode 3 method - α_{cr} factor ($3 \leq \alpha_{cr} < 10$). This study also showed that methods that amplify horizontal loads or include fictitious lateral forces tend to accentuate shear force values, being closer to the to those obtained by the geometrically exact analysis.

This closing paragraph is taken as an opportunity to reinforce the limitations of approximate methods. Chen and Toma [18] report that approximate methodologies are recommended only for regular framed structures subjected to regular load distributions. EN 1993-1-1:2005 [13] stresses that the approximate method is acceptable for regular framed structures subject to a regular loading. Dória et al. [19] state that methods based on the ratio Δ_2 / Δ_1 are not adequate to assess second-order effects in structures. Instead of the B_2 factor, these authors suggest the α_{cr} factor, from Eurocode 3, as a more adequate indicator of the importance of second-order effects in structures.

ACKNOWLEDGEMENTS

The authors would like to thank Capes, CNPq and Fapes for the financial support.

REFERENCES

[1] D. M. Oliveira, "Estudo dos processos aproximados utilizados para a consideração das não-linearidades física e geométrica na análise global das estruturas de concreto armado," Ph.D. dissertation, Univ. Fed. Minas Gerais, Belo Horizonte, 2007.

[2] M. R. Horne, "An approximate method for calculating the elastic critical loads of multi-storey plane frames," *Struct. Eng. J.*, vol. 53, no. 6, pp. 242–248, Jun 1975.

[3] B. R. Wood, P. F. Adams, and D. Beaulieu, "Column design by P delta method," *J. Struct. Div.*, vol. 102, no. ST2, pp. 411–427, Feb 1976.

[4] W. J. LeMessurier, "A practical method of second order analysis part 1 – pin jointed systems," *Eng. J.*, vol. 13, pp. 89–96, 1976.

[5] W. J. LeMessurier, "A practical method of second order analysis part 2 – rigid frames," *Eng. J.*, vol. 14, pp. 49–67, 1977.

[6] M. Franco, *Problemas de Estabilidade nos Edifícios de Concreto Armado: Publicação Técnica*. São Paulo: Inst. Eng., 1985.

[7] M. Franco and A. C. Vasconcelos, *Avaliação Prática dos Efeitos de 2° Ordem em Edifícios Altos: Publicação Técnica*. São Paulo: Inst. Eng., 1991.

[8] A. C. Vasconcelos, “Critérios para dispensa de consideração do efeito de 2ª ordem,” in *Reun. An. IBRACON: Colóq. Estabil. Glob. Estrut. Concr. Armado*, São Paulo, 1985.

[9] Associação Brasileira de Normas Técnicas, *Projeto de Estruturas de Concreto, Procedimento*, NBR 6118, 2014.

[10] American Institute of Steel Construction, *Manual of Steel Construction-Load and Resistance Fator Design Specification for Structural Steel Buildings*, ANSI/AISC 360-16, 2016.

[11] Associação Brasileira de Normas Técnicas, *Projeto de Estruturas de Aço e Estruturas Mistas de Aço e Concreto de Edifícios*, NBR 8800, 2008.

[12] Associação Brasileira de Normas Técnicas, *Projeto de Estruturas de Aço e Estruturas Mistas de Aço e Concreto de Edifícios*, NBR 8800, 1986.

[13] European Standard, *Design of Steel Structures - Part 1-1. General Rules and Rules for Buildings*, Eurocode 3, 2005. [English version].

[14] R. L. G. Silva, “Avaliação dos efeitos de 2º ordem em edifícios de aço utilizando métodos aproximados e análise rigorosa,” M.S. thesis, Univ. Fed. Minas Gerais, Belo Horizonte, 2004.

[15] R. D. Ziemian, *Guide to Stability Design Criteria for Metal Structures*. USA: Wiley, 2010.

[16] A. Rutenberg, "A direct P-delta analysis using standard plane frame computer programs," *Comput. Struc.*, vol. 14, pp. 97–102, Feb 1981.

[17] E. Wilson and A. Habibullah, "Static and dynamic analysis of multi-story buildings including P-Delta effects," *Earthq. Spectra*, vol. 3, no. 2, pp. 289–298, May 1987.

[18] W. F. Chen and S. Toma, *Advanced Analysis of Steel Frames*. Boca Raton: CRC Press, 1994.

[19] A. S. Dória, M. Malite, and L. C. M. Vieira, “On frame stability analysis,” in *Proc. Ann. Stab. Conf.*, Missouri, 2013.

[20] C. Carter, *The Evolution of Stability Provisions in the AISC Specification, Steel Day Eve.* New York: AISC, 2013.

[21] D. W. White, A. E. Surovek, B. N. Alemdar, C.-J. Chang, Y. D. Kim, and G. H. Kuchenbecker, "Stability analysis and design of steel building frames using the 2005 AISC specification," *Steel Struct.*, vol. 6, pp. 71–91, 2006.

[22] A. Badke-Neto and W. G. Ferreira, *Dimensionamento de Elementos de Perfis de Aço Laminados e Soldados: Com Exemplos Numéricos*, 3a ed. Vitória: GSS, 2016.

[23] I. MacPhedran and G. Grondin, “A brief history of beam-column design,” in *CSCE Ann. Gen. Meet. Conf.*, Yellowknife, 2007.

[24] Y. P. Souza et al., *Introdução à Teoria da Estabilidade Elástica - Conceitos, Implementações Computacionais e Aspectos Normativos*. 3a ed. Vitória: LBF, 2018.

[25] W. B. Ferreira, L. A. R. Luchi and W. G. Ferreira, “Estabilidade de estruturas projetadas com lajes planas protendidas,” in *The 7th Int. Struct. Eng. Constr. Conf. – New Develop. Struct. Eng. Constr.*, Honolulu, 2013.

[26] J. M. Araújo, *Projeto Estrutural de Edifícios de Concreto Armado*, 3a ed. Rio Grande: Dunas, 2014.

[27] A. C. Avakian, Estruturas aporticadas mistas aço-concreto: avaliação de metodologias de análise,” M.S. thesis, Univ. Fed. Rio de Janeiro, Rio de Janeiro, 2007.

[28] Canada Standards Association, *Limits States Design of Steel Structures*, CAN/CSA-S16.1-M94, 1994.

[29] C. Bernuzzi and B. Cordova, *Structural Steel Design to Eurocode 3 and AISC Specifications*. Oxford: John Wiley & Sons, 2016.

[30] J.-P. Muzeau, *La Construction Métallique Avec les Eurocodes*. Saint-Denis, France: Afnor et Groupe Eyrolles, 2014.

Author contributions: LBL: conceptualization, writing, numerical simulation; WGF: conceptualization, writing, data curation, supervision; PMMPPC: writing, data curation, formal analysis; AMCS: data curation, formal analysis, final review.

Editors: Sergio Hampshire C. Santos, Guilherme Aris Parsekian.

IBRACON Structures and Materials Journal
Revista IBRACON de Estruturas e Materiais
ISSN 1983-4195 ismj.org

ORIGINAL ARTICLE

Optimized design of concrete-filled steel columns

Dimensionamento otimizado de pilares mistos de aço preenchidos com concreto

Jéssica Salomão Lourenção[a]
Paulo Augusto Tonini Arpini[a]
Gabriel Erlacher[a]
Élcio Cassimiro Alves[a]

[a]Universidade Federal do Espírito Santo – UFES, Departamento de Engenharia Civil, Vitória, ES, Brasil

Received 13 October 2020
Accepted 16 April 2021

Abstract: The objective of this paper is to present the formulation of the optimization problem and its application to the design of concrete-filled composite columns with and without reinforcement steel bars, according to recommendations from NBR 8800:2008, NBR 16239:2013 and EN 1994-1-1:2004. A comparative analysis between the aforementioned standards is performed for various geometries considering cost, efficiency and materials in order to verify which parameters influence the solution of the composite column that satisfies the proposed problems. The solution of the optimization problem is obtained by using the genetic algorithm method featured in MATLAB's guide toolbox. For the examples analyzed, results show that concretes with compressive strength greater than 50MPa directly influence the solution of the problem regarding cost and resistance to normal forces.

Keywords: composite filled columns, optimization, hollow sections, genetic algorithm.

Resumo: O objetivo deste trabalho é apresentar a formulação do problema de otimização e suas aplicações para pilares mistos de aço preenchidos com concreto, com e sem armadura, segundo as normas ABNT NBR 8800:2008, ABNT NBR 16239:2013 e EN 1994-1-1:2004. Uma análise comparativa entre as normas supracitadas e entre as geometrias estudadas em termos de custo, eficiência, contribuição dos materiais na solução é realizada de modo a verificar os parâmetros que influenciam na solução do pilar misto que satisfaça os problemas propostos. A solução do problema de otimização, é obtida através do Método do Algoritmo Genético disponível no toolbox do Matlab. Para os exemplos analisados, os resultados apontam que os concretos com resistência acima de 50MPa influenciam diretamente na solução do problema tanto no custo, quanto no esforço normal resistente.

Palavras-chave: pilares mistos preenchidos, otimização, perfis tubulares, algoritmo genético.

How to cite: J. S. Lourenção, P. A. T. Arpini, G. Erlacher, and E. C. Alves, "Optimized design of concrete-filled steel columns," *Rev. IBRACON Estrut. Mater.*, vol. 15, no. 1, e15102, 2022, https://doi.org/10.1590/S1983-41952022000100002

1 INTRODUCTION

When filled with concrete and subjected to compression, tubular steel profiles are commonly referred to as composite filled columns. The combined use of steel and concrete in structural elements is widely used in civil construction since it presents a number of advantages such as increased load bearing capacity, dismissal of wooden formwork during construction and protection against fire and corrosion.

Composite filled columns usually employ steel profiles with rectangular (RHS), square (SHS) or circular (CHS) hollow sections as outer casing, with or without the addition of longitudinal rebar, depending on load type and magnitude. In Brazil, procedures for the design of concrete-filled composite columns are currently prescribed by ABNT NBR 8800 [1] – Design of steel structures and steel-concrete composite structures. However, particularities concerning the structural behavior of tubular steel profiles resulted in the publication of ABNT NBR 16239 [2] – Design of steel structures and

Corresponding author: Élcio Cassimiro Alves. E-mail: elcio.calves1@gmail.com
Financial support: None.
Conflict of interest: Nothing to declare.

steel-concrete composite structures featuring tubular profiles, by the Brazilian Association of Technical Standards. This standard was created to provide specific equations for the design of composite filled columns, since ABNT NBR 8800 [1] only presents one curve for determining the reduction factor associated with axial strength as a function of slenderness, for all types of composite columns, without distinction, which considerably underestimates the ultimate strength of composite filled columns. In Europe, the design of composite columns is standardized by EN 1994-1-1 [3] – Design of steel-concrete composite columns – Part 1-1: General rules and rules for buildings.

Since numerous cross-section geometries are available for composite columns, it may be challenging to define the best and most cost-efficient option, that is, the optimum geometry for a given load configuration and other parameters that influence the ultimate strength of the structural element. Generally, the variables bearing the most influence on the final cost of composite filled columns are: the cost of concrete, which depends on compressive strength, the cost of the structural profile and the cost of longitudinal rebar. It is highlighted here that structural connections and architectural aspects are not included in the scope of this research. Furthermore, costs attributed to labor are directly proportional to the topology of the structure. Previous studies indicate that the use of optimization techniques during structural design results in a 15% to 20% reduction in weight and/or dimensions of structural elements [4], [5].

Optimal cross-sections may be obtained by inserting structural optimization techniques in computer programs that perform iterative calculations, in which design variables are updated until the minimum cost for a given column is determined. This procedure must also account for structural safety and stability criteria defined by design standards. However, authors such as Santoro and Kripka [6] and Tormen et al. [7] stress that using financial cost as the only optimization parameter is not enough to arrive at an optimum solution, additional variables such as CO_2 emissions attributed to the life-cyle of materials may also be a preponderant factor for determining the best result.

This research aims to present the formulation for the design optimization of concrete-filled composite columns with and without longitudinal rebar, in addition to comparing results between the design standards ABNT NBR 8800 [1], ABNT NBR 16239 [2] and EN 1994-1-1 [3]. Numerical examples are presented, and results for different standards and geometries are compared, considering the structure at ambient temperature. The program was developed with the Guide tool and the optimization problem was solved using the Genetic Algorithm *toolbox* from Matlab. Finally, the results obtained are used for determining which parameters bear the most influence on the final cost and efficiency of the structures analyzed herein.

2 BIBLIOGRAPHY REVIEW

In recent decades, concrete-filled steel-concrete composite columns have been the subject of numerous experimental, theoretical and numerical studies.

De Nardin [8] performed experiments to assess the influence of cross-section geometry and thickness of the tubular profile on the axial strength of composite filled columns. The study included SHS, CHS and RHS profiles filled with concrete. Results obtained for ultimate strength were similar to those observed experimentally, even without considering concrete confinement effects.

Duarte et al. [9] compared the axial strength of composite columns filled with conventional and rubberized concrete. Both types of column present similar results concerning the total energy absorbed, but the rubberized concrete increased the ductility of structural elements and reduced environmental impacts by using discarded tires and less natural aggregates.

Dundu [10], analyzed the behavior of 24 steel-concrete composite columns axially compressed until structural failure. Specimens were divided into two groups, with differences in the strength of steel and concrete, as well as different column diameters. The first group featured the use of concrete with higher compressive strength, and presented the buckling of the gross composite section as an ultimate limit state. The second group was characterized by columns with larger diameter and stronger steel, reaching structural failure by concrete crushing and yielding of the steel section. Experimental results were observed to be conservative when compared to strength predictions from EN 1994-1-1 [3].

Gajalakshmi and Helena [11] performed an experimental analysis of the damage observed in composite filled columns subjected to quasi-static loading. The tests were divided into two phases: During the first phase, specimens were subjected to loads with variations in amplitude and constant axial forces while the second phase featured constant amplitudes. Results show an increase in the ductility of the structure, which was able to absorb twice the amount of energy in some cases.

Kuranovas et al. [12] analyzed experimental data from 1303 concrete-filled steel columns. Specimens featured CHS and RHS subjected to compression and to axial-compression and bending-. Experimental results were compared to strength predictions from EN 1994-1-1 [3], and good agreement was observed when compared to the literature for concretes with compressive strength of up to 75MPa, value in which the ultimate load obtained experimentally is observed to be inferior and thus more conservative than results obtained using Eurocode.

Caldas et al. [13] performed a study to assist in the review of ABNT NBR 8800:1986 and presented procedures for the design of concrete-filled steel-concrete composite columns subjected to combined bending moment and axial force.

The study was based on the European standard EN 1994-1-1 [3] and the American standard ANSI/AISC 360-05, both of which served as the theoretical basis for the proposal of two design procedures for the review. Authors compared the results obtained with the proposed models to a finite element analysis, and observed acceptable agreement. Furthermore, design model I is observed as more conservative than design model II since the former is a simplified formulation originally proposed for the design of steel structures. This behavior becomes more evident when both models are applied to columns with relatively smaller slenderness and lower values of steel contribution factors.

Oliveira [14] studied the behavior of circular composite filled columns by performing a theoretical-experimental analysis to assess the influence of compressive strength of concrete, column slenderness, tube thickness and load type on the ultimate strength of the structural elements. Experimental tests were performed in 64 columns subjected to pure compression. Results were compared to design standards and show that the numerical model accurately represents the behavior of the columns, but the ultimate strengths obtained numerically are lower than those observed experimentally.

Papavasileiou et al. [15] investigated the cost-benefit ratio of concrete-encased composite columns and composite filled columns as an alternative for the use of steel I-beam columns. A comparison between column types was performed using structural optimization, seeking to minimize financial costs and safety restrictions imposed by EN 1993-1-1:2005 and EN 1994-1-1:2004. Optimized results favor the use of composite elements in structural systems that require an increased number of columns. The authors also indicate that fire-resistance is amplified when composite columns are used.

Aghdamy et al. [16] presented a study on the design of concrete-filled composite columns subjected to axial and lateral impact loads. The model proposed by the authors accounts for the effects attributed to concrete confinement. The ratio between tube thickness and diameter, slenderness ratio and impact speed were observed as the governing factors for determining ultimate strength.

Tao et al. [17] evaluated the effects of concrete confinement in concrete-filled tubular columns subjected to axial compression. The analysis was performed by introducing novel functions for determining parameters related to confined concrete. The proposed model was observed as more versatile than other experimental approaches. Adjustments of the model are also proposed in order to allow the consideration of concretes with higher compressive strengths.

Thai et al. [18], proposed a hybrid elasto-plastic model to show the effects of considering initial local geometric imperfections and residual stresses in second order analyses of the structure.

Wang et al. [19] elaborated simplified systems to determine the axial strength of steel-concrete composite tubular columns. The ultimate strength, axial stiffness and yield strength of steel of the structural elements was determined via finite element analysis. The numerical models proved useful for evaluating the ductility and strain capacity of structural elements.

Improvements introduced by ABNT NBR 16239 [2] in relation to ABNT NBR 8800 [1] are detailed by Canales [20], since the most recent standard prescribes a specific procedure in item 1.3 b for the design of bars subjected to compression and featuring seamless hot-rolled tubular steel profiles or heat treated profiles with and without longitudinal welds. The new methodology allows a more efficient and economical design of composite filled columns if compared to ABNT NBR 8800 [1]. The author provided spreadsheets to assist in the design of steel tubular columns and composite filled columns. Results show that the improvements detailed on the most recent standard directly impacts the magnitude of the compressive design strength of columns, since the design procedures from ABNT NBR 8800 [1] are more efficient for cases in which the steel profile significantly contributes for the ultimate strength of the composite column.

Studies on the design optimization of steel-concrete composite filled columns are relatively recent. Among existing research papers, Papavasileiou and Charmpis [21] present a cost-optimization study of steel-concrete composite beams and columns in multi-story buildings subjected to seismic loading. The authors implemented a probabilistic optimization method similar to Genetic Algorithms called “Evolution Strategies”. The method proved to be efficient when applied to practical scenarios.

Lourenção and Alves [22] used Matlab to develop a formulation for minimizing the total cost of composite filled columns, following prescriptions from ABNT NBR 8800 [1] and from ABNT NBR 16239 [2]. Solutions were obtained using the interior point method and sequential quadratic programming, considering tube dimensions as continuous variables. Results indicated a significant reduction in the total cost of composite filled columns in comparison to other methods available in the pertinent literature.

Pekbey et al. [23] performed analyses to determine column shapes able to bear the highest ultimate load without inducing buckling, considering column height and volume as problem variables. As such, optimization procedures were developed to maximize the lowest eigenvalue via analyzing the total volume of the composite column. The optimization model was validated by comparing results with a numerical analysis performed with Ansys and experimental examples. Optimized results showed that the experimental data used as reference provided inaccurate indications of optimal cross-section.

Brauns and Skadins [24] proposed a formulation of the optimization problem for concrete filled columns aimed at minimizing the stress distribution on the internal walls and along the thickness of the profile. They concluded that the optimization of working conditions and cross section area of a composite structure, as well as the prevention of failure due to insufficient thickness of structural steel and fire may be obtained by using appropriate strengths for concrete and steel.

Despite the publication of numerous studies on composite filled columns in recent years, optimization analyses using genetic algorithms (GA) and featuring a comparison between prescriptions from ABNT NBR 8800 [1], ABNT NBR 16239 [2] and EN 1994-1-1 [3] are not observed in the literature. Table 1 presents the most notable experimental and numerical studies focused on the design of composite filled columns. The bottom line of the table presents the main characteristics of the optimization procedure proposed in this paper, included in order to provide an overview of the main differences in comparison with other methods, namely the inclusion of genetic algorithm optimization based on the aforementioned standards, as well as the consideration of high strength concrete.

2.1 Genetic Algorithm Method

The genetic algorithms proposed by John Holland during the 60's are mathematical models inspired by the principles of Darwinian natural selection, in which, given an initial population, new populations are created by genetic crossing, and the most suitable individuals are selected as the solution of a given problem.

Examples of GA applied to structural engineering include the optimization of steel-concrete composite beams [25], spatial steel frames [4], [26], railway viaducts [27], bridges [28]–[30] and life-cycle analysis of bridges [31]. The present work uses the Genetic algorithm native to the *Optimization Toolbox*™ from Matlab 2016a, namely the function ga. The initial population contains 120 individuals and the following, 60. The rate of elite individuals and crossing of the intermediate type are 0,05 and 0,8, respectively, whereas the mutation rate is random. The GA is performed primarily with an entirely random initial population, thereby obtaining an optimal local response. Subsequently, the algorithm is executed again with the previously obtained answer added to the initial population. More details can be found on the Matlab documentation.

Table 1 – Most notable studies on composite columns.

Author	Version of ABNT NBR 8800	ABNT NBR 16239	EN 1994-1-1	High strength concrete	Numerical Analysis	Theoretical-experimental analysis	Design	Continuous optimization	GA Optimization
De Nardin [8]	1986			x		x			
Pekbey et al. [23]					x		x	x	
Caldas et al. [13]	1986				x		x		
Oliveira [14]						x			
Dundu [10]						x			
Gajalakshmi and Helena [11]						x			
Tao et al. [17]					x	x			
Papavasileiou et al. [15]			x					x	
Canales [20]	2008	x					x		
Thai et al. [18]					x	x	x		
Aghdamy et al. [16]					x	x	x		
Papavasileiou and Charmpis [21]							x	x	
Papavasileiou and Charmpis [21]					x		x	x	
Duarte et al. [9]						x			
Wang et al. [19]						x			
Wang et al. [19]					x		x		
Brauns and Skadins [24]					x		x	x	
Kuranovas et al. [12]			x	x		x	x		
Lourenção and Alves [22]	2008	x					x	x	
PRESENT PAPER	2008	x	x	x			x		x

3 FORMULATION OF THE OPTIMIZATION PROBLEM

The design of composite filled columns is based on determining the loads acting on the structure, followed by comparing load values with the pertinent design resistances. As such, the optimization problem is based on finding an optimal solution that minimizes a pre-determined objective or fitness function, which in this case is total cost of the column. The function to be minimized in this research is given by Equation 1 and includes the costs of concrete, steel profile and reinforcement steel bars.

$$f_{(min)} = C_c A_c L + C_a A_a L \rho_a + C_s A_s L \rho_s \tag{1}$$

In Equation 1, C_c = cost of industrial concrete (R$/m^3); A_c = cross-section are of concrete (m^2); C_a = cost of the steel profile (not including the type of tubular profile) (R$/kg); A_a = cross-sectional area of profiled steel (m^2); ρ_a = specific mass of the steel profile (kg/m^3); C_s = cost of longitudinal steel reinforcement (R$/kg); A_s = Cross-sectional area of steel reinforcement (m^2); ρ_s = specific mass of steel reinforcement (kg/m^3); and L = length of the column under analysis (m).

3.1 Design Variables

The design variables of the computer program developed for this research are shown in Figure 1, according to cross-section type:

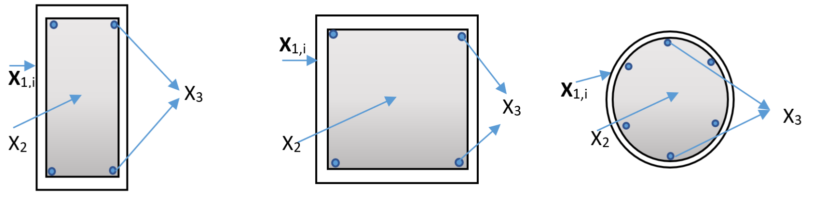

Figure 1. Groups of parameters that define the design variables.

Where:

$x_{1,i}$ – vector containing the geometric properties of the tubular profile, extracted from commercially available tubular profile catalogues. The definition of each vector element according to cross-section type is given by Table 2.

Table 2 – Definition of design variables.

Variables	Rectangular Section	Square Section	Circular Section
Width	$x_{1,1} = b$	$x_{1,1} = b = h$	-
Height	$x_{1,2} = h$	$x_{1,1} = b = h$	-
Diameter	-	-	$x_1 = d$
Thickness	$x_{1,3} = t$	$x_{1,2} = t$	$x_{1,2} = t$
Area of Steel	$x_{1,4} = A_a$	$x_{1,3} = A_a$	$x_{1,3} = A_a$
Moment of inertia - *x* axis	$x_{1,5} = I_{ax}$	$x_{1,4} = I_{ax}$	$x_{1,4} = I_{ax}$
Moment of inertia - *y* axis	$x_{1,6} = I_{ay}$	$x_{1,5} = I_{ay}$	$x_{1,5} = I_{ay}$
Plastic section modulus - x axis	$x_{1,7} = Z_{ax}$	$x_{1,6} = Z_{ax}$	$x_{1,6} = Z_{ax}$
Plastic section modulus - y axis	$x_{1,8} = Z_{ay}$	$x_{1,7} = Z_{ay}$	$x_{1,7} = Z_{ay}$

x_2 – represents the characteristic strength of concrete, that may vary throughout the optimization process; x_3 – total cross-section area of longitudinal reinforcement taken as a discrete variable as a function of the number of bars, if applicable.

3.2 Constraint Functions

The constraints of the problem are taken from the three standards. Interaction curves ($N \times M$) for each standard are given in Figure 2.

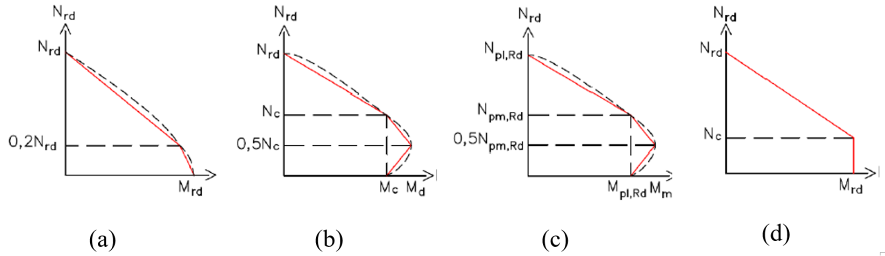

Figure 2 – Interaction diagrams for bending moment vs. axial force –**(a)** Design model I ABNT NBR 8800 [1]; **(b)** Design model II ABNT NBR 8800 [1]; **(c)** ABNT NBR 16239 [2]; **(d)** EN 1994-1-1 [3].

3.2.1 ABNT NBR 8800 [1] and ABNT NBR 16239 [2]

- Resistant design forces must be larger than applied design loads

$$N_{Rd} \geq N_{Sd} \tag{2}$$

$$M_{x,Rd} \geq M_{x,Sd} \tag{3}$$

$$M_{y,Rd} \geq M_{y,Sd} \tag{4}$$

Where: N_d, $M_{x,d}$, $M_{y,d}$ are the design resistance to axial force and design resistance to bending moment about the x and y axes, respectively, with subscript *R* indicating resistant, and subscript *S* indicating applied load.

- Resistance to combined loads must be higher than applied combined loads
  - Design model I (ABNT NBR 8800 [1]):

$$\frac{N_{Sd}}{N_{Rd}} \geq 0,2 \quad \frac{N_{Sd}}{N_{Rd}} + \frac{8}{9}\left(\frac{M_{x,Sd}}{M_{x,Rd}} + \frac{M_{y,Sd}}{M_{y,Rd}}\right) \leq 1,0 \tag{5}$$

$$\frac{N_{Sd}}{N_{Rd}} < 0,2 \quad \frac{N_{Sd}}{2N_{Rd}} + \left(\frac{M_{x,Sd}}{M_{x,Rd}} + \frac{M_{y,Sd}}{M_{y,Rd}}\right) \leq 1,0 \tag{6}$$

  - Design model II (ABNT NBR 8800 [1]):

$$\frac{M_{x,tot,Sd}}{\mu_x M_{c,x}} + \frac{M_{y,tot,Sd}}{\mu_y M_{c,y}} \leq 1,0 \tag{7}$$

  - Design model from ABNT NBR 16239 [2]:

$$N_{Sd} \leq N_c \quad \frac{M_{x,Sd}}{M_{x,Rd}} + \frac{M_{y,Sd}}{M_{y,Rd}} \leq 1,0 \tag{8}$$

$$N_{Sd} > N_c \quad \frac{N_{Sd} - N_c}{N_{Rd} - N_c} + \frac{M_{x,Sd}}{M_{x,Rd}} + \frac{M_{y,Sd}}{M_{y,Rd}} \leq 1,0 \tag{9}$$

The design resistance to axial force is given by:

$$N_{Rd} = \chi N_{pl,Rd} \tag{10}$$

Where χ is the reduction factor and $N_{pl,Rd}$ is the design plastic resistance to normal forces of the gross cross-section, given by Equation 11.

$$N_{pl,Rd} = A_a f_{yd} + \alpha A_c f_{cd} + A_s f_{sd} \tag{11}$$

Where α =0,95 for circular sections and α =0,85 for other section types.

The reduction factor χ is determined by Equations 12 and 13, according to ABNT NBR 8800 [1]. However, ABNT NBR 16239 [2] recommends the use of Equation 14.

$$\lambda_{0,m} \le 1,5 \quad \chi = 0,658^{\lambda_{0,m}{}^2} \tag{12}$$

$$\lambda_{0,m} > 1,5 \quad \chi = \frac{0,877}{\lambda_{0,m}{}^2} \tag{13}$$

$$\chi = \frac{1}{\left(1+\lambda_{0,m}{}^{4,48}\right)^{\frac{1}{2,24}}} \tag{14}$$

Where:

$$\lambda_{0,m} = \sqrt{\frac{N_{pl,R}}{N_e}} \tag{15}$$

Where $N_{pl,R}$ is the value of $N_{pl,Rd}$ with resistance factors γ_a , γ_c and γ_s taken as 1,0 and N_e is the elastic critical buckling load

The modulus of elasticity of concrete is defined according to recommendations from ABNT NBR 6118 [32], since it is a more recent standard.

$$E_c = \propto_i E_{ci} \begin{cases} \propto_i = 0,8 + 0,2\dfrac{f_{ck}}{80} \le 1.0 \\ E_{ci} = \begin{cases} \propto_e 5600\sqrt{f_{ck}} & 20MPa \le f_{ck} \le 50MPa \\ \propto_e 21500\sqrt[3]{f_{ck}+1,25} & 50MPa < f_{ck} \le 90MPa \end{cases} \end{cases} \tag{16}$$

Where: α_e=1,2 if basalt and diabase are used as aggregates, 1,0 for granite and gneiss, 0,9 for granite and 0,7 for sandstone.

- Applicability limits for tubular sections:
  Rectangular Square Circular

$$\frac{x_{1,1}}{x_{1,3}} \le 2,26\sqrt{\frac{E_a}{f_y}}e \tag{17}$$

$$\frac{x_{1,2}}{x_{1,3}} \le 2,26\sqrt{\frac{E_a}{f_y}} \quad \frac{x_{1,1}}{x_{1,2}} \le 2,26\sqrt{\frac{E_a}{f_y}} \quad \frac{x_{1,1}}{x_{1,2}} \le 0,15\frac{E_a}{f_y}$$

Where: E_a is the modulus of elasticity of steel and f_y is the yield strength of steel.

- Steel contribution factor of the composite section

$$0,2 < \delta = \frac{A_a f_{yd}}{N_{Rd}} < 0,9 \tag{18}$$

Where: A_a cross-sectional area of the structural steel profile; f_{yd} is the design yield strength of the profiled steel.

If longitudinal reinforcement is used:

- Number of bars (n_B):
  - o Rectangular and square sections

$$n_B \ge 4 \tag{19}$$

  - o Circular sections

$$n_B \ge 6 \tag{20}$$

- Minimum and maximum area of longitudinal reinforcement

$$max\left(0,004A_c; 0,15\frac{N_{Sd}}{f_{sd}}\right) \le A_s \le 0,04A_c \tag{21}$$

Where: A_c is cross-sectional area of concrete; A_s is the cross-sectional area of longitudinal reinforcement; f_{yd} is the design yield strength of steel for the reinforcement bars.

- Maximum and minimum bar spacing in each direction for:
  - o Rectangular sections

$$s_x = \frac{x_{1,1} - 2x_{1,3} - 2d' - n_{Bx}\varnothing_b}{n_{Bx} - 1} \tag{22}$$

$$max\left(2\,cm; \varnothing_b\right) \le s_x \le min\left[40\,cm; 2min\left(x_{1,1} - 2x_{1,3}; x_{1,2} - 2x_{1,3}\right)\right] \tag{23}$$

$$s_y = \frac{x_{1,2} - 2x_{1,3} - 2d' - n_{By}\varnothing_b}{n_{By} - 1} \tag{24}$$

$$max\left(2\,cm; \varnothing_b\right) \le s_y \le min\left[40\,cm; 2min\left(x_{1,1} - 2x_{1,3}; x_{1,2} - 2x_{1,3}\right)\right] \tag{25}$$

  - o Square sections

$$s_x = \frac{x_{1,1} - 2x_{1,2} - 2d' - n_{Bx}\varnothing_b}{n_{Bx} - 1} \quad (26)$$

$$max\left(2\,cm;\varnothing_b\right) \le s_x \le min\left[40\,cm;2\left(x_{1,1} - 2x_{1,2}\right)\right] \quad (27)$$

$$s_y = \frac{x_{1,1} - 2x_{1,2} - 2d' - n_{By}\varnothing_b}{n_{By} - 1} \quad (28)$$

$$max\left(2\,cm;\varnothing_b\right) \le s_y \le min\left[40\,cm;2\left(x_{1,1} - 2x_{1,2}\right)\right] \quad (29)$$

o Circular sections

$$s = \frac{2\pi\left(\frac{x_{1,1}}{2} - x_{1,2} - d' - \frac{\varnothing_b}{2}\right) - n_B\varnothing_b}{n_B} \quad (30)$$

$$max\left(2\,cm;\varnothing_b\right) \le s \le 40cm \quad (31)$$

3.3 EN 1994-1-1 [3]

Constraints for this standard are identical to those detailed in section 3.2.1, with the exception of the following:

- Resistance to combined loads must by higher than applied combined loads

$$\frac{M_{x,Ed}}{\mu_x M_{pl,x,Rd}} \le \alpha_M \quad (32)$$

$$\frac{M_{y,Ed}}{\mu_y M_{pl,y,Rd}} \le \alpha_M \quad (33)$$

$$\frac{M_{x,Ed}}{\mu_x M_{pl,x,Rd}} + \frac{M_{y,Ed}}{\mu_y M_{pl,y,Rd}} \le 1,0 \quad (34)$$

Where α_m is taken as 0,9 for steels in which $235MPa \le f_y \le 355MPa$ and 0,8 if $420MPa \le f_y \le 460MPa$.

Thus, the design plastic resistance to normal forces of the gross-section for square and rectangular sections are determined by Equation 35. EN 1994-1-1 [3] also accounts for increases in concrete strength induced by concrete confinement effects in circular hollow sections, provided $\lambda < 0,5$ and the ratio $e/D < 0,1$, where e is given by M_{Sd}/N_{Sd} and D is the diameter of the steel profile. Should these conditions be satisfied, the design resistance to normal forces considering concrete confinement for circular sections is given by Equation 40.

$$N_{pl,Rd} = A_a f_{yd} + \alpha A_c f_{cd} + A_s f_{sd} \quad (35)$$

Where $\alpha = 1,0$ for concrete-filled tubular sections and 0,85 for other section types. The normal resistant effort is given by:

$$N_{Rd} = \chi N_{pl,Rd} \tag{36}$$

Where: χ is a resistance reduction factor determined in accordance with EN 1994-1-1 [3].

$$\chi = \frac{1}{\Phi + \sqrt{\Phi^2 - \lambda^2}} \tag{37}$$

and,

$$\Phi = 0,5\left[1 + \alpha\left(\lambda - 0,2\right) + \lambda^2\right] \tag{38}$$

In which,

$$\lambda = \sqrt{\frac{N_{pl,Rk}}{N_{cr}}} \tag{39}$$

Where $N_{pl,Rk}$ is equal to $N_{pl,Rd}$ if resistant factors γ_a , γ_c e γ_s are taken as 1,0.

For circular sections, the plastic resistance to normal forces for the gross-section is given by:

$$N_{pl,Rd} = \eta_a A_a f_{yd} + A_c f_{cd}\left(1 + \eta_c \frac{t}{d}\frac{f_{yk}}{f_{ck}}\right) + A_s f_{sd} \tag{40}$$

Where:

$$\eta_c = \begin{cases} \eta_{c0}\left(1 + 10\frac{e}{D}\right) for\ e/D \le 0,1 \\ 0 \qquad\qquad for\ e/D > 0,1 \\ \eta_{c0} = 4,9 - 18,5\lambda + 17\lambda^2 \end{cases} \tag{41}$$

$$\eta_a = \begin{cases} \eta_{a0} + \left(1 - \eta_{a0}\right)\left(10\frac{e}{D}\right) for\ e/D \le 0,1 \\ 1 \qquad\qquad for\ e/D > 0,1 \\ \eta_{a0} = 0,25\left(3 + 2\lambda\right) \end{cases} \tag{42}$$

- Applicability limit for tubular sections:
  Rectangular Square Circular

$$\frac{x_{1,1}}{x_{1,3}} \le 52\sqrt{\frac{235}{f_y}}\, e$$

$$\frac{x_{1,2}}{x_{1,3}} \leq 52\sqrt{\frac{235}{f_y}} \quad \frac{x_{1,1}}{x_{1,2}} \leq 52\sqrt{\frac{235}{f_y}} \quad \frac{x_{1,1}}{x_{1,2}} \leq 90\sqrt{\frac{235}{f_y}} \tag{43}$$

If longitudinal reinforcement is used:

- Number of bars (n_B):
    - o Rectangular and Square sections

$$n_B \geq 4 \tag{44}$$

- o Circular sections

$$n_B \geq 4 \tag{45}$$

- Minimum and maximum area of longitudinal reinforcement

$$max\left(0,003A_c;0,10\frac{N_{Sd}}{f_{sd}}\right) \leq A_s \leq 0,06A_c \tag{46}$$

- Minimum and maximum bar spacing in each direction for:
  o Rectangular Sections

$$s_x = \frac{x_{1,1} - 2x_{1,3} - 2d' - n_{Bx}\varnothing_b}{n_{Bx} - 1} \tag{47}$$

$$max\left(2cm;\varnothing_b\right) \leq s_x \leq 40cm \tag{48}$$

$$s_y = \frac{x_{1,2} - 2x_{1,3} - 2d' - n_{By}\varnothing_b}{n_{By} - 1} \tag{49}$$

$$max\left(2cm;\varnothing_b\right) \leq s_y \leq 40cm \tag{50}$$

- o Square Sections

$$s_x = \frac{x_{1,1} - 2x_{1,2} - 2d' - n_{Bx}\varnothing_b}{n_{Bx} - 1} \tag{51}$$

$$max\left(2cm;\varnothing_b\right) \leq s_x \leq 40cm \tag{52}$$

$$s_y = \frac{x_{1,1} - 2x_{1,2} - 2d' - n_{By}\varnothing_b}{n_{By} - 1} \tag{53}$$

$$max\left(2cm;\varnothing_b\right) \leq s_y \leq 40cm \tag{54}$$

o Circular Sections

$$s = \frac{2\pi\left(\frac{x_{1,1}}{2} - x_{1,2} - d' - \frac{\varnothing_b}{2}\right) - n_B \varnothing_b}{n_B} \quad (55)$$

$$max\left(2cm;\varnothing_b\right) \le s \le 40cm \quad (56)$$

4. RESULTS AND DISCUSSION

To illustrate the advantages of implementing the formulation described herein, three case studies are presented, shown in Figure 3. All examples include the three types of cross-section, designed using the three standards previously mentioned, in addition to considering columns with and without longitudinal reinforcement. On the first example, columns are subjected to pure compression; the second example includes bending about one principal axis in addition to compression; and the third considers the level of compression along with bending about both principal axes.

The costs of steel (R$ 5,01/kg) and concrete were extracted from the SINAPI table, composed by Caixa Econômica Federal in March of 2020 [33]. Prices from the table already include labor costs attributed to mixing and pumping the concrete. The modulus of elasticity of concrete is defined considering concretes using granite/gneiss as aggregates. The cost per kilogram of structural profile was obtained from consulting the company Vallourec [34], which informed a price of R$4,50/kg for circular profiles and R$5,50/kg for rectangular profiles. Furthermore, since the examples consider discrete variables, compressive strengths of concrete range from 20MPa to 90MPa in 5MPa increments. The diameter of steel reinforcement bars considered range from 8mm to 16mm, respecting the constraint functions established for minimum and maximum reinforcement area.

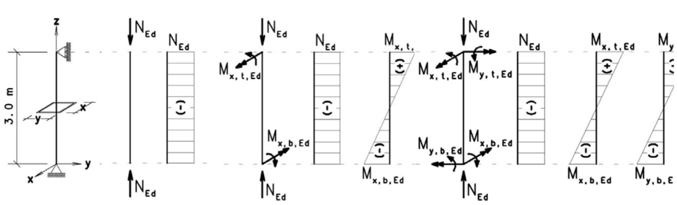

(a) Column (b) Axial Force (Example 1) (c) Combined Flexure (x axis) and Compression (Example 2) (d) Combined Flexure (x and y axes) and Compression (Example 3)

Figure 3 – Sequence of the four load cases analyzed and the respective axial forces and bending moments applied

It is important to note that reference prices obtained are applicable to the southeastern region of Brazil and may differ from other regions of the country. Table 3 summarizes the cost for each material and the source from which they were obtained. Figure 4a presents the data entry screen of the program and Figure 4b shows the result output.

Table 3. Cost of materials

Concrete f_{ck}(MPa)	Average Price (R$/m^3)	Concrete f_{ck}(MPa)	Average Price (R$/m^3)	Source
20	295,00	55	520,13	Table SINAPI – Price of materials (Caixa Econômica Federal). Reference month: February/2020. Locality: Vitória/ES
25	307,42	60	584,82	
30	317,77	65	640,46	
35	329,15	70	696,09	
40	341,57	75	751,73	
45	384,01	80	807,36	
50	455,43	85	891,53	
		90	952,81	
Steel CA50	5,01			
VMB350	4,50			Vallourec. Reference: March/2020
VMB350	5,50			

The Transportation cost of structural profiles usually represent 1% to 3% of the total cost of a steel structural systems. This is comparable to the costs of the structural design (1% to 3%) detailing (2% a 5%) [35] and assembly (20% a 30%) in relation to the cost of the entire structure [36]. Since only isolated structural elements are analyzed here, these values can later be proportionally added to all results.

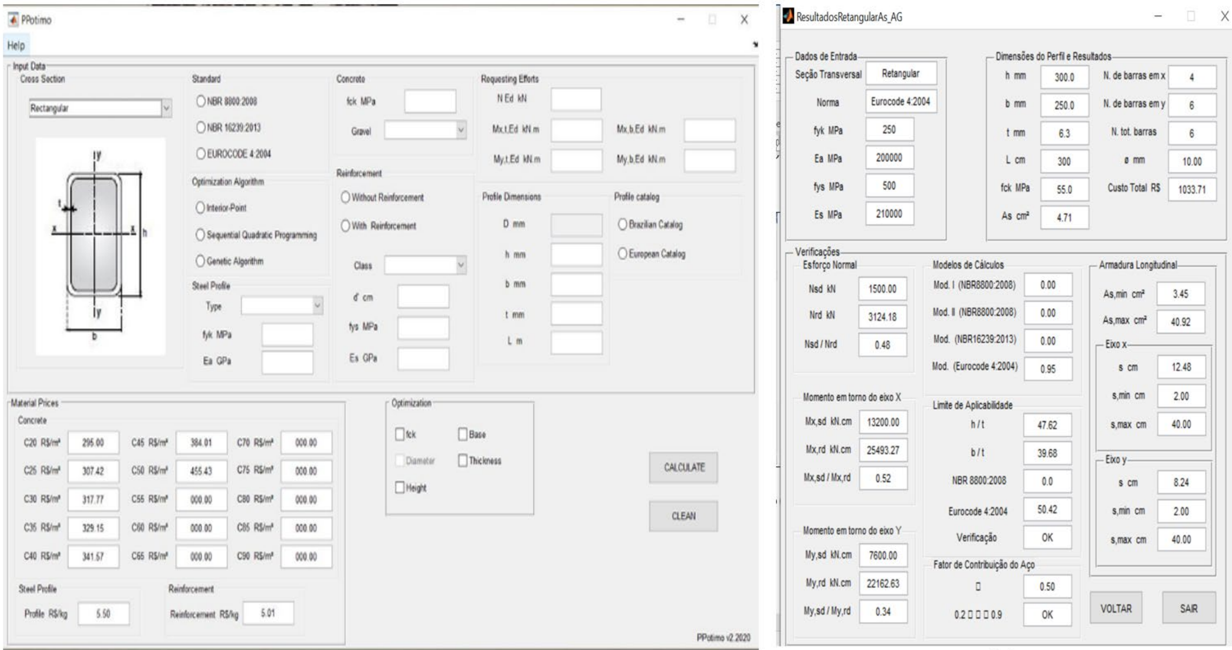

(a) (b)

Figure 4. (a) Input screen of the developed software; **(b)** Output screen.

4.1 Example 1 – Design optimization of columns subjected to pure compression

In this example columns were subjected to an axial force (N_{Sd}) of 1000 kN. The initial solution is a square column with cross-section dimensions b:h of 150 mm, tube thickness of 12,5 mm, compressive strength of concrete (f_{ck}) of 30 MPa, yield strength of steel (f_{yk}) equal to 250 MPa and a length of 3m. All three sections were analyzed and results are shown in Table 4. This example was validated using data from the software PilarMisto 3.04.11 provided by Lourenção and Alves [22] (Caldas et al. [37]) using the standard ABNT NBR 8800 [1]. The active constraint (AC) for all columns in this example was the resistance to normal forces.

As shown in Table 4, in 72% of the solutions, the optimum design features concrete with f_{ck} larger than 50MPa. Even though these grades of concrete are of higher cost, if the ratio cost/strength is considered, the increased expenditure is not a decisive factor. Table 4 also shows that results obtained with GA are lesser in value than the initial solution. Comparing the solution presented by Lourenção and Alves [22], using continuous variables, with the best solution obtained via GA when using ABNT NBR 16239: 2013, it is observed that the final cost of the column is 11.52% more expensive when compared to the square section and 4.6% cheaper when compared to the circular section. However, the value of f_{ck} for the circular sections was the same obtained by Lourenção e Alves[22].

Figure 5 presents graphs for the analyses performed, based on the results obtained. Figure 5a shows the ratio between cost and applied load for different cross-section geometries. For this example, ABNT NBR 16239 [2] produced the best solutions when applied to the design of circular columns without longitudinal reinforcement, followed by EN 1994-1-1 [3]. The least favorable solution is obtained from the design procedure provided by ABNT NBR 8800 [1] considering longitudinal reinforcement.

Table 4 – Optimization Results Example 1: L=3m; N_{Sd}=1000kN

ABNT NBR 8800		D mm	t mm	f_{ck} MPa	N_{Rd} kN	$M_{x,Rd}$ kN·m	$M_{y,Rd}$ kN·m	N	ϕ mm	δ	CT R$	RA
		150:150	**12,5**	**30**	**1555**	**82,29**	**82,29**				**904,60**	
Lourenção e Alves[22] Interior Point Method	ABNT NBR 16239	140,1:141,1	3,6	90	1000,0	27,3	27,3				306,50	N_{Rd}
	ABNT NBR 8800	168,3	5	75	1163,6	37,1	37,1			0,37	316,74	N_{Rd}
Circular without Reinforcement	ABNT NBR 161239	273	6,4	90	1016,8	35,2	35,2			0,52	292,52	N_{Rd}
	EN 1994- 1-1	323,8	6,4	40	1034,2	39,5	39,5			0,46	306,89	N_{Rd}
Circular with Reinforcement	ABNT NBR 8800	323,8	6,4	65	1537,2	90,9	90,9	6	12,5	0,56	570,03	N_{Rd}
	ABNT NBR 16239	273	6,4	55	1692,5	90,9	90,9	6	12,5	0,56	570,03	N_{Rd}
	EN 1994-1-1	323,8	6,4	35	1080,7	47,3	47,3	7	10	0,54	487,09	N_{Rd}
Square without Reinforcement	ABNT NBR 8800	140	6,4	90	1188,9	43,2	43,2			0,46	468,4	N_{Rd}
	ABNT NBR 161239	130	5	80	1002,2	30,3	30,3			0,44	341,8	N_{Rd}
	EN 1994-1-1	140	5	85	1001,7	38,8	38,8			0,45	378,02	N_{Rd}
Square without Reinforcement	ABNT NBR 8800	130	6,4	65	1014,7	37,3	37,3	4	12,5	0,48	474,11	N_{Rd}
	ABNT NBR 16239	120	5,6	90	1001,0	28,8	28,8	6	10	0,41	409,29	N_{Rd}
	EN 1994-1-1	140	5	70	1001,8	41,6	41,6	12	10	0,37	479,32	N_{Rd}
Rectangular without Reinforcement	ABNT NBR 8800	130:180	6,4	70	1217,1	59,6	45,7			0,5	512,32	N_{Rd}
	ABNT NBR 161239	120:160	5	70	1011,6	39,2	30,8			0,45	367,29	N_{Rd}
	EN 1994-1-1	120:170	6,4	70	1037,6	56,4	42,6			0,55	481,98	N_{Rd}
Rectangular with Reinforcement	ABNT NBR 8800	150:200	6,4	25	1293,8	74,5	60,0	6	10	0,62	633,62	N_{Rd}
	ABNT NBR 16239	150:200	6,4	25	1463,4	74,5	60,0	6	10	0,62	633,62	N_{Rd}
	EN 1994-1-1	150:200	6,4	25	1191,3	83,8	67,0	4	10	0,78	615,09	N_{Rd}

Figure 5b presents a comparative analysis between solutions obtained with GA and the initial solution, in addition to comparing solutions for each geometry and the overall optimal solution for this case. All solutions obtained with GA were significantly smaller in magnitude than the initial solution, with the least favorable solution obtained with ABNT NBR 8800 [1] showing a reduction of 40% in relation to the original solution. If solutions are compared with each other, it is observed that the optimum case corresponds to the circular column designed using ABNT NBR 16239 [2]. The least favorable solution corresponds to the rectangular column. The graph also indicates that results obtained with EN 1994-1-1 [3] are very similar to those of ABNT NBR 16239 [2].

Alternatively, Figure 5c presents a composition of the cost of the composite filled column, and Figure 5d shows the contribution of each material to the resistance to normal forces (N_{Rd}) for different geometries. As observed in Figure 5c, the material with the most impact on the cost of the column is the structural profile, accounting for at least 80% of the price. However, the material that most contributes to the resistant strength of the column is the concrete with additional longitudinal reinforcement (Figure 5d), corroborating results obtained via GA.

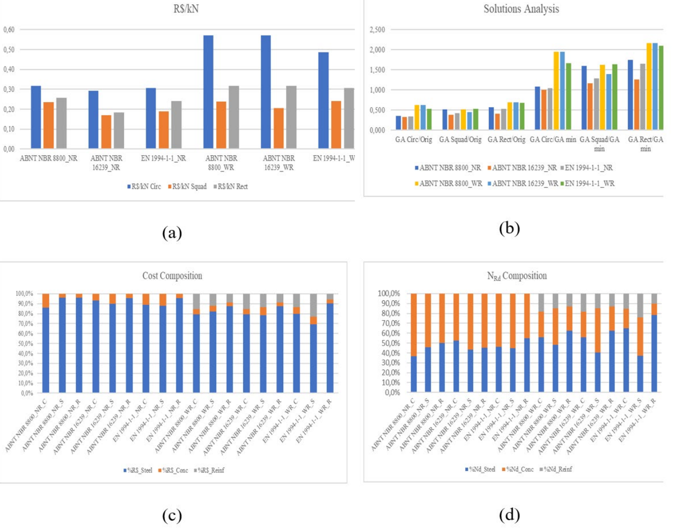

(a) (b) (c) (d)

Figure 5 – (a) Ratio R$/$N_{Sd}$; (b) Ratio AG/Original Solution; (c) Cost composition of composite filled columns (d) Composition of the resistance to normal forces of the composite filled column.

4.2 Example 2 – Design Optimization of Columns Subjected to Combined Axial force and Bending Moment

Columns in this example are subjected to a compressive force (N_{Sd}) of 1500 kN in addition to end moments $\left(M_{x,Sd}\right)$ of magnitude 132 kN·m about the x axis. The initial solution was proposed by Canales [20] using design prescriptions from ABNT NBR 16239 [2], verified by Lourenção and Alves [22] for a circular profile with a diameter of 323,8 mm, wall thickness of 10,3 mm, and a length of 4m, f_{ck} of 30 MPa and f_{yk} of 250 MPa. Table 5 presents the results for this example.

Table 5 – Optimization Results Example 2: L=4m; N_{Sd}=2000kN; $M_{x,Sd}$=132kN·m

Canales [20] ABNT NBR 16239		D mm	t mm	f_{ck} MPa	N_{Rd} kN	$M_{x,Rd}$ kN·m	$M_{y,Rd}$ kN·m	n	ϕ mm	δ	CT R$	RA
		323,8	10,3	30	3430	260,06	260,06				1525,17	
Lourenção e Alves [22] (Interior Point Method)	ABNT NBR 16239	286,2	5,7	90	4377,0	252,8	252,8			0,28	935,80	
Circular without Reinforcement	ABNT NBR 8800	323,8	7,1	80	4803,01	206,317	206,317			0,28	1240,70	IA-I
	ABNT NBR 161239	273	6,4	90	4001,76	132,34	132,34			0,27	960,00	IA-III
	EN 1994-1-1	323,8	6,4	40	3209,85	193,185	193,185			0,44	1005,30	IA-IV
Circular with Reinforcement	ABNT NBR 8800	323,8	6,4	65	4359,09	219,892	219,892	6	12,5	0,28	1211,90	IA-I
	ABNT NBR 16239	273	6,4	55	3275,01	153,045	153,045	6	12,5	0,35	983,80	IA-III
	EN 1994-1-1	323,8	6,4	35	3206,29	213,112	213,112	6	10	0,45	1075,60	IA-IV
Square without Reinforcement	ABNT NBR 8800	270	8	80	4317,56	224,6	224,6			0,38	1648,49	IA-I
	ABNT NBR 161239	240	6,4	70	3310,65	138,6	138,6			0,38	1157,38	IA-III
	EN 1994-1-1	250	6,4	80	3309,53	166,2	166,2			0,37	1221,24	IA-IV
Square without Reinforcement	ABNT NBR 8800	260	8	90	4425,6	214,7	210,9	6	12,5	0,34	1713,77	IA-I
	ABNT NBR 16239	240	6,4	65	3425,52	145,8	149,2	6	12,5	0,36	1261,73	IA-III
	EN 1994-1-1	250	6,4	75	3380,92	171,2	173,6	6	10	0,36	1282,86	IA-IV
Rectangular without Reinforcement	ABNT NBR 8800	200:350	8	75	3643,17	271,241	168,741			0,4	1624,95	IA-I
	ABNT NBR 161239	200:300	6,4	60	2978,92	173,011	123,176			0,41	1139,44	IA-III
	EN 1994-1-1	200:300	6,4	60	2658,45	189,441	135,15			0,42	1139,40	IA-IV
Rectangular with Reinforcement	ABNT NBR 8800	240:280	7,1	85	4239,9	225,889	183,62	8	16	0,3	1686,18	IA-I
	ABNT NBR 16239	200:300	6,4	55	3082,79	182,604	130,653	6	12,5	0,39	1241,36	IA-III
	EN 1994-1-1	200:320	6,4	70	2643,99	254,391	170,676	4	12,5	0,48	1339,07	IA-IV

Table 5 shows that in 89% of cases, the optimum solution is obtained for concretes with f_{ck} larger than 50MPa, with this being the case in 100% of columns featuring square and rectangular sections. The active constraint was the interaction curve for each standard presented in Figure 2, for ABNT NBR 8800 [1], this was the case for the design model I (Figure 2a). Furthermore, ABNT NBR 8800 [1] presents the most conservative results for square and rectangular sections with and without longitudinal reinforcement, with the GA solution presenting a higher cost than the solution found by Canales [20], in which the original column features a circular cross-section. Remaining approaches yielded results smaller than those presented by the author. Among the methodologies tested, once more the optimum solution corresponds to the circular column designed with provisions from ABNT NBR 16239[2], which presented results like those obtained with EN 1994-1-1[1]. Alternatively, the least favorable solutions correspond to the square columns.

Comparing the solution presented by Lourenção and Alves [22], using continuous variables, with the best solution obtained via GA when using ABNT NBR 16239 [2], it is observed that the final cost of the column is 5% more expensive. However, both solutions indicate the same optimal value of f_{ck}

In similar fashion to the previous example, Figure 6 presents an analysis of the solutions and the parameters that influenced them the most.

Figure 6a shows the ratio between cost of the columns and design applied load. The graph shows that ABNT NBR 16239 [2] presents the best solutions for all sections and for all columns without longitudinal steel reinforcement. ABNT NBR 8800 [1] yields the most conservative results when compared to other standards. The graph in Figure 6b shows that results obtained with EN1994-1 [3] are slightly larger, albeit close to ABNT NBR 16239 [2].

The graphs in Figures 6c and Figure 6d present the cost composition of the columns and the material contribution to the resistance to normal forces (N_{Rd}), respectively, as a function of materials. Steel is observed to bear the highest impact on the cost of columns, with an average contribution of 83%.

Concrete and steel reinforcement present the largest contributions to column strength, showing an average of 63%, while the structural profile correspond, in average, to 37% of the total resistance. These results explain the reason why optimum solutions usually feature concrete with higher values of compressive strength f_{ck}.

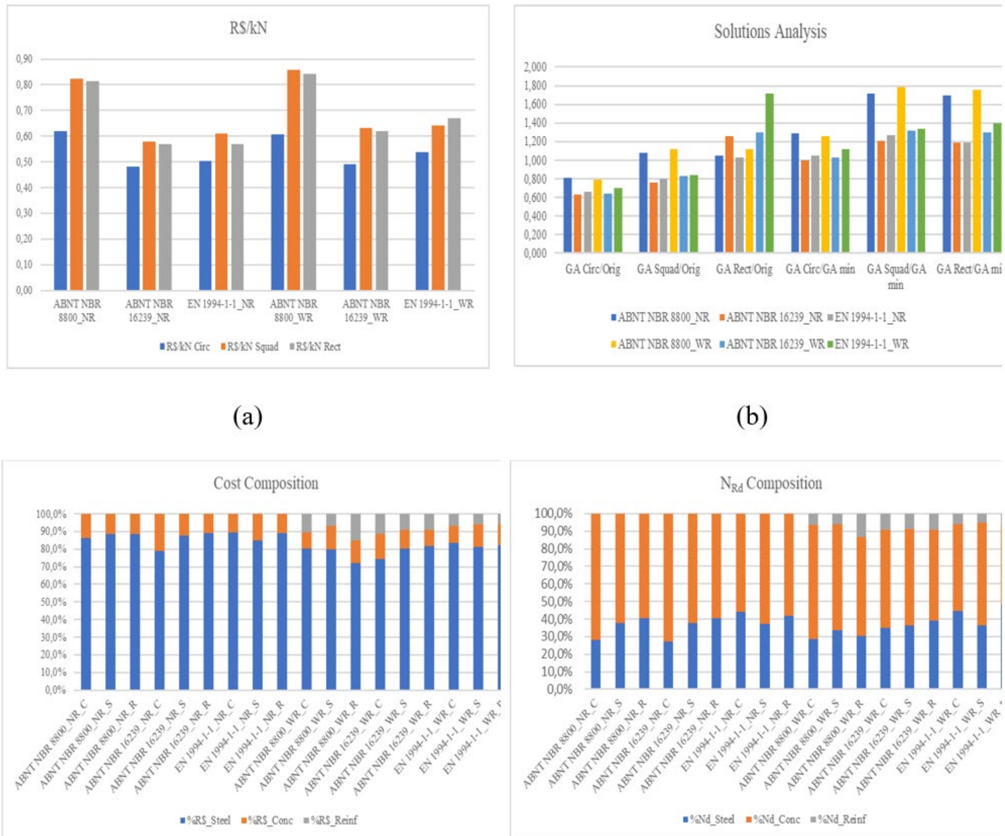

(c) (d)

Figure 6 – (a) Ratio R$/NSd; (b) Ratio AG/Original Solution; (c) Cost composition of composite filled columns (d) Composition of the resistance to normal forces of the composite filled column.

4.3 Example 3 – Design optimization of columns subjected to combined axial force and bending about the x and y axes

In addition to the 1500 kN compressive force (N_{Sd}), and the 132 kN·m bending moment about the x axis $\left(M_{x,Sd}\right)$, in this example columns are also subjected to a bending moment of 76 kN·m in the y direction $\left(M_{y,Sd}\right)$. The initial solution corresponds to a column with a width of 180 mm, height of 300 mm, wall thickness equal to 12,5 mm, and a length of 3 m, f_{ck} of 40 MPa and f_{yk} of 250 MPa. The solution for this column was obtained with the software PilarMisto 3.04.11 [37] using ABNT NBR 8800 [1] as a basis for design, and verified by Lourenção and Alves [22].

Table 6 presents the optimized results for this example, which show that the active constraint (AC) that governs this example corresponds once more to the interaction curves previously shown. It is observed that 56% of the solutions feature concrete with f_{ck} larger than 50MPa.

The analysis of results shows that all solutions obtained via GA, with the exception of the solution obtained with ABNT NBR 8800 [1], performed better when compared to the solutions found by Lourenção and Alves [22]. This result was expected, considering that the solutions obtained for circular and square sections are better than solutions obtained for rectangular sections, as presented in the previous examples.

Table 6 – Optimization Results: L=3m; N_{Sd}=1500kN; $M_{x,Sd}$=132kN·m;$M_{y,Sd}$=76kN·m

Original Solution- Rectangular ABNT NBR 8800:2008		D mm	t mm	f_{ck} MPa	N_{Rd} kN	$M_{x,Rd}$ kN·m	$M_{y,Rd}$ kN·m	n	ϕ mm	D	CT R$	RA
		180:300	**12,5**	**40**	**3890**	**405,78**	**227,01**				**1.494,20**	
Lourenção e Alves [22] (Interior Point Method	ABNT NBR 8800	200:400	7,9	90	5098,0	341,6	186,5				1404,60	IA-I
Circular without Reinforcement	ABNT NBR 8800	355,6	8	55	5034,71	270,0	270,0			0,37	1067,60	IA-I
	ABNT NBR 161239	323,8	8	30	3303,19	209,6	209,6			0,54	912,40	IA-III
	EN 1994-1-1	323,8	6,4	45	3614,66	195,2	195,2			0,41	763,60	IA-IV
Circular with Reinforcement	ABNT NBR 8800	323,8	7,1	80	5563,45	257,8	257,8	9	12,5	0,26	1060,80	IA-I
	ABNT NBR 16239	323,8	6,4	35	3534,47	209,9	209,9	6	12,5	0,41	838,00	IA-III
	EN 1994-1-1	323,8	6,4	40	3587,69	215,3	215,3	6	10	0,42	809,60	IA-IV
Square without Reinforcement	ABNT NBR 8800	290	8	90	5597,35	255,6	255,6			0,33	1346,50	IA-I
	ABNT NBR 161239	270	8	40	3441,23	214,6	214,6			0,55	1146,30	IA-III
	EN 1994-1-1	260	6,4	75	3873,78	180,4	180,4			0,37	964,10	IA-IV
Square without Reinforcement	ABNT NBR 8800	290	8	65	4896,18	267,0	267,0	4	16	0,38	1371,10	IA-I
	ABNT NBR 16239	260	8	55	4069,92	209,0	209,0	4	16	0,44	1216,10	IA-III
	EN 1994-1-1	260	6,4	70	3943,11	185,7	185,7	6	10	0,48	1009,50	IA-IV
Rectangular without Reinforcement	ABNT NBR 8800	250:320	8,8	80	5067,5	290,9	235,8				1413,50	IA-I
	ABNT NBR 161239	200:250	8	40	3479,57	230,7	199,9			0,54	1148,30	IA-III
	EN 1994-1-1	240:280	6,4	75	3801,71	192,0	168,4			0,38	963,20	IA-IV
Rectangular with Reinforcement	ABNT NBR 8800	250:320	8	80	5154,12	286,7	226,1	6	12,5	0,35	1391,10	IA-I
	ABNT NBR 16239	240:280	8	45	3706	219,1	193,1	4	16	0,48	1191,40	IA-III
	EN 1994-1-1	240:280	6,4	80	3085,56	236,9	210,3	6	10	0,48	1028,90	IA-IV

Figure 7 shows the results for this example, in similar to fashion to previous analyses.

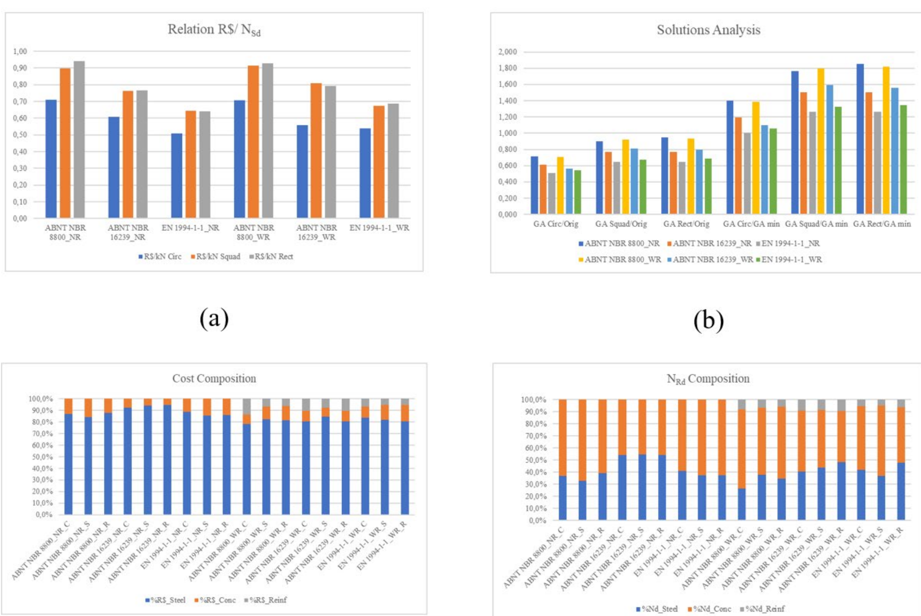

(a) (b)

(c) (d)

Figure 7 – (a) Ratio R$/NSd; (b) Ratio AG/Original Solution; (c) Cost composition of composite filled columns (d) Composition of the resistance to normal forces of the composite filled column.

Figure 7a shows that the most efficient results are provided by EN 1994-1-1 [3] without reinforcement, while their least efficient counterparts are obtained with ABNT NBR 8800 [1]. The same relation between GA results and the initial solution shown in previous examples is observed here (Figure 7b), meaning that the optimization procedure returned lower values than the original solution for all cases, with the circular column featuring as the best possible solution. Figure 7b shows that the best optimized solution is a result of using EN 1994-1-1 [3] as a basis for design, while ABNT NBR 8800 [1] remains the most conservative approach among all standards.

Following the same logic from previous examples, Figure 7c and Figure 7d show the cost composition and resistance contribution of materials. The steel profile is the largest contributor to the total cost of the columns, but not for their ultimate strength. With the exception of results obtained with ABNT NBR 16239 [2] without longitudinal reinforcement, all methods indicate that concrete and longitudinal steel reinforcement are the most significant contributors to column strength. This behavior is clearly observed in solutions obtained with a ABNT NBR 8800 [1].

5. CONCLUSIONS

Results show that the use of concrete with compressive strength (f_{ck}) larger than 50 MPa is attractive for the cases analyzed herein. More than 70% of the optimized solutions feature theses values of f_{ck} , despite this material presenting a higher financial cost. It is important to note that results might have been different if transportation costs were accounted for. Nonetheless, the added cost would be proportionally included in each solution, as recommended by transportation and assembly manuals provided by CBCA [34]. As such, optimum solutions would remain the same.

It is noted that the design model I from ABNT NBR 8800 [1] governed all cases studied. Thus, this would be the recommended approach for designing the columns should this standard be chosen as a basis for design.

Furthermore, as a general assessment, ABNT NBR 16239 [2] present the best results for designing composite filled columns. This is a result of the latter standard prescribing general design procedures for all types of composite columns, disregarding particularities attributed to the use of tubular steel profiles such as resistance reduction factors for compressive strength and effective flexural stiffness of the columns. As such, ABNT NBR 16239 [2] provides adjustments to take full advantage of the mechanical characteristics of tubular profiles, consequently resulting in less conservative and more economical solutions. The European standard EN 1994-1-1 [3] presents excellent results in comparison with ABNT NBR 8800 [1], possibly due to the latter disregarding effects attributed to concrete confinement in concrete-filled composite tubular columns.

Considering material contributions to cost and axial strength of the columns, all solutions indicate that the structural profile correspond to the larger portion of the total cost of the columns, while high-strength concrete and longitudinal reinforcement presented the largest contributions to column strength. In this case, the optimization procedure implemented was proven as useful during the decision-making process of the structural design. For all cases, GA efficiently indicated the best solutions as those featuring concrete with higher values of f_{ck}. Furthermore, due to the structural profile presenting a large impact on financial cost but a relatively small contribution to resistance, if the program intelligently reduces the dimensions of the profile, the solution obtained will always be ideal.

In closure, when adequately implemented, design optimization procedures will always produce better results than traditional design methods. However, as stated by Santoro and Kripka [6] and Tormen et al. [7], additional parameters should be considered in optimization studies, such as the life-cycle analysis of materials and the environmental impacts attributed to their use.

BIBLIOGRAPHY

[1] Associação Brasileira de Normas Técnicas, *Projeto de Estruturas de Aço e de Estruturas Mistas de Aço e Concreto de Edifícios – Procedimento*, ABNT NBR 8800, 2008.

[2] Associação Brasileira de Normas Técnicas, *Projeto de Estruturas de Aço e de Estruturas Mistas de Aço e Concreto de Edificações com Perfis Tubulares*, ABNT NBR 16239, 2013.

[3] European Commitee for Standardization, *Design of Composite Steel and Concrete Structures. Part 1-1: General Rules and Rules for Buildings*, EN 1994-1-1: Eurocode 4, 2004.

[4] J. A. Lazzari, E. C. Alvez, and A. F. G. Calenzani, "Dimensionamento otimizado de pórticos em estruturas de aço via algoritmos genéticos," *Rev. Estrutura Aco*, vol. 9, no. 1, pp. 101–121, 2020.

[5] J. F. I. Oliveira and A. C. O. Miranda, "Structural optimization using multi-objective genetic algorithm," *IJERA*, vol. 10, no. 1, pp. 1–12, 2020, http://dx.doi.org/10.9790/9622-1003020112.

[6] J. F. Santoro and M. Kripka, "Minimizing environmental impact from optimized sizing of reinforced concrete elements," *Comput. Concr.*, vol. 25, no. 2, pp. 111–118, 2020, http://dx.doi.org/10.12989/cac.2020.25.2.111.

[7] A. F. Tormen, Z. M. C. Pravia, F. B. Ramires, and M. Kripka, "Optimization of steel concrete composite beams considering cost and environmental impact," *Steel Compos. Struct.*, vol. 34, no. 3, pp. 409–421, 2020, http://dx.doi.org/10.12989/scs.2020.34.3.409.

[8] S. de Nardin, "Estudo téorico-experimental de pilares mistos compostos por tubos de aço preenchidos com concreto de alta resistência," M.S. thesis, EESC-USP, São Carlos, 1999.

[9] A. P. C. Duarte, N. Silvestre, J. Brito, E. Júlio, and J. D. Silvestre, "On the sustainability of rubberized concrete filled square steel tubular columns," *J. Clean. Prod.*, vol. 170, pp. 510–521, 2018, http://dx.doi.org/10.1016/j.jclepro.2017.09.131.

[10] M. Dundu, "Compressive strength of circular concrete filled steel tube columns," *Thin-walled Struct.*, vol. 56, pp. 62–70, 2012, http://dx.doi.org/10.1016/j.tws.2012.03.008.

[11] P. Gajalakshmi and J. H. Helena, "Behavior of concrete-filled steel columns subjected to lateral cyclic loading," *J. Construct. Steel Res.*, vol. 75, pp. 55–63, 2012, http://dx.doi.org/10.1016/j.jcsr.2012.03.006.

[12] A. Kuranovas, D. Goode, A. K. Kvedaras, and S. Zhong, "Load-bearing capacity of concrete-filled steel columns," *J. Civ. Eng. Manag.*, vol. 15, no. 1, pp. 21–33, 2009, http://dx.doi.org/10.3846/1392-3730.2009.15.21-33.

[13] R. B. Caldas, R. H. Fakury, and J. B. M. Sousa Jr., "Bases do dimensionamento de pilares mistos de aço e concreto segundo o projeto de revisão da ABNT NBR 8800," *Rev. Esc. Minas*, vol. 60, no. 2, pp. 271–276, 2007, http://dx.doi.org/10.1590/S0370-44672007000200009.

[14] W. L. A. Oliveira, "Análise teórico-experimental de pilares mistos preenchidos de seção circular," M.S. thesis, EESC-USP, São Carlos, 2008.

[15] G. S. Papavasileiou, N. Nicolaou, and D. C. Charmpis, "Comparative assessment of buildings with pure steel or steel-concrete composite columns using structural design optimization," in *Proc. 4th Eccomas Thematic Conf. Comput. Methods Struct. Dyn. Earthq. Eng.*, Greece, 2013.

[16] S. Aghdamy, D. P. Thambiratnam, M. Dhanasekar, and S. Saiedi, "Computer analysis of impact behavior of concrete filled steel tube columns," *Adv. Eng. Softw.*, vol. 89, pp. 52–63, 2015, http://dx.doi.org/10.1016/j.advengsoft.2015.06.015.

[17] Z. Tao, Z. Wang, and Q. Yu, "Finite element modelling of concrete-filled steel stub columns under axial compression," *J. Construct. Steel Res.*, vol. 89, pp. 121–131, 2013, http://dx.doi.org/10.1016/j.jcsr.2013.07.001.

[18] H. Thai, B. Uy, M. Khan, Z. Tao, and F. Mashiri, "Numerical modelling of concrete-filled steel box columns incorporating high strength materials," *J. Construct. Steel Res.*, vol. 102, pp. 256–265, 2014, http://dx.doi.org/10.1016/j.jcsr.2014.07.014.

[19] Z.-B. Wang, Z. Tao, L.-H. Han, B. Uy, D. Lam, and W.-H. Kang, "Strength, stiffness and ductility of concrete-filled steel columns under axial compression," *Eng. Struct.*, vol. 135, pp. 209–221, 2017, http://dx.doi.org/10.1016/j.engstruct.2016.12.049.

[20] A. F. Canales, "Estudo do dimensionamento de pilares de aço tubulares e pilares mistos de perfis tubulares preenchidos com concreto de acordo com a ABNT NBR 16239," Undergraduate thesis, UTFPR, Campo Mourão, 2014.

[21] G. S. Papavasileiou and D. C. Charmpis, "Seismic design optimization of multi–storey steel–concrete composite buildings," *Comput. Struc.*, vol. 170, pp. 49–61, 2016, http://dx.doi.org/10.1016/j.compstruc.2016.03.010.

[22] J. Lourenção and E. C. Alves, "Dimensionamento otimizado de pilares mistos preenchidos de aço e concreto," *Rev. Port. Eng. Estrut.*, no. 8, pp. 33–48, Nov 2018.

[23] Y. Pekbey, A. Ozdamar, and O. Sayman, "Buckling optimization of composite columns with variable thickness," *J. Reinf. Plast. Compos.*, vol. 26, no. 13, pp. 1337–1356, 2007, http://dx.doi.org/10.1177/0731684407079772.

[24] J. Brauns and U. Skadins, " On stress-state optimization in steel-concrete composite structures," *IOP Conf. Series: Materials Science Eng.* ., 2017

[25] A. B. Senouci and M. S. Al-Ansari, "Cost optimization of composite beams using genetic algorithms," *Adv. Eng. Softw.*, vol. 40, no. 11, pp. 1112–1118, 2009, http://dx.doi.org/10.1016/j.advengsoft.2009.06.001.

[26] M.-B. Prendes-Gero, A. Bello-García, J.-J. del Coz-Díaz, F.-J. Suárez-Domínguez, and P.-J. García No., "Optimization of steel structures with one genetic algorithm according to three international building codes," *Rev. Constr.*, vol. 17, no. 1, pp. 47–59, 2018, http://dx.doi.org/10.7764/RDLC.17.1.47.

[27] J. Malveiro, D. Ribeiro, C. Sousa, and R. Calçada, "Model updating of a dynamic model of a composite steel-concrete railway viaduct based on experimental tests," *Eng. Struct.*, vol. 164, pp. 40–52, 2018, http://dx.doi.org/10.1016/j.engstruct.2018.02.057.

[28] C. Liu, A. Hammad, and Y. Itoh, "Multiobjective optimization of bridge deck rehabilitation using a genetic algorithm," *Microcomputers Civ. Eng.*, vol. 12, no. 6, pp. 431–443, 1997, http://dx.doi.org/10.1111/0885-9507.00075.

[29] C. K. Fu, Y. Zhai, and S. Zhou, "Optimum design of welded steel plate girder bridges using a genetic algorithm with elitism," *J. Bridge Eng.*, vol. 10, pp. 291–301, 2005, http://dx.doi.org/10.1061/(ASCE)1084-0702(2005)10:3(291).

[30] M. Z. Abd Elrehim, M. A. Eid, and M. G. Sayed, "Structural optimization of concrete arch bridges using Genetic Algorithms," *Ain Shams Eng. J.*, vol. 10, no. 3, pp. 507–516, 2019, http://dx.doi.org/10.1016/j.asej.2019.01.005.

[31] H. Cho, D. Min, and K. Lee, "Optimum life-cycle design of orthotropic steel deck bridges," *Steel Struct.*, vol. 1, pp. 141–152, 2001.

[32] Associação Brasileira de Normas Técnicas, *Projeto de Estruturas de Concreto Armado-Procedimentos*, ABNT NBR 6118, 2014.

[33] Caixa Econômica Federal. Sistema Nacional de Preços e Índices para a Construção Civil. http://www.caixa.gov.br/poder-publico/apoio-poder-publico/sinapi/Paginas/default.aspx (accessed Mar. 27, 2020).

[34] Vallourec Tubos do Brasil, *Tubos Estruturais de Seção Circular, Square e Rectangular.* Belo Horizonte, 2017, pp. 56. Accessed: Sept. 21, 2020. [Online]. Available: https://www.famsteel.com.br/blog/catalogos-Tables/catalogo-vallourec-tubos-estruturais/

[35] CBCA, *Rev. Constr. Met.*, vol. 118, 2015.

[36] I. H. Bellei, F. O. Pinho, and M. O. Pinho, *Edifícios de Múltiplos Andares em Aço*, 2a. ed. São Paulo: PINI, 2008.

[37] R. B. Caldas, R. H. Fakury, J. B. M. Souza Jr., *PilarMisto 3.04.11: Verificação de Pilares Mistos de Aço e Concreto Segundo a ABNT ABNT NBR 8800 e a ABNT NBR 14323:2010*. Belo Horizonte: UFMG, Dep. Eng. Estrut..

Author contributions: JSL: conceptualization, data curation, formal analysis, methodology, writing; PATA: data curation, formal analysis, methodology, writing; GE: formal analysis, writing; ECA: conceptualization, formal analysis, methodology, supervision, writing.

Editors: Túlio Nogueira Bittencourt, Guilherme Aris Parsekian.

IBRACON Structures and Materials Journal
Revista IBRACON de Estruturas e Materiais
ISSN 1983-4195 ismj.org

ORIGINAL ARTICLE

Correlation between concrete strength properties and surface electrical resistivity

Correlação entre as propriedades de resistência do concreto e a resistividade elétrica superficial

Carla Cavalcante Araújo[a]
Gibson Rocha Meira[a,b]

[a]Universidade Federal de Paraíba – UFPB, Civil and Environmental Engineering Post-Graduate Program, João Pessoa, PB, Brasil
[b]Instituto Federal da Paraíba, Science and Technology of Paraíba – IFPB, João Pessoa, PB, Brasil

Received 27 August 2020
Accepted 18 April 2021

Abstract: Periodic inspections in reinforced concrete structures are important to be carried out to assess their state of conservation. In this scenario, non-destructive tests can be a suitable option since destructive tests are invasive and may be difficult to be performed in some cases. Considering this option, correlations between non-destructive test parameters and the concrete properties to be analyzed are useful tools that make easier the structure inspection. In the present work, correlations between the compressive strength (f_c) and splitting tensile strength (f_t) and surface electrical resistivity (ρ) of concretes were studied. Brazilian concretes of six different mixtures were analyzed at five different ages and correlation curves between strength properties and surface electrical resistivity of concrete were obtained, which are represented by the general relationships $f_c = 14.18 \cdot \ln(\rho) + 18.43$ and $f_t = 0.69 \cdot \ln(\rho) + 2.15$ for compressive strength and splitting tensile strength, respectively. In addition, a general curve considering literature data and results from this work was proposed to represent the relationship between compressive strength and surface electrical resistivity - $f_c = 11.89 \cdot \ln(\rho) + 18.90$.

Keywords: concrete, compressive strength, electrical properties, non-destructive testing, tensile properties.

Resumo: A realização de inspeções periódicas em estruturas de concreto armado é importante para a avaliação do seu estado de conservação. Neste cenário, ensaios não destrutivos podem ser uma opção adequada, uma vez que os testes destrutivos são invasivos e, em alguns casos, podem ser difíceis de serem realizados. Considerando essa opção, correlações entre parâmetros de ensaio não destrutivos e propriedades do concreto a serem analisadas são ferramentas úteis que facilitam a inspeção da estrutura. No presente trabalho, foram estudadas correlações entre a resistência à compressão (f_c), a resistência à tração por compressão diametral (f_t) e a resistividade elétrica superficial (ρ) de concretos. Concretos brasileiros com seis traços distintos foram analisados em cinco idades diferentes e foram obtidas curvas de correlação entre propriedades de resistência e resistividade elétrica superficial do concreto, as quais são representadas pelas relações gerais $f_c = 14{,}18 \cdot \ln(\rho) + 18{,}43$ e $f_t = 0{,}69 \cdot \ln(\rho) + 2{,}15$ para resistência à compressão e resistência à tração por compressão diametral, respectivamente. Além disso, foi proposta uma curva geral, considerando dados da literatura e resultados deste trabalho, para representar a relação entre a resistência à compressão e a resistividade elétrica superficial - $f_c = 11{,}89 \cdot \ln(\rho) + 18{,}90$.

Palavras-chave: concreto, resistência à compressão, propriedades elétricas, ensaios não destrutivos, propriedades de tração.

How to cite: C. C. Araújo, and G. R. Meira, "Correlation between concrete strength properties and surface electrical resistivity," *Rev. IBRACON Estrut. Mater.*, vol. 15, no. 1, e15103, 2022, https://doi.org/10.1590/S1983-41952022000100003

1 INTRODUCTION

Environmental aggressiveness associated with deficiencies in the quality of concrete structures has been causing, prematurely, loss of performance of reinforced concrete structures. In order to evaluate the state of conservation and

Corresponding author: Gibson Meira. E-mail: gibsonmeira@yahoo.com, gibson.meira@ifpb.edu.br
Financial support: Coordination for the Improvement of Higher Education Personnel (CAPES).
Conflict of interest: Nothing to declare.

carry out preventive maintenance of these structures, periodic inspections are needed. In this scenario, non-destructive tests (NDT) are an important tool for this kind of inspection and help on a more suitable analysis of the structure [1].

Considering the concrete structure degradation condition, destructive tests may be infeasible or bring risks to the structure. Differently, NDT offer significant advantages with respect to its quick response, lower cost, absence of damage risk to the structure damage, immediate availability of results and the easiness of taking as more measurements as necessary [2].

Regarding the use of NDT for concrete structures inspection, correlations between NDT parameters and the concrete properties to be analyzed are necessary and make easier the analysis of structures inspection data. However, it is recommended that if there is a significant change in the materials characteristics, a new correlation should be established to provide greater reliability for the estimated property [3]. In this scenario, there are available NDT that can be used to evaluate some concrete properties, such as their compressive strength, modulus of elasticity and durability parameters [4].

One of the most studied concrete properties associated with NDT is the compressive strength, which is linked to the structural safety. On the other hand, sclerometry and ultrasonic pulse velocity (UPV) tests are NDT widely used to evaluate reinforced concrete structures. As a result, there are already several studies that propose correlation curves between these last tests and compressive strength, both individually and by the combination of these non-destructive tests [1], [5], [6].

Surface electrical resistivity of concrete is a property measured by a NDT and it is closely related to the concrete microstructure. It is used to evaluate the concrete resistance to the chloride penetration and to the carbonation front advance, which are the main causes of reinforcement corrosion. However, there are few studies that suggest other applications for the surface electrical resistivity test. Some authors, such as Lübeck et al. [7], Chen et al. [8], Bem et al. [9] and Mendes et al. [10], observed that the concrete resistivity increases as the compressive strength increases, whereas Medeiros-Junior and Lima [11] report that electrical resistivity measurements can be used to predict the compressive strength of Portland cement pastes.

For this reason, it is expected that the surface electrical resistivity test can be used to estimate the compressive strength and tensile strength of concrete due to the test susceptibility to variations in the materials microstructure, as well as the fact that these concrete properties increase with the progress of the cement hydration. Besides that, although the relation between tensile strength and compressive was already widely studied [12-14] and follows a power function [12-17], the surface electrical resistivity can be introduced in this scenario and generate a new approach on this last relation, considering these three variables.

Regarding the few studies that focused on the relationship between compressive strength of concrete and its surface electrical resistivity, and the absence of studies focused on the relationship between this electrical property and concrete tensile strength, this work aimed to analyze the possible correlations between compressive and splitting tensile strength and surface electrical resistivity for concretes ranged between 30 and 50 MPa of compressive strength. A new approach on the relationship between tensile strength and compressive strength considering the surface electrical resistivity was also presented.

2 SURFACE ELECTRICAL RESISTIVITY OF CONCRETE

2.1 General aspects

Electrical resistivity can be defined as the ability of a material to withstand the electrical current passage. Therefore, resistivity is the inverse of conductivity [9]. In the concrete, electrical resistivity is a property that characterizes the difficulty with which the ions move in the concrete aqueous phase, subjected to an electrical field [18]. Consequently, resistivity is a parameter that is related to the transport of aggressive agents into concrete, such as chloride ions and carbon dioxide [11]. A low value of electrical resistivity is generally correlated with a high chloride penetration rate or with a high rate of carbonation front advance and, consequently, a greater susceptibility to reinforcement corrosion. That is, the higher the concrete electrical resistivity is, the greater its resistance to the penetration of aggressive agents [19]. RILEM TC 154-EMC [19] report that depending on how the concrete resistivity is measured, different information will be obtained. The apparent electrical resistivity is obtained in the case of the surface electrical resistivity measurements on concrete. Volumetric resistivity is obtained when measurements are made through a concrete mass.

The volumetric electrical resistivity test is standardized in some countries [20]-[22] and is based on the measurement of the resistance between two electrodes (in general plates) positioned on concrete opposite surfaces. However, it can present some complexity for assembling the test cell and has limitation to be used on site [23].

The test that measures surface electrical resistivity was originally developed by geologists to measure soil resistivity [24]. This method was adapted for use in concrete by means of a similar apparatus, which adopts a probe with four equally spaced electrodes set up in a linear array and put in contact with the concrete surface. It is called the four-point method or Wenner method [24], [25]. This property is measured by reading the electrical current between the outer electrodes and the potential difference between the inner electrodes placed on the concrete surface [23].

Additionally, other techniques have been developed and adapted for both the measurement of surface electrical resistivity (in real structures and in specimens used in laboratory experiments), such as the surface disc test, and the bulk electrical resistivity measurement, which differ in terms of the number of used electrodes and their positioning on the concrete surface [19], [26]. However, Wenner method is still the one widely used.

The surface electrical resistivity test can be considered an important tool to be used to verify concrete quality and in service life analysis of concrete structures, since it can be correlated with different properties of the material, such as the resistance for transporting chloride ions, moisture content, degree of cement paste hydration, corrosion probability, Young's modulus and compressive strength [9], [27].

In relation to the compressive strength property, the literature shows some studies that analyzed the relationship between surface electrical resistivity and compressive strength, through the attainment of correlation curves [28]. However, similar relationship analysis considering the tensile strength were not identified in literature.

Andrade and D'Andrea [27], Wei et al. [29] and Medeiros-Junior et al. [11], Bem et al. [9] are researchers that, although their main objective was to study the influence of different factors on surface electrical resistivity measurements, they also obtained correlation curves between compressive strength and surface electrical resistivity (Table 1), which are mainly represented by logarithmic functions.

Table 1. Correlation curves between compressive strength (f_c) and surface electrical resistivity (ρ) for cementitious materials – literature data.

Author	Equation	Determination coefficient (r^2)	Specimens	Cement type	Age of test (days)	Additional information
Andrade and D'Andrea (2011) [27]	$f_c = 6.897 \cdot \ln(\rho) + 6.827$	N.I.	Concrete cylinders (150 mm x 300 mm)	N.I.	N.I.	Four-point method (Wenner method) / ρ by Ω·m.
Ramezanianpour et al. (2011) [30]	$f_c = 3.587\rho - 9.186$	0.87	Concrete cylinders (100 mm x 200 mm) and concrete cubes with 100 mm of edges	OPC	728	Four-point method (Wenner method) / ρ by kΩ·cmΩ·cmΩ·cm.
	$f_c = 33.58 \cdot \ln(\rho) - 27.28$	0.88				
Wei et al. (2012) [29]	$f_{c28} = 8.76.(\rho_{24h}) + 20.4$	0.963	N.I	N.I.	28 – f_c	Electrical resistivity of cement paste in the fresh state measured by a non-contact device / ρ by Ω·m.
					1 – ρ	
Medeiros-Junior et al. (2014) [31]	$f_c = 21.24 \cdot \ln(\rho) + 11.20$	0.823	Concrete cylinders (100 mm x 200 mm) and concrete cubes with 250 mm of edges	FPC	28	Four-point method (Wenner method) / ρ by kΩ·cm.
	$f_c = 49.05 \cdot \ln(\rho) - 43.03$	0.995			91	
	$f_c = 32.34 \cdot \ln(\rho) - 68.97$	0.997		PSC	28	
	$f_c = 65.36 \cdot \ln(\rho) - 208.67$	0.995			91	
	$f_c = 41.50 \cdot \ln(\rho) - 61.38$	0.999		PPC	28	
	$f_c = 70.34 \cdot \ln(\rho) - 175.80$	0.993			91	
	$f_c = 14.66 \cdot \ln(\rho) + 23.29$	0.992		HSPC	28	
	$f_c = 32.28 \cdot \ln(\rho) - 6.92$	0.999			91	
Bem et al. (2018) [9]	$f_c = 21.49 \cdot \ln(\rho) - 2.71$	0.81	Concrete cylinders (100 mm x 200 mm)	FPC	28	Four-point method (Wenner method) / ρ by kΩ·cm.
Sabbağ and Uyanik (2018) [28]	$f_c = 57.2 \cdot \ln(\rho) - 84.3$	0.92	Unreinforced and reinforced cubes (150 x 150 x 150 mm)	FPC	7 – 90	Four-point method (Wenner method) / ρ by kΩ·cm.

N.I. – Not informed f_c – Compressive strength ρ – Surface electrical resistivity

OPC – Portland plain cement FPC – Filler modified Portland cement PSC – Portland slag cement

PPC – Portland pozzolan cement HSPC – High early strength Portland cement

2.2 Influencing parameters

Wenner method is a non-destructive test with a simple operation procedure, thorough which the generated data are immediately obtained. On the other hand, it is affected by some factors such as the moisture content of concrete. Therefore, measurements of surface electrical resistivity must be performed under certain humidity and temperature conditions, as well as meet some geometric criteria in relation to the tested surface.

Among all influencing factors, the moisture content is one of the most important variables, because the electric current that passes through the concrete is driven by the aqueous solution in the pores. In this sense, Chen et al. [8] verified that the electrical resistivity measurements on dry specimens, which were in the oven or in the air with 40% of relative humidity, were unstable or even undetected. On the other hand, these measurements in specimens in the saturated dry surface or saturated wet surface condition had similar resistivity values. Therefore, it is suggested that the samples should be wetted prior to resistivity measurements, in particular to correlate these measurements with concrete properties.

Some papers report that temperature changes have certain effects on concrete resistivity. When temperature increases, the electrons move faster, increasing conductivity, thus reducing electrical resistivity considering a constant humidity level [7], [26]. Therefore, to eliminate the effect of temperature on surface electrical resistivity measurements, most laboratory studies are performed in environments with controlled temperature, usually between 20 ºC and 25 ºC [26].

In Wenner method, electrical resistivity measurements are performed considering a semi-infinite and homogeneous medium. This fact leads to a distortion in the measured values, since concrete is a heterogeneous material and the cylindrical or prismatic specimens have a relatively small size, diverging from the ideal condition of having an infinitely large geometry. To rectify this kind of distortion, a correction is suggested. The data from surface electrical resistivity measurements from cylindrical or prismatic specimens must be multiplied by a geometric correction factor [27], [32].

Regarding the limited size of the specimens, the spacing between the electrodes must be adjusted to avoid electrodes near the ends of the specimens. Spacing between electrodes ranging from 3 to 5 centimeters are usual [19]. Otherwise, the electric current may flow not only through the concrete specimen, but also through air at its edges, resulting in overestimated resistivity values, because air is always more resistant than concrete [33].

The electrical resistivity measurements are also influenced by the concrete mixtures. Considering the w/c ratio, the resistivity values decrease as the w/c ratio increases. This behavior can be explained by the fact that the aqueous solution in the concrete porous network acts as a conductive media [31]. Thus, concretes with a higher w/c ratio have greater porosity and, therefore, the possibility of greater presence of water in their porous network. Taking into account the type of cement, concretes manufactured with Portland-slag cement (ASTM Type IS) have higher resistivity compared to Portland-pozzolan cement (ASTM Type IP) and high early strength Portland cement (ASTM type III). This behavior is related to the pore refinement effect and reduction of concrete permeability, due to the significant amount of mineral additions [7], [31]. Considering the amount of coarse aggregate, the aggregates have a higher electrical resistivity compared to the hardened cement paste. Sengul [34] and Hou et al. [35] observed that the increase in aggregate amount and the reduction in cement paste content for a given volume of concrete resulted in higher resistivity values due to the replacement of cement paste by coarse aggregates.

3 MATERIALS AND EXPERIMENTAL PROGRAM

This work used concretes from two suppliers of ready-mix concrete, which are here identified as A and B concrete families. Concretes from three different compressive strength classes were used, which should belong to C30 (30 MPa), C40 (40 MPa) and C50 (50 MPa) classes.

The present research was divided in three steps. The first step consisted in the characterization of the materials used on concretes production (fine aggregates, coarse aggregates and cements). The second step comprised the casting of the concrete specimens, the wet curing for seven days, the conducting of the surface electrical resistivity test and the evaluation of the compressive and splitting tensile strengths. The last three tests were performed at five concrete ages (3, 7, 28, 90 and 120 days). The third step consisted in data treatment and analysis.

3.1 Materials characterization

In relation to the fine aggregate, A concretes family used two types of sand (here called AS1 and AS2 sands) and B concretes family used a single type of sand (here called BS1 sand). Regarding the coarse aggregates, A and B concretes used two types of gravel (here referred to as AG1 and AG2 gravels for A concretes family, and BG1 and BG2 gravels for B concretes family).

These aggregates were characterized in regard to particle size distribution, bulk density, specific density for fine aggregate, specific density for coarse aggregate and powder material (fine material passing through the 75 μm sieve per wash), following the recommendations of Brazilian standards NBR NM 248 [36], NBR NM 45 [37], NBR NM 52 [38], NBR NM 53 [39] and NBR NM 46 [40], respectively.

A and B concrete families used the same type of cement, Brazilian Portland cement of high early strength (ASTM type III). However, they were obtained from different cement plants. For this reason, they are called here as A and B cements, respectively. These cements were characterized in relation to their specific weight and Blaine specific surface, following the recommendations of Brazilian standards NBR 16605 [41] and NBR 16372 [42], respectively. Furthermore, the cements were also characterized in relation to their chemical composition, by X-ray fluorescence (XRF), and granulometric distribution by the laser diffraction granulometry test.

3.2 Concrete specimens and tests

The casting of cylindrical specimens was performed at the construction site, according to guidelines contained in the Brazilian standard NBR 5738 [43]. The specimens were demolded after 24 hours and then cured in lime-saturated water until the age of 7 days. Thirty-two cylindrical specimens with 10 cm in diameter and 20 cm in height were cast at the same moment for each concrete mixture, totalizing 192 specimens.

Each concrete mixture used in the casting of the specimens was collected from a single concrete mixer truck during the discharge operation, after removal of the first 15% and before the discharge of 85% of the total volume was completed, according to the Brazilian standard NBR NM 33 [44].

The surface electrical resistivity, compressive strength and splitting tensile strength tests were performed at the ages of 3, 7, 28, 90 and 120 days in each concrete mixture, with three specimens being tested at each age. The non-destructive tests were carried out on the same cylindrical specimens used for compressive and splitting tensile strength tests, just before they were tested. Furthermore, two additional specimens of each concrete mixture were also used only for resistivity tests. Thus, the evolution of this property over time could be analyzed based on the same specimens.

The surface electrical resistivity test adopted was the Wenner method (four-point method) and it was performed following the RILEM TC 154-EMC recommendations [19]. Each cylindrical specimen was tested on a saturated dry surface condition, following RILEM TC 154-EMC [19] and Chen et al. [8] recommendations. Three centimeters spacing between electrodes was used to avoid the edge effect. Moreover, a geometric correction factor was also adopted to correct the data provided by the equipment.

Considering the cylindrical shape and dimensions of the specimens, the value used for correcting the measured data was based on recommendations proposed by Morris et al. [32] and UNE 83988-2 [45]. Eight resistivity measures were performed on the lateral surface of each specimen, with an MKII resistivity meter from CNS Farnell. Then, the mean and standard deviation of the measurements were obtained. Figure 1 shows the experimental arrangement of the tests on the cylindrical specimens.

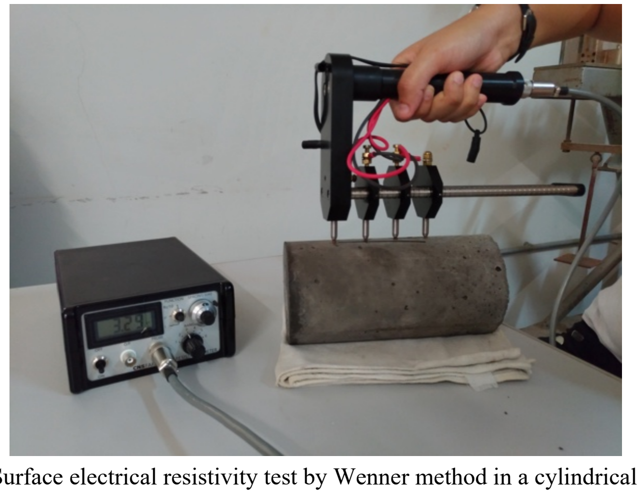

Figure 1. Surface electrical resistivity test by Wenner method in a cylindrical specimen.

Compressive strength was measured in accordance with the guidelines of the Brazilian standard NBR 5739 [46]. During the rupture of all cylindrical specimens, a confined neoprene cushion of 10 cm in diameter and 1 cm thick, with 68 shore A hardness, was used. Tensile strength was obtained by splitting tension test, following the Brazilian standard NBR 7222 [47] recommendations.

4 RESULTS AND DISCUSSION

4.1 Materials characterization

Table 2 presents the physical characteristics of fine aggregates. All the characteristics presented by the fine aggregates meet the requirements of the Brazilian standards adopted in this work.

Table 2. Physical characteristics of fine aggregates.

Code	Maximum diameter (mm)	Fineness module	Specific density (g/cm^3)	Bulk density (g/cm^3)	Powder material (%)
AS1	2.36	1.88	2.64	1.61	3.59
AS2	2.36	1.98	2.67	1.71	4.53
BS1	1.18	1.96	2.62	1.56	2.21

Table 3 presents the physical characteristics of coarse aggregates. Table 3 shows that the coarse aggregate AG1 could not be classified in any size distribution interval, due to the excessive presence of fine materials observed in its granulometry test. This situation was confirmed by its high percentage of powder material (4.76%), which is much higher than the maximum acceptable limit for coarse aggregates, which is 1%, according to the Brazilian standard NBR 7211 [48]. Except for AG1 gravel, all other gravels presented values of physical characteristics that meet the requirements of the Brazilian standards adopted in this work.

Table 3. Physical characteristics of coarse aggregates.

Code	Size distribution interval (mm/mm)	Maximum diameter (mm)	Fineness module	Specific density (g/cm^3)	Bulk density (g/cm^3)	Powder material (%)
AG1	-	12.50	5.34	2.77	1.65	4.76
AG2	9.5/25	25.00	8.50	2.78	1.52	0.42
BG1	4.75/12.5	12.50	7.00	2.76	1.43	0.34
BG2	9.5/25	25.00	9.10	2.77	1.46	0.12

Chemical and physical characteristics of the used cements are presented in Table 4. By means of the values of the Blaine specific surface in Table 4 and the analysis of Figure 2, in which the granulometric distribution curves obtained by the laser diffraction granulometry test are presented, it is noted that the A cement is slightly finer grained than B cement. Chemical analysis demonstrates that in relation to the major oxide components, the respective amounts are quite close. As a result, it can be accepted that the cements are chemically similar.

Table 4. Chemical composition and physical properties of cements.

Analyzed characteristics		A Cement	B Cement
Chemical composition (%) XRF	Calcium oxide (CaO)	59.33%	58.51%
	Silicon dioxide (SiO_2)	24.99%	25.49%
	Ferric oxide (Fe_2O_3)	4.05%	5.89%
	Aluminum oxide (Al_2O_3)	3.91%	4.55%
	Sulfuric oxide (SO)	3.76%	2.42%
	Magnesium oxide (MgO)	2.33%	1.98%
	Phosphorus pentoxide (P_2O_5)	0.48%	0.03%
	Titanium dioxide (TiO_2)	0.46%	0.44%
	Sodium oxide (Na_2O)	0.33%	0.28%
	Potassium oxide (K_2O)	0.33%	0.20%
	Strontium oxide (SrO)	0.10%	0.04%
	Manganese oxide (MnO)	0.04%	0.14%
	Chloride (Cl)	0.03%	-
	Chromium oxide (Cr_2O_3)	0.03%	-
	Zinc Oxide (ZnO)	0.02%	-
	Zirconium dioxide (ZrO_2)	-	0.02%
	Nickel oxide (NiO)	-	0.02%
Specific weight (g/cm^3)		3.07	3.08
Blaine specific surface (cm^2/g)		3855.63	3377.34

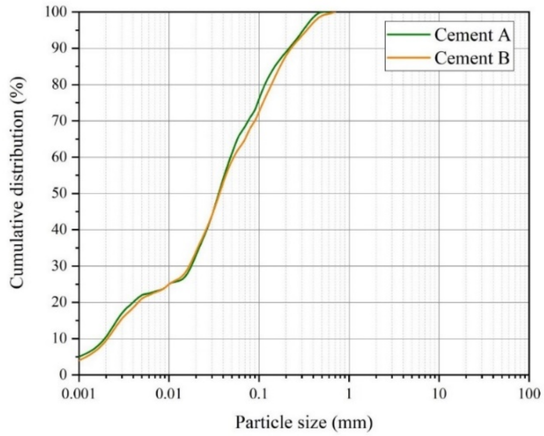

Figure 2. Particle size distribution curves of cements obtained by means of laser diffraction test.

The compositions of the concrete mixtures are shown in Table 5. The codes used to identify the concrete mixtures refer to the compressive strength class and to the used cement. For example, C40-A means a concrete of compressive strength class C40 (40 MPa) that used A cement. High w/c ratios for concretes C30-B and C40-B are observed and this influenced on compressive and splitting tensile strength results presented in next sections.

Table 5. Concrete mixtures.

Concrete	Concrete mixtures (by weight)					
	Portland cement A (kg/m³)	**AS1 sand (kg/m³)**	**AS2 sand (kg/m³)**	**AG1 gravel (kg/m³)**	**AG2 gravel (kg/m³)**	**w/c ratio**
C30-A	304	-	875	325	720	0.54
C40-A	393	-	798	315	680	0.45
C50-A	497	348	348	318	616	0.41
	Portland cement B (kg/m³)	**BS1 sand (kg/m³)**		**BG1 gravel (kg/m³)**	**BG2 gravel (kg/m³)**	**w/c ratio**
C30-B	316	987		421	645	0.69
C40-B	328	994		515	601	0.60
C50-B	491	1007		540	550	0.41

4.2 Compressive strength

The average compressive strength values (f_c) are shown in Figure 3 considering the age of the tests (3, 7, 28, 90 and 120 days). All concretes presented a tendency of compressive strength increase in the first days, which tended to a stabilization after 28 days. This behavior is similar to those observed in literature when using the same kind of cement, high early strength Portland cement [2], [5]. Concrete mixtures with higher w/c ratio presented lower compressive strength results, as expected.

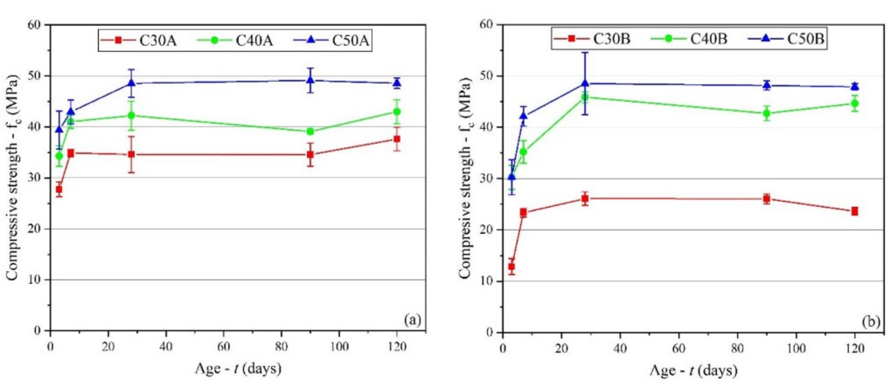

Figure 3. The evolution of average compressive strength (f_c) with age for A concretes (a) and B concretes (b) families.

This increase tendency is explained by the fact that the compressive strength is correlated to solid/space ratio, as a consequence of Power's law [49]. The higher solid/space ratio means the more hydration products and consequently the higher concrete strength.

In Figure 3, it can be seen that some concretes did not reach the expected compressive strength at 28 days for their respective compressive strength class. However, these concretes were not discarded in the analysis carried out in the present research, since the focus of this work is on the relationship between surface electrical resistivity and compressive and splitting tensile strength, considering different concrete mixture characteristics.

4.3 Splitting tensile strength

The average tensile strength values (f_t) are shown in Figure 4 considering the age of the tests (3, 7, 28, 90 and 120 days). Similarly to compressive strength, all concretes presented an increase tendency of tensile strength in the first days, which changed to a stabilization trend after 28 days.

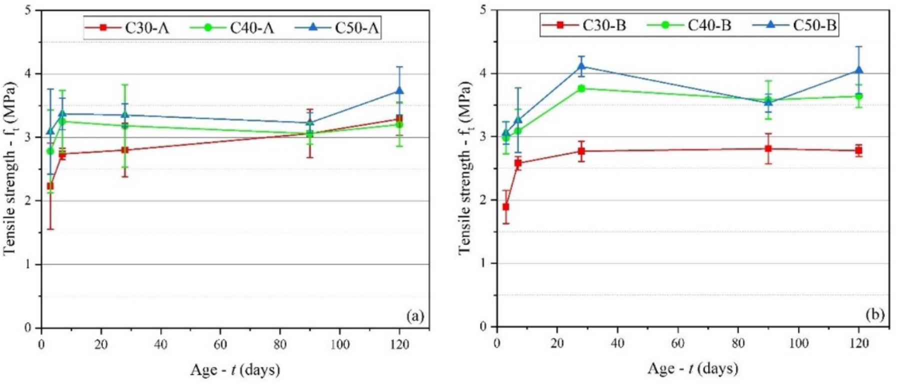

Figure 4. The evolution of average splitting tensile strength (f_t) with age for A concretes (a) and B concretes (b) families.

Comparing A and B concretes (Figures 4a and 4b), a slight tendency of higher values for C40-B and C50-B concretes can be seen. The higher powder material content of AG1 gravel (see Table 5) may have contributed to a weaker interfacial transition zone in A concretes [49], which explains this behavior. However, as concrete C30-B had a significantly higher w/c ratio, the previous aspect was not enough to overcome the influence of w/c on splitting tensile strength and consequently it presented lower values.

4.4 Surface electrical resistivity

The average values of surface electrical resistivity, expressed in Figure 5, were obtained for each concrete from the measurements performed continuously on the same two specimens at the five pre-established ages (3, 7, 28, 90 and 120 days). Surface electrical resistivity increases as the age and hydration level of concrete increase [28], [50]. Furthermore, there is an inverse relationship between the open porosity of concrete and surface electrical resistivity [30]. Results on this work follow this behavior and show an increase trend of resistivity along time and, in general, higher values for less porous concretes (with lower w/c ratio). This increase tendency is more pronounced in the first 28 days, where the hydration products are formed on a larger scale, specially for the kind of cement used in this research.

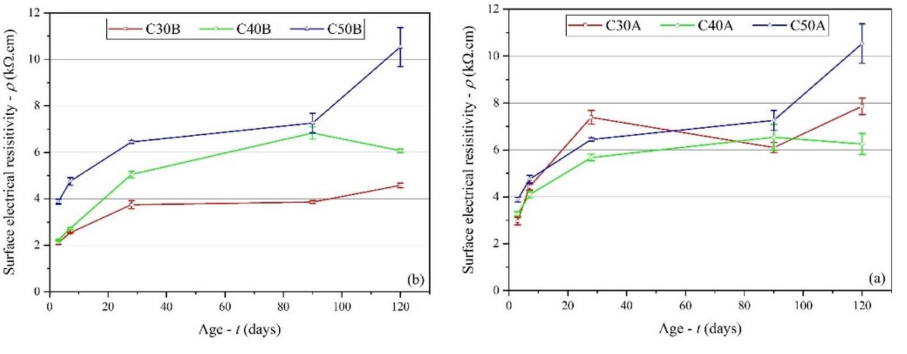

Figure 5. The evolution of average surface electrical resistivity (ρ) with age for A concretes (a) and B concretes (b) families.

Another way to analyze the evolution of surface electrical resistivity is by fitting the power function presented in Equation 1 to experimental data. In this Equation, ρ is the average surface electrical resistivity, a and b are fitting coefficients and t is the concrete age. This equation was chosen because it presented the best fitting to the experimental data, with higher determination coefficients. Fitting results are presented in Figure 6.

$$\rho = a.t^{b} \tag{1}$$

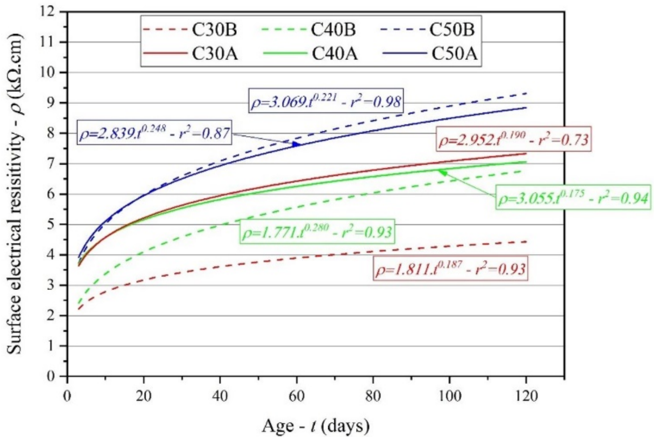

Figure 6. Fitting curves to represent the evolution of surface electrical resistivity (ρ) with concrete age.

The curves presented in Figure 6 show similar growth trends for the six curves, with higher increase tendencies for less porous concretes. From Figures 5 and 6 it can be also seen that C30-A concrete presented higher values than C30-B concrete and quite close (but still slightly higher) to C40-A (Figure 6). Respect to the lower values of C30-B in comparison with C30-A, this can be explained by the higher porosity of the first concrete (Table 5). Respect to C30-A values being slightly higher than C40-A values, the behavior of C30-A concrete may be influenced by a heterogeneous distribution of coarse aggregates and the possibility of its higher presence close to the specimen's surface.

In this sense, literature shows that it is not only the paste porosity that exerts influence on the electrical resistivity measurements. Sengul [34] and Hou et al. [35] observed that the increase in the quantity of coarse aggregate and, consequently, the reduction in the cement paste content result in higher values of surface electrical resistivity. Thus, considering the possibility of a higher content of coarse aggregate close to C30-A specimen surfaces, this could explain their obtained values of surface electrical resistivity.

4.5 Correlation between compressive strength and surface electrical resistivity

Correlation curves between compressive strength (f_c) and surface electrical resistivity (ρ) of concrete were generated by means of nonlinear curves fitting. Initially, the experimental data were grouped into each class (C30, C40 and C50), i.e., the strength values of the C30-A concrete were brought together to the strength values of the C30-B concrete and so on. This was done due to the similarity of A and B cement properties and the good harmony of data within each compressive strength class (see Figure 7). After the formation of the sets, initial fittings were performed. The choice of the best fitting function was based on the criterion of higher determination coefficient (r^2). The r^2 results obtained for each of the curves as well as the tested functions are presented in Table 6.

Table 6 shows that the correlation curves generated by the logarithmic function are the ones that best fit the experimental data, which is in line with the literature review (Table 1). Therefore, the logarithmic function was selected to represent the relationship between concrete compressive strength (f_c) and surface electrical resistivity (ρ) in this work. During the fitting process, a statistical treatment was performed for the identification and elimination of spurious data (outliers). As a result, the correlation curves generated are presented in Figure 7. Equations 2 to 4 represent de relationships between compressive strength and surface electrical resistivity for concretes C30, C40 and C50, respectively.

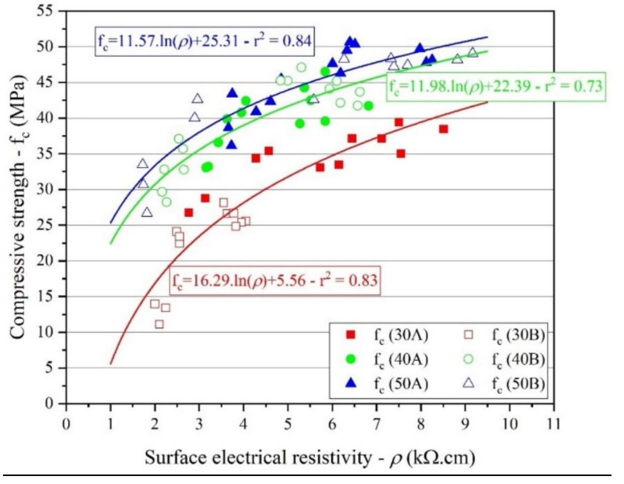

Figure 7. Correlation curves between compressive strength (f_c) and surface electrical resistivity (ρ) for each compressive strength class.

Table 6. Determination coefficients (r^2) of the fitting functions tested for the relationship between compressive strength (f_c) and surface electrical resistivity (ρ).

Curve function	Coefficient of determination (r^2)		
	C30	**C40**	**C50**
Exponential ($f_c = a^{(\rho)}$)	0.58	0.53	0.61
Linear ($f_c = a\cdot(\rho) + b$)	0.67	0.52	0.63
Logarithmic ($f_c = a\cdot\ln(\rho) + b$)	0.83	0.73	0.84
Power ($f_c = a\cdot(\rho)^b$)	0.67	0.63	0.74

$$f_c = 16.29\ ln(\rho) + 5.56 \quad r^2=0.83\ (C30) \tag{2}$$

$$f_c = 11.98\ ln(\rho) + 22.39 \quad r^2=0.73\ (C40) \tag{3}$$

$$f_c = 11.57\ ln(\rho) + 25.31 \quad r^2=0.84\ (C50) \tag{4}$$

Additionally, the experimental data were grouped in a single set and a general curve was defined regardless of the compressive strength classes of concrete, after a complementary statistical treatment, which allowed the elimination of few additional spurious data (Figure 8). Equation 5 represents this relationship. As could be expected, there was a reduction in the determination coefficient, but it still represents a good value, considering data nature.

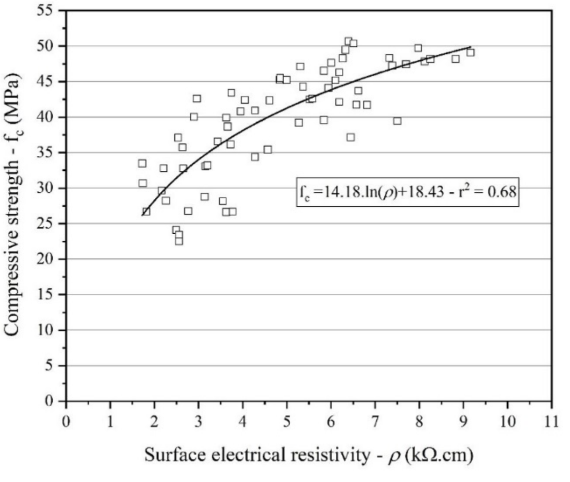

Figure 8. General correlation curve between compressive strength (f_c) and surface electrical resistivity (ρ) considering present data.

$$f_c = 14.18\ ln(\rho) + 18.43 \quad r^2 = 0.68 \tag{5}$$

A comparison between the curves proposed by several other authors and the proposal in this work is presented in Figure 9 (geometric correction factors for compressive strength and resistivity data were adopted when necessary). This figure shows that there is a good harmony among the curves obtained in this research and the majority of those proposed in the literature. Medeiros-Junior et al. [31] curves, as well as Ramezanianpour et al. [30], Bem et al. [9] and Sabbağ and Uyanik [28] curves are not far from those proposed in this work and Andrade and D'Andrea [27] curve covered a data range not covered by other studies. In fact, there is a region represented by the grey region in Figure 9, where most curves fit, which allows to propose a general curve to represent the behavior of all data. This general curve is represented by the function $f_c = 11.89 \cdot \ln(\rho) + 18.90$, with a determination coefficient of 0.51 (Figure 10), which seems to be acceptable for a diverse database.

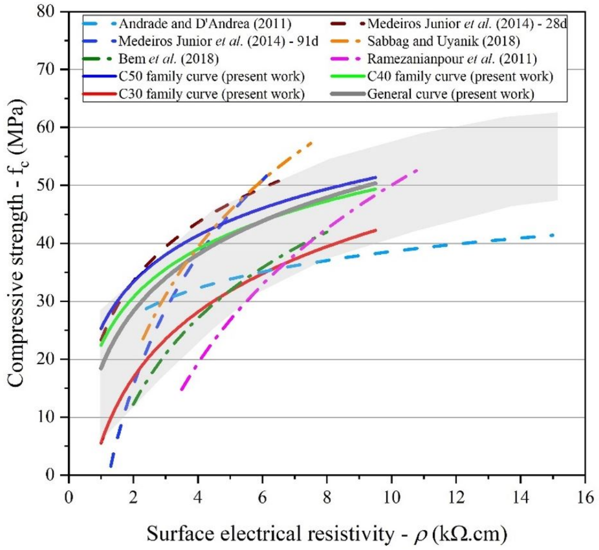

Figure 9. Comparison between correlation curves (f_c versus ρ) proposed in literature and those from this work.

There is still a lack of studies aimed in obtaining correlation curves between the concrete compressive strength and the surface electrical resistivity. During the accomplishment of this work, only few studies on this subject could be observed in literature [9], [27], [28], [31] based on the Wenner method in saturated specimens and more research in necessary to expand the literature database. At this moment, Figure 10 represents the database that could be worked on.

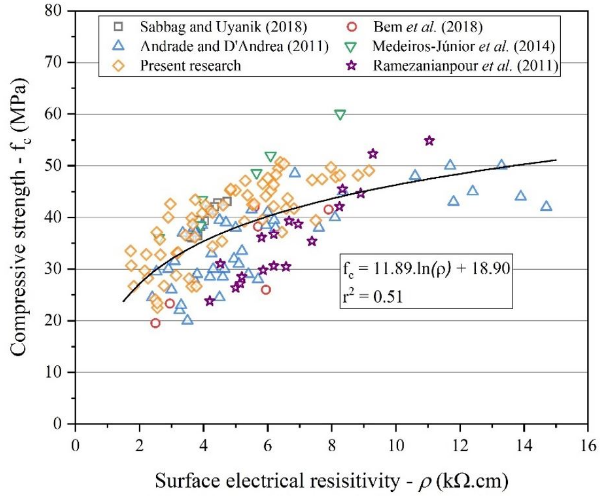

Figure 10. General correlation curve between compressive strength (f_c) and surface electrical resistivity (ρ) considering literature and present data.

4.6 Correlation between splitting tensile strength and surface electrical resistivity

The correlation curves between concrete splitting tensile strength (f_t) and surface electrical resistivity (ρ) were either grouped into each compressive strength class (C30, C40 and C50). The reason for this was the same presented in previous section. The fitting procedures followed the same steps detailed in section 4.5. The obtained correlation curves are presented in Figure 11 and show that splitting tensile strength increases as surface electrical resistivity increases. This behavior is explained by the fact that both properties are dependent on the solid space relation. As more hydrated products are generated and the solid space relation increases, concrete becomes less porous. As a consequence, splitting tensile strength increases and the surface electrical resistivity, which is influenced by the lower water content in concrete porous network, becomes higher.

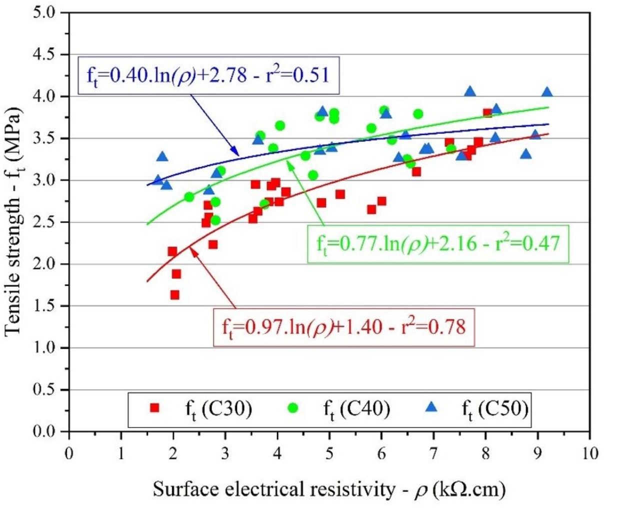

Figure 11. Correlation curves between splitting tensile strength (f_t) and surface electrical resistivity (ρ) for compressive strength classes C30, C40 and C50.

Equations 6 to 8 represent de relationships between splitting tensile strength and surface electrical resistivity for concretes C30, C40 and C50, respectively. They show less expressive determination coefficients than those obtained in previous section. The higher dispersion of data can be attributed to the higher dependence of tensile strength on the interfacial transition zone (ITZ) characteristics [49]. This means that there are aspects like the calcium hydroxide crystals orientation in ITZ that affect tensile strength but do not influence concrete resistivity in a similar way.

$$f_t = 0.97\, ln(\rho) + 1.40 \quad r^2=0.78 \text{ (C30)} \tag{6}$$

$$f_t = 0.77\, ln(\rho) + 2.16 \quad r^2=0.47 \text{ (C40)} \tag{7}$$

$$f_t = 0.40\, ln(\rho) + 2.78 \quad r^2=0.51 \text{ (C50)} \tag{8}$$

As it was done in previous section, the experimental data were grouped in a single set and a general curve was obtained after the fitting process (Figure 12). Equation 9 represents this relationship. As could be expected, there was a reduction in the determination coefficient, but it still represents a good value, considering data nature. No literature data on the relationship between splitting tensile strength and surface electrical resistivity for concretes could be found.

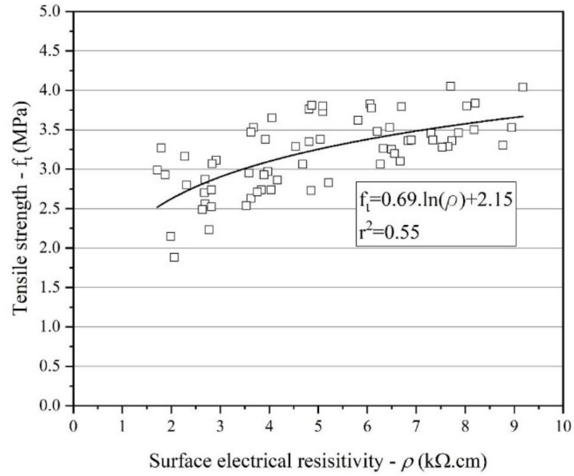

Figure 12. General correlation curve between splitting tensile strength (f_t) and surface electrical resistivity (ρ) considering present data.

$$f_t = 0.69\ ln(\rho) + 2.15 \quad r^2=0.55 \tag{9}$$

4.7 Correlation between splitting tensile strength and compressive strength

Although the correlation between tensile strength and compressive strength was widely studied in literature [12-17] and it is not the aim of this paper, it is also presented here as part of the data analysis. Figure 13 presents this correlation, which follows a square root of compressive strength function (a particular case of the power function $f_t = a \cdot f_c^{\,b}$). As can be seen, less points were depicted in Figure 13, which is a consequence of using average results for each age and concrete mixture. In previous sections (4.5 and 4.6), individual results could be used as resistivity measurements are not destructive and were taken just before the destructive tests, resulting in more data available.

This behavior based on square root of compressive strength function is not far from that proposed by ACI [17] (also based on square root of compressive strength) and from that proposed by a Brazilian standard [16], which confirms that the relationship between tensile strength and compressive strength follows a power function as previously observed in literature [12-15].

Regarding that compressive strength at 28 days is a property regularly obtained for concretes and that surface electrical resistivity is a NDT that can be easily carried out at older ages, a relationship between splitting tensile strength (f_t) and surface electrical resistivity (ρ) considering the compressive strength at 28 days (f_{c28}) and the surface electrical resistivity at this same age (ρ_{28}) is proposed (Equation 10). It is presented in Figure 14 and shows a good harmony between measured and predicted data.

$$f_t = [0.594 + 0.127 ln(\rho / \rho_{28})].f_{c28}^{\,0.458} \quad r^2=0.80 \tag{10}$$

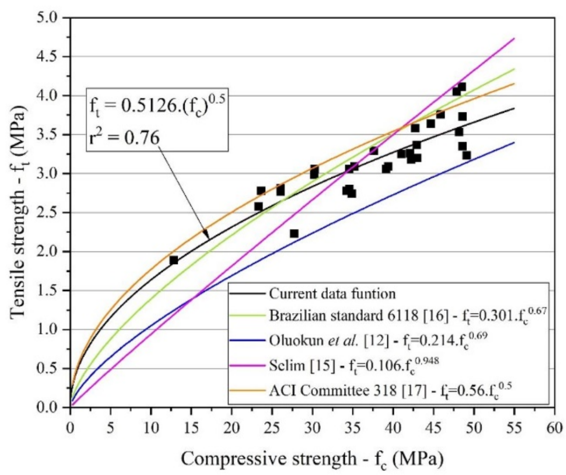

Figure 13. General correlation curve between splitting tensile strength (f_t) and compressive strength (f_c) considering present data and literature correlation curves

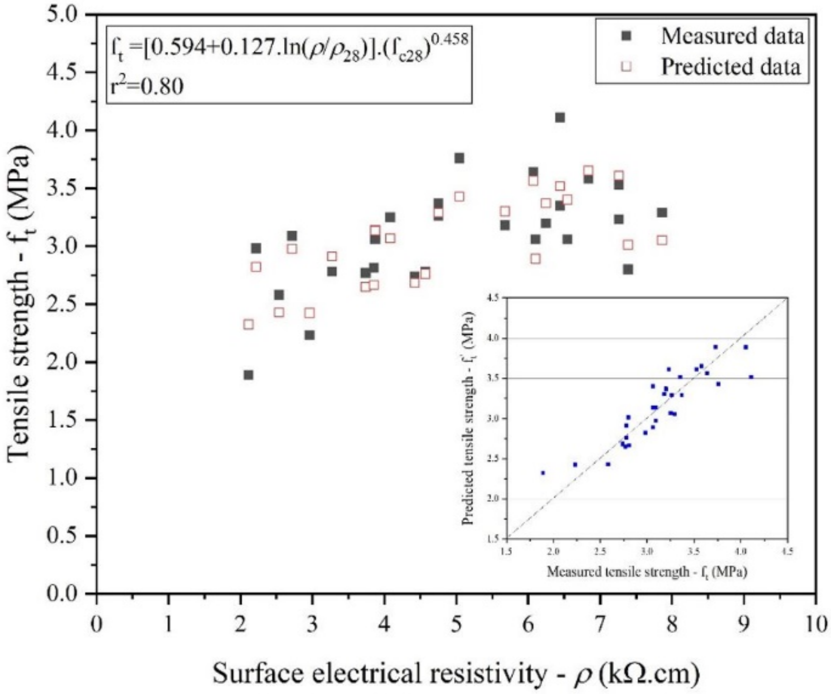

Figure 14. Relationship between splitting tensile strength (f_t) and surface electrical resistivity (ρ) considering the compressive strength at 28 days (f_{c28}) and the surface electrical resistivity at this same age (ρ_{28}) for present data

5 CONCLUSIONS

This research obtained correlation curves between compressive strength, splitting tensile strength and surface electrical resistivity. Based on the results, the following conclusions were drawn:

a) The behavior of surface electrical resistivity measurements in relation to time presented an expected growth tendency for all concrete mixtures, as a consequence of cement paste hydration process. This increase tendency is more pronounced in the first 28 days, where the hydration products are formed on a larger scale, even more for the kind of cement used in the present research. After this age, there is a stabilization tendency;

b) To represent the relationship between compressive strength (f_c) and surface electrical resistivity (ρ) for the studied concretes, four correlation curves are proposed following logarithmic functions, being $f_c = 16.29\cdot\ln(\rho) + 5.56$ indicated for C30 concrete family; $f_c = 11.98\cdot\ln(\rho) + 22.39$ indicated for C40 concrete family; $f_c = 11.57\cdot\ln(\rho) + 25.31$ indicated for C50 concrete family; and $f_c = 14.18\cdot\ln(\rho) + 18.43$ indicated for the total data set. All the proposed curves provide an estimation of compressive strength of concrete, from the value of the surface electrical resistivity measured in cylindrical specimen with 10 cm in diameter and 20 cm in height. They are applicable to concretes with materials and compositions similar to those shown here and with values of compressive strength within the range from 25 MPa to 50 MPa at 28 days;

c) With respect to the curves achieved in this research and those found in the literature concerning the relationship between compressive strength and surface electrical resistivity obtained under the saturated dry surface condition, the few literature data available show that there is a good harmony among the curves obtained in this research and the majority of those proposed in the literature. As a result, a general correlation curve could be proposed by the function $f_c = 11.89\cdot\ln(\rho) + 18.90$, which is not far from that proposed in "b" item;

d) In a similar way as compressive strength, the relationship between splitting tensile strength (f_t) and surface electrical resistivity (ρ) was represented by four correlation curves that followed logarithmic functions, being $f_t = 0.97\cdot\ln(\rho) + 1.40$ indicated for C30 concrete family; $f_t = 0.77\cdot\ln(\rho) + 2.16$ indicated for C40 concrete family; $f_t = 0.40\cdot\ln(\rho) + 2.78$ indicated for C50 concrete family; and $f_t = 0.69\cdot\ln(\rho) + 2.15$ indicated for the total data set. All the proposed curves provide an estimation of splitting tensile strength of concrete, from the value of the surface electrical resistivity measured in the same way and with the same validity pointed out in "b" item.

e) The relationship between splitting tensile strength (f_t) and surface electrical resistivity (ρ) considering the compressive strength at 28 days (f_{c28}) and the surface electrical resistivity at this same age (ρ_{28}) can be represented by the function $f_t = [0.594+0.127\ln(\rho/\rho_{28})]\cdot f_{c28}^{0.458}$.

ACKNOWLEDGEMENTS

The authors thank the Coordination for the Improvement of Higher Education Personnel (CAPES) for the financial support to this work. The authors also express their gratitude to the Laboratory of Tests of Materials and Structures of the UFPB (LABEME) and to the laboratory of the Research Group on Construction and Waste Materials of the IFPB (GMAT) for the availability of instruments and facilities for conducting the tests.

REFERENCES

[1] M. A. P. Irrigaray, "*Estimation of the concrete compression strength by the ultrasonic pulses velocity in the concrete slurry*," Ph.D. dissertation, Federal Univ. Santa Catarina, 2012.

[2] M. D. Machado, "*Correlation curves to characterize concrete used in Rio de Janeiro through non - destructive tests*," M.S. thesis, Federal Univ. Rio de Janeiro, Rio de Janeiro, 2005.

[3] V. M. Malhotra, "In Situ/Non-destructive Testing of Concrete - A Global Review," in *Situ/Non-destructive Testing of Concrete* (Special Publication SP-82). Detroit, USA: American Concrete Institute, 1984, pp. 1–16.

[4] F. R. Andriolo and B. C. Sgarboza, *Concrete Inspection and Quality Control*. São Paulo, Brazil, Newswork, 1993.

[5] A. C. J. Evangelista, "*Evaluation of concrete strength using different non-destructive tests*," Ph.D. dissertation, Federal Univ. Rio de Janeiro, 2012.

[6] K. Rashid and R. Waqas, "Compressive strength evaluation by non-destructive techniques: an automated approach in construction industry," *J. Build. Eng.*, vol. 12, pp. 147–154, Apr. 2017. http://dx.doi.org/10.1016/j.jobe.2017.05.010.

[7] A. Lübeck, A. L. G. Gastaldini, D. S. Barin, and H. C. Siqueira, "Compressive strength and electrical properties of concrete with white Portland cement and blast-furnace slag," *Cement Concr. Compos.*, vol. 34, pp. 392–399, Feb. 2012. http://dx.doi.org/10.1016/j.cemconcomp.2011.11.017.

[8] C. T. Chen, J. J. Chang, and W. C. Yeih, "The effects of specimen parameters on the resistivity of concrete," *Constr. Build. Mater.*, vol. 71, pp. 35–43, Oct. 2014. http://dx.doi.org/10.1016/j.conbuildmat.2014.08.009.

[9] D. H. Bem, D. P. B. Lima, and R. A. Medeiros-Junior, "Effect of chemical admixtures on concrete's electrical resistivity," *Int. J. Build. Pathol. Adaptation*, vol. 36, pp. 174–187, Apr. 2018. http://dx.doi.org/10.1108/IJBPA-11-2017-0058.

[10] S. Mendes, R. Oliveira, C. Cremonez, E. Pereira, and R. A. Medeiros-Junior, "Electrical resistivity as a durability parameter for concrete design: experimental data versus estimation by mathematical model," *Constr. Build. Mater.*, vol. 192, pp. 610–620, Dec. 2018. http://dx.doi.org/10.1016/j.conbuildmat.2018.10.145.

[11] R. A. Medeiros-Junior and M. G. Lima, "Electrical resistivity of unsaturated concrete using different types of cement," *Constr. Build. Mater.*, vol. 107, pp. 11–16, Mar. 2016. http://dx.doi.org/10.1016/j.conbuildmat.2015.12.168.

[12] F. A. Oluokum, "Prediction of concrete tensile strength from its compressive strength: evaluation of existing relations for normal weight concrete," *ACI Mater. J.*, vol. 88, pp. 302–309, May/Jun. 1991.

[13] M. F. M. Zain, H. B. Mahmud, A. Ilham, and M. Faizal, "Prediction of splitting tensile strength of high-performance concrete," *Cement Concr. Res.*, vol. 32, pp. 1251–1258, 2002.

[14] C. Chhorn, S. J. Hong, and S. W. Lee, "Relationship between compressive and tensile strengths of roller-compacted concrete," *J. Traffic Transp. Eng.*, vol. 5, pp. 215–223, 2018. http://dx.doi.org/10.1016/j.jtte.2017.09.002.

[15] P. Selim, "Experimental investigation of tensile behaviour of high strength concrete," *Indian J. Eng. Mater. Sci.*, vol. 15, pp. 467–472, 2008.

[16] Associação Brasileira de Normas Técnicas, *Design of structural concrete - Procedure*, 2003.

[17] ACI Committee 318, *Building code requirements for structural concrete (ACI 318-11) and commentary*. Farmington Hills: American Concrete Institute, 2011.

[18] G. M. Barrow, *Physical Chemistry.* Barcelona, Spain: Reverté, 1964.

[19] R. Polder et al., "Test methods for on site measurement of resistivity of concrete," *Mater. Struct.*, vol. 33, pp. 603–611, 2000. http://dx.doi.org/10.1007/BF02480599.

[20] Spanish Association for Standardisation and Certification, *Concrete durability: Determination of the electrical resistivity. Part1: Direct test (reference method), UNE 83988-1, AENOR*, Madrid, Spain, 2008.

[21] Associação Brasileira de Normas Técnicas, *Concrete hardened - Determination of electrical-volumetric resistivity - Test method*, ABNT NBR 9204, 2012.

[22] ASTM International, *Standard Test Method for Bulk Electrical Resistivity or Bulk Conductivity of Concrete*, C1876, 2019.

[23] L. Santos, "*Evaluation of the electrical resistivity of concrete as a parameter for the prediction of the initiation of corrosion induced by chlorides in concrete structures*," M.S. thesis, University of Brasília, Brasília, DF, 2006.

[24] F. Wenner, "A Method of measuring earth resistivity," *Bull. Bur. Stand.*, vol. 12, pp. 469–478, 1915.

[25] A. G. Abreu, "*Effect of Mineral Additions on the Electrical Resistivity of Conventional Concretes*," M.S. thesis, Federal University of Rio Grande do Sul, 1998.

[26] P. Azarsa and R. Gupta, "Electrical Resistivity of Concrete for Durability Evaluation: A Review," *Adv. Mater. Sci. Eng.*, vol. 2017, pp. 1–30, May 2017. http://dx.doi.org/10.1155/2017/8453095.

[27] C. Andrade and R. D'Andrea, "The electrical resistivity as a control parameter of the concrete and its durability," *J. ALCONPAT*, vol. 1, pp. 90–98, 2011.

[28] N. Sabbağ and O. Uyanık, "Determination of the reinforced concrete strength by apparent resistivity depending on the curing conditions," *J. Appl. Geophys.*, vol. 155, pp. 13–25, Feb. 2018. http://dx.doi.org/10.1016/j.jappgeo.2018.03.007.

[29] X. Wei, L. Xiao, and Z. Li, "Prediction of standard compressive strength of cement by the electrical resistivity measurement," *Constr. Build. Mater.*, vol. 31, pp. 341–346, Jun. 2012. http://dx.doi.org/10.1016/j.conbuildmat.2011.12.111.

[30] A. Ramezanianpour, A. Pilvar, A. Mahdikhani, and F. Moodi, "Practical evaluation of relationship between concrete resistivity, water penetration, rapid chloride penetration and compressive strength," *Constr. Build. Mater.*, vol. 25, no. 5, pp. 2472–2479, 2011. http://dx.doi.org/10.1016/j.conbuildmat.2010.11.069.

[31] R. A. Medeiros-Junior, M. G. Lima, M. H. F. Medeiros, and L. V. Real, "Investigation of the compressive strength and electrical resistivity of concrete with different types of cement," *J. ALCONPAT*, vol. 4, pp. 113–128, 2014.

[32] W. Morris, E. I. Moreno, and A. A. Sagués, "Practical evaluation of resistivity of concrete in test cylinders a Wenner array probe," *Cement Concr. Res.*, vol. 26, pp. 1779–1787, Dec. 1996. http://dx.doi.org/10.1016/S0008-8846(96)00175-5.

[33] M. H. F. Medeiros, "Study of variables that influence the resistivity measurements of reinforced concrete structures," *Civ. Eng. J. Univ. Minho*, vol. 12, pp. 55–64, 2001.

[34] O. Sengul, "Use of electrical resistivity as an indicator for durability," *Constr. Build. Mater.*, vol. 73, pp. 434–441, Dec 2014. http://dx.doi.org/10.1016/j.conbuildmat.2014.09.077.

[35] T. Hou, V. K. Nguyen, Y. Su, Y. Chen, and P. Chen, "Effects of coarse aggregates on the electrical resistivity of Portland cement concrete," *Constr. Build. Mater.*, vol. 133, pp. 397–408, Feb. 2017. http://dx.doi.org/10.1016/j.conbuildmat.2016.12.044.

[36] Associação Brasileira de Normas Técnicas, *Aggregates - Determination of the granulometric composition*, ABNT NBR NM 248, 2003.

[37] Associação Brasileira de Normas Técnicas, *Aggregates - Determination of bulk density and volume of voids*, ABNT NBR NM 45, 2006.

[38] Associação Brasileira de Normas Técnicas, *Fine aggregate - Determination of specific weight and bulk density*, ABNT NBR NM 52, 2009.

[39] Associação Brasileira de Normas Técnicas, *Coarse aggregate - Determination of density, apparent density and water absorption*, ABNT NBR NM 53, 2009.

[40] Associação Brasileira de Normas Técnicas, *Aggregates - Determination of fine material passing through the 75 μm sieve per wash*, ABNT NBR NM 46, 2003.

[41] Associação Brasileira de Normas Técnicas, *Portland cement and other powdered materials - Determination of specific mass, A*BNT NBR 16605, 2017.

[42] Associação Brasileira de Normas Técnicas, *Portland cement and other powdered materials - Determination of fineness by the air permeability method (Blaine method)*, ABNT NBR 16372, 2015.

[43] Associação Brasileira de Normas Técnicas, *Concrete - Procedure for casting and curing of specimens*, ABNT, 2016.

[44] Associação Brasileira de Normas Técnicas, *Concrete - Sampling of fresh concrete*, ABNT NBR NM 33, 1998.

[45] Asociacion Espanola de Normalizacion, *Concrete durability: Determination of the electrical resistivity. Part1: Four-points or Wenner method*, UNE 83988-2, 2014.

[46] Associação Brasileira de Normas Técnicas, *Concrete - Compression test of cylindrical specimens*, ABNT NBR 5739, 2007.

[47] Associação Brasileira de Normas Técnicas, *Concrete and mortar - Determination of the tensile strength by diametrical compression of cylindrical test specimens*, ABNT NBR 7222, 2011.

[48] Associação Brasileira de Normas Técnicas, *Concrete aggregates – Specification*, ABNT NBR 7211, 2009.

[49] P. K. Mehta and P. J. M. Monteiro, *Concrete: Microstructure, Properties, and Materials*, 3rd ed. New York, NY, USA: McGraw-Hill, 2006.

[50] P. Ghosh and Q. Tran, "Influence of parameters on surface resistivity of concrete," *Cement Concr. Compos.*, vol. 62, pp. 134–145, Jul. 2015.

Author contributions: CCA: experimental work, formal analysis, writing; GRM: conceptualization, funding acquisition, supervision, formal analysis, writing.

Editors: David Oliveira, Guilherme Aris Parsekian.

IBRACON Structures and Materials Journal
Revista IBRACON de Estruturas e Materiais
ISSN 1983-4195 ismj.org

ORIGINAL ARTICLE

A simplified approach to reliability evaluation of deep rock tunnel deformation using First-Order Reliability Method and Monte Carlo simulations

Uma abordagem simplificada para avaliação de confiabilidade em túneis rochosos profundos utilizando o Método de Confiabilidade de Primeira Ordem e Simulações de Monte Carlo

Caio Cesar Cardoso da Silva[a]
Mauro de Vasconcellos Real[b]
Samir Maghous[c]

[a]Universidade Federal do Rio Grande do Sul, Programa de Pós-graduação em Engenharia Civil, Porto Alegre, RS, Brasil
[b]Universidade Federal do Rio Grande, Programa de Pós-graduação em Engenharia Oceânica, Rio Grande, RS, Brasil
[c]Universidade Federal do Rio Grande do Sul, Programa de Pós-graduação em Engenharia Civil, Porto Alegre, RS, Brasil

Received 13 March 2021
Accepted 19 April 2021

Abstract: The Monte Carlo simulation (MCS) and First-Order Reliability Method (FORM) provide a reliability analysis in axisymmetric deep tunnels driven in elastoplastic rocks. The Convergence-Confinement method (CV-CF) and Mohr-Coulomb (M-C) criterion are used to model the mechanical interaction between the shotcrete lining and ground through deterministic parameters and random variables. Numerical models synchronize tunnel analytical models and reliability methods, whereas the limit state functions control the failure probability in both ground plastic zone and shotcrete lining. The results showed that a low dispersion of random variables affects the plastic zone's reliability analysis in unsupported tunnels. Moreover, the support pressure generates a significant reduction in the plastic zone's failure, whereas the increase of shotcrete thickness results in great reduction of the lining collapse probability.

Keywords: axisymmetric deep tunnels, shotcrete lining, CV-CF method, MCS, FORM.

Resumo: Este trabalho propõe uma análise de confiabilidade em túneis profundos axissimétricos, escavados em maciços rochosos elasto-plásticos, utilizando o Método de Confiabilidade de Primeira Ordem e simulações de Monte Carlo. O método Convergência-Confinamento (CV-CF) e o critério de Mohr-Coulomb (M-C) são utilizados para modelar analiticamente a interação mecânica entre o revestimento de concreto projetado e o maciço escavado, através de parâmetros determinísticos e variáveis aleatórias. Modelos numéricos são sincronizados com os modelos analíticos de túneis e os métodos de confiabilidade, enquanto as funções estado-limite definem a probabilidade de falha na zona plástica do maciço rochoso e no revestimento de concreto projetado. Os resultados mostram que uma baixa dispersão das variáveis aleatórias afeta a confiabilidade da zona plástica na análise de túneis sem revestimento. Além disso, a pressão de suporte gera uma redução significativa na falha da zona plástica, enquanto o aumento da espessura do concreto projetado resulta em uma grande redução da probabilidade de colapso do revestimento.

Palavras-chave: túneis profundos axissimétricos, concreto projetado, método CV-CF, simulações de Monte Carlo, FORM.

How to cite: C. C. C. Silva, M. V. Real, and S. Maghous, “A simplified approach to reliability evaluation of deep rock tunnel deformation using First-Order Reliability Method and Monte Carlo simulations,” *Rev. IBRACON Estrut. Mater.*, vol. 15, no. 1, e15104, 2022, https://doi.org/10.1590/S1983-41952022000100004

Corresponding author: Caio Cesar Cardoso da Silva. E-mail: caiocesarcardosodasilva@gmail.com
Financial support: This study was financed in part by the Coordenação de Aperfeiçoamento de Pessoal de Nível Superior - Brazil (CAPES) - Finance Code 001.
Conflict of interest: We wish to confirm that there are no known conflicts of interest associated with this publication.

1 INTRODUCTION

Several geotechnical and structural parameters are involved in deep tunnels and underground excavation analysis, which induce high or undefined structural risks. The reliability analysis evaluates structural failure probabilities in tunnels by applying random and deterministic parameters in analytical solutions or numerical methods.

The first serious discussions and analyses of tunnel reliability emerged during the 1990s with [1]-[6]. Low and Tang [5] focused on identifying and evaluating the reliability and risk parameters through numerical procedures, synchronizing reliability codes developed in software like Microsoft Excel, and analytical methods for axisymmetric tunnels. This work used the First Order Reliability Method (FORM) and Monte Carlo Simulation (MCS) in the reliability study. Low and Tang [7], [8] developed and improved the FORM numerical procedures. Li and Low [9] conducted a series of reliability analyses of an axisymmetric tunnel, considering normal and non-normal random variables of the rock mass and the Low and Tang [5] FORM algorithm. The internal pressure produces a reduction of risk; moreover, the authors checked the reliability results using MCS. Lü and Low [10] and Song et al. [11] studied the reliability of axisymmetric tunnels through the FORM and Second-Order Reliability Method (SORM), synchronizing these methods with analytical solutions based on Mohr-Coulomb (M-C) and Hoek Brown criteria.

Bjureland et al. [12] applied the MCS associated with the Convergence-Confinement method (CV-CF method) to analyze the failure probability in a shotcrete lining of a circular tunnel. The M-C criterion describes the plasticity behavior for the excavated rock mass, and the Observational method checks the failure results, verifying the necessity of putting into action security measures.

The present paper analyses the reliability methods impact on analytical tunneling methods, examining two different tunnels with statistical and deterministic distinct parameters. This study aims to investigate the reliability results of the plastic zone excavation and the shotcrete lining for both tunnels, establishing interesting comparisons between them. For this, the reliability procedures associate the use of the FORM Low and Tang method, developed in Low and Tang [5], and the MCS. The reliability algorithms, developed in VBA and MATLAB codes, employ two analytical methodologies for axisymmetric tunnels: the M-C plasticity criterion for excavated rock masses and the CV-CF method to analyze the interaction between the shotcrete lining and rock mass.

2 RELIABILITY CONCEPTS

2.1 Reliability Index: The Low and Tang FORM Interpretation

Hasofer and Lind [13] defined the second-moment reliability index β as a better approach in civil engineering design in comparison with usual safety factors [7]. Equation 1, proposed by Low and Tang [7], represents the matrix formulation of the Hasofer-Lind reliability index for correlated normal variables:

$$\beta = \min_{x \in F} \sqrt{\left[\frac{x_i - \mu_i}{\sigma_i}\right]^T \left[\mathbf{R}\right]^{-1} \left[\frac{x_i - \mu_i}{\sigma_i}\right]} \tag{1}$$

where x_i is the set of random variables of the vector $\boldsymbol{x}$, μ_i is the set of mean values of the vector $\boldsymbol{\mu}$, and σ_i is the set of standard deviations of the vector $\boldsymbol{\sigma}$. The domain F represents the failure regions, whereas $[\mathbf{R}]$ is the correlation matrix, expressed by [14]:

$$\left[\mathbf{R}\right] = \begin{bmatrix} 1 & \rho_{1,2} & \cdots & \rho_{1,n} \\ \rho_{2,1} & 1 & \cdots & \rho_{2,n} \\ \vdots & \vdots & \ddots & \vdots \\ \rho_{n,1} & \rho_{n,2} & \cdots & 1 \end{bmatrix} \tag{2}$$

where $\rho_{i,j}$ is the correlation coefficient between two random variables x_i and x_j $(i \neq j)$.

For the non-normal distributions, the basic idea is to calculate the equivalent normal mean μ^N and equivalent standard deviation σ^N, which replaces the values of μ and σ in Equation 1. The Rackwitz-Fiessler transformation defines the following analytical solution for μ^N and σ^N [15]:

$$\mu^N = x - \sigma^N \Phi^{-1}\left[F(x)\right] \tag{3}$$

$$\sigma^N = \frac{\phi\left\{\Phi^{-1}\left[F(x)\right]\right\}}{f(x)} \tag{4}$$

In Equation 3, $\Phi^{-1}[\cdot]$ is the inverse of the cumulative distribution function (CDF) (standard normal), and $F(x)$ is the original non-normal CDF, evaluated for $\boldsymbol{x}$. In Equation 4, $\phi\{\}$ is the probability density function (pdf) of the standard normal distribution, whereas $f(x)$ is the original non-normal pdf, evaluated for $\boldsymbol{x}$.

In a classical explanation, β is the smallest distance from the mean value point to the limit state surface in units of directional standard deviations [7]. Low and Tang [5], [7] proposed an alternative interpretation of the reliability index β, which is a simple method of defining the index, in the original space of the random variables, through the perspective of an expanding ellipsoid. Figure 1 shows this interpretation.

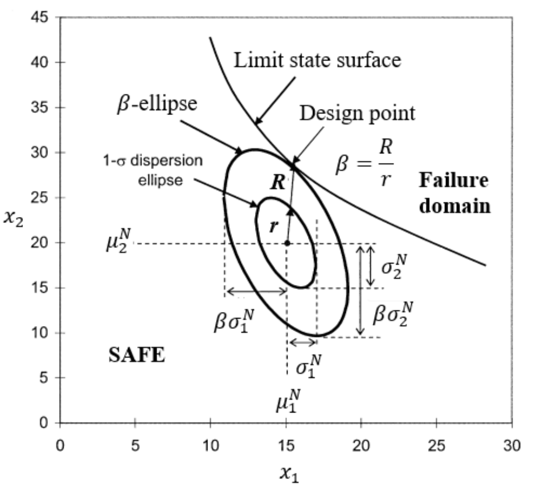

Figure 1. Equivalent dispersion ellipsoids illustrated in the plane [8].

As shown in Figure 1, the design point is a tangency point of the expanding dispersion ellipsoid with the limit state surface, which separates safe values from unsafe values (failure domain). The reliability index β is the axis ratio R/r of the ellipse that touches the limit state surface [8]. The dispersion ellipsoid expands from the mean-value point according to the following probability density function of a multivariate normal distribution [8]:

$$f(x) = \frac{1}{(2\pi)^{\frac{n}{2}} |C|^{0.5}} \exp\left[-\frac{1}{2}\beta^2\right] \tag{5}$$

where to minimize β, defined by Equation 1, is to maximize the value of the probability density function defined by Equation 5. Hence, it is possible to define the smallest dispersion ellipsoid tangent to the limit state surface (see Figure 1) and the most probable failure point (design point).

Low and Tang [5] described that if each axis of the $(1-\sigma)$ dispersion ellipsoid, in Figure 1, is parallel to the coordinate axis, the random variables are uncorrelated. So, in correlated normal random variables, each axis of the $(1-\sigma)$ dispersion ellipsoid is inclined about the coordinate axis.

The index β is particularly useful in evaluating the failure probability through the application of the CDF of β, $\Phi(\beta)$, and considering standard normal variables [9]:

$$p_{\mathrm{f}} \approx 1-\Phi(\beta) \tag{6}$$

Low and Tang [8] performed a new efficient algorithm using FORM, where the first and third terms under the square root in Equation 1 are equivalent standard vectors $[n]$. Thus, Equation 1 is defined as:

$$\beta = \min_{x \in F} \sqrt{[n]^T [\mathbf{R}]^{-1} [n]} \tag{7}$$

The optimization routine *Solver* of Microsoft Excel solves Equation 7. Autonomously, the routine changes the values of components n_{i} (computing the parameters $\boldsymbol{\mu}^N$ and $\boldsymbol{\sigma}^N$, when necessary) and subjecting the limit state function to a zero-value restriction. The components in the original space, x_{i}, are program-calculated from:

$$x_{\mathrm{i}} = F^{-1}\left[\Phi\left(n_{\mathrm{i}}\right)\right] \tag{8}$$

2.2 Monte Carlo Simulation

The Monte Carlo Simulation (MCS) consists of developing an analytical and numerical model and using many simulations or cycles to check the real behavior of a system. Each cycle provides output variables (results) based on random input variables, using statistical methods and probability distributions [16].

Considering a random variable *X,* with a CDF $F_X(x_{\mathrm{i}})$, to generate sample x_{i} values included in *X,* the MCS code needs to accomplish some steps. First, MATLAB numerical procedures generate a sample value of u_{i} between 0 and 1 for a random variable with uniform distribution. Next, the inverse of F_X computes a sample value of x_{i} ($x_{\mathrm{i}} = F_X^{-1}(u_{\mathrm{i}})$).

For two correlated normal random variables, the numerical procedure generates two random numbers u_1 and u_2, used to compute the random variables *x* and *y* from the following equations [17]:

$$x = \mu_X + \sigma_X \sqrt{-2\ln u_1}\cos(2\pi u_2) \tag{9}$$

$$y = \mu_{Y|X} + \sigma_{Y|X} \sqrt{-2\ln u_1}\sin(2\pi u_2) \tag{10}$$

where the mean and standard deviation of the variable *y*, which are dependent on *x* value, are evaluated through the following equations:

$$\mu_{Y|X} = \mu_Y + \rho_{X,Y}\frac{\sigma_Y}{\sigma_X}\left(x-\mu_X\right) \tag{11}$$

$$\sigma_{Y|X} = \sigma_Y \sqrt{1-(\rho_{X,Y})^2} \tag{12}$$

Each MCS cycle consists of introducing random input variables in an appropriated mathematical model: the limit state or performance functions $Z = g(x_1, x_2, \ldots, x_n) = 0$. A negative performance function implies random variables located in a failure domain. After the implementation of all cycles, the following relation, between the total failure cycles N_f and the total cycles of MCS *N*, checks the failure probability p_f [15]:

$$p_f = \frac{N_f}{N} \tag{13}$$

Figure 2 shows a flowchart with the steps of the MCS numerical procedure developed in MATLAB. In summary, the numerical procedure considers a predefined number of cycles and checking the failure cycles, N_f. Equation 14 checks the failure probability estimation error through a normal distribution approximation, with a reliability interval of 95%.

$$e(\%) = 200 \times \left(\sqrt{\frac{1 - p_f}{N \times p_f}} \right) \tag{14}$$

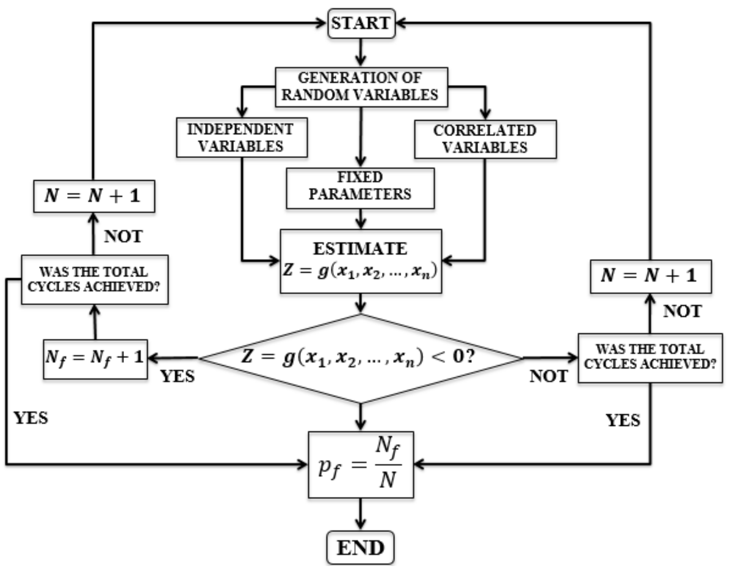

Figure 2. Flowchart of the MCS procedure.

3 ANALYTICAL FRAMEWORK FOR ELASTOPLASTIC DEFORMATION IN AXISYMMETRIC TUNNELS

3.1 Elastoplastic fields in the surrounding rock mass

Figure 3 shows the axisymmetric tunnel characteristics, excavated in a homogeneous elastic-plastic rock mass and with a radius R_i. The cylindrical coordinate system $\underline{e}_r$, $\underline{e}_\theta$, and $\underline{e}_z$ represents the stress and displacement components. The stresses $\sigma_{rr}(r)$ and $\sigma_{\theta\theta}(r)$ are the in-plane normal components of the rock stress tensor $\underline{\underline{\sigma}}$, whereas P_∞ and P_i is the far-field pressure and uniform support pressure into the excavation. It is assumed that the stress component $\sigma_{zz}(r)$ does not vary, which implicitly amounts to disregarding the confinement losses along the z-axis direction.

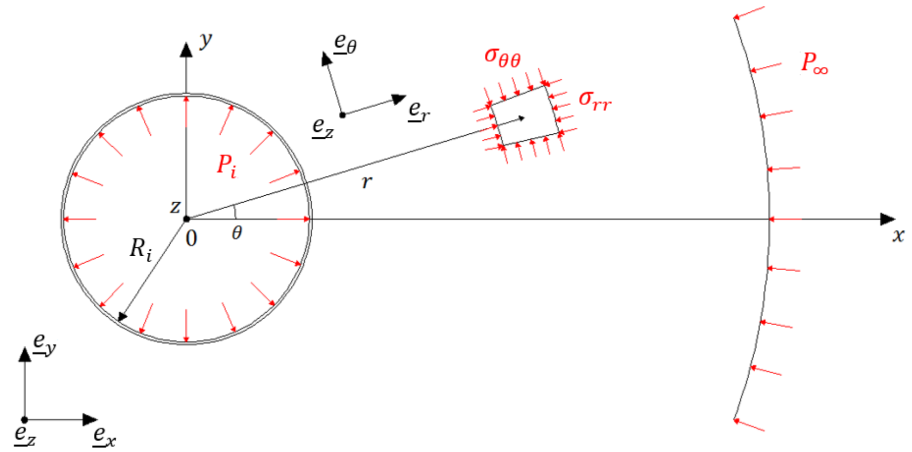

Figure 3. Cross-section of an axisymmetric tunnel within an elastic-plastic rock mass.

In the fully elastic regime, the radial displacement $u_{ie}(r)$ at any a point of the rock mass located at distance r from the center of the excavation is given by ([18], [19]):

$$u_{ie}(r) = -\left(\frac{1+\nu}{E}\right)(P_\infty - P_i)\frac{R_i^2}{r} \tag{15}$$

where ν and E are the Poisson's rate and Young's modulus, respectively.

In the elastoplastic regime, the mechanical analysis of the tunnel deformation indicates that two regions should be distinguished, as illustrated in Figure 4: the elastoplastic region $R_i \le r \le R_p$ undergoing irreversible strains, and the elastic behavior region $r \ge R_p$. The plastic radius $r = R_p$ defines the limit between the elastic and elastoplastic regions of the rock mass.

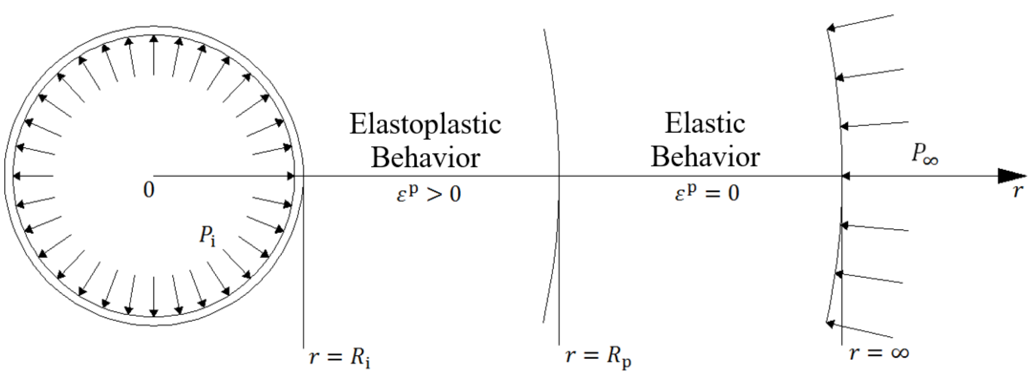

Figure 4. Axisymmetric tunnel within an elastoplastic rock mass.

The analytical methods use the M-C criterion concepts for the elastoplastic behavior, defined according to Salençon [18] and Corbetta [19]. The plastic radius R_p is:

$$R_p = R_i\left[\frac{2(P_\infty + a)}{(K_p+1)(P_i+a)}\right]^{\frac{1}{K_p-1}} \tag{16}$$

where:

$$K_\mathrm{p} = \frac{1+\sin\varphi}{1-\sin\varphi} \tag{17}$$

$$a = \frac{c}{\tan\varphi} \tag{18}$$

in which c is the cohesion and φ is the friction angle. The limit pressure P_lim defines a rock mass pressure when $r = R_\mathrm{p}$ as follows:

$$P_\mathrm{lim} = \frac{2P_\infty + a\left(1-K_\mathrm{p}\right)}{\left(K_\mathrm{p}+1\right)} \tag{19}$$

Referring to Figure 4, the radial displacement u_ip in the elastoplastic region $R_\mathrm{i} \le r \le R_\mathrm{p}$ is defined by:

$$u_\mathrm{ip}(r) = r\left(\frac{1+\nu}{E}\right)\left[A + B\left(\frac{r}{R_\mathrm{p}}\right)^{K_\mathrm{p}-1} + C\left(\frac{R_\mathrm{p}}{r}\right)^{K_\mathrm{b}+1}\right] \tag{20}$$

where Equation 21 defines the dilatancy coefficient K_b, ψ representing the dilatancy angle, whereas Equations 22, 23 and 24 characterize the parameters A, B, and C.

$$K_b = \frac{1+\sin\psi}{1-\sin\psi} \tag{21}$$

$$A = \left(1-2\nu\right)\left(P_\infty + a\right) \tag{22}$$

$$B = -\left[\frac{\left(1-\nu\right)\left(K_\mathrm{b}K_\mathrm{p}+1\right)}{K_\mathrm{p}+K_\mathrm{b}}\right]\left[\frac{2\left(P_\infty + a\right)}{\left(K_\mathrm{p}+1\right)}\right] \tag{23}$$

$$C = -2\left(1-\nu\right)\left[\frac{\left(K_p-1\right)\left(P_\infty + a\right)}{K_p+K_b}\right] \tag{24}$$

3.2 Convergence-confinement method

The CV-CF method allows modeling in a simplified manner the evolution of normalized radial displacement U_i of the rock mass and support, or the convergence at the tunnel wall, associated with the internal pressure P_i in a specific cross-section of the tunnel wall. The convergence U_i is given by:

$$U_\mathrm{i} = \frac{\left|u_\mathrm{i}\left(r = R_\mathrm{i}\right)\right|}{R_\mathrm{i}} \tag{25}$$

where $u_i(r = R_i)$ is the radial displacement at the tunnel wall, defined by Equation 15 (elastic behavior) or Equation 20 (elastoplastic behavior). The principle of the CV-CF method is schematized in Figure 5.

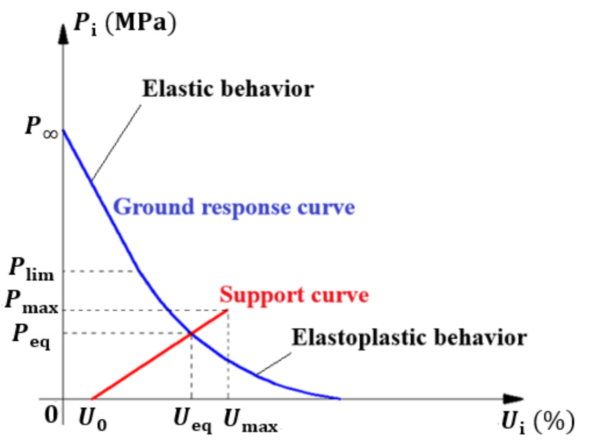

Figure 5. Schematized description of the Convergence-confinement method for a specific cross-section of a tunnel.

Figure 5 shows the Ground response curve, or Convergence curve (CV), which describes only the mechanical behavior of the unsupported excavation wall, while the Support curve, or Confinement curve (CF), describes the mechanical behavior of the elastic shotcrete lining.

When the excavation front is close to a specific cross-section, changes occur in the ground stress state. At some distance, before the excavation reaches the cross-section, there are small changes of the stress state, and elastic convergence U_{ie} occurs as P_i decreases. The internal pressure P_i continues to decrease where, eventually, the decrement of stresses in the rock mass will reach a limit P_{lim}, and the stresses cause plastic behavior of the ground in a zone with a radius R_p surrounding the tunnel periphery [12]. Thus, considering an interval $P_\infty \geq P_i \geq P_{lim}$, the CV curve shows an elastic behavior (blue curve in Figure 5), and for the interval $P_{lim} \geq P_i \geq 0$, the CV curve shows an elastoplastic behavior. Equations 16 and 19 defines R_p and P_{lim}.

The CF curve avoids the ground confinement loss, which causes normalized radial displacements of the rock mass. According to the red curve in Figure 5, a ground confinement loss generates a growing internal pressure P_i and convergence U_i on the cross-section lining. Moreover, numerical or analytical approaches estimate the convergence U_0 at the beginning of the support installation. Panet and Guenot [20] proposed an analytical approximation for U_0:

$$U_0 = \left[1 - \left(\frac{0.84R_p}{d_0 + 0.84R_p}\right)^2\right]\left[U_{i,\infty} - 0.27\left(\frac{1+\nu}{E}P_\infty\right)\right] + 0.27\left(\frac{1+\nu}{E}P_\infty\right) \tag{26}$$

where $U_{i,\infty}$ is the convergence for elastoplastic behavior, at a larger distance between the excavation face and the cross-section (Equation 25 with $P_i = 0$).

The pressure at the shotcrete lining is evaluated as [21]:

$$P_i = K_s\left(U_{i,s} - U_0\right) \tag{27}$$

In Equation 27, $U_{i,s}$ is the shotcrete convergence (determined when P_i varies between 0 and P_{max} in Equation 27), and K_s is the support stiffness coefficient, calculated according to the relation R_i / t_s ([22], [23]):

$$\begin{cases} K_{\mathrm{s}} = \dfrac{E_{\mathrm{s}}}{\left(1-\nu_{\mathrm{s}}\right)} \dfrac{t_{\mathrm{s}}}{R_{\mathrm{i}}} & \text{for } \dfrac{R_{\mathrm{i}}}{t_{\mathrm{s}}} > 10 \\ K_{\mathrm{s}} = \dfrac{E_s\left[R_i^2 - (R_i - t_s)^2\right]}{\left(1-\nu_{\mathrm{s}}\right)\left[\left(1-\nu_{\mathrm{s}}\right)R_{\mathrm{i}}^2 + (R_i - t_s)^2\right]} & \text{for } \dfrac{R_{\mathrm{i}}}{t_{\mathrm{s}}} \leq 10 \end{cases} \tag{28}$$

where t_s is the shotcrete lining thickness, while E_s and ν_s are the Young modulus and the Poisson Coefficient of the support, respectively. The maximum support pressure P_{max} is defined by the following Equation:

$$\begin{cases} P_{\max} = \dfrac{\sigma_{\mathrm{s}} t_{\mathrm{s}}}{R_{\mathrm{i}}} & \text{for } \dfrac{R_{\mathrm{i}}}{t_{\mathrm{s}}} > 10 \\ P_{\max} = \dfrac{\sigma_{\mathrm{s}}}{2}\left[1 - \dfrac{(R_{\mathrm{i}} - t_{\mathrm{s}})^2}{R_{\mathrm{i}}^2}\right] & \text{for } \dfrac{R_{\mathrm{i}}}{t_{\mathrm{s}}} \leq 10 \end{cases} \tag{29}$$

σ_s standing for the uniaxial compressive strength of the support lining.

The maximum convergence U_{max} is evaluated by setting $P_i = P_{max}$ into Equation 27. Referring to Figure 5, the equilibrium state of the structure ($U_i = U_{eq}$ and $P_i = P_{eq}$) is defined as the intersection point between the CV and CF curves. The design value P_{eq} can be computed combining Equations 16, 20 and 27:

$$P_{\mathrm{eq}} - K_{\mathrm{c}}\left\{\left(\frac{1+\nu}{E}\right)\left[A + B\left(\frac{R_{\mathrm{i}}}{R_{\mathrm{p}}}\right)^{K_{\mathrm{p}}-1} + C\left(\frac{R_{\mathrm{p}}}{R_{\mathrm{i}}}\right)^{K_{\mathrm{b}}+1}\right] - U_0\right\} = 0 \tag{30}$$

By using Equation 16 one can calculate R_p with $P_i = P_{eq}$. Then Equation 30 is solved numerically by the bisection method inside the MCS MATLAB code.

4 PERFORMANCE FUNCTIONS AND ADOPTED PARAMETERS

The limit state function, or performance function, $g_1(x)$ refers to the plastic zone's reliability analyses, whereas $g_2(x)$ refers to the shotcrete lining reliability. The functions $g_1(x)$ and $g_2(x)$ consider the relationship between an accepted resistance and a demand (loading), according to the equations below ([9], [13]):

$$g_1(x) = L - \frac{R_{\mathrm{p}}}{R_{\mathrm{i}}} = L - \left[\frac{2\left(P_\infty + a\right)}{\left(K_{\mathrm{p}}+1\right)\left(P_{\mathrm{i}}+a\right)}\right]^{\frac{1}{K_{\mathrm{p}}-1}} \tag{31}$$

$$g_2(x) = U_{\max} - U_{\mathrm{eq}} = R_{\mathrm{i}}\left[\frac{P_{\max} + P_{\mathrm{eq}} + 2K_{\mathrm{s}}U_0}{K_{\mathrm{s}}}\right] \tag{32}$$

The ratios L and U_{max} are the allowed largest values (resistances) for the following demands (loadings): plastic zone ratio (R_p / R_i) and design convergence ratio (U_{eq}). Equation 31 evaluates R_p / R_i using Equation 16, while Equation 32 evaluates U_{max} by fixing $U_{i,s} = U_{max}$ in Equation 27, with $P_i = P_{max}$. When $g_1(x)$ takes a negative value, an unacceptable large plastic zone occurs, and it exceeds the L ratio. If $g_2(x)$ takes a negative value, the radial displacement U_{eq} exceeds the largest support displacement U_{max}.

The geotechnical random variables were obtained in the research of Hoek [6] (tunnel A) and Brantmark [24] (tunnel B). Tables 1 and 2 show the geotechnical statistical parameters for tunnels A and B.

Table 1. Geotechnical statistical parameters for tunnel A [6].

Geotechnical parameter	Mean (μ)	Standard Deviation (σ)	Coefficient of Variation (δ)
Friction angle (φ)	22.85°	1.31°	0.06
Cohesion (c)	0.230 MPa	0.068 MPa	0.30
Deformation modulus (E)	373 MPa	48 MPa	0.13
Far field stress (P_∞)	2.50 MPa	0.25 MPa	0.10

Table 2: Geotechnical statistical parameters for tunnel B [24].

Geotechnical parameter	Mean (μ)	Standard Deviation (σ)	Coefficient of Variation (δ)
Friction angle (φ)	35.00°	0.50°	0.01
Cohesion (c)	1.30 MPa	0.13 MPa	0.10
Deformation modulus (E)	5000 MPa	500 MPa	0.10
Far field stress (P_∞)	8.00 MPa	0.80 MPa	0.10

All statistical parameters described in Tab. 1 and 2 are normally distributed. However, it is considered a negative correlation between c and φ, with the following correlation coefficients: $\rho_{c,\varphi} = -0.5$ for tunnel A and $\rho_{c,\varphi} = -0.9$ for tunnel B. It should be emphasized that the correlation between some of the design parameters significantly affects the reliability predictions. In that respect, the assumption of negatively correlated shear strength parameters was found to be conservative with respect to uncorrelated variables [25]. The analysis developed, for instance, in Laso et al. [4] has included the correlation between some of the relevant problem parameters, such as correlation between the ground Young modulus and ground density, shotcrete average resistance and shotcrete layer thickness, as well as between tunnel radius and shotcrete layer thickness. Although the subject of correlation is not fully addressed in the present reliability study, this important issue will be foreseen in the continuation line of this research.

The rock mass failure criterion features a non-associated flow rule in both tunnels, with the following deterministic parameters: $\psi = 0$ and $K_\mathrm{b} = 1$ (Equation 21) for tunnel A; $\psi = 20^\circ$ and $K_\mathrm{b} = 2.04$ for tunnel B. The Poisson coefficients are $\nu = 0.30$, and $\nu = 0.25$, for tunnels A and B, respectively. For both tunnels, a radius of $R_\mathrm{i} = 4.5\mathrm{m}$ is adopted.

Table 3 shows the statistical parameters for the shotcrete lining. Both tunnels use the same parameters, which are statistically independent and normally distributed. The Poisson coefficient is $\nu_\mathrm{c} = 0.25$.

Table 3. Statistical parameters of shotcrete support [24].

Shotcrete parameter	Mean (μ)	Standard Deviation (σ)	Coefficient of Variation (δ)
Deformation modulus (E_s)	16,000 MPa	800 MPa	0.05
Uniaxial compressive strength (σ_s)	30 MPa	1.5 MPa	0.05

Li and Low [9] suggested applying the lognormal or beta distribution instead of the normal distribution when the coefficient of variation a random variable (ratio between standard deviation and mean) is 0.25 or higher. This is necessary to avoid negative geotechnical parameters, which is irrational. All coefficients of variation are smaller than 0.25 in tunnels A and B, except for the cohesion c in tunnel A, where, alternatively, the cohesion is constrained to be greater than zero.

5 RELIABILITY ANALYSIS REGARDING THE EXTENT OF PLASTIC ZONE

This section analyzes the reliability of tunnels A and B, contemplating the performance function of Equation 31. The first reliability analysis performs the characterization of the fixed resistances in $g_1(x)$ regarding unsupported tunnels, whereas the second analysis of the reliability methods will contemplate the shotcrete lining. The 2007 FORM algorithm of Low and Tang and MCS compute the reliability indexes and failure probabilities, employing the analytical theories explained in section 2.

In summary, the Low and Tang algorithm is a code developed in Visual Basic (VBA) language and Microsoft Excel. A constrained optimization routine, denominated *Solver*, assists in the FORM procedure development, where the equations and parameters described in sections 2.1 and 4 have been employed directly in the Excel worksheets. Low and Tang [7], [8], and Li and Low [9] give more details about the FORM algorithm of Low and Tang.

First, it is necessary to verify the results obtained by FORM and MCS to check the algorithms' proper operation. Li and Low [9] analyzed the plastic zone reliability, employing the FORM Low and Tang code, the performance function $g_1(x)$, and tunnel A parameters. Thus, Table 4 shows a comparison between results of this work and Li and Low [9], with the following deterministic values: the parameters of tunnel A, $P_\infty = 2.50\text{MPa}$, $L = 3.00$, $0 \le P_i \le 0.30\text{MPa}$ and 5E+06 Monte Carlo simulations, which generates an error between $0.15\% \le e \le 3.92\%$ when $0 \le P_i \le 0.30\text{MPa}$.

Table 4: Failure probabilities results p_f considering tunnel A.

	Results of this work		Li and Low [9]
$P_i\,(\text{MPa})$	FORM Low and Tang	MCS	FORM Low and Tang
0 (unsupported tunnel)	24.30%	24.68%	24.40%
0.10	6.26%	6.42%	6.31%
0.20	0.87%	0.89%	0.88%
0.30	0.06%	0.05%	0.06%

The failure probabilities evaluated in Tab. 4 have shown a good agreement with the Li and Low [9] results, considering both FORM and MCS results of this work. Thus, considering random variables with normal distribution, the reliability algorithms used in this work have shown efficiency when applied in unsupported and supported tunnels analysis.

The first analysis intends to verify the influence of resistance L in the reliability index β, on the plastic zone reliability in tunnels A and B. Figure 6 shows the β values evaluated for the statistical parameters of unsupported tunnels A and B, employing FORM Low and Tang algorithm, and varying the resistance L, in Equation 31, considering the following intervals: $2.30 \le L \le 3.00$ for tunnel A and $1.10 \le L \le 1.70$ for tunnel B.

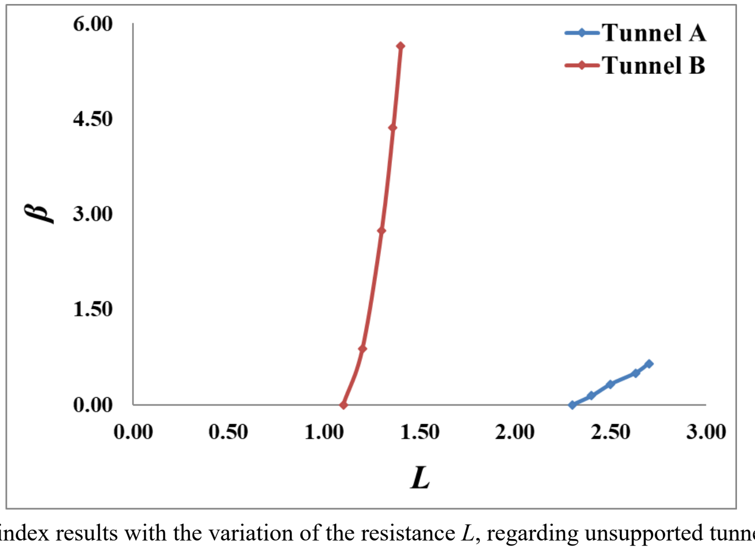

Figure 6. Reliability index results with the variation of the resistance L, regarding unsupported tunnels A and B ($P_i = 0$).

Comparing the curves in Figure 6, a great sensibility on the β variation with the increase of L occurs for tunnel B (red curve). For example, the index in tunnel B increases from $\beta = 0.88$ to $\beta = 2.74$ if the resistance increases from $L = 1.40$ to $L = 1.50$. On the other hand, tunnel A (blue curve) does not show a considerable increase in β, i.e., the index increases from $\beta = 0.14$ to $\beta = 0.32$ when L increases from $L = 2.70$ to $L = 2.80$. Table 5 illustrates the values of β and p_f according to the curves of Figure 6.

Table 5. Reliability index and failure probabilities of the plastic zone.

TUNNEL A			TUNNEL B		
L	***β***	***p*f (%)**	***L***	***β***	***p*f (%)**
2.70	0.14	44.45	1.40	0.88	18.85
2.80	0.32	37.30	1.50	2.74	0.31
2.90	0.50	31.12	1.60	4.35	6.82E-4
3.00	0.65	25.86	1.70	5.64	8.57E-7

The results of Tab. 5 highlight the p_f reduction in both studies. In tunnel A, p_f decreases from 44.45% to 25.86% between $L = 2.70$ and $L = 3.00$, while in tunnel B p_f decreases from 18.85% to 8.57E-07% between $L = 1.40$ and $L = 1.70$. In contrast, the reliability index β increases from 0.14 to 0.65 for tunnel A and from 0.88 to 5.64 for tunnel B, with L variation. The greater variation of reliability results in tunnel B is a consequence of the correlation between the random variables and the plastic zone results R_p / R_i, performed by MCS.

Figure 7 illustrates the correlation between the random variables and R_p / R_i through dispersion charts, using 30E+03 Monte Carlo simulations. The number of simulations was varied to assess the accuracy of the MCS results. The errors in estimating the failure probability were 1.28% and 2.40%, checked through Equation 14, using the parameters of unsupported tunnels A and B ($P_i = 0$).

There is a strong correlation between the plastic zone and the parameters (c, φ and P_∞) in tunnel B (Figures 7b). It does not occur with tunnel A parameters, which are more dispersed than tunnel B parameters (Figures 7a). About these figures, when the resistance L is close to the plastic zone average, $L \approx \mu_{R_p/R_i} \approx 2.70,$ the R_p / R_i results are more dispersed in the failure zone $(L > 2.70)$. Due to this, the reliability results of tunnel A, in Figure 6 and Table 5, shows a low variation when adopting $2.30 \le L \le 3.00$. In contrast, when $L \approx \mu_{R_p/R_i} \approx 1.40$ for tunnel B, the strong correlation causes a little R_p / R_i dispersion in the failure zone $(L > 1.40)$, and a great variation in reliability results when adopting $1.10 \le L \le 1.70$.

In an overall analysis, these results say that the designers must be careful when adopting elevated values for L, in reliability analysis that involves highly correlated parameters. For this purpose, this study adopted the average resistance values in the performance function $g_1(x)$: $L = 1.40$ for tunnel B, and, for comparison purposes, $L = 2.70$ for tunnel A.

Turning now to the shotcrete lining tunnels, the Low and Tang FORM algorithm and MCS estimates the plastic zone reliability through Equation 31. Tables 6 and 7 summarizes the β and p_f results of the plastic zone. The following interval constraints the shotcrete lining pressure P_i: $0.10\ \text{MPa} \le P_i \le 0.50\ \text{MPa}$. The MCS results for $P_i = 0.1$ and $0.2\ \text{MPa}$ consider 30E+03 simulations in both tunnels, whereas the MCS results for $P_i = 0.3$ and $0.4\ \text{MPa}$ consider 20E+06 simulations in both tunnels. Regarding $P_i = 0.5\ \text{MPa}$, the MCS results refer to 10E+07 simulations for tunnel A and 20E+06 simulations for tunnel B. The number of simulations increases with P_i to keep the error below 10%.

The results in Tables 6 and 7 show that p_f is greater in tunnel A than in tunnel B, when the support pressure $P_i \le 0.3\ \text{MPa}$, whereas the opposite occurs when $P_i \ge 0.4\ \text{MPa}$. This shows the importance of adopting an appropriate lining for tunnel safe. The p_f and β results obtained by the Low and Tang Algorithm and MCS show good concordance. The P_i variation in both tunnels reported reductions of p_f and increases in β.

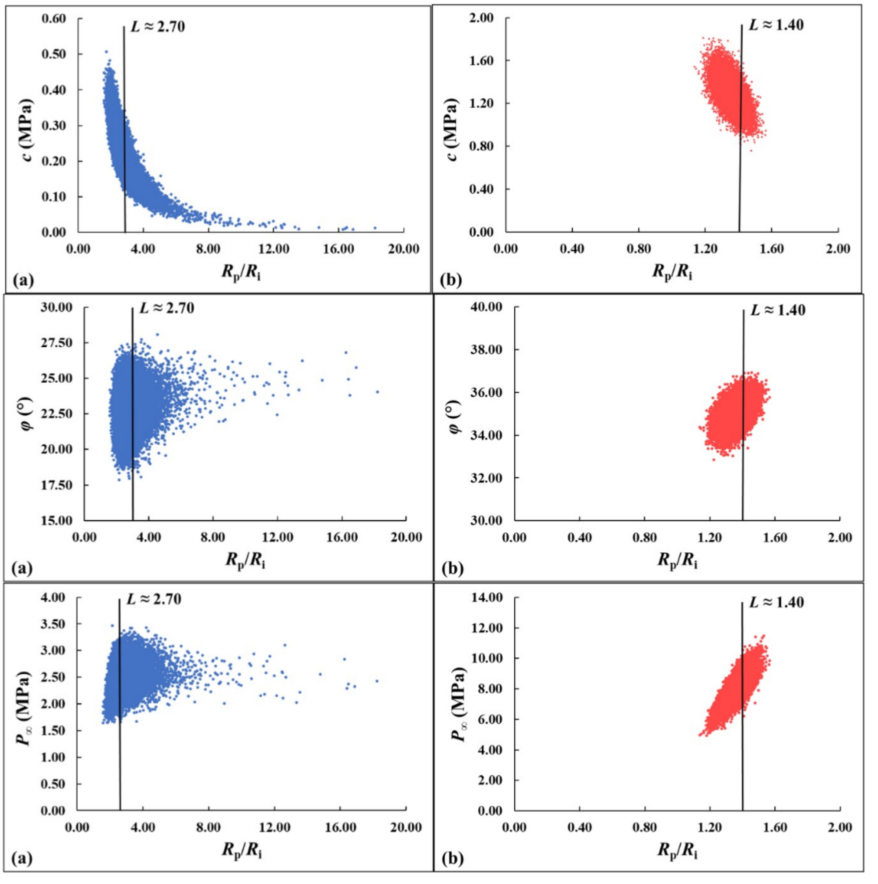

Figure 7. Dispersion results of the plastic zone (R_p / R_i) regarding cohesion (c), friction angle (φ), and far-field stress (P_∞): (a) Tunnel A; (b) Tunnel B.

Table 6. Reliability results for the performance function $g_1(x)$ of tunnel A.

Support Pressure (P_i) (MPa)	Low and Tang Algorithm		MCS	
	β	p_f (%)	p_f (%)	e (%)
0 (unsupported)	0.14	44.27	44.75	1.28
0.10	0.95	17.09	17.40	2.52
0.20	1.76	3.90	3.94	5.68
0.30	2.58	0.50	0.51	0.63
0.40	3.39	0.04	0.03	2.56
0.50	4.19	1.38E-03	7.90E-04	7.12

Table 7. Reliability results for the performance function $g_1(x)$ of tunnel B.

Support Pressure (P_i) (MPa)	Low and Tang Algorithm		MCS	
	β	p_f (%)	p_f (%)	e (%)
0 (unsupported)	0.88	18.85	18.75	2.40
0.10	1.46	7.22	7.21	4.14
0.20	2.05	2.04	2.04	7.99
0.30	2.64	0.41	0.43	0.68
0.40	3.25	0.06	0.06	1.81
0.50	3.86	5.58E-03	5.80E-03	5.88

The MCS code provides the plastic zone histograms in Figures 8a and 8b, where the MATLAB application *Distribution Fitter* adjusts probability distribution functions with these histograms.

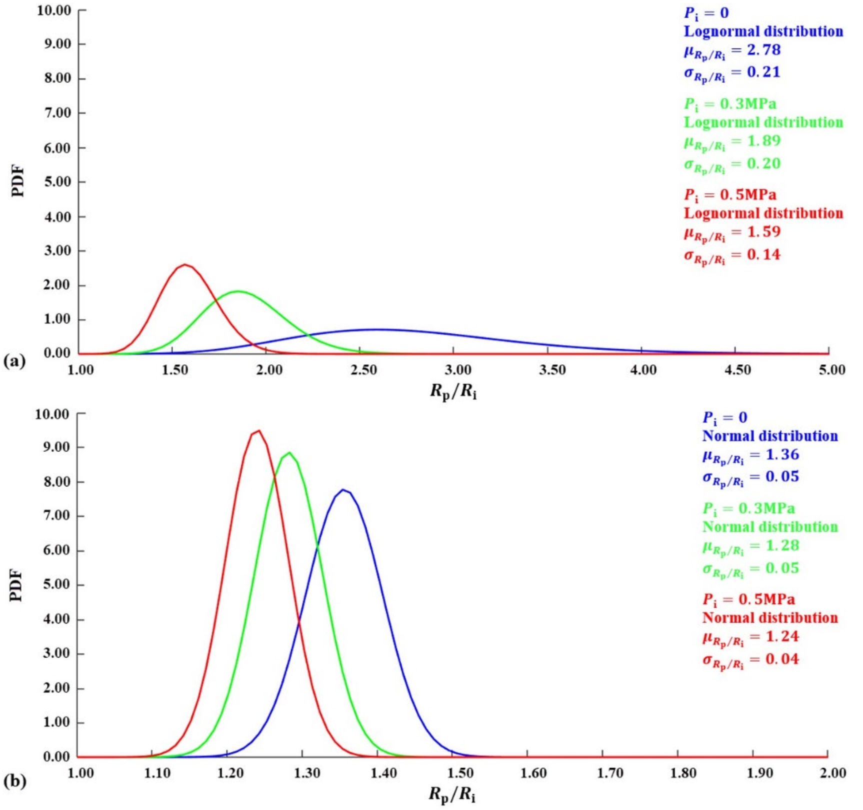

Figure 8. Probability Distribution Functions (PDF) of the plastic zone through Monte Carlo simulations: (a) Tunnel A; (b) Tunnel B.

The plastic zone intervals of PDF curves of Tunnel B (Figure 8b) is smaller than the intervals of tunnel A (Figure 8a). It occurs because the standard deviations $\left(\sigma_{R_p/R_i}\right)$ for tunnel B are smaller than the σ_{R_p/R_i} values of tunnel A. Also, the mean values $\left(\mu_{R_p/R_i}\right)$ of tunnel B are smaller than μ_{R_p/R_i} of tunnel A, due to the higher geotechnical parameters of tunnel B.

Figures 8a and 8b emphasize the histogram distribution types. Tunnel A fits the Lognormal distribution for all histograms, whereas tunnel B fits the Normal distribution for all histograms.

All PDF curves exhibit reductions in the statistical parameters when P_i increases. In Figure 8a, the mean and standard deviation reduces from $\mu_{R_p/R_i} = 2.78$ and $\sigma_{R_p/R_i} = 0.21$ $(P_i = 0)$ to $\mu_{R_p/R_i} = 1.59$ and $\sigma_{R_p/R_i} = 0.14$ $(P_i = 0.5 \text{ MPa})$, whereas in Figure 8b, the parameters reduce from $\mu_{R_p/R_i} = 1.36$ and $\sigma_{R_p/R_i} = 0.05$ $(\mathrm{P_i} = 0)$ to $\mu_{R_p/R_i} = 1.24$ and $\sigma_{R_p/R_i} = 0.04$ $(P_i = 0.5 \text{ MPa})$. To summarize, the P_i increasing causes the reliability index increasing and failure probability reduction during the reliability analyses.

6 RELIABILITY ANALYSIS REGARDING THE TUNNEL CONVERGENCE

In this section, the reliability analysis evaluates the probability of P_{eq} and U_{eq} exceeding the allowed parameters P_{max} and U_{max}. The MCS employs the CV-CF method linked with the performance function $g_2(x)$ (Equation 32). The shotcrete lining parameters are those described in section 4 and Table 3.

As evaluated in the previous section, Equation 14 checks the MCS accuracy considering some number of simulations and a shotcrete lining thickness $t_c = 10 \text{ cm}$. This work adopts 5E+06 simulations, which generate the following results for tunnels A and B: $p_f = 4.06\%$ with an error of 0.43% and $p_f = 19.21\%$ with an error of 0.18%.

Figure 9 shows the variation of the failure probability (p_f) with the increase of t_c. The results were obtained using 5E+06 MCS cycles for each t_c, where in tunnel A the error varies between $0.43\% \le e \le 6.02\%$ regarding $10\text{cm} \le t_c \le 13\text{cm}$, and in tunnel B the error varies between $0.18\% \le e \le 3.32\%$ regarding $10\text{cm} \le t_c \le 20\text{cm}$. The increase of t_c produces a considerable p_f reduction in tunnel A. The increase of just one centimeter in t_c of tunnel A reduces p_f from 4.06% $(t_c = 10\text{ cm})$ to 0.93% $(t_c = 11\text{ cm})$, p_f arrives at 0.02% when $t_c = 13\text{ cm}$. With the tunnel B parameters, Figure 9 shows a reduction from $p_f = 19.21\%$ $(t_c = 10\text{ cm})$ to $p_f = 1.15\%$ $(t_c = 16\text{ cm})$, p_f arrives at 0.08% when $t_c = 20\text{ cm}$. These results say that tunnel B needs more shotcrete than tunnel A to get acceptable reliability levels due to the far-field pressure in tunnel B is much higher than in tunnel A.

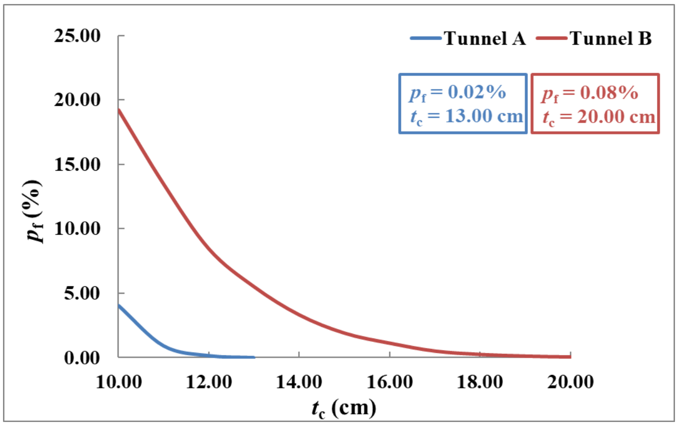

Figure 9. Failure probability reduction with the increasing of t_c, concerning the performance function $g_2(x)$.

Table 8 exhibits the design and maximum support parameters, considering $t_c = 13\text{ cm}$ for tunnel A and $t_c = 20\text{ cm}$ for tunnel B, which keep an adequate structural safety level for the support $(p_f < 0.10\%)$. The convergences U_{eq} and U_{max} have been calculated using the convergence U_0 of the support installation as the origin, whereas the radial displacements u_{eq} and u_{max} have been calculated through Equation 25, i.e., $u_{eq} = |U_{eq} \times R_i|$ and $u_{max} = |U_{max} \times R_i|$.

Table 8. Statistical design parameters for the shotcrete support.

	P_{eq} (MPa)		P_{max} (MPa)		U_{eq} (%)		U_{max} (%)		u_{eq} (mm)		u_{max} (mm)	
	μ	σ	μ	σ	μ	σ	μ	σ	μ	σ	μ	σ
Tunnel A	0.53	0.11	0.87	0.04	0.11	0.02	0.18	0.01	4.70	1.00	7.93	0.56
Tunnel B	0.91	0.11	1.33	0.07	0.12	0.01	0.18	0.01	5.40	0.64	7.93	0.56

The results in Table 8 reveal a difference of 72% between the P_{eq} mean values for tunnels A and B, whereas the difference between the U_{eq} mean values is only 9%. Concerning P_{max} and U_{max}, the thickness t_c controls the support resistance, which increases the stiffness value (K_c) and P_{max}, but does not change U_{max} in both tunnels.

Figures 10a and 10b illustrate the failure probability through the u_{eq} and u_{max} histograms obtained with the parameters of Table 8.

The histograms in Figures 10a and 10b show the support failure region, between 6.00 and 7.00 mm approximately, where $g_2(x) < 0$. The area of this region is proportional to the failure probability, p_f. From Figure 9, it can be seen that p_f on $t_c = 13\text{ cm}$ (tunnel A) and $t_c = 20\text{ cm}$ (tunnel B) have close values. This occurs due to u_{eq} standard deviations since the u_{eq} histogram in Figure 10a is sparser than the corresponding histogram in Figure 10b. As well as in Figure 10, it is easy to evaluate the failure probability through $g_2(x)$, according to Figures 11a and 11b.

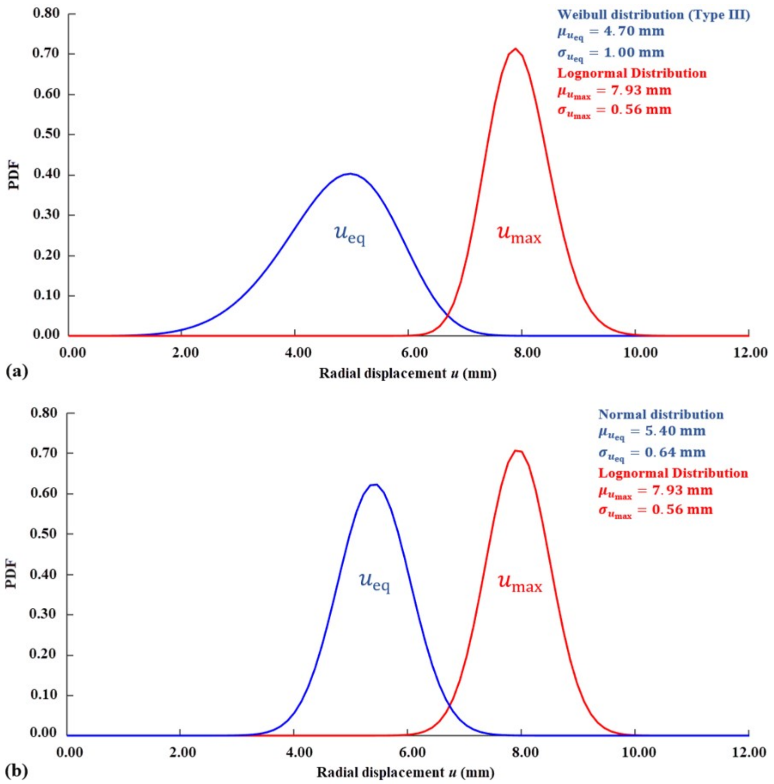

Figure 10. Demand and resistance histograms, generated using 5E+06 Monte Carlo simulations: (a) Tunnel A; (b) Tunnel B.

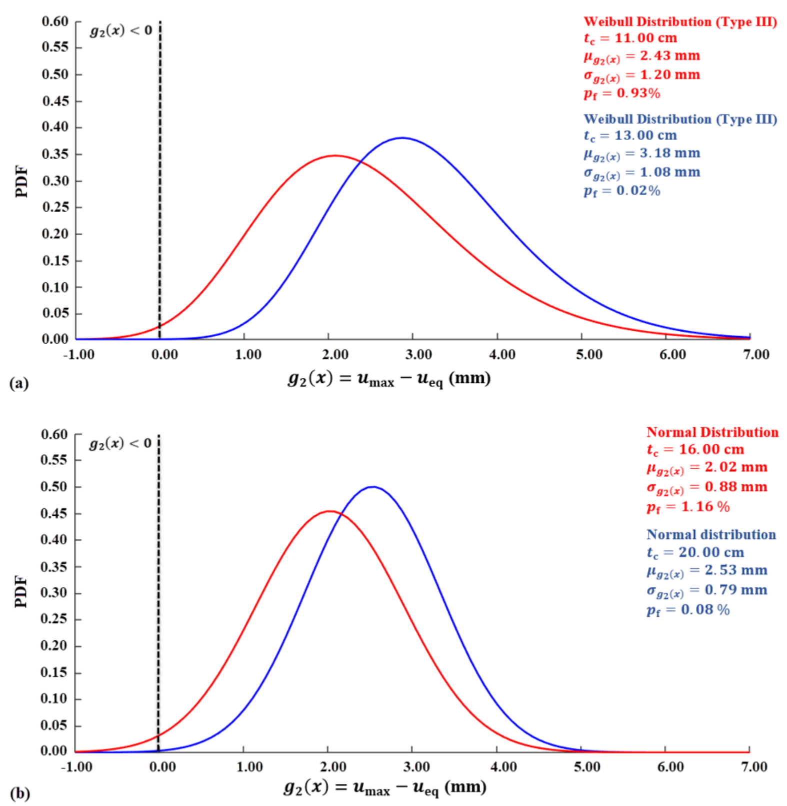

Figure 11. Histograms of performance function $g_2(x)$, generated using Monte Carlo simulations: (a) Tunnel A; (b) Tunnel B.

The negative values of $g_2(x)$, located on the left side of the dashed line in Figures 11a and 11b represents a failure point of the shotcrete lining. That is to say that the area below the histograms and on the left side of the dashed line (in Figure 11) has the same value of the failure probability, p_f. It is possible to see in Figures 11a and 11b, that this area reduces with the increase of t_c, and, therefore, also reduces p_f. Similar to earlier findings, the standard deviation in tunnel A is greater than tunnel B in histograms of Figure 11.

Figures 12a and 12b show an analysis through the CV-CF method, using the mean values of tunnels A and B to verify the accordance with the results defined in Table 8. In these cases, it has been considered $t_c = 13$ cm and $t_c = 20$ cm for tunnels A and B, respectively. The results in Figure 12 must be interpreted with caution due to U_{eq} referring to the shotcrete lining displacement, which starts from the displacement U_0.

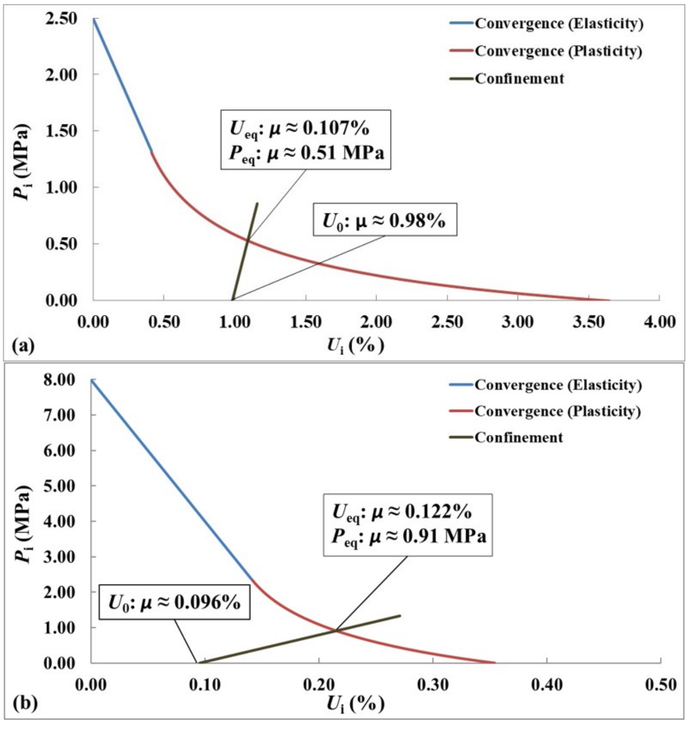

Figure 12. CV-CF method analysis with mean values of: (a) tunnel A; (b) tunnel B.

There are similarities between the design parameters defined in Figures 12a and 12b and the design parameters of Table 8, where it can be seen that the interaction between the Convergence and Confinement curves has been influencing the reliability analysis. The Confinement curve of tunnel A tends to perform better than tunnel B due to the internal pressure P_i being higher in tunnel B.

These results suggest that the shotcrete lining of tunnel A, considering $t_c = 13$ cm, produces acceptable stiffness results K_s, which increases the inclination of the Convergence curve in Figure 12. Tunnel B, likewise, produces acceptable K_s results using $t_c = 20$ cm. The designer must consider adopting support parameters higher than the before adopted, aiming to increase K_s, thus keeping the failure probability low.

7 SUMMARY AND CONCLUSIONS

This study performed a reliability analysis in deep axisymmetric tunnels, integrating FORM and MCS methods with tunnel analytical methodologies. VBA and MATLAB codes verified the reliability in rock masses and shotcrete lining, examining two different tunnels.

The first aim was to check the plastic zone reliability through VBA FORM and MATLAB MCS algorithms. The reliability results verification has shown an excellent agreement between the reliability indexes and failure probabilities, obtained by both algorithms, and with the Li and Low [9] results.

The reliability study of the variation in the resistance *L*, considering unsupported tunnels, suggests that, in general, it is necessary to pay attention to the adopted *L* value in rock masses with low dispersion. This work recommends adopting a resistance value *L* around the mean value to avoid higher p_f values.

The increase of internal pressure P_i produces great changes in the plastic zone reliability. Both tunnels develop significant p_f reductions when $P_i = 0.3\text{MPa}$: p_f reduces 43.80% in tunnel A and 18.40% in tunnel B. The support pressure $P_i = 0.3\text{MPa}$ maintains reliability percentages above 99% in both tunnels; moreover, for $P_i \geq 0.3\text{MPa}$, p_f results are close to 0%.

The MCS code used the CV-CF method equations to provide the convergence reliability. A shotcrete thickness $t_c = 11\text{ cm}$ results $p_f = 0.93\%$ in tunnel A, whereas $t_c = 16\text{ cm}$ results $p_f = 1.15\%$ in tunnel B. When t_c increases for 13 cm in tunnel A, the failure probability reduces to $p_f = 0.02\%$; whereas for tunnel B, p_f reduces to 0.02% when t_c increases to 20 cm. These findings suggest that tunnel A must have a shotcrete thickness between $t_c = 11\text{ cm}$ and $t_c = 13\text{ cm}$. Tunnel B must have a shotcrete thickness between $t_c = 16\text{ cm}$ and $t_c = 20\text{ cm}$. In summary, the failure probabilities are smaller than 0.1%, considering $t_c = 13\text{ cm}$ in tunnel A and $t_c = 20\text{ cm}$ for tunnel B. Moreover, the internal design pressure P_{eq} for these thicknesses is greater than 0.3MPa , which keeps plastic zone failures close to zero.

This paper contributes to check safety or failure probabilities in tunnel design stages. The reliability codes provided statistical data for different rock mass parameters. So, designers and engineers can use these methodologies to ensure security in underground design.

A natural progression of this work is to link two-dimensional and three-dimensional numerical models with the reliability codes. Moreover, this study suggests using reliability analysis in different cross-section geometries and supports (steel lining, precast concrete lining, bolts).

ACKNOWLEDGEMENTS

The authors acknowledge UFRGS and FURG for their support and CNPq and CAPES for their research grants.

CITATIONS

[1] S. Kohno, “Reliability-based design of tunnel support systems,” Ph.D. dissertation, Univ. Illinois, Urbana, United States of America, 1989.

[2] E. Laso, “Application of Level II reliability methods to the design of tunnels liners,” Ph.D. dissertation, Univ. Politéc. Madrid, Madrid, Spain, 1991. [in Spanish].

[3] S. Kohno, A. H.-S. Ang, and W. H. Tang, "Reliability evaluation of idealized tunnel system," *Struct. Saf.*, vol. 11, no. 1, pp. 81–93, 1992.

[4] E. Laso, M. S. G. Lera, and E. Alarcón, "A level II reliability approach to tunnel support design," *Appl. Math. Model.*, vol. 19, no. 1, pp. 371–382, 1995.

[5] B. K. Low and W. H. Tang, "Efficient reliability evaluation using spreadsheet," *J. Eng. Mech.*, vol. 123, no. 1, pp. 749–752, 1997.

[6] E. Hoek, "Reliability of Hoek-Brown estimates of rock mass properties and their impact on design," *Int. J. Rock Mech. Min. Sci.*, vol. 35, no. 1, pp. 63–68, 1998.

[7] B. K. Low and W. H. Tang, "Reliability analysis using object-oriented constrained optimization," *Struct. Saf.*, vol. 26, no. 1, pp. 69–89, 2004.

[8] B. K. Low and W. H. Tang, "Efficient spreadsheet algorithm for first-order reliability method," *J. Eng. Mech.*, vol. 133, no. 1, pp. 1378–1387, 2007.

[9] H. Li and B. K. Low, "Reliability analysis of circular tunnel under hydrostatic stress field," *Comput. Geotech.*, vol. 37, no. 1-2, pp. 50–58, 2010.

[10] Q. Lü and B. K. Low, "Probabilistic analysis of underground rock excavations using response surface method and SORM," *Comput. Geotech.*, vol. 38, no. 8, pp. 1008–1021, 2011.

[11] L. Song, H.-Z. Li, C. L. Chan, and B. K. Low, "Reliability analysis of underground excavation in elastic-strain-softening rock mass," *Tunn. Undergr. Space Technol.*, vol. 60, no. 1, pp. 66–79, 2016.

[12] W. Bjureland, J. Spross, F. Johansson, A. Prästings, and S. Larsson, "Reliability aspects of rock tunnel design with the observational method," *Int. J. Rock Mech. Min. Sci.*, vol. 1, no. 98, pp. 102–110, 2017.

[13] A. M. Hasofer and N. C. Lind, "Exact and invariant second moment cod format," *J. Eng. Mech.*, no. 100, pp. 111–121, 1974.

[14] A. K. Verma, D. R. Karanki, and S. Ajit, *Reliability and Safety Engineering*. London: Springer Verlag London Ltd., 2016.

[15] A. S. Nowak and K. R. Collins, *Reliability of Structures.* New York: Mc Graw Hill, 2000.

[16] B. M. Ayyub and R. H. McCuen, *Probability, Statistics, and Reliability for Engineers and Scientist*, 1st ed. New York: Taylor & Francis Group, 2011.

[17] A. H.-S. Ang and W. H. Tang, *Probability Concepts in Engineering Planning and Design, vol. II: Decision, Risk, and Reliability*, 1st ed. New York: John Wiley & Sons, Inc., 1984.

[18] J. Salençon, "Contraction quasi-statique d'une cavite a symetrie spherique ou cylindrique dans un milieu elasto-plastique," *Ann. Ponts Chaussees*, vol. 4, pp. 231–236, 1969.

[19] F. Corbetta, "Nouvelles méthodes d'étude des tunnels profonds: calculs analytiques et numériques," Ph.D. dissertation, Éc. Natl. Super. Mines, Paris, France, 1990.

[20] M. Panet and A. Guenot, "Analysis of convergence behind the face of a tunnel", in *Tunnelling 82, Proc. 3rd Int. Symp.*, Brighton, 1982, pp. 197–204.

[21] D. Bernaud, "Tunnels profonds dans les milieux viscoplastiques: approaches experimentale et numerique," Ph.D. dissertation, L'Ec. Natl. Ponts et Chaussées, Paris, France, 1991.

[22] M. Panet and P. Guellec, "Contribution à l'etude du Soutènement d'un Tunnel à l'Arrière du Front de Taille," in *Proc. 3rd Int. Cong. Rock Mechanics*, Denver, 1982.

[23] E. Hoek and E. T. Brown, *Underground Excavations in Rock*, 1st ed. London: E&FN Spon, 1980.

[24] J. Brantmark, "Rock support in weak rock – a case study based on the Uri Project," Ph.D. dissertation, KTH Roy. Inst. Technol., Stockholm, Sweden, 1998.

[25] A. Hamrouni, D. Dias, and B. Sbartai, "Reliability analysis of shallow tunnels using the response surface methodology," *Undergr. Space*, vol. 1, no. 2, pp. 246–258, 2017.

Author contributions: CCCS: conceptualization, investigation, data curation, methodology, validation, writing, review, editing; MVR: conceptualization, data curation, formal analysis, project administration, supervision, review, editing; SM: conceptualization, formal analysis, project administration, supervision, review, editing.

Editors: David Oliveira, Guilherme Aris Parsekian.

IBRACON Structures and Materials Journal
Revista IBRACON de Estruturas e Materiais
ISSN 1983-4195 ismj.org

ORIGINAL ARTICLE

Effect of the water/binder ratio on the hydration process of Portland cement pastes with silica fume and metakaolin

Efeito da relação água/aglomerante no processo de hidratação de pastas de cimento Portland com sílica ativa e metacaulim

Mara Monaliza Linhares Pereira[a]
Ana Luiza Rocha de Souza[a]
Valdirene Maria Silva Capuzzo[a]
Rodrigo de Melo Lameiras[a]

[a]Universidade de Brasília – UnB, Departamento de Engenharia Civil e Ambiental, Programa de Pós-graduação em Estruturas e Construção Civil, Brasília, DF, Brasil

Received 03 January 2021
Accepted 02 May 2021

Abstract: The microstructure of cement pastes is important to understand the effect of some parameters in the hydration process. In this context, this study had as objective to evaluate the effect of different water/binder (w/b) ratios in the hydration process of cementitious pastes produced with and without incorporation of silica fume and metakaolin. The pastes were obtained with water/binder ratios of 0.3, 0.4 e 0.5, with replacement, by weight, of Portland cement for silica fume and metakaolin, in the contents of 10% and 20%, respectively. It was performed the X-ray diffraction test of the pastes in the ages of 1, 3, 7, and 28 days, to evaluate the hydration evolution of the cementitious materials. According to the results obtained, it was observed that the cementitious pastes presented similar mineralogical phases, except for the pastes containing metakaolin due to the formation of new aluminate phases. With the increase of the water/binder ratio, the pozzolanic reactions and hydration occurred in greater proportion, standing out the metakaolin with greater reactivity.

Keywords: cementitious pastes, water/binder, X-ray diffraction, silica fume, metakaolin.

Resumo: A microestrutura das pastas de cimento é importante para compreender o efeito de alguns parâmetros no processo de hidratação. Nesse contexto, este trabalho teve como objetivo avaliar o efeito de diferentes relações água/aglomerante (a/agl) no processo de hidratação de pastas cimentícias produzidas com e sem incorporação de sílica ativa e metacaulim. As pastas foram obtidas com relações água/aglomerante de 0,3, 0,4 e 0,5, com substituição em massa do cimento Portland por sílica ativa e metacaulim, nos teores de 10% e 20%, respectivamente. Foi realizado o ensaio de difração de raios-X das pastas nas idades de 1, 3, 7 e 28 dias, para avaliar a evolução da hidratação dos materiais cimentícios. De acordo com os resultados obtidos, observou-se que as pastas cimentícias apresentaram fases mineralógicas semelhantes, com exceção das pastas contendo metacaulim devido à formação de novas fases aluminato. Com o aumento da relação água/aglomerante, as reações pozolânicas e de hidratação ocorreram em maior proporção, se destacando o metacaulim com maior reatividade.

Palavras-chave: pastas cimentícias, água/aglomerante, difração de raios-X, sílica ativa, metacaulim.

How to cite: M. M. L. Pereira, A. L. R. Souza, V. M. S. Capuzzo, and R. M. Lameiras, "Effect of the water/binder ratio on the hydration process of Portland cement pastes with silica fume and metakaolin," *Rev. IBRACON Estrut. Mater.*, vol. 15, no. 1, e15105, 2022, https://doi.org/10.1590/S1983-41952022000100005

1 INTRODUCTION

Understanding the influence of each phase of cementitious pastes is important for the development of a transition zone more efficient, with greater hydration speed, and better performance of the mechanical properties and durability. The deformation

Corresponding author: Mara Monaliza Linhares Pereira. E-mail: maramonaliza19@gmail.com
Financial support: CAPES, CNPq, FAP-DF (Process: 0193.001700/2017).
Conflict of interest: Nothing to declare.

capacity of concrete is connected to intrinsic characteristics of cement hydration products, aggregates, transition zone, and pores, besides other particular variables to process, such as hydration speed and climatic conditions [1]. The Portland cement, when hydrated, has as main phases the hydrated calcium silicate (C-S-H) and the calcium hydroxide (CH), which are directly connected to the physical and mechanical properties of construction materials [1], [2]. Also, the water/cement (w/c) ratio is one of the parameters to control the micro and nanostructure of these phases [1].

Due to the environmental impact caused by the extraction of raw materials and CO_2 emission in cement production has been sought a reduction of the consumption of this constituent of concrete, together with the need to increase the durability [3], [4]. In this context, it arises as an alternative the using supplementary cementitious materials (SCMs) in partial replacement to Portland cement [4]–[8]. Among these materials, metakaolin and silica fume, are the mineral additions most commonly used in the last years in the production of cementitious materials and have a high reactivity due to their pozzolanic activity [9]–[14]. These SCMs generally provide more silica and alumina to the cementitious matrix, thus, the final composition of the C-S-H and the quantity, secondary phases, are affected [2].

Numerous researchers investigated the effects of these SCMs in the performance of cementitious materials such as cement pastes, mortars, and concretes [2]–[4], [7], [9], [11]–[15], [16]–[19]. The mineral additions cause influence on the hydration kinetics of cement Portland, and through chemical activity, forms secondary hydrated products. As a consequence of this behavior, the microstructure of the cementitious matrix suffers a change [20]. According to these researches, the SCMs improve the properties of mechanical strength and increase the durability of the structures due to their pozzolanic reactions and the high fineness that contributes to the refinement of pores, decreasing of this way the final porosity and improving the cohesion of the mixture in the fresh state [9], [18], [21].

The hydration reactions of the cement and the release of heat are directly related to several parameters: the composition of the binder, type and content of the supplementary cementitious materials used in replacement to clinker, chemical admixture added, water/cement ratio and curing temperature. Independent of these parameters, a series of simultaneous and successive reactions are responsible for the gain of consistency or loss of workability, which generates the consolidation of suspensions and consequent resistance gain [22]. Furthermore, understand the microstructure of cement pastes is important to understand the effect of various conditions on the hydration process [23].

Although the effect of the water/binder (w/b) ratio and the effect of supplementary cementitious materials (SCMs) have already been objective of several studies [9]–[11], [14], [19], most of these studies are limited to evaluate the effects on physical and mechanical properties in different cementitious matrices. Also, the studies that evaluate the joined effect of the w/b ratio and SCMs in the microstructure of Portland cement pastes are still limited. Therefore, there is a need for studies to better understand the combined effect of the water/binder factor and additions of silica fume and metakaolin in the hydration process through the development of the microstructure of cementitious pastes.

Taking into consideration the importance of the presence of water in the hydration process and the lack of more comprehensive studies to understand the effect of the synergy between pozzolanic additions and the water/binder ratio, the present article aimed to evaluate the joint effect of different w/b ratios and supplementary cementitious materials in the hydration process of cementitious pastes through the microstructural analysis of X-ray diffraction.

2 MATERIALS AND EXPERIMENTAL PROGRAM

2.1 Materials

2.1.1 Portland cement

The cement used was of type V (CP V), characterized by conferring a high resistance in the first moments of concrete curing, according to NBR 16697 [24]. The choice of this binder happened of using cement with lower content of pozzolanic additions in its composition when in comparison to other types of cement available on the market, seeking this way to avoid combined effects and evaluate the influence of metakaolin and silica fume in cementitious pastes. Table 1 presents the data obtained, as well as the methods used, in the physical and chemical characterization of this material. The chemical characterization was obtained through the X-ray fluorescence spectrometry (XRF) test, performed on an EDX 720 Shimadzu device. Before performing the XRF test, it was performed the loss on ignition test with the base on the guidelines of ABNT NM 18 [25].

Table 1. Properties and characteristics of the Portland cement (CP V).

Properties and characteristics		Results	Limits[a]	Test method
Setting time	Initial (min)	120	≥ 60	ABNT NBR 16607 [26]
	Final (min)	175	≤ 600	
Water content of normal consistency paste (%)		35.50	-	ABNT NBR 16606 [27]
Fineness index on sieve #200 (%)		0.90	≤ 6.0	ABNT NBR 11579 [28]
Specific mass (g/cm^3)		3.00	-	ABNT NBR 16605 [29]
Compressive strength (MPa)	1 day	25.4	≥ 14.0	ABNT NBR 7215 [30]
	3 days	36.1	≥ 24.0	
	7 days	42.7	≥ 34.0	
Chemical composition, in oxides (%)	CaO	63.61	-	-
	SiO_2	19.91	-	-
	Al_2O_3	4.20	-	-
	Fe_2O_3	2.20	-	-
	MgO	1.78	≤ 6.5	-
	Na_2O	0.38	-	-
	K_2O	0.36	-	-
	TiO_2	0.23	-	-
	P_2O_5	0.17	-	-
	MnO	0.07	-	-
	LOI [b]	3.36	≤ 6.5	ABNT NM 18 [25]

[a] Limits established by the ABNT NBR 16697 [24]. [b] Loss on ignition (LOI)

According to Table 1, the chemical composition indicates a predominance of calcium oxide and silicon dioxide, as expected for the type of cement used and also observed in the studies of [3], [11], [31].

The X-ray diffraction test of Portland cement was also performed to identify the compounds of crystalline phases. For this test, it was used the RIGAKU X-ray diffractometer model ULTIMA IV, operating with a tungsten filament as a cathode and a copper X-ray tube (CuKa = 1.54056A), under 35 kV power and 15 mA current, in the range of 2θ equal to 2° until 60°. The scanning velocity was 5º/min and steps of 0.05º. As presented in Figure 1, observing the diffractogram were identified the compounds alite, gypsum, belite, ferrite, and calcite, which are compounds formed from the materials used in the production of cement.

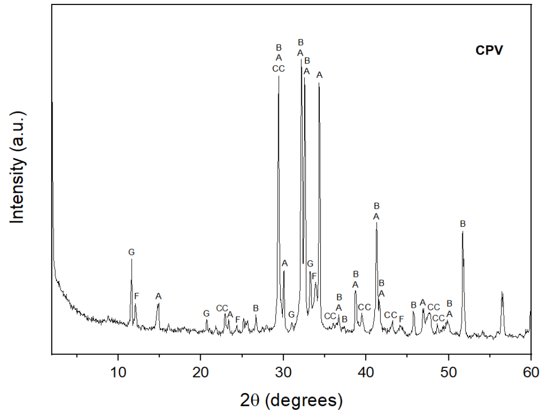

Figure 1. X-ray diffractogram of the Portland cement (CP V). G-gypsum, F-ferrite, A-alite, CC-calcite, B-belite.

2.1.2 Metakaolin

It was used a metakaolin of high reactivity as partial substitution, by weight, of CP V, in the cementitious pastes. This material is characterized by containing a high content in alumina and being quite fine, as can be verified in Table 2, where are the results of the analysis of some physical properties and the chemical characterization obtained through the X-ray fluorescence spectrometry (XRF) test.

Table 2. Physical and chemical properties of the metakaolin.

Properties and characteristics		Results	Test method
Specific mass (g/cm^3)		2.60	ABNT NBR 16605 [29]
Diameter below which it finds 10% of the particles – D10 (μm)		1.77	Laser granulometry
Mean diameter (μm)		18.27	
Diameter below which it finds 90% of the particles – D90 (μm)		39.36	
Chemical composition, in oxides (%)	SiO_2	50.54	-
	CaO	0.00	-
	Al_2O_3	42.28	-
	Fe_2O_3	3.23	-
	TiO_2	1.63	-
	K_2O	1.07	-
	MgO	1.02	-
	SO_3	0.09	-
	ZrO_2	0.03	-
	Cr_2O_5	0.03	-
	SrO	0.01	-

From Table 2, it is possible to observe some main chemical compounds for its mineral formation. Metakaolin is obtained from the calcination of kaolinitic clays, so it is basically composed of silica (SiO_2) and alumina (Al_2O_3) in the amorphous phase, as confirmed with the obtained chemical composition.

The granulometric curve of the metakaolin was obtained through the laser granulometry test, and it is presented in Figure 2. This test was performed using a particle size analyzer model CILAS 1180 in liquid mode with an analysis range from 0.04 to 2500.00 μm.

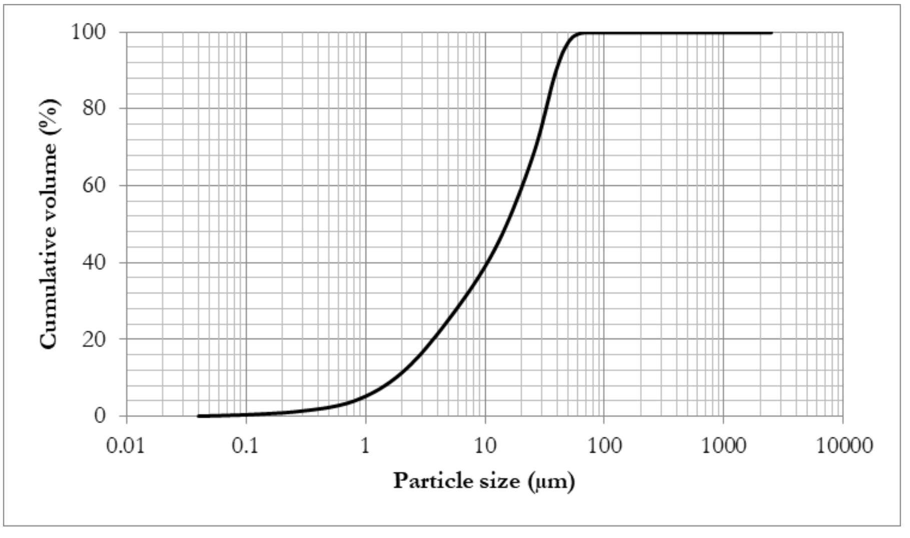

Figure 2. Granulometric curve of the metakaolin.

Also, it was performed the X-ray diffraction test for metakaolin through the same X-ray diffractometer model used in the characterization of CP V cement, operating only with a different 2θ interval, which was equal to 2° until 80° for the metakaolin. It is important to reinforce that despite the change of the interval for this material, it was followed the same standardization for other parameters, mainly in the placing of the material in the sample holder, to avoid any interference in the peaks due to the targeting of the crystalline plane during the execution of the test. In the diffractogram presented in Figure 3, it can be identified peaks of quartz, kaolinite, and muscovite, beyond the presence of an amorphous halo that characterizes the reactivity of this material.

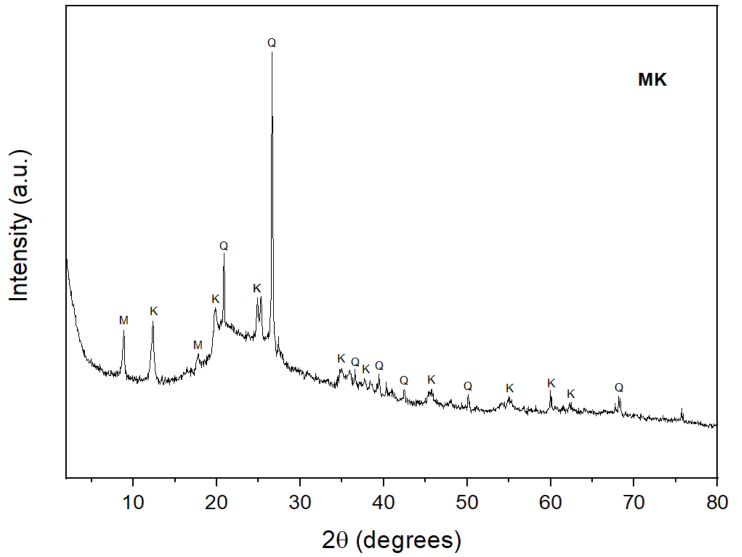

Figure 3. X-ray diffractogram of the metakaolin. M-muscovite, K-kaolinite, Q-quartz.

2.1.3 Silica fume

It was also used, in binary mixtures, a densified silica fume as partial substitution, by weight, of CP V, in cementitious pastes. This material is a pozzolanic mineral addition that presents fine particles and has a high specific area, as can be verified in Table 3, which presents the results of physical and chemical characterization of the silica fume. In the same way that for the previous materials, the chemical characterization was obtained through the X-ray fluorescence spectrometry (XRF) test, and before performing the test, it was performed the loss on ignition test with a base on the guidelines of ABNT NM 18 [25].

Table 3. Physical and chemical properties of the silica fume.

Properties and characteristics		Results	Limits[(a)]	Test method
Apparent density (kg/m^3)		595.07	-	ABNT NM 45 [32]
Fineness in the sieve 45 µm (%)		9.10	10.0	ABNT NBR 13956-4 [33]
Specific mass (g/cm^3)		2.16	-	ABNT NBR 16605 [29]
Specific surface area values (B.E.T.) (m^2/g)		19.72	15 ≤ B.E.T. ≤ 30	ASTM C1069 [34]
Diameter below which it finds 10% of the particles – D10 (µm)		5.19	-	Laser granulometry
Mean diameter (µm)		31.55	-	
Diameter below which it finds 90% of the particles – D90 (µm)		58.75	-	
Chemical composition, in oxides (%)	SiO_2	94.33	≥ 85	-
	K_2O	1.04	-	-
	CaO	0.78	-	-
	MgO	0.49	-	-
	Na_2O	0.39	-	-
	Fe_2O_3	0.19	-	-
	P_2O_5	0.14	-	-
	MnO	0.06	-	-
	TiO_2	0.02	-	-
	Al_2O_3	< 0.01	-	-
	LOI [(b)]	2.28	≤ 6.0	ABNT NM 18 [25]

(a) Limits established by the ABNT NBR 13956-1 [35]. (b) Loss on ignition (LOI)

From Table 3, it is possible to observe that the main chemical compound of the silica fume was silicon dioxide, which was already expected for this type of material, due to its obtaining to be from the production of metallic silicon or iron-silicon alloys.

The granulometric curve of the silica fume was obtained through the laser granulometry test, and it is presented in Figure 4. This test was performed using a particle size analyzer model CILAS 1180, which provides a measuring range of particle size between 0.04 to 2500.00 µm. For this test, the silica fume was placed under the effect of ultrasonic pulses for 60 seconds to deagglomerate the particles, which were placed in the equipment. However, even after 60 seconds on ultrasound, as it was a densified silica, it was still observed a large number of particles with large diameters, as observed in the results obtained from the laser granulometry test, presented in Table 3.

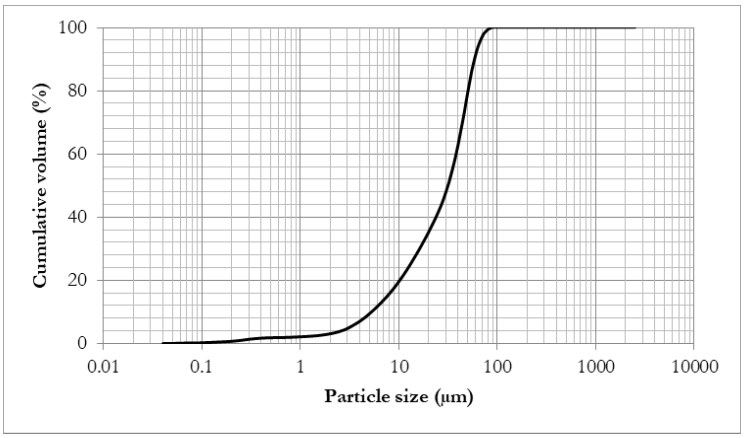

Figure 4. Granulometric curve of the silica fume.

For the mineralogical characterization of the silica fume, it was performed the X-ray diffraction test, through the same equipment and parameters used in the test for characterization of the cement CP V, in which the silica fume presented a high degree of amorphism. In the diffractogram presented in Figure 5, it can be identified as characteristic peaks, the potassium chloride and silicon carbide.

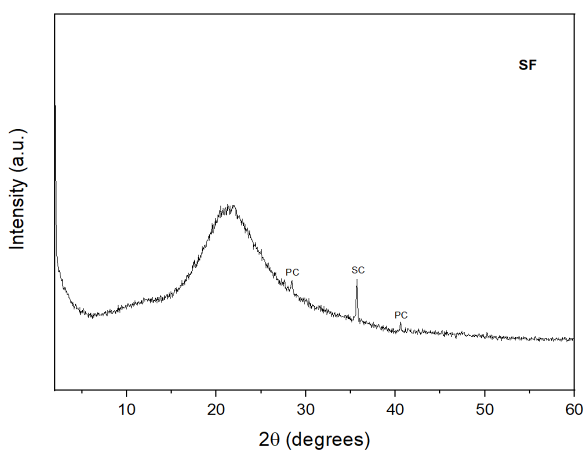

Figure 5. X-ray diffractogram of the silica fume. PC-potassium chloride, SC-silicon carbide.

2.1.4 Potable water

For the production of cement pastes, it was used the water provided by the water supply company of the Brasilia region, free of visible impurities and following of the ABNT NBR 15900-1 [36].

2.2 Composition and preparation of cementitious pastes

To evaluate the combined effect of the water/binder ratio and supplementary cementitious materials in the hydration process of cementitious matrices, it was studied a total of 9 Portland cement pastes varying the supplementary cementitious material, substituted concerning the cement mass, and the w/b ratio. A nomenclature was defined for each sample to be studied to distinguish with more facility, starting by the cement paste without SCMs (reference paste), followed by two more percentages of substitution of the metakaolin or silica fume by the cement mass (20% and 10%, respectively), and three distinct water/binder ratios (0.30, 0.40 and 0.50). It was opted to work with mass substitutions thinking about getting a reduction of the consumption of Portland cement in the cementitious pastes and as a measure of reducing retraction problems for Portland cement pastes with low water/binder ratio. Also, the content of the SCMs was chosen thought of other studies that observed optimum contents in a range of 8% to 20% for metakaolin [3], and 5 to 15% for silica fume [2]. Table 4 presents the adopted nomenclatures, being that REF meaning reference, MK is metakaolin, SF is silica fume, and the last number is the water/binder ratio.

Table 4. Nomenclature and composition of the traces.

w/b ratio	Abbreviation	Cementitious pastes
0.30	REF03	100% CP V
	MK03	80% CP V + 20% metakaolin
	SF03	90% CP V + 10% silica fume
0.40	REF04	100% CP V
	MK04	80% CP V + 20% metakaolin
	SF04	90% CP V + 10% silica fume
0.50	REF05	100% CP V
	MK05	80% CP V + 20% metakaolin
	SF05	90% PC V + 10% silica fume

The pastes were produced following the recommendations of ABNT NBR 16606 [27], using a mechanical mixer and the mixing sequence was performed in the following order: firstly, it was placed in the vat all the quantity of water, it was added the cement, followed of mineral addition when necessary, and it was performed the mixture during 30 seconds, at low speed. Then, it was turned off the mixer for 60 seconds to perform the scraping of the inner walls of the vat, causing all the paste adhered to them to stay at the bottom of the vat. Finally, the mixer was turned on again at high speed for 60 seconds.

After all the mixing and molding process, the cementitious paste samples were kept in a humid chamber for 24 hours, in which at that moment it became all necessary care with the samples so that no changes would occur in the w/b ratio. After the 24 hours period, the samples were placed in submerged curing of water saturated with lime, until the age of performing of the X-ray diffraction test, 1, 3, 7, and 28 days.

2.3 X-ray diffraction (XRD)

The X-ray diffraction test (XRD) was performed on the pastes at 1, 3, 7, and 28 days of hydration, to identify the crystalline phases of the studied cementitious pastes. Upon completing the ages need for the performing of the test, the samples were broken and it was stopped the hydration of these pastes with the fragments of the internal part of the specimens, using the stoppage procedure described by Scrivener et al. [37]. The procedure consisted of the immersion of the fragments in isopropanol for 6 hours and drying in an oven at ± 40 °C for 24 hours. Then, the samples were stored in a desiccator containing silica gel and soda-lime until the day of the performance of the test.

For the performance of the X-ray diffraction test, the granulometry of the samples was reduced, until all the material passed through the sieve 200 (0.075 μm). Then, the sample in powder was spread over the excavated glass slide, making movements not oriented, avoiding the overlapping of the crystals and the favoring of some compounds in detriment to others, during the X-ray scanning. For all samples, it was followed the same procedure for placing the material in the sample holder, to avoid any interference in the crystalline peaks.

It was performed the tests on the same X-ray diffractometer model used in the characterization of the SCMs, operating with a tungsten filament as a cathode and a copper X-ray tube (CuKa = 1.54056A), under 35 kV power and 15 mA current, in the range of 2θ equal to 2° until 60°. The scanning velocity was 5°/min and steps of 0.05º. The identification of the crystalline phases was performed with the aid of the JADE 3.0 software.

3 RESULTS AND DISCUSSIONS

3.1 Evaluation of the effect of water/binder ration on pastes by age in the hydration process

The diffractograms of the cement pastes without supplementary cementitious materials (SCMs), reference pastes, are presented in Figure 6 after 1 day (A), 3 days (B), 7 days (C), and 28 days (D) of hydration for the water/binder ratios of 0.3, 0.4 and 0.5.

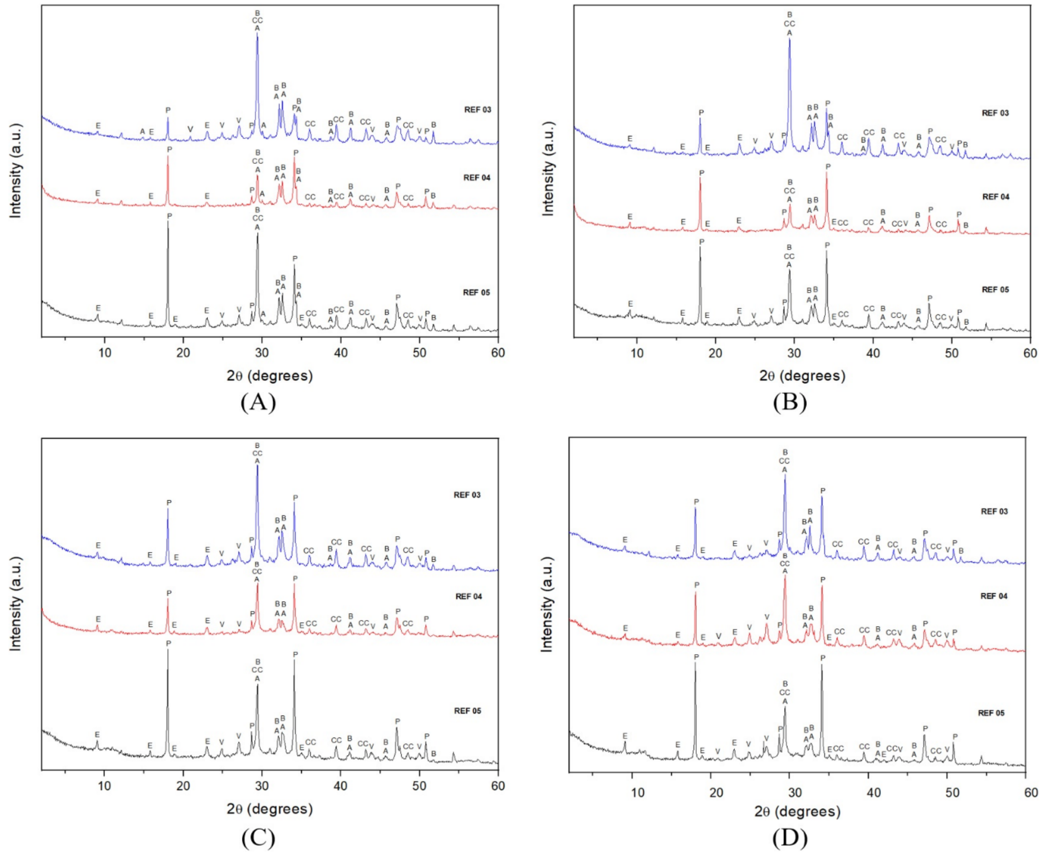

Figure 6. Diffractograms of the cement pastes without supplementary cementitious materials (SCMs), with 1 day (A), 3 days (B), 7 days (C), and 28 days (D) of hydration. E- ettringite, P-portlandite, V-vaterite, A-alite, CC-calcite, B-belite.

During the hydration process, it was observed the hydration products of the aluminate and silicate phases which are: ettringite (E) and calcium hydroxide or portlandite (P), respectively, beyond some compounds present in the clinker that are the phases alite (A) and belite (B), and the products of calcium carbonate, calcite (CC) and vaterite (V).

With the advancement of hydration, it was possible to observe in all the reference pastes studied the increment of the portlandite peaks that are generated by the reactions of the silicate phases (alite and belite) with water, a behavior that is proven when observing the decrease of the peaks of alite and belite, that even decreasing still continue present until at 28 days. Another product that also presented a slight increment in its peaks and until the emergence of others was ettringite, which is the first product of hydration of the aluminate phases present in the Portland cement clinker. The presence of the calcium carbonate products in the pastes can be attributed to the chemical composition of Portland cement, which according to NBR 16697 [24] is allowed to have up to 10% of carbonate material. The presence of the carbonate material was confirmed through the mineralogical characterization of Portland cement, presented in Figure 1.

During the hydration of the cement, another main phase formed from the reactions of alite and belite is the hydrated calcium silicate (C-S-H) which does not have crystalline peaks, presenting this way an amorphous structure, which when present in the evolution of the cement hydration has its identification through the formation of amorphous halo in the X-ray diffractogram. The presence of C-S-H can also be identified using the X-ray diffraction technique together with the Rietveld method, for the performing of a quantitative analysis of the hydration products present in the studied material. Since quantification is not the objective of the study, in the qualitative analysis performed for the studied cementitious pastes, from the diffractograms in Figure 6, it was possible to identify the presence of C-S-H through the amorphous halo at 28 days of hydration, being more intense for the water/binder ratio of 0.5.

It was also possible to observe, through the diffractograms, the importance of water in the hydration reactions, because at all ages with the increase of the water/binder ratio, it was noted an increment in the intensity of the peaks of portlandite and a reduction in the intensity of the alite and belite phases, being that in the cementitious pastes with a water/binder ratio of 0.5, it was achieved the highest intensities for the products of portlandite. This situation can be confirmed through Neville and Brooks [38], who observed an interesting aspect when citing that there is a minimum water/cement ratio necessary for complete hydration, approximately 0.36 in mass, this is, for values below 0.36, there is not enough space for the accommodation of all hydration products. This is due to the hydration can only occur when the capillary pores contain enough water to ensure a relative humidity internal high and not just the amount of water needed for the chemical reactions. Thus, through the qualitative analysis, it was confirmed that for very low water/binder values, there are less intense peaks of portlandite due to not having enough water for occurring total hydration, while for high values of w/b there is a high intensity of portlandite peaks.

Figure 7 are presented the diffractograms of cement pastes containing 10% of mass substitution of silica fume after 1 day (A), 3 days (B), 7 days (C), and 28 days (D) of hydration for the three different water/binder ratios.

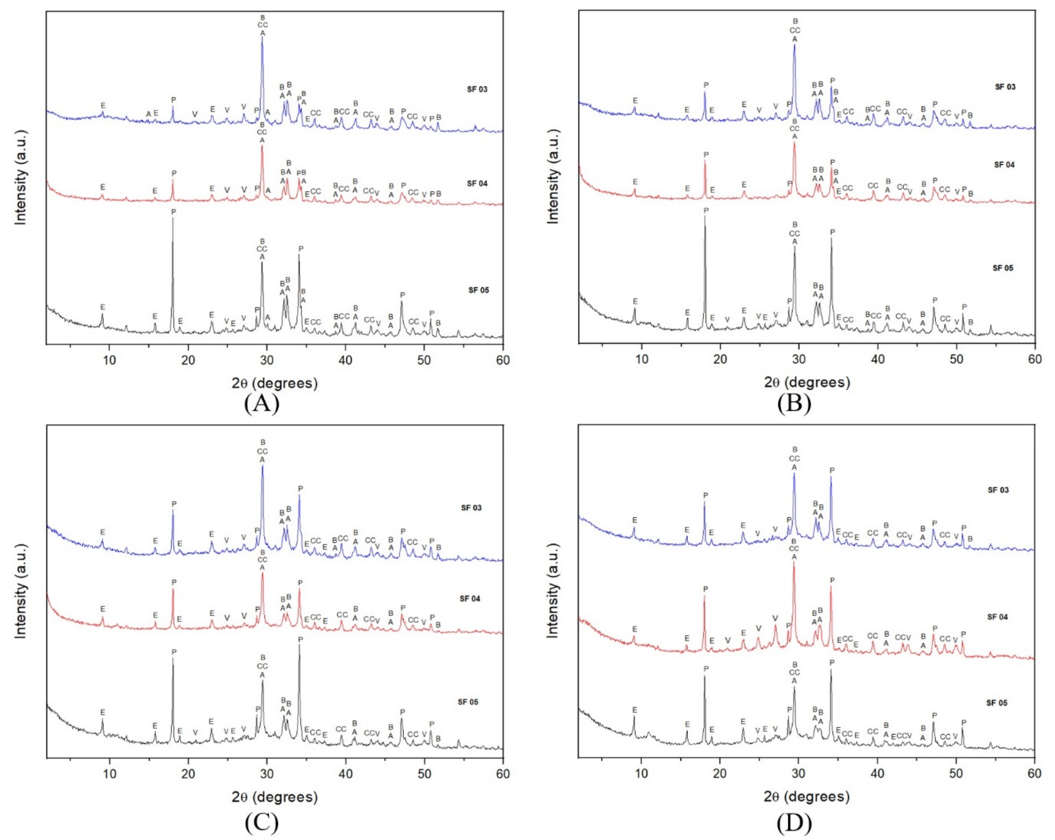

Figure 7. Diffractograms of the cementitious pastes with the replacement of Portland cement by 10% of silica fume, with 1 day (A), 3 days (B), 7 days (C), and 28 days (D) of hydration. E-ettringite, P-portlandite, V-vaterite, A-alite, CC-calcite, B-belite.

As observed through the qualitative analysis of the diffractograms in Figure 7, during the hydration process over the ages of pastes containing 10% of silica fume also presented the aluminates and silicates phases, represented by ettringite (E) and portlandite (P), the alite (A) and belite (B) phases, and the calcium carbonate products that are calcite (CC) and vaterite (V). With the advancement of the hydration, during the studied ages, it was observed the increase of the portlandite peaks, which appear from the reactions of the alite and belite phases, these reactions are proven through the reduction of the anhydrous cement peaks, which remain present until at 28 days. The ettringite peaks also presented slight increments in their intensities, due to the synergy between the materials. Also, the presence of calcite and vaterite, as previously mentioned, it is due to the type of cement CPV used, which presents until 10% of the limestone filler in its composition.

For cementitious pastes containing silica fume was also confirmed the importance of the water in the hydration process, because with the increase of the water/binder ratio was observed a behavioral trend similar to reference cementitious pastes. For a lower w/b ratio, there is less intensity of the portlandite peaks, observing yet that in the initial ages this difference is greater, but it is due to the insufficient time for hydration reactions to happen completely.

Even working with 10% of silica fume, which is a reactive pozzolanic material, having a higher w/b ratio, it was noted in the diffractograms a greater intensity of portlandite due to the greater amount of water in the mixture. However, it was noted consumption of portlandite and formation of C-S-H, for the age of 28 days, due to the effect of the pozzolanic reaction generated by silica fume, viewed through the identification of the presence of amorphous halo. Besides, as for a w/b ratio of 0.5 has a greater amount of portlandite available in the cementitious matrix to react with the silica fume, is observed an amorphous halo from the 3 days of hydration, presenting at 28 days an amorphous halo more intense.

Through the qualitative analysis of the diffractograms of cementitious pastes containing 10% of silica fume, it was observed that the water/binder ratios of 0.3 and 0.4 did not present any difference of behavior during the hydration process. While that to the w/b ratio of 0.5 there is a greater amorphous halo, due to the consumption of portlandite generated by the pozzolanic addition, besides a greater intensity in the ettringite peaks, which is a hydration product that due to its microstructural morphology it is more susceptible to rupture.

The diffractograms of the cement pastes containing 20% of mass substitution of Portland cement by metakaolin are presented in Figure 8 after 1 day (A), 3 days (B), 7 days (C), and 28 days (D) of hydration for the three different water/binder ratios.

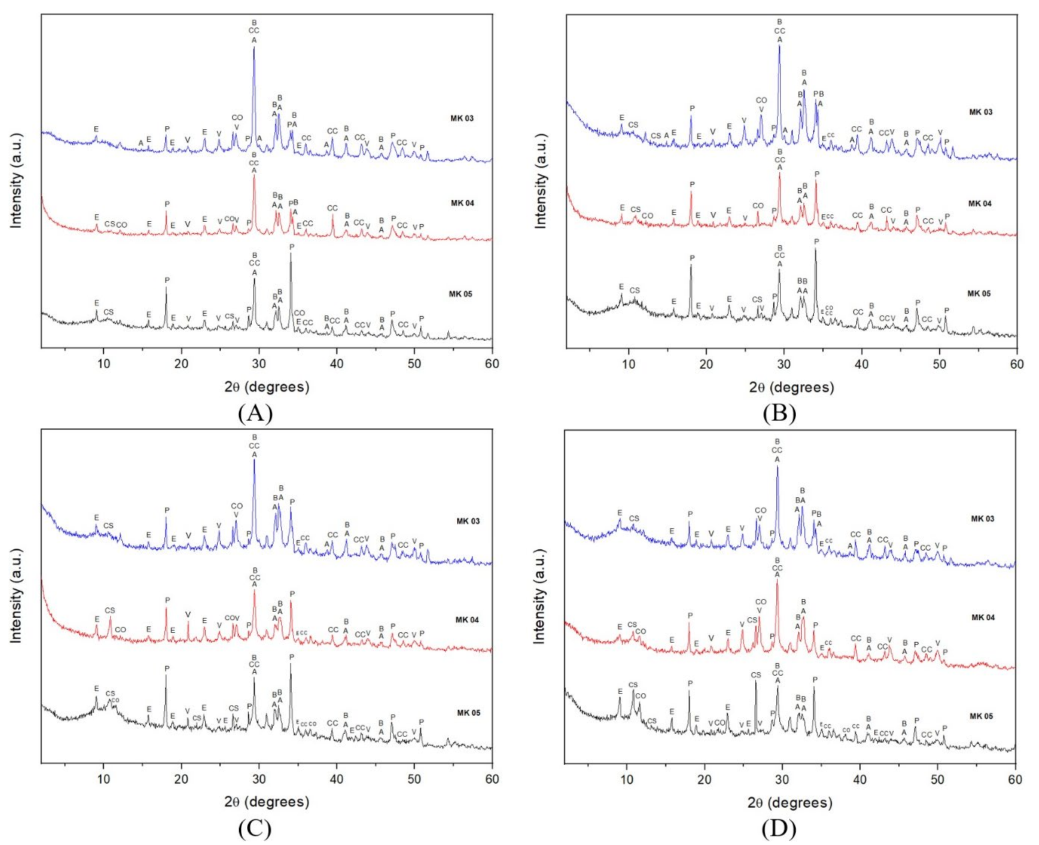

Figure 8. Diffractograms of the cementitious pastes with the replacement of Portland cement by 20% of metakaolin, with 1 day (A), 3 days (B), 7 days (C), and 28 days (D) of hydration. E- Ettringite, P-portlandite, V-vaterite, A-alite, CC-calcite, B-belite, CS-hydrated calcium aluminum silicate, CO-hydrated calcium aluminum oxide.

Through the qualitative analysis of the diffractograms in Figure 8, it can be seen that during the hydration process, over the ages, the pastes containing 20% of metakaolin presented the aluminate and silicate phases which are: ettringite (E) and portlandite (P), the alite (A) and belite (B) phases, beyond of the calcite (CC) and vaterite (V).

It was identified yet two new hydration products named in this study by hydrated calcium aluminum silicate (CS) and hydrated calcium aluminum oxide (CO). These products were formed from the pozzolanic reaction of metakaolin, which happens through the interaction between metakaolinite and calcium hydroxide. The formation of the CS and CO phases in the pastes containing metakaolin is also responsible for the formation of the hydrated calcium carboaluminates, known as hemicarboaluminate (hc) and monocarboaluminate (mc), when in the presence of limestone filler. Also, these carboaluminates (hc and mc) were identified in the study by Antoni [6] when utilizing cementitious pastes substituting Portland cement with 30% of metakaolin and 15% of limestone filler.

With the advance of the hydration, during the studied ages, it was observed that until at 7 days it was possible to view an increment in the intensity of the portlandite peaks, being that at 28 days these peaks have already suffered a decrease of the intensity, in consequence of the pozzolanic reaction, which formed many more CS and CO products at 28 days than in the first 7 days of hydration. The increase of the portlandite crystals in the cementitious matrix is associated with the hydration reactions of the alite and belite phases, confirmed through the decrease of the anhydrous cement peaks present in the diffractograms analyzed in Figure 8. Besides, the ettringite peaks presented considerable increments in their intensities for all ages, while that the calcite peaks decreased at 28 days of hydration, due to the synergy between the materials, to probably form the CS and CO products.

Regarding the amount of water present in the hydration process, it was observed that cementitious pastes with a water/binder ratio of 0.3 presented a lower intensity in the portlandite peaks and presence of amorphous halo since the initial ages, while at 28 days of hydration, the portlandite peaks suffered a reduction and the amorphous halo an increase, indicating a high pozzolanicity and formation of C-S-H for the metakaolin used in the study. Already the cementitious pastes with a w/b ratio of 0.4 did not present a very different behavior when compared to pastes with a w/b ratio of 0.3, only a lesser presence of amorphous halo for the early ages. When analyzing the cementitious pastes with a w/b ratio of 0.5, it can be observed that in the early ages already existed the predominance of portlandite peaks, and with just 3 days it was already possible to identify the consumption of these crystals, beyond the increase of the amorphous halo and ettringite peaks, indicating the action of the pozzolanic reaction. Besides, the cementitious pastes with a greater amount of water presented, throughout the hydration process, peaks with higher intensities for CS and CO products, mainly for the age of 28 days, confirming that the increase of the w/b ratio favors the growth not only from portlandite crystals but also the formation of the CS and CO peaks, for pastes containing metakaolin.

The results found are consistent with the results of some researchers who presented a similar behavior in the hydration process for the mineralogical phases identified in this study, mainly for the portlandite peaks (P), which in the cementitious pastes containing metakaolin and silica fume, decreased at 28 days due to the progress of hydration of the alite and belite phases and of the pozzolanic reactions [9]–[11], [14], [19].

It was still observed the importance of water in the hydration reactions, because when increasing the water/binder ratio in all cementitious pastes, it was noted a growth in the intensity of the portlandite peaks, a reduction in the intensity of the alite and belite phases, and the presence of more intense amorphous halo, mainly for the water/binder ratio of 0.5 in the age of 28 days. The w/b ratio of 0.5 presented better hydration due to having a larger amount of water, generating greater efficiency in the hydration process, and with this, more reinforced hydration products. However, the disadvantage of this higher w/b ratio was in the increase generated in the ettringite peaks for all pastes.

3.2 Evaluation of the influence of supplementary cementitious materials (SCMs)

Figure 9 is presented the diffractograms of the cementitious pastes with 28 days of hydration, in which was used three different water/binder ratios and two supplementary cementitious materials (SCMs) with 10 and 20% of mass substitution on Portland cement, that were the silica fume and metakaolin, respectively. It is important to note that to make the comparative analysis, the cementitious pastes presented in Figure 9, were prepared with different contents of Portland cement due to the percentage of substitution performed being different for the silica fume and metakaolin. Also, it was opted to work with mass substitutions due to the use of SCMs in the study, in which by adding SCMs through the replacement of cement, it can be avoided practical problems with water demand, hydration heat, retraction, and others in the cementitious matrix, mainly for Portland cement pastes with low water/binder ratio.

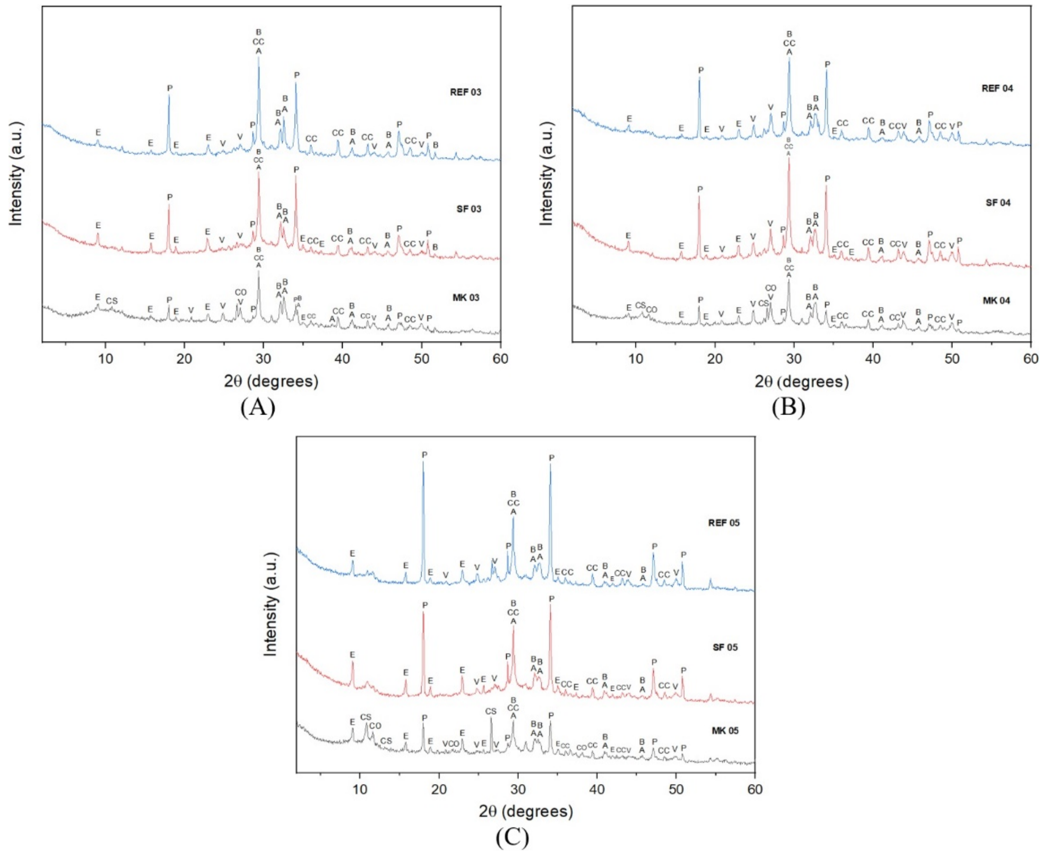

Figure 9. Diffractograms of the cement pastes without supplementary cementitious materials (REF), with the replacement of Portland cement by 10% of silica fume (SF) and with the replacement of Portland cement by 20% of metakaolin (MK), with 28 days of hydration for water/binder ratio of 0.3 (A), 0.4 (B), and 0.5 (C). E- Ettringite, P-portlandite, V-vaterite, A-alite, CC-calcite, B-belite, CS-hydrated calcium aluminum silicate, CO-hydrated calcium aluminum oxide.

Regarding the reference cementitious pastes (REF), through the qualitative analysis for the pastes containing silica fume (SF 03, SF 04, and SF 05), it is possible to observe that the replacement of Portland cement by 10% of this mineral addition generated a decrease in the intensity of the peaks of the mineralogical phases identified in the diffractograms, highlighting mainly the peaks referring to portlandite (P). This behavior was due to the replacement of cement and pozzolanic reactions, in which the SiO_2 particles, present in the silica fume, react chemically with the calcium hydroxide, formed by the cement hydration, to form secondary hydrated calcium silicate (C-S-H), behavior also observed in the studies of [10], [39]–[41]. This increment of C-S-H can be viewed through the amorphous halos formed for the cementitious pastes containing silica fume, which have greater intensities when compared with the amorphous halos present in the reference pastes.

It can still be observed that the intensities of the peaks referring to the alite (A) and belite (B) phases decreased, while that for the ettringite peaks was noticed a growth in all pastes containing silica fume concerning reference pastes, indicating the acceleration of the hydration and cement substitution. All these results are connected to the effects obtained by the utilization of the silica fume together with the Portland cement, which due to its properties of highly reactive materials occurs a pozzolanic reaction that generates an increase in the degree of cement hydration. The silica fume particles can act as nucleation points that also cause an acceleration in cement hydration [11], [42], [43]. These results presented for the pastes containing silica fume were also observed in other studies, which evidenced the same qualitatively phenomenon, in which the pozzolanic reaction of this material could clearly reduce the calcium hydroxide content [10], [11], [14], [19], [23], [44].

In the diffractograms of the pastes containing metakaolin (MK 03, MK 04, and MK 05), through the qualitative analysis, it was observed when comparing with reference cementitious pastes (REF) that, when replacing 20% of Portland cement by metakaolin, it was also occurred a decrease in the intensity of the calcium hydroxide (P) crystals, being of form more effective than the observed for the replacement of 10% of Portland cement by silica fume. This behavior is due to not only the different percentages for the cement contents but also due to the pozzolanic reactions because the metakaolin is a highly reactive and finely ground pozzolan, rich in SiO_2 and Al_2O_3 in its chemical composition. Thus, beyond the silica particles, the alumina contained in the metakaolin when getting in contact with portlandite reacts and forms secondary C-S-H together with aluminate phases, constituting the pozzolanic reactions, and thereby generating the decrease of the mineralogical phases of portlandite, observed in these pastes. This behavior was also observed in other studies through the phases identified, in which the use of metakaolin provided a higher consumption of portlandite, which resulted in less intensity of peak portlandite [4], [5], [8], [11], [13], [14], [19], [44], [45]. The presence of the amorphous structures of C-S-H can be confirmed through the amorphous halos, observed in the analyzes performed for Figure 9, in which it was clearly identified this behavior due to the pozzolanic reactions present. When compared with the other pastes in Figure 9, it was observed that the amorphous halos of pastes containing metakaolin are the most intense for all water/binder ratios, thus demonstrating a greater presence of amorphous structures.

As expected, it was also presented for the peaks referring to the silicate phases (alite and belite) a decrease of the intensity in relation to both reference pastes and pastes containing silica. Already for the ettringite products, it can be observed that for pastes containing metakaolin occurred an increase concerning reference pastes, a behavior also viewed for pastes containing silica fume, but to a lower proportion. Through these results, it is noted that the samples with metakaolin presented a higher degree of hydration in the cementitious pastes. This behavior for metakaolin can be justified through its pozzolanic properties, in which the effects of nucleation can act with more intensity in the case of the hydration products of the aluminate phase, thereby increasing the evolution of the hydration for pastes containing this material [4], [8], [11], [13], [43].

In general, the replacement of Portland cement by different supplementary cementitious materials (SCMs) presented results in the X-ray diffractograms that evidenced the performance of the pozzolanic reactions generated by these materials during the hydration process, causing the consumption or formation of certain mineralogical phases identified in the study. Also, when comparing the behavior of the influence of silica fume and metakaolin, it can be concluded that the replacement of Portland cement by silica fume caused a slight impact on its reactions, but the impact caused by metakaolin is more intense in the cementitious pastes, indicating a greater pozzolanic performance and increase of the hydration effects due to the high presence of alumina and fineness in its properties [8], [14], [46]. In other words, the metakaolin showed a high pozzolanicity due to be a pozzolanic material and highly reactive, presenting physical characteristics, as extremely fine particles and the high specific area, besides the chemical characteristics, which generate a pozzolanic reaction from the interaction between silica and alumina, present in the metakaolin. It is also important to highlight that these results are associated with the difference of the cement contents between the cementitious pastes containing SCMs and to the results of chemical and physical characterization presented by the silica fume, which is a densified silica fume, with a larger diameter of the particles when compared with the metakaolin, according to the results of laser granulometry.

4 CONCLUSIONS

Cementitious pastes with different water/binder ratios and with the replacement of Portland cement by 10% of silica fume and 20% of metakaolin were produced to evaluate the hydration process, through the microstructural analysis, using the X-ray diffraction test, in the ages of 1, 3, 7, and 28 days of hydration. Based on the results obtained from the experimental program conducted, it can be concluded that:

- All the cementitious pastes presented similar mineralogical phases, except for pastes containing metakaolin, which during the hydration process presented the formation of aluminate phases, due to the presence of alumina in this material, denominated in this study as hydrated calcium aluminum silicate (CS) and hydrated calcium aluminum oxide (CO). These new products were formed from the metakaolin pozzolanic reaction, mainly at 28 days of hydration, where was it identified an increase in the intensity of the CS and CO peaks.
- From the variation of the water/binder ratio, it is possible to observe the importance of water in the hydration reactions, in which through the qualitative analysis, it was noted that by increasing the water/ binder ratio, the pastes obtained an increment in the portlandite and ettringite peaks, and consequently a higher consumption in the alite and belite phases, mainly for the water/binder ratio of 0.5, which presented in all pastes these behaviors in a more intense way. Already for very low values of water/binder, there are less intense peaks of portlandite due to not having the presence of water enough in the cementitious matrix to occur total hydration.
- The metakaolin influenced the cementitious pastes of form more expressive than silica fume, as it is a pozzolanic material rich in silica and alumina, which when entering in contact with portlandite reacted and formed secondary C-S-H together with new aluminate phases, constituting the pozzolanic reactions. The presence of metakaolin indicated a greater pozzolanic performance and increase of the hydration effects, a

behavior proven through the intensities of the mineralogical phases and of the formation of amorphous halos, which for cementitious pastes containing metakaolin presented of form more intense.

In general, when increasing the water/binder ratio, the pozzolanic and hydration reactions continued to occur, being that in a greater proportion, especially the metakaolin with greater reactivity.

ACKNOWLEDGEMENTS

The authors wish to thank the Universidade de Brasília (UnB/Brazil) and the financial support provided by the Conselho Nacional de Desenvolvimento Científico e Tecnológico (CNPq/Brazil), the Coordenação de Aperfeiçoamento de Pessoal de Nível Superior (CAPES/Brazil), and the Fundação de Apoio à Pesquisa do Distrito Federal (FAPDF/Brazil–Process: 0193.001700/2017).

REFERENCES

[1] F. Pelisser, P. J. P. Gleize, and M. D. Michel, "Propriedades nanomecânicas de pastas de cimento," *Rev. IBRACON Estrut. Mater.*, vol. 4, no. 4, pp. 561–574, 2011, http://dx.doi.org/10.1590/S1983-41952011000400003.

[2] J. E. Rossen, B. Lothenbach, and K. L. Scrivener, "Composition of C-S-H in pastes with increasing levels of silica fume addition," *Cement Concr. Res.*, vol. 75, pp. 14–22, 2015, http://dx.doi.org/10.1016/j.cemconres.2015.04.016.

[3] C. P. Figueiredo, F. B. Santos, O. Cascudo, H. Carasek, P. Cachim, and A. Velosa, "The role of metakaolin in the protection of concrete against the deleterious action of chlorides O papel do metacaulim na proteção dos concretos contra a ação deletéria de cloretos," *Rev. IBRACON Estrut. Mater.*, vol. 7, no. 4, pp. 685–708, 2014, http://dx.doi.org/10.1590/S1983-41952014000400008.

[4] L. Krajči, I. Janotka, F. Puertas, M. Palacios, and M. Kuliffayová, "LONG: term properties of cement composites with various metakaolinite content," *Ceram. Silik.*, vol. 57, no. 1, pp. 74–81, 2013.

[5] G. Puerta-Falla, M. Balonis, G. Le Saout, N. Neithalath, and G. Sant, “The influence of Metakaolin on limestone reactivity in cementitious materials,” in *Calcined Clays for Sustainable Concrete*, K. Scrivener and A. Favier, Eds., Dordrecht: Springer, 2015, pp. 11–19. http://dx.doi.org/10.1007/978-94-017-9939-3_2.

[6] M. Antoni, J. Rossen, F. Martirena, and K. Scrivener, "Cement substitution by a combination of metakaolin and limestone," *Cement Concr. Res.*, vol. 42, no. 12, pp. 1579–1589, 2012, http://dx.doi.org/10.1016/j.cemconres.2012.09.006.

[7] S. Tongbo, W. Bin, Z. Lijun, and C. Zhifeng, “Meta-Kaolin for high performance concrete,” in *Calcined Clays for Sustainable Concrete*, K. Scrivener and A. Favier, Eds., Dordrecht: Springer, 2015, pp. 467–477. http://dx.doi.org/10.1007/978-94-017-9939-3_58.

[8] P. Mikhailenko, F. Cassagnabère, A. Emam, and M. Lachemi, "Influence of physico-chemical characteristics on the carbonation of cement paste at high replacement rates of metakaolin," *Constr. Build. Mater.*, vol. 158, pp. 164–172, 2018, http://dx.doi.org/10.1016/j.conbuildmat.2017.10.021.

[9] D. da Silva Andrade, J. H. da Silva Rêgo, P. Cesar Morais, and M. Frías Rojas, "Chemical and mechanical characterization of ternary cement pastes containing metakaolin and nanosilica," *Constr. Build. Mater.*, vol. 159, pp. 18–26, 2018, http://dx.doi.org/10.1016/j.conbuildmat.2017.10.123.

[10] Z. Zhang, B. Zhang, and P. Yan, "Comparative study of effect of raw and densified silica fume in the paste, mortar and concrete," *Constr. Build. Mater.*, vol. 105, pp. 82–93, 2016, http://dx.doi.org/10.1016/j.conbuildmat.2015.12.045.

[11] J. H. S. Rêgo, M. F. Rojas, A. M. Terrades, L. Fernández-Carrasco, E. R. Morales, and M. I. S. Rojas, "Effect of partial substitution of highly reactive mineral additions by Nanosilica in cement pastes," *J. Mater. Civ. Eng.*, vol. 31, no. 1, pp. 1–11, 2019, http://dx.doi.org/10.1061/(ASCE)MT.1943-5533.0002567.

[12] H. M. Khater, "Influence of metakaolin on resistivity of cement mortar to Magnesium chloride solution," *J. Mater. Civ. Eng.*, vol. 23, no. 9, pp. 1295–1301, 2011, http://dx.doi.org/10.1061/(ASCE)MT.1943-5533.0000294.

[13] S. Barbhuiya, P. L. Chow, and S. Memon, "Microstructure, hydration and nanomechanical properties of concrete containing metakaolin," *Constr. Build. Mater.*, vol. 95, pp. 696–702, 2015, http://dx.doi.org/10.1016/j.conbuildmat.2015.07.101.

[14] P. Ghoddousi and L. Adelzade Saadabadi, "Study on hydration products by electrical resistivity for self-compacting concrete with silica fume and metakaolin," *Constr. Build. Mater.*, vol. 154, pp. 219–228, 2017, http://dx.doi.org/10.1016/j.conbuildmat.2017.07.178.

[15] H. F. Campos, T. M. S. Rocha, G. C. Reus, N. S. Klein, and J. Marques Fo., "Determination of the optimal replacement content of Portland cement by stone powder using particle packing methods and analysis of the influence of the excess water on the consistency of pastes," *Rev. IBRACON Estrut. Mater.*, vol. 12, no. 2, pp. 210–232, 2019, http://dx.doi.org/10.1590/s1983-41952019000200002.

[16] D. Alonso-Domínguez, I. Álvarez-Serrano, E. Reyes, and A. Moragues, "New mortars fabricated by electrostatic dry deposition of nano and microsilica additions: Enhanced properties," *Constr. Build. Mater.*, vol. 135, pp. 186–193, 2017, http://dx.doi.org/10.1016/j.conbuildmat.2017.01.011.

[17] I. P. Sfikas, E. G. Badogiannis, and K. G. Trezos, "Rheology and mechanical characteristics of self-compacting concrete mixtures containing metakaolin," *Constr. Build. Mater.*, vol. 64, pp. 121–129, 2014, http://dx.doi.org/10.1016/j.conbuildmat.2014.04.048.

[18] L. Feng, P. Zhao, Z. Wang, J. Gao, X. Su, and H. Li, "Improvement of mechanical properties and chloride ion penetration resistance of cement pastes with the addition of pre-dispersed silica fume," *Constr. Build. Mater.*, vol. 182, pp. 483–492, 2018, http://dx.doi.org/10.1016/j.conbuildmat.2018.06.053.

[19] G. Ling et al., "Rheological behavior and microstructure characteristics of SCC incorporating metakaolin and silica fume," *Materials*, vol. 11, no. 12, pp. 2576, 2018, http://dx.doi.org/10.3390/ma11122576.

[20] J. Hoppe Fo., A. Gobbi, E. Pereira, R. S. Tanaka, and M. H. F. De Medeiros, "Atividade pozolânica de adições minerais para cimento portland (Parte ii): índice de atividade pozolânica com cimento portland (IAP), difração de raios-x (DRX) e termogravimetria (TG/DTG)," *Rev. Mat.*, vol. 22, no. 3, 2017, http://dx.doi.org/10.1590/S1517-707620170003.0207.

[21] Z. Zhang, B. Zhang, and P. Yan, "Hydration and microstructures of concrete containing raw or densified silica fume at different curing temperatures," *Constr. Build. Mater.*, vol. 121, pp. 483–490, 2016, http://dx.doi.org/10.1016/j.conbuildmat.2016.06.014.

[22] R. C. O. Romano, M. A. Cincotto, and R. G. Pileggi, "Hardening phenomenon of Portland cement suspensions monitored by Vicat test, isothermal calorimetry and oscillatory rheometry," *Rev. IBRACON Estrut. Mater.*, vol. 11, no. 5, pp. 949–959, 2018, http://dx.doi.org/10.1590/s1983-41952018000500003.

[23] D. C. S. Garcia, M. M. N. S. Soares, A. C. S. Bezerra, M. T. P. Aguilar, and R. B. Figueiredo, "Microstructure and hardness of cement pastes with mineral admixture," *Rev. Mat.*, vol. 22, no. 2, 2017, http://dx.doi.org/10.1590/S1517-707620170002.0145.

[24] Associação Brasileira de Normas Técnicas, *Cimento Portland – Requisitos*, NBR 16697, 2018.

[25] Associação Brasileira de Normas Técnicas, *Cimento Portland – Análise Química - Determinação de Perda ao Fogo*, NM 18, 2012.

[26] Associação Brasileira de Normas Técnicas, *Cimento Portland – Determinação dos Tempos de Pegas*, NBR 16607, 2018.

[27] Associação Brasileira de Normas Técnicas, *Cimento Portland – Determinação da Pasta de Consistência Normal*, NBR 16606, 2017.

[28] Associação Brasileira de Normas Técnicas, *Cimento Portland – Determinação do Índice de Finura por Meio da Peneira 75 µm (no 200)*, NBR 11579, 2013.

[29] Associação Brasileira de Normas Técnicas, "*Cimento Portland e Outros Materiais em Pó – Determinação da Massa Específica*, NBR 16605, 2017.

[30] Associação Brasileira de Normas Técnicas, *Cimento Portland – Determinação da Resistência à Compressão de Corpos de Prova Cilíndricos*, NBR 7215, 2019.

[31] B. S. Santos, D. D. M. Albuquerque, and D. V. Ribeiro, "Efeito da adição do metacaulim na carbonatação de concretos de cimento Portland," *Rev. IBRACON Estrut. Mater.*, vol. 13, no. 1, pp. 10–18, 2020, http://dx.doi.org/10.1590/S1983-41952020000100002.

[32] Associação Brasileira de Normas Técnicas, *Agregados – Determinação da Massa Unitária e do Volume de Vazios*, NM 45, 2006.

[33] Associação Brasileira de Normas Técnicas, *Sílica Ativa para Uso com Cimento Portland em Concreto, Argamassa e Pasta – Parte 4: Determinação da Finura por Meio da Peneira 45 µm*, NBR 13956-4, 2012.

[34] American Society for Testing and Materials, *Standard Test Method for Specific Surface Area of Alumina or Quartz by Nitrogen Adsorption*, C1069, 2014.

[35] Associação Brasileira de Normas Técnicas, *Sílica Ativa para Uso com Cimento Portland em Concreto, Argamassa e Pasta – Parte 1: Requisitos*, NBR 13956-1, 2012.

[36] Associação Brasileira de Normas Técnicas, *Água para Amassamento do Concreto. Parte 1: Requisitos*, NBR 15900-1, 2009.

[37] B. Scrivener, K. Snellings, and R. Lothenbach, *A Practical Guide to Microstructural Analysis of Cementitious Materials*. Boca Raton: CRC Press, 2016.

[38] A. M. Neville and J. J. Brooks, *Tecnologia do Concreto*, 2a ed. Porto Alegre: Bookman, 2013.

[39] A. Hermann, E. A. Langaro, S. H. L. Silva, and N. S. Klein, "Empacotamento de partículas de cimento e sílica ativa em pastas pelo uso de modelo analítico," *Rev. IBRACON Estrut. Mater.*, vol. 9, no. 1, pp. 48–65, 2016, http://dx.doi.org/10.1590/S1983-41952016000100004.

[40] V. M. Silva, "Ação da carbonatação em vigas de concreto armado em serviço, construídas em escala natural e reduzida," Ph.D. dissertation, Univ. São Paulo, São Carlos, 2007.

[41] V. M. S. Capuzzo, C. M. C. Gurjão, and J. B. L. Liborio, "Influência da carbonatação e das adições minerais na porosidade do concreto," in *I Enc. Luso-Bras. Degrad. Estrut. Concr. Arm.*, Salvador, 2014.

[42] D. Y. Lei, L. P. Guo, W. Sun, J. Liu, X. Shu, and X. L. Guo, "A new dispersing method on silica fume and its influence on the performance of cement-based materials," *Constr. Build. Mater.*, vol. 115, pp. 716–726, 2016, http://dx.doi.org/10.1016/j.conbuildmat.2016.04.023.

[43] B. Lothenbach, K. Scrivener, and R. D. Hooton, "Supplementary cementitious materials," *Cement Concr. Res.*, vol. 41, no. 12, pp. 1244–1256, 2011, http://dx.doi.org/10.1016/j.cemconres.2010.12.001.

[44] M. H. F. Medeiros, J. W. Raisdorfer, and J. Hoppe Fo., "Influência da sílica ativa e do metacaulim na velocidade de carbonatação do concreto: relação com resistência, absorção e relação a/c," *Ambient. Constr.*, vol. 17, no. 4, pp. 125–139, 2017, http://dx.doi.org/10.1590/s1678-86212017000400189.

[45] D. Zhao and R. Khoshnazar, "Microstructure of cement paste incorporating high volume of low-grade metakaolin," *Cement Concr. Compos.*, vol. 106, pp. 103453, 2020, http://dx.doi.org/10.1016/j.cemconcomp.2019.103453.

[46] N. Shafiq, M. F. Nuruddin, S. U. Khan, and T. Ayub, "Calcined kaolin as cement replacing material and its use in high strength concrete," *Constr. Build. Mater.*, vol. 81, pp. 313–323, 2015, http://dx.doi.org/10.1016/j.conbuildmat.2015.02.050.

Author contributions: MMLP and ALRS: conceptualization, methodology, writing, data curation; VMSC and RML: methodology, data curation, formal analysis.

Editors: Edna Possan, Guilherme Aris Parsekian.

IBRACON Structures and Materials Journal
Revista IBRACON de Estruturas e Materiais
ISSN 1983-4195 ismj.org

ORIGINAL ARTICLE

Influence of the supplementary reinforcement on the shear strength of beams with prefabricated truss stirrups

Influência da armadura suplementar na resistência ao cisalhamento de vigas com estribos treliçados pré-fabricados

Rosângela Silva Pinto[a]
Vanessa Carolaine Sousa[a]
Luamim Sales Tapajós[b]
Maurício de Pina Ferreira[c]
Aarão Ferreira Lima Neto[a]

[a]Universidade Federal do Pará – UFPA, Nucleus of Amazonian Development in Engineering, Postgraduate Program in Infrastructure Engineering and Energy Development, Tucuruí, PA, Brasil

[b]Universidade Federal do Oeste do Pará – UFOPA, Faculty of Civil Engineering, Itaituba, PA, Brasil

[c]Universidade Federal do Pará – UFPA, Institute of Technology, Faculty of Civil Engineering, Belém, PA, Brasil

Received 22 October 2020
Accepted 05 May 2021

Abstract: This paper presents the results of seven experimental tests in reinforced concrete wide beams, aiming to investigate their performance when subjected to shear, using prefabricated truss stirrups as shear reinforcement, as well as a supplementary reinforcement to control cracks by delamination. The main analysed variables were: position of the supplementary reinforcement, inclination of the shear reinforcement, and spacing between stirrups. Results showed that strength increments of up to 142% were obtained using the prefabricated truss stirrups. Furthermore, the experimental results were compared with the theoretical shear strength estimates of the tested beams, following the recommendations of NBR 6118 (2014), Eurocode 2 (2004), and ACI 318 (2014), in order to evaluate the safety level of these codes when designing concrete elements subjected to shear with the reinforcement used in this paper.

Keywords: shear, shear reinforcement, supplementary reinforcement.

Resumo: Este trabalho apresenta os resultados dos ensaios em sete vigas faixa de concreto armado, cujo objetivo foi o de investigar o desempenho dessas peças ao cisalhamento, adotando-se os estribos treliçados pré-fabricados como armadura transversal, acrescidos de uma armadura suplementar, para evitar a propagação de fissuras por delaminação. As principais variáveis analisadas foram: posição da armadura suplementar, inclinação da armadura transversal e espaçamento entre camadas de estribos. Comparando os resultados das vigas armadas ao cisalhamento com a viga de referência, verificou-se que a armadura transversal utilizada neste trabalho levou a um acréscimo de até 142% na resistência última das vigas. Além disso, foram comparados os resultados experimentais com as estimativas teóricas de resistência ao cisalhamento das vigas ensaiadas, seguindo as recomendações da NBR 6118 (2014), Eurocode 2 (2004) e ACI 318 (2014), a fim de se avaliar o nível de segurança dessas recomendações para o dimensionamento de elementos de concreto ao cisalhamento com a armadura adotada neste artigo.

Palavras-chave: cisalhamento, armadura transversal, armadura suplementar.

How to cite: R. S. Pinto; V.C. Sousa; L.S. Tapajós; M.P. Ferreira; A.F. Lima Neto "Influence of the Supplementary Reinforcement on the Shear Strength of Beams with Prefabricated Truss Stirrups," *Rev. IBRACON Estrut. Mater.*, vol. 15, no. 1, e15106, 2022, https://doi.org/10.1590/S1983-41952022000100006

Corresponding author: Aarão Ferreira Lima Neto. E-mail: aaraon@ufpa.br
Financial support: None.
Conflict of interest: Nothing to declare.

1. INTRODUCTION

Reinforced concrete elements subjected to shear are likely to fail in a brittle way, and several authors [1-9] suggest that using shear reinforcement is the best way to improve both the shear strength and deformation capacity of reinforced concrete structural members.

However, in some cases (Figure 1), there may be difficulty in reinforcing the concrete element due to the conflict between flexural and shear reinforcement, which is the need to involve the longitudinal bars, in the case of closed stirrups (Figure 1b and Figure 1c) or the positioning of the flexural reinforcement, in the case of studs (Figure 1e).

Thus, one of the solutions to avoid clashes when positioning the transverse and longitudinal reinforcement is the use of shear reinforcement with internal anchorage, positioned between the top and bottom flexural reinforcement (Figure 1f). In addition, shear reinforcement with internal anchorage can be prefabricated, as they do not depend on the flexural reinforcement position, making the construction process faster. This greater agility in the construction process can reduce the work costs, as commented by some authors [10-12].

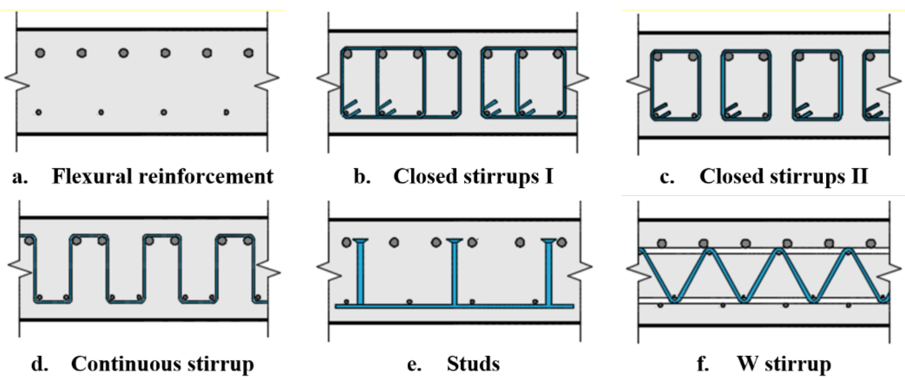

Figure 1. Shear reinforcement detailing in one-way shear (Tapajós [13])

Nevertheless, a significant reduction of the structural performance of the transverse reinforcement has been described when they are not anchored within the flexural reinforcement (see [14] and [15]). Some authors [16-18] observed that using shear reinforcement with internal anchorage in flat slabs subjected to two-way shear led to premature failures associated with the delamination effect.

Even so, it is possible to mention studies where the use of shear reinforcement with internal anchorage had satisfactory performance, and the development of cracks by delamination was not observed in some papers [19-21]. It is also worth mentioning the study of Ferreira et al. [22], who tested prefabricated truss stirrups with internal anchorage in reinforced concrete wide beams, observing the delamination in some specimens. However, Tapajós [13] tested the shear reinforcement developed by Ferreira et al. [22] with and without the addition of a u-hook as supplementary reinforcement to avoid delamination, noting that it would be possible to obtain a performance similar to that of beams with closed stirrups anchored to flexural reinforcement and studs.

Thus, this study aimed to investigate the influence of supplementary reinforcement on the shear performance of reinforced concrete elements with the prefabricated truss stirrups, as well as the angle of inclination and spacing of shear reinforcement. Seven wide beams were tested, varying the angle of inclination of the shear reinforcement and the supplementary u-hooks' position. In addition, the experimental results were compared with theoretical ones according to the recommendations of codes NBR 6118 [23], Eurocode 2 [24], and ACI 318 [25].

2. DESIGN RECOMMENDATIONS

The recommendations presented in [23-25] were used to estimate the tested specimens' shear resistance. It is relevant to highlight that the safety factors implicit and explicitly presented in the design equations were removed in this section to compare theoretical and experimental strengths properly.

2.1. NBR 6118 (2014)

The Brazilian code presents two design models to estimate the shear strength of reinforced concrete elements. Model I considers that the shear strength of transversely reinforced beams ($V_{R,csI}$) is given by the sum of the contributions given by concrete ($V_{R,cI}$) and steel ($V_{R,sI}$), as shown in Equation 1, as well as this model assumes an inclination of the strut equal to 45°. The concrete contribution is calculated with Equation 2, which estimates the shear strength of a beam without transverse reinforcement and considers only the concrete's tensile strength. The contribution given by the shear reinforcement is calculated using Equation 3, and the maximum shear strength ($V_{R,max\ I}$) of a beam is limited by Equation 4, which estimates the failure of the compressed strut.

$$V_{R,cs\ I} = V_{R,c\ I} + V_{R,s\ I} \tag{1}$$

$$V_{R,c\ I} = 0.6 f w_{ctk,inf} \tag{2}$$

$$V_{R,s\ I} = \left(\frac{A_{sw}}{s}\right) 0.9 d f_{yw} \left(sen\alpha + \cos\alpha\right) \tag{3}$$

$$V_{R,\max\ I} = 0.27\left(1 - \frac{f_c}{250}\right) f_c b_w d \left(\cot\alpha + 1\right) \tag{4}$$

Where: $f_{ctk,\inf} = 0.7 f_{ct,m}$, is the fragile tensile strength of concrete in 5% of cases;
$f_{ct,m}$ is the average tensile strength of concrete, for concretes with a maximum strength of 50 MPa, calculated with $f_{ct,m} = 0.3 f_c^{2/3}$;
f_c is the compressive strength of concrete;
b_w is the width of the beam section;
d is the effective depth of the beam section;
A_{sw} is the area of reinforcement of one layer of transverse reinforcement;
s is the spacing between the transverse reinforcement layers;
f_{yw} is the yield strength of the transverse reinforcement, limited to 500 MPa;
α is the angle of inclination of the transverse reinforcement in relation to the longitudinal axis.

Model II of NBR 6118 [23] considers, as well as Model I, that the shear strength of transversely reinforced beams ($V_{R,csII}$) is given by the contribution of concrete ($V_{R,cII}$) and shear reinforcement ($V_{R,sII}$), according to Equation 5. In addition, Model II also considers the effects of diagonal cracking, which reduces the strut's inclination and, consequently, concrete contribution. In this model, the Brazilian code allows the variation of the strut's angle between 30° and 45°, and concrete contribution shall be calculated with Equation 6. In this case, concrete's contribution is a function of the applied shear force (V), calculated through an iterative process. The contribution of transverse reinforcement is calculated with Equation 7 and the maximum shear strength ($V_{R,max\ II}$) with Equation 8.

$$V_{Rcs,\ II} = V_{R,c\ II} + V_{R,s\ II} \tag{5}$$

$$V_{R,c\ II} = V_{R,c\ I} \frac{V_{R,\max\ II} - V}{V_{R,\max\ II} - V_{R,c\ I}} \le V_{R,c\ I} \tag{6}$$

$$V_{R,s\ II} = \frac{A_{sw}}{s} 0.9 d f_{yw} \left(cotg\theta + cotg\alpha\right) sen\alpha \tag{7}$$

$$V_{R,\max\ II} = 0.54\left(1 - \frac{f_c}{250}\right) f_c b_w d \ \mathrm{sen}^2\theta \left(\cot\alpha + \cot\theta\right) \tag{8}$$

2.2. Eurocode 2 (2004)

Eurocode 2 [24] indicates the use of Equation 9 to estimate the contribution portion of concrete to the shear strength of beams ($V_{R,c}$).

$$V_{R,c} = \max \begin{cases} \left(0.18k(100\rho_l f_c)^{1/3}\right) b_w d \\ 0.035k^{\frac{3}{2}} \sqrt{f_c}\, b_w d \end{cases} \tag{9}$$

Where:
k considers the reduction in shear strength due to the size effect, calculated with Equation 10.

$$k = 1 + \sqrt{\frac{200}{d}} \leq 2 \tag{10}$$

ρ_l is the portion related to the longitudinal reinforcement ratio, calculated with $\rho_l = \frac{A_s}{b_w d} \leq 2$, where A_s is the area of longitudinal reinforcement of the beam.

Eurocode 2 [24] suggests Equation 11 to check the shear strength of transversely reinforced beams ($V_{R,cs}$). The code also recommends that the strut's angle of inclination may vary from 21.8° to 45°. The maximum shear strength ($V_{R,max}$) shall be estimated with Equation 12.

$$V_{R,cs} = \max \begin{cases} \frac{A_{sw}}{s} 0.9d\, f_{yw} \left(\cot\theta + \cot\alpha\right) sen\alpha \\ V_{R,c} \end{cases} \tag{11}$$

Where:

$$V_{R,\max} = \frac{0.9 b_w d v_1 f_c \left(\cot\theta + \cot\alpha\right)}{1 + \cot^2\theta} \tag{12}$$

Where ν1 is determined with Equation 13;

$$v_1 = 0.6\left[1 - \frac{f_c}{250}\right] \tag{13}$$

As EC2 [24] admits the strut's angle variation, it suggests that Equations 11 and 12 shall be equalized to check the strength so that the smallest strut angle can be found through the derived equation (see Equation 14).

$$\cot\theta = \sqrt{\frac{b_w s v_1 f_c}{A_{sw} f_{yw} \mathrm{sen}\alpha}} \tag{14}$$

2.3. ACI 318 (2014)

The American code considers the one-way shear strength of reinforced concrete elements to be similar to the strength of a beam, so Equation 15 is used to estimate the shear strength of beams without transverse reinforcement ($V_{R,c}$). Among the variables that influence shear strength, the code adopts only the strength of concrete.

$$V_{R,c} = 0.17\sqrt{f_c}\,b_w d \tag{15}$$

Where:

f_c is the compressive strength of concrete, obtained by testing cylindrical specimen;

b_w is the width of the beam;

d is the effective depth of the beam.

For the case of beams with transverse reinforcement, ACI 318 [25] considers that the shear strength ($V_{R,cs}$) is given by the sum of the contributions of concrete and the transverse reinforcement ($V_{R,s}$), calculated with Equation 16, recalling that the code estimates that the inclination of the compressed strut is equal to 45°. The contribution portion of the shear reinforcement is calculated with Equation 17. In addition, the American code limits the maximum shear strength of beams given by Equation 18, which refers to failure due to crushing of the strut ($V_{R,max}$).

$$V_{R,cs} = V_{R,c} + V_{R,s} \tag{16}$$

$$V_{R,s} = \left(\frac{d}{s}\right) A_{sw} f_{yw} \left(sen\alpha + \cos\alpha\right) \tag{17}$$

$$V_{R,\max} = 0.66\sqrt{f_c}\,b_w d \tag{18}$$

Where:

s is the spacing between the transverse reinforcement layers;

A_{sw} is the area of reinforcement of one layer of transverse reinforcement;

f_{yw} is the yield strength of the transverse reinforcement, limited to 420 MPa;

α is the angle of inclination of the transverse reinforcement in relation to the longitudinal one.

3. EXPERIMENTAL PROGRAM

The experimental program was developed at the Federal University of Pará and consisted of seven tests in reinforced concrete wide beams. The main variables were: the position of supplementary reinforcement; spacing, and inclination of the transverse reinforcement, as shown in Table 1 and Figure 2. This paper presents only the results of beams with prefabricated truss stirrups. Tests with other types of shear reinforcement, such as closed stirrups and studs, are presented in other research [13][22].

Table 1. Characteristics of the tested beams.

Beam	φ_w(mm)	A_{sw}(mm)	α (°)	s (mm)	ρ_w (%)	f_{yw} (MPa)	*U-Hooks*
VR	-	-	-	-	-	-	-
V1	6.3	196.39	90	100	0.39	571	T+C
V2							T
V3		202.62	60		0.45		T+C
V4							T
V5	5.0	123.70	90	60	0.41	676	T+C
V6							T

Obs.: b_w = 500 mm; h = 210 mm; L = 2300 mm; a = 620 mm; d = 177 mm; a/d = 3.5; A_s = 3434 mm²; f_{ys} = 550 MPa; φ_f = 25 mm; $\varphi_{f'}$ = 12.5 mm; f_{cm} = 29 MPa; T = supplementary reinforcement on the tensile face; C = supplementary reinforcement on the compression face; $\rho_w = \dfrac{A_{sw}}{b_w s sin\alpha}$

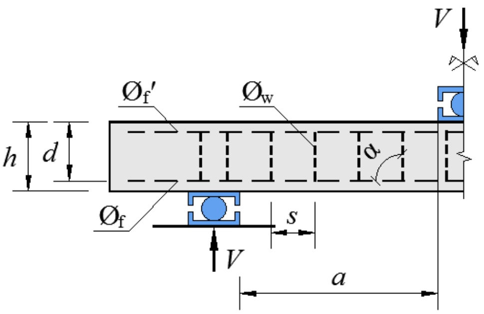

Figure 2. Variables in the experimental program

The test system is shown in Figure 3, consisting of a simply-supported system, where constant and controlled loading was applied by a hydraulic testing machine (capacity of 3000 kN). All beams were 2300 mm long, 500 mm wide, and 210 mm deep; the a/d ratio was approximately 3.5 to avoid arch action, according to an analysis made by Fisker and Hagsten [26], to allow better visualization of the performance of the transverse reinforcement. The reference beam did not have transverse reinforcement, making it possible to evaluate the increase in the other beams' shear strength due to the transverse and supplementary reinforcement arrangements. The longitudinal reinforcement was kept constant for all tested beams, consisting of 7 bars of 25 mm in diameter in the tensile area and 7 bars of 12.5 mm in diameter in the compression area.

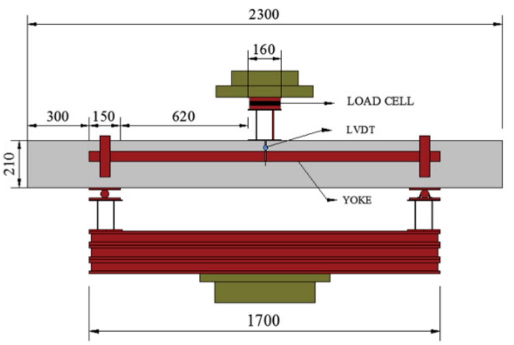

a. Detail of the test system

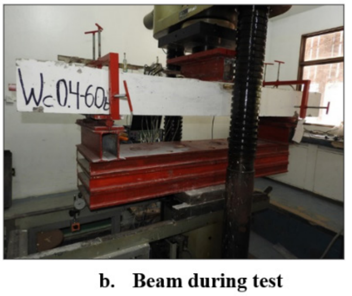

b. Beam during test

Figure 3. Test arrangements.

The shear reinforcement used in this study was composed of prefabricated truss stirrups, developed by Ferreira et al. [22], manufactured in modules and installed between the bottom and top flexural reinforcement shown in Figure 4a. In addition to the transverse reinforcement, u-hook-shaped delamination control reinforcement was used, according to the model adopted by Tapajós [13], as shown in Figure 4b. Figure 4c shows the shear reinforcement's detail. Figure 4d shows the stirrups module manufactured for this research, and Figure 4e shows the supplementary reinforcement positioned in one of the tested specimens.

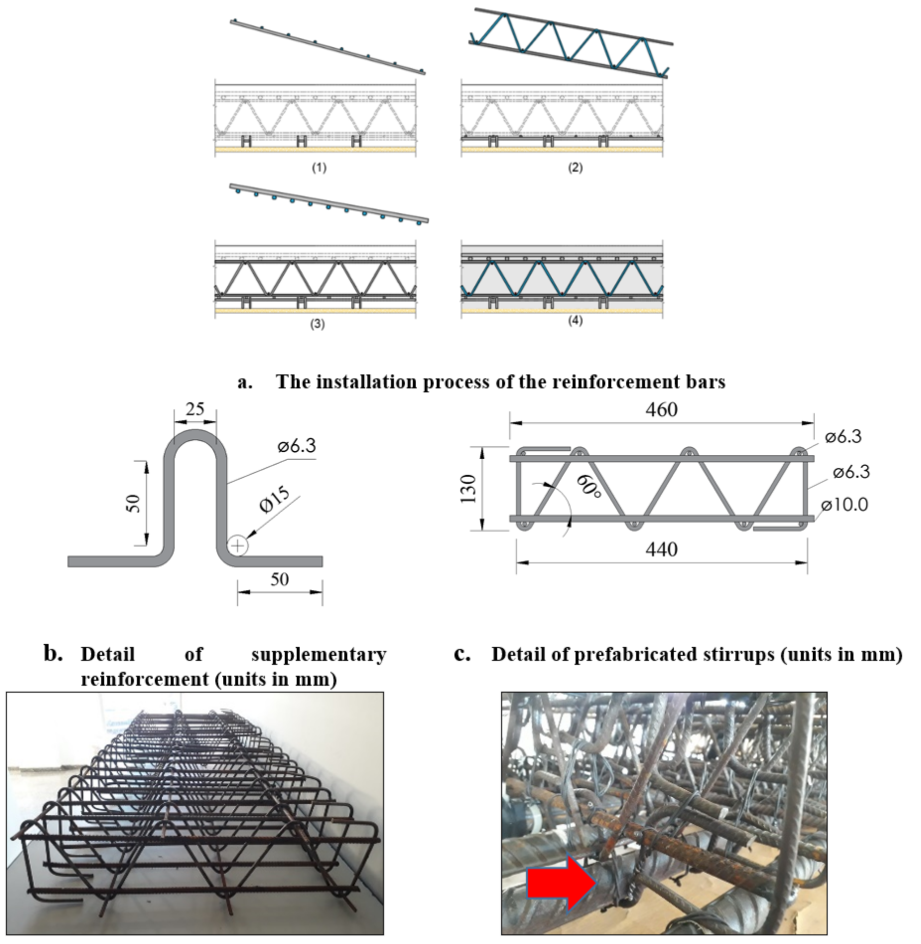

a. The installation process of the reinforcement bars

b. Detail of supplementary reinforcement (units in mm)

c. Detail of prefabricated stirrups (units in mm)

d. Shear reinforcement module

e. Supplementary reinforcement

Figure 4. Prefabricated truss stirrups.

Shear reinforcement with inclinations of 60° and 90° were used to evaluate the influence of their inclination in the shear resistance of the tested beams. To analyse the influence of layer's spacing on the shear strength, two arrangements were adopted: stirrups with 6.3 mm in diameter spaced every 100 mm (ρ_w = 0.39% for V1 and V2 and ρ_w = 0.45% for V3 and V4) and stirrups with 5 mm in diameter spaced every 60 mm (ρ_w = 0.41%), both arrangements having approximately the same transverse reinforcement ratio. Finally, to observe each specimen's behaviour depending on the supplementary reinforcement position, beams with the u-hooks on their tensile and compression parts were tested, as well as specimens that only had u-hooks on the tensile zone of the beam. All beams with prefabricated truss stirrups had two vertical legs and five inclined legs at 60°. In this paper, any inclined leg relates to a 0.87 vertical leg (sin 60°), so there are approximately 6.35 legs by layer of the prefabricated truss stirrup. Figure 5 shows a summary of the tested beams.

Regarding the variables involved, beam VR is a reference specimen without shear reinforcement. Beams V1 and V2 had vertical (90°) prefabricated truss stirrups made with 6.3 mm bars spaced at each 100 mm, and beam V1 had supplementary reinforcement arranged in the tensile and compression faces of the specimen, while beam V2 only had supplementary reinforcement on the tensile face. Beams V3 and V4 had the same shear reinforcement of beams V1 and V2, but with stirrups inclined at 60°. Beam V3 had supplementary u-hooks on both faces, while in beam V4, they were placed only on the tensile face. Finally, beams V5 and V6 were tested to evaluate the influence of spacing between layers, their shear reinforcement being manufactured with stirrups of 5 mm in diameter, spaced every 60 mm and with an angle of inclination of 90°, beam V5 having supplementary reinforcement on both faces, whereas beam V6 only had it on the tensile face. In this way, all beams with shear reinforcement had approximately the same transverse reinforcement ratio.

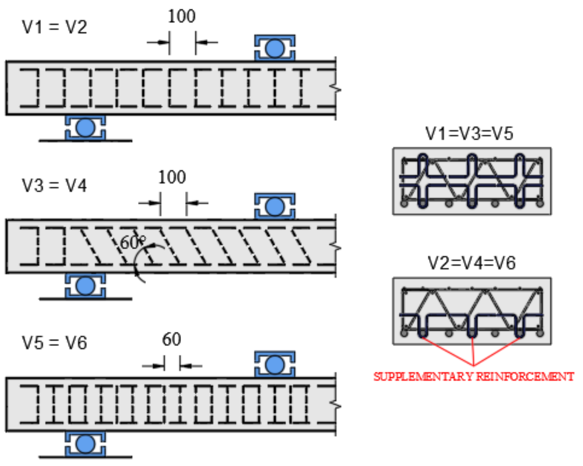

Figure 5. Characteristics of the tested beams (units in mm)

Concrete was produced with *CP IV-Z* cement (Portland cement with pozzolanic addition). The coarse aggregate adopted had a maximum size of 19 mm and granitic origin, and medium sand was used as fine aggregate. Concrete was mixed to reach grade C30. All the beams were cast on the same day, and after 60 days, the tests were carried during a week. The compressive strength of concrete was obtained through axial compression tests, as recommended by NBR 5739 [27]. On the day of each beam's test, three concrete cylindrical specimens were tested to obtain the mean and characteristic value of concrete's compressive strength. The mean value of concrete compressive strength in all tests is considered as f_{cm} = 29 MPa, while the characteristic value of compressive strength of concrete is the mean value less than 4 MPa, due to rigorous control in the laboratory (f_{ck} = 25 MPa). Thus, to calculate the beams' strength according to the design codes, the mean values were used. For reinforcement, CA-60 steel was used for the bars with 5 mm in diameter and CA-50 steel for the other diameters. The steel's mechanical properties were obtained through tensile tests, following the recommendations of NBR 6892 [28]. Table 1 presents materials properties used to estimate shear strength by theoretical recommendations.

Strain gauges (SG) were attached to the beams' upper side face, in the midspan between the supports in the beams' longitudinal direction, to measure the compression strains of concrete. Regarding the flexural reinforcement instrumentation, two SG were attached to each beam's central bar in the midspan to obtain the maximum tensile strains, adopting the average of the two measured values.

Concerning the shear reinforcement, two SG were attached to each instrumented bar, choosing to instrument the layers arranged in the middle of the shear span, where it is estimated that the greatest strains in transverse reinforcement occur, as observed by Ferreira et al. [22] and Tapajós [13]. SG were also used in the supplementary reinforcement to observe its behaviour during the test. Figure 6 shows the complete instrumentation arrangement of the tested beams.

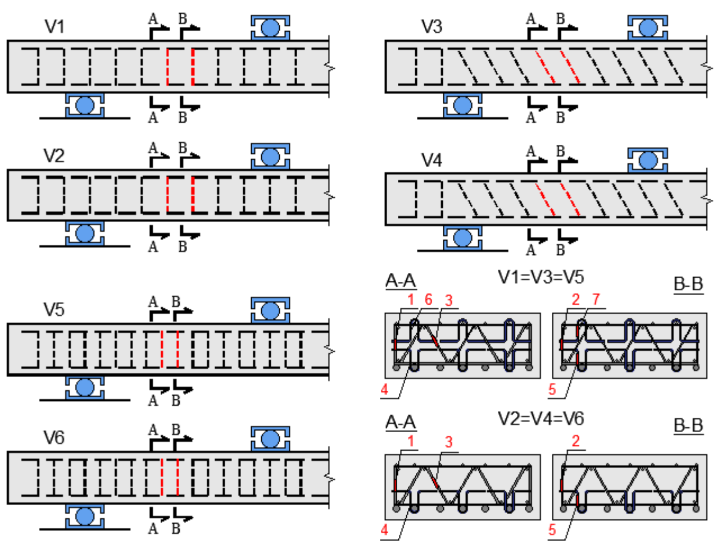

Figure 6. Instrumentation arrangement of the beams.

4. RESULTS AND DISCUSSIONS

4.1. Ultimate strength and theoretical estimates

Table 2 shows the experimental results of the tested beams, related to their ultimate strengths, as well as the comparison with their flexural strength estimates (V_{flex}), the performance in relation to the reference beam, to observe the increase in strength due to the transverse reinforcement, and the comparison with the theoretical shear strength estimates, obtained following the recommendations of models I and II of NBR 6118 [23], Eurocode 2 [24] and ACI 318 [25], as presented in section 2.

It was observed that all tested beams had an ultimate strength lower than the estimated flexural strength, contributing to the understanding that the specimens' failure was related to shear. Concerning the comparison with the reference beam, all specimens showed a significant increase in strength, varying between 89% and 158%, showing that the prefabricated truss stirrups contribute to the increase in shear strength, as observed by Ferreira et al. [22].

Table 2. Failure Loads of the tested beams.

Beam	V_u (kN)	V_u/V_{flex}	V_u/V_{ref}	$V_u/V_{R.NBR}(kN)$		V_u/EC2	V_u/ACI
				I	II		
VR	145.0	0.37	1.00	1.38	1.38	1.18	1.79
V1	281.5	0.72	2.07	1.08	0.87	0.67	1.24
V2	256.5	0.66	1.89	0.98	0.80	0.61	1.13
V3	351.0	0.90	2.58	1.10	0.94	0.74	1.25
V4	269.0	0.69	1.98	0.84	0.72	0.57	0.96
V5	345.5	0.89	2.57	1.30	1.05	0.83	1.50
V6	302.0	0.77	2.23	1.13	0.92	0.72	1.30
Average				**1.12**	**0.95**	**0.76**	**1.31**
Coefficient of Variation (%)				**16.3**	**22.4**	**26.9**	**20.4**

The beams with supplementary reinforcement at both end showed greater strength than the specimens with the u-hooks only on the tensile face. Tapajós [13] research points to a better performance of beams with supplementary reinforcement when compared with those without it. However, the comparison between the arrangement on the two faces or only on the tensile face was not addressed.

Concerning the transverse reinforcement's inclination, specimens with truss stirrups inclined at 60° had greater strength than those with the same arrangement and inclination of 90°. As pointed out by several studies, this result was expected, including Melo et al. [29] on inclined stirrups' better performance compared to vertical stirrups.

Regarding stirrup spacing, it was observed that beams with a spacing of 60 mm between layers of transverse reinforcement, V5, and V6, reached higher strengths than the specimens with a spacing of 100 mm between layers, V1, and V2. It is worth mentioning that both specimens had approximately the same transverse reinforcement ratio. V3 and V4 were cast with inclined shear reinforcement. These beams reach a strength greater than V1 and V2, in order of comparison, due to a better anchorage because the inclined shear reinforcement while had a similar strength than the beams with lower spacing between layers.

When comparing the theoretical and experimental results, it was observed that Model II of NBR 6118 [23] presented the average results closest to the experimental ones, however with most results against safety and the second highest coefficient of variation. In contrast, Model II of the same code presented the least dispersion of results among the recommendations evaluated, with the second average of results closer to the experimental ones and few results against safety. Eurocode 2 [24] presented the least safe average of results and the higher dispersion. However, it is worth mentioning that all recommendations showed results against safety, including ACI 318 [25], which presents more conservative recommendations. This behaviour may be related to the high transverse reinforcement ratio adopted in this research since, as the transverse reinforcement ratio increases, there is a trend towards more unsafe results, as verified by Tapajós [13]. It is also observed that Model I of the Brazilian code and the American code set the value of the strut's angle of inclination at 45°, while Model II of the Brazilian code and the recommendations of the European code allow the reduction of this angle, leading to higher strength estimates when compared with the other two models. It is worth mentioning that these results were obtained without considering the safety coefficients of the codes. Figure 7 shows the comparison of experimental and theoretical results.

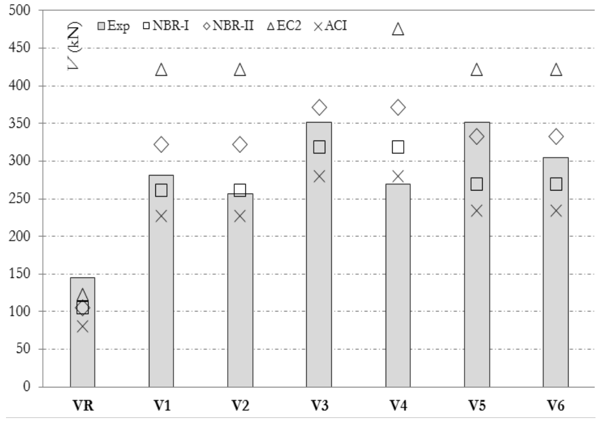

Figure 7. Comparison of experimental and theoretical results.

4.2. Vertical displacement and strain of the flexural reinforcement

Figure 8 shows the graph that correlates the shear force and displacement for the seven tested beams. All beams showed similar behaviour to the reference beam for the same loading level and concerning beams V1, V2, V3, V4, V5, and V6, close displacements among them were observed for the same loading level. However, after reaching approximately 200 kN, more significant displacements were noticed in beam V4. Only beam V5 showed a further increase in strength after reaching the peak.

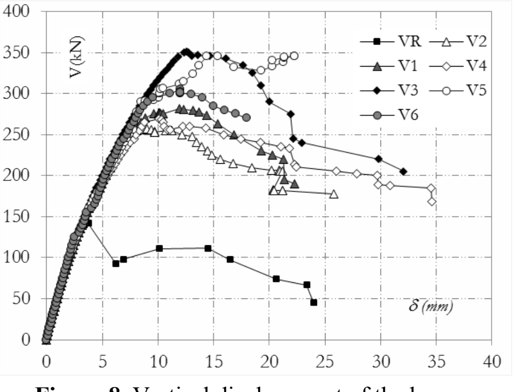

Figure 8. Vertical displacement of the beams.

Figure 9 shows the graph of shear force x strain of the flexural reinforcement. For all beams, the flexural bars did not reach the yield strain, ruling out the possibility of flexural failure, as observed in Table 2, comparing the ultimate strength with the flexural strength estimate.

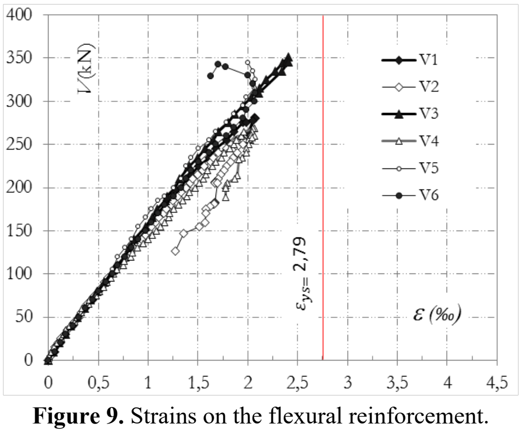

Figure 9. Strains on the flexural reinforcement.

4.3. Strain of the transverse reinforcement

Figure 10 shows the graphs of the relation between the strain of stirrups and the shear force. Two yield strain lines are presented since the beams V1, V2, V3, and V4 were produced with bars of 6.3 mm in diameter and beams V5 and V6 with bars of 5 mm in diameter. The result seen in Figure 9 follows the instrumentation arrangement shown in Figure 5, with Figure 9a showing the strain readings of bar 1 from the tested beams, Figure 9b the strain of bar 2, and Figure 10c the strain of bar 3.

Figure 10a shows that only beam V5 presented yield of the shear reinforcement at position 1, suggesting that it is the least required position during the test. It is also believed that this beam presented yield of the transverse reinforcement due to the lower area of reinforcement per layer. The same did not happen with the other beam with smaller spacing, V6, probably because it only had supplementary reinforcement on the tensile face.

In Figure 10b, it is possible to observe higher strains at position 2 of the instrumentation, estimating that this stirrup layer was the most stressed during the tests. Besides, stirrups yielded in all beams where supplementary reinforcement was placed in both edges of the shear reinforcement, confirming that they are relevant to improve anchorage conditions and the tested beams' structural performance.

Position 3 of the instrumentation refers to the same layer at position 1, but on one of the bar's inclined legs, located closer to the center of the beam's cross-section. In Figure 10c, it is possible to observe that the strains were higher than those at position 1, which shows greater stress concentrations in the central region of the beam and inclined legs, as also observed by Tapajós [13]. It was also possible to notice that all the reinforcement at position 3 yielded, pointing out a good performance of the prefabricated truss stirrups and confirming the failure mode associated with shear.

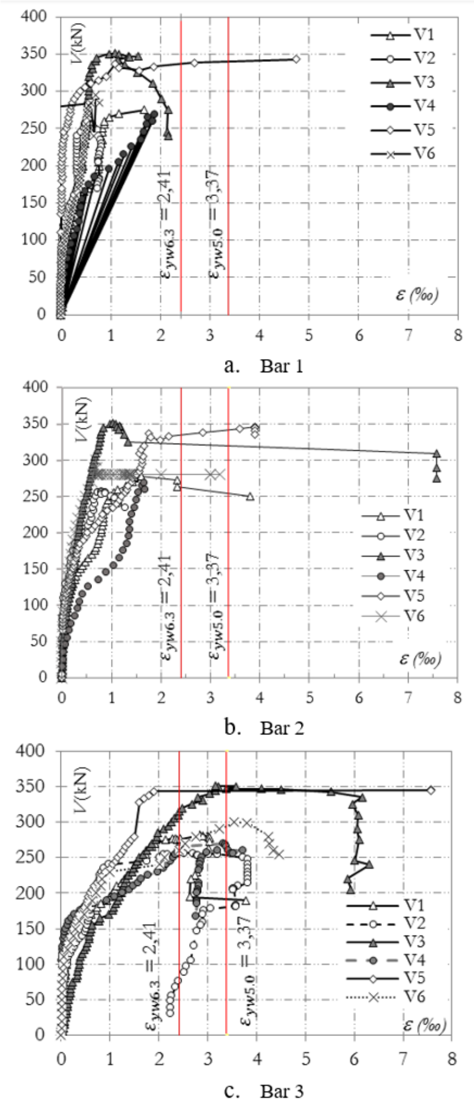

Figure 10. Strain of the shear reinforcement.

4.4. Strain of the supplementary reinforcement

Figure 11 shows the result of strains of the supplementary reinforcement of the tested beams. Tapajós [13] had observed higher strengths and strains on the truss stirrups in the beams with supplementary reinforcement than in the beams without supplementary reinforcement, but he did not complete the instrumentation of these u-hooks to prove their efficiency. However, in this research, it was possible to prove that this supplementary reinforcement works during the test.

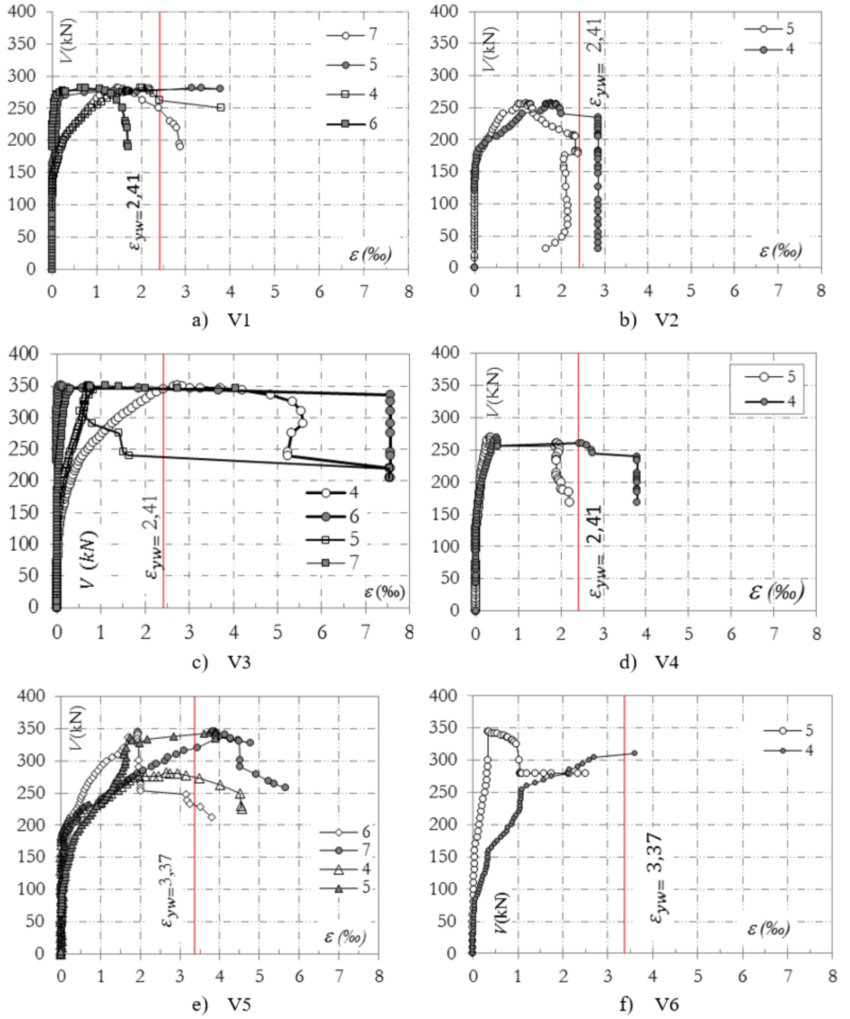

Figure 11. Strains on the supplementary reinforcement.

In general, the beams V1, V3, and V5, which were produced with supplementary reinforcement on the tensile and compression faces, presented higher strains than the beams V2, V4, and V6, which only had u-hooks on the tensile face. Thus, u-hooks on both edges of the shear reinforcement improved the tested beams' performance, as their transverse reinforcement reached higher strengths, with positive reflections on their ultimate strengths.

In most of the tested beams, the supplementary reinforcement only reached the yield strain after the beam reached its maximum strength, which indicates that this supplementary reinforcement acts sewing the cracks by delamination, avoiding a brittle failure of the specimens. Besides, the behaviour of beam V5 stands out, where all the instrumented u-hooks reached the yield strain, some of them even before the specimen reached its maximum strength. Thus, it is estimated that the conditions presented by this specimen were the most favourable in this study to ensure better anchorage of the prefabricated truss stirrups, together with the supplementary reinforcement on both faces.

4.5. Cracking patterns

Figure 12 shows the tested beams' cracking patterns, where it is possible to observe that all beams have failed due to shear, with the inclination of the main crack varying between 22° and 31°. Cracks by delamination were observed in all tested specimens. However, these cracks were controlled, unlike the beams tested by some authors [13][22] that did not have supplementary reinforcement, validating the hypothesis that these u-hooks contribute to preventing this propagation, as seen in the strain gauges' readings. It was also found that the beams with the smallest spacing between the layers of shear reinforcement showed a greater inclination for their main failure cracks.

It was observed that beams with supplementary reinforcement in both faces presented less delamination crack on the top face of the specimen when compared to the beams with u-hooks on the bottom face. The beams with shear reinforcement inclined at 60° could control satisfactory the cracks by delamination due to the increase of length anchorage compared to the vertical stirrups. Concerning spacing, the lower spacing between the layers contributes to control the crack propagation.

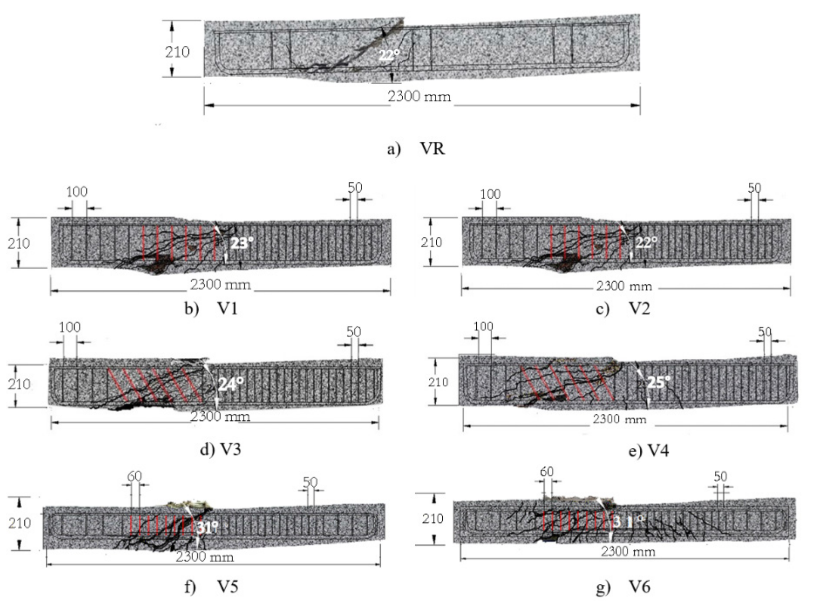

Figure 12. Cracking patterns of the specimens.

5. CONCLUSIONS

This study analysed the behaviour of reinforced concrete wide beams subjected to shear with prefabricated truss stirrups proposed by Ferreira et al. [22] and supplementary reinforcement tested by Tapajós [13]. In addition to the experimental investigation, the ultimate strengths of the tested specimens were also compared with the strength estimates following the recommendations of NBR 6118 [23], Eurocode 2 [24], and ACI 318 [25].

Concerning the use of the supplementary reinforcement, it was found that the shear reinforcement has a better performance when this supplementary reinforcement is used on both faces of the beam, instead of just adopting it on the tensile face. Regarding the inclination of the transverse reinforcement, specimens that had an inclination of 60° showed greater strength when compared with similar specimens with an inclination of 90°. Regarding the spacing between shear reinforcement layers, the strengths were higher for beams with less spacing and a lower area of reinforcement per layer than for the specimens with a greater area of reinforcement per layer and greater spacing, even though they had approximately the same transverse reinforcement ratio.

When comparing theoretical and experimental results, results against safety were observed for all recommendations, with a greater amount for Model II of NBR 6118 [23] and Eurocode 2 [24]. This behaviour was in line with what was observed by Tapajós [13], who points out a trend towards more unsafe results with a higher transverse reinforcement ratio when adopting the prefabricated truss stirrups as shear reinforcement.

Concerning the design of beams with prefabricated truss stirrups, with transverse reinforcement ratio approximately equal to 0.40%, Model I of NBR 6118 [23] and ACI 318 [25] are more recommended, if the supplementary reinforcement is used on the tensile and compression faces of the beam, with no results against safety in these arrangements. It is worth mentioning that these recommendations are specific and were obtained based on this study, so for broader conclusions and conditions, it is necessary to carry out further experimental research to observe the performance.

6. ACKNOWLEDGMENTS

The authors would like to thank CAPES, CNPq, NUMEA, LEC CAMTUC/UFPA, and NDAE/UFPA for their support in the development of this research.

7. REFERENCES

[1] Y. Yoon, W. D. Cook, and D. Mitchell, "Minimum shear reinforcement in normal, medium, and high-strength concrete beams," *ACI Struct. J.*, vol. 93, no. 5, pp. 576–584, 1996.

[2] G. Russo and M. Pauletta, "Seismic behavior of exterior beam-column connections with plain bars and effects of upgrade," *ACI Struct. J.*, vol. 109, no. 2, pp. 225–233, 2012.

[3] B. Bresler and A. C. Scordelis, "Shear strength of reinforced concrete beams," *ACI Struct. J.*, vol. 60, no. 1, pp. 51–74, 1963.

[4] K. N. Rahal and K. S. Al-Shaleh, "Minimum transverse reinforcement in 65 MPa concrete beams," *ACI Struct. J.*, vol. 101, no. 6, pp. 872–878, 2004.

[5] C. Cucchiara, M. Fosseti, and M. Papia, "Minimum transverse reinforcement in 65 MPa concrete beams," *Struct. Eng. Mech.*, vol. 42, pp. 551–570, 2012.

[6] N. Spinella, P. Colajanni, and A. Recupero, "A simple plastic model for shear critical sfrc beams," *J. Struct. Eng.*, vol. 136, no. 4, pp. 390–400, 2010.

[7] P. Colajanni, A. Recupero, and N. Spinella, "Generalization of shear truss model to the case of SFRC beams with stirrups," *Comput. Concr.*, vol. 9, no. 3, pp. 227–244, 2012.

[8] N. Spinella, P. Colajanni, and L. La Mendola, "Nonlinear analysis of beams reinforced in shear with stirrups and steel," *ACI Struct. J.*, vol. 109, no. 1, pp. 53–64, 2012.

[9] G. Russo, D. Mitri, and M. Pauletta, "Shear strength design formula for RC beams with stirrups," *Eng. Struct.*, vol. 51, pp. 226–235, 2013.

[10] W. De Corte and V. Boel, "Effectiveness of spirally shaped stirrups in reinforced concrete beams," *Eng. Struct.*, vol. 52, pp. 667–675, 2013.

[11] C. G. Karayannis and C. E. Chalioris, "Shear tests of reinforced concrete beams with continuous rectangular spiral reinforcement," *Constr. Build. Mater.*, vol. 46, pp. 86–97, 2013.

[12] A. S. Lubell, E. C. Bentz, and M. P. Collins, "Shear Reinforcement Spacing in Wide Members," *ACI Struct. J.*, vol. 106, no. 2, pp. 205–214, 2009.

[13] L. S. Tapajós, "Cisalhamento em elementos de concreto armado com estribos desconectados," Dissertação de Mestrado, Instituto de Tecnologia, Universidade Federal do Pará, Belém, 2017, 98p.

[14] P. E. Regan, "Shear Reinforcement of Flat Slabs. International Workshop on Punching Shear Capacity of RC Slabs – Proceedings," *TRITA-BKN Bulletin*, vol. 57, pp. 99–107, 2000.

[15] R. Beutel and J. Hegger, "The Effect of Anchorage on the Effectiveness of the Shear Reinforcement in the Punching Zone," *Cement Concr. Compos.*, vol. 24, pp. 539–549, 2002.

[16] T. Yamada, A. Nanni, and K. Endo, "Punching Shear Resistance of Flat Slabs: Influence of Reinforcement Type and Ratio," *ACI Struct. J.*, vol. 88, no. 4, pp. 555–563, 1992.

[17] R. B. Gomes and M. A. S. Andrade, "Does a punching shear reinforcement need to embrace a flexural reinforcement of a RC flat slab?," in *Proc. Int. Workshop on Punching Shear Capacity of RC Slabs*, Jun. 2000, pp. 109-117.

[18] P. E. Regan and F. Samadian, "Shear Reinforcement against Punching in Reinforced Concrete Flat Slabs," *Struct. Eng.*, vol. 79, no. 10, pp. 24–31, 2001.

[19] H. Park, K. Ahn, K. Choi, and L. Chung, "Lattice Shear Reinforcement for Slab-Column Connections," *ACI Struct. J.*, vol. 104, no. 3, pp. 294–303, 2007.

[20] L. M. Trautwein, T. N. Bittencourt, R. B. Gomes and J. C. D. Bella, "Punching Strength of Flat Slabs with Unbraced Shear Reinforcement," *ACI Struct. J.*, vol. 108, no. 2, pp. 197–205, 2011.

[21] A. P. Caldentey, P. P. Lavaselli, H. C. Peiretti, and F. A. Fernández, "Influence of Stirrup Detailing on Punching Shear Strength of Flat Slabs," *Eng. Struct.*, vol. 49, pp. 855–865, 2013.

[22] M. P. Ferreira, R. N. M. Barros, M. J. M. Pereira Filho, L. S. Tapajós and F. S. Quaresma, "One-Way Shear Resistance of RC Members with Unconnected Stirrups," *Lat. Am. J. Solids Struct.*, vol. 13, pp. 2670–2690, 2016.

[23] Associacao Brasileira de Normas Tecnicas, *Projeto de Estruturas de Concreto – Procedimento*, NBR 6118, 2014.

[24] European Committee for Standardization, *Eurocode 2: Design of Concrete Structures—Part 1-1: General Rules and Rules for Buildings,* EN 1992-1-1, 2004.

[25] American Concrete Institute, *Building Code Requirements for Structural Concrete*, ACI 318, 2014.

[26] J. Fisker and L. G. Hagsten, "Mechanical Model for the Shear Capacity of R/C Beams without Stirrups: A proposal Based on Limit Analysis," *Eng. Struct.*, vol. 115, pp. 220–231, 2016.

[27] Associacao Brasileira de Normas Tecnicas. *Concreto – Ensaio de compressão de corpos-de-prova cilíndricos*, NBR 5739, 2007.

[28] Associacao Brasileira de Normas Tecnicas. *Materiais metálicos – Ensaio de tração à temperatura ambiente*, NBR 6892, 2013.

[29] G. S. S. Melo, A. E. G. Coelho, and D. R. C. Oliveira, "RC flat slabs with inclined stirrups as shear reinforcement," in *Proc. Int. Workshop on Punching Shear Capacity of RC Slabs*, Jun. 2000, pp. 155-162.

Author contributions: RSP and LST: conceptualization, formal analysis, writing-original draft; writing-review & editing; VCS: data curation, investigation; MPF and AFLN: conceptualization, funding acquisition, project administration, resources, supervision, writing-original draft, writing-review & editing.

Editors: Samir Maghous, Guilherme Aris Parsekian.

IBRACON Structures and Materials Journal
Revista IBRACON de Estruturas e Materiais
ISSN 1983-4195 ismj.org

ORIGINAL ARTICLE

Use of recycled aggregates from civil construction in self-compacting mortar

Uso de agregados reciclados da construção civil na argamassa autoadensável

Fernanda Rodrigues Santos Valle[a]
Paulo Cesar Gonçalves[a]
Maria Gabriela A. Ranieri[b]
Mirian de Lourdes Noronha Motta Melo[c]
Valquíria Claret dos Santos[a]

[a]Universidade Federal de Itajubá – UNIFEI, Instituto de Recursos Naturais – IRN, Itajubá, MG, Brasil
[b]Universidade Federal de Itajubá – UNIFEI, Instituto de Engenharia de Produção e Gestão – IEPG, Itajubá, MG, Brasil
[c]Universidade Federal de Itajubá – UNIFEI, Instituto de Engenharia Mecânica – IEM, Itajubá, MG, Brasil

Received 02 December 2020
Accepted 26 May 2021

Abstract: The utilization of wastes from demolition in civil construction in self compacting concrete (SCM) has the potential to reduce both the environmental impact and financial cost. In this context, this article aims to verify the behavior of the incorporation of recycled aggregates of civil construction in the mix designs of self-compacting mortar (SCM) in replacing cement, presenting as an interesting alternative to natural raw materials. This study used the EMMA® software to optimize the choice of percentages of fine recycled aggregates when replacing cement. The proportions chosen were 0%, 5%, 15%, and 25%, through the analysis of the granular packing curve of the respective mix designs. The proportion of 0% has in its composition cement, metakaolin, sand, superplasticizer (SP) and water. The parameters obtained, through tests in the fresh state of the mini-slump and mini-funnel V, certified the samples as SCM. The compressive strength and flexural tensile strength tests in the hardened state demonstrated a reduction in mechanical properties of the material with cement replacement. It is concluded that the waste used brick and ceramic can be added in replacement to the cement in SCM without significant loss of properties in the fresh and hardened state.

Keywords: self-compacting mortar (SCM), ceramic waste, construction waste, metakaolin, granular packing.

Resumo: A utilização de resíduos de demolição da construção civil em concreto autoadensável (CAA) tem o potencial de reduzir o impacto ambiental e o custo financeiro. Nesse contexto, este artigo tem como objetivo verificar o comportamento da incorporação de agregados reciclados da construção civil nos traços de argamassas autoadensáveis (AAA) em substituição ao cimento, apresentando-se como uma alternativa interessante às matérias-primas naturais. Este estudo usou o *software* EMMA® para otimizar a escolha das porcentagens de agregados reciclados finos ao substituir o cimento. As proporções escolhidas foram 0%, 5%, 15% e 25%, através da análise da curva de empacotamento de partículas dos respectivos traços. A proporção de 0% tem em sua composição cimento, metacaulim, areia, superplastificante (SP) e água. Os parâmetros obtidos, por meio de testes no estado fresco do *mini-slump* e mini-funil V, certificaram as amostras como AAA. Os ensaios de resistência à compressão e a tração na flexão no estado endurecido demonstraram redução nas propriedades mecânicas do material com a substituição do cimento. Conclui-se que os resíduos usados de tijolo e cerâmica podem ser adicionados em substituição ao cimento na AAA sem perda significativas de propriedades no estado fresco e endurecido.

Palavras-chave: argamassa autoadensável (AAA), resíduo cerâmico, resíduo de construção, metacaulim, empacotamento de partículas.

How to cite: F. R. S. Valle, P. C. Gonçalves, M. G. A. Ranieri, M. L. N. M. Melo, and V. C. Santos, "Use of recycled aggregates from civil construction in self-compacting mortar," *Rev. IBRACON Estrut. Mater.*, vol. 15, no. 1, e15107, 2022, https://doi.org/10.1590/S1983-41952022000100007

Corresponding author: Valquíria Claret dos Santos. E-mail: valquiria@unifei.edu.br
Financial support: None.
Conflict of interest: Nothing to declare.

1 INTRODUCTION

Self-compacting concrete (SCC) is a concrete that is able to flow and compact in several forms by simply using its weight and without the need for vibration equipment [1]. In rheological terms, SCC has a significant variation in plastic viscosity that interfere in obtaining concrete with adequate fluidity and stability. Due to this parameter combination, the SCC has several advantages, such as fluidity and filling capacity [2].

In studies of Silva et al. [3], the percentage replacement of cement in SCC by masonry wastes was carried out, which caused decreased strength in the samples in relation to the reference mix design. It was observed in the results that for replacement level greater than 40%, the mechanical strength reduced, in the order of 50% in the tensile and compression strengths. However, this fact did not prevent its use because it is possible to find another purpose that is not necessarily structural for the concrete. Besides that, this replacement brings positive impacts to the environment, as raw material consumption and solid waste generated in construction and demolition are high.

One of the methods of self-compacting concrete mixes is to study the properties of self-compacting mortars (SCM). At the same time, determining the rheological characteristics of self-compacting mortars is more accurate, less labor intensive and lower costs. Therefore, the influence of modifying additives on the properties of self-compacting concrete was studied in its mortar phase. Mortar serves as the basis for the workability properties of self-compacting concrete (SCC) and these properties can be evaluated with self-compacting mortars (SCM). In fact, evaluating SCM properties is an integral part of the SCC project

The SCC is characterized by the use of a greater amount of fines and cement. In this context, this work aims to use the fines from wastes from demolition in civil construction and, at the same time, reduce the amount of cement, promoting environmental impact and cost reduction. The objective of this study is to prove the feasibility of replacing the percentage of cement in the SCC with wastes from demolition in civil construction. The brick and ceramic wastes used were ground to obtain a finer granulometry in search of better results.

2 THEORETICAL FOUNDATION

2.1 Solid construction and demolition wastes as recycled aggregates

Civil construction is one of the most active sectors of the country's economy, with around 15% of Brazilian Gross domestic product [4], representing one of the most important in the country's production. However, the consumption of raw materials and energy demanded by this sector implies a great environmental impact, being the one that generates the most solid waste. In recent decades, construction and demolition waste has attracted the attention of many researchers in all parts of the world. Only in the European community, around 3000 million tons of waste are produced annually [5]. This fact, added to the increasing difficulty in obtaining raw material for the production of concrete due to environmental and social issues, has led to the search for viable alternatives. An important alternative in the civil construction scenario is the reuse of solid waste generated by construction and demolition, whether for use as coarse aggregates to be incorporated the concrete, as fine aggregates in the production of mortars. Many challenges still need to be overcome in the proper use of recycled aggregates from civil construction, still requiring many research to consolidate this alternative.

Bravo et al. [5] researched about the durability of concrete with incorporation of recycled aggregates for construction and demolition. The incorporation of recycled aggregates demands a higher w/c ratio, in comparison with mixture that use natural aggregates, to ensure adequate workability, resulting in more porous cementitious matrices and, consequently, the entry of external agents that reduce the durability of the concrete. Another important analysis showed that carbonation resistance was the most affected with the insertion of recycled aggregates. As a result of greater porosity, the carbonation depth in concrete with coarse recycled aggregates was on the order of 22% higher than concrete with natural aggregate and, when replacing 100% of fine recycled aggregates, the increase was above 110%. It is noteworthy, however, maintaining the same compressive strength in mixture that use recycled aggregate leads to less workability, requiring the use of superplasticizers [6].

Another property of concrete affected by the insertion of construction and demolition aggregates is the reduction of the elasticity modulus, resulting in greater retraction. Butler et al. [7] analyzed the effects of the insertion of recycled aggregates from various sources on the mechanical properties of concrete and observed that maintaining the same compressive strength, equivalent to the concrete mixed with natural aggregate, the values of elasticity modulus showed a reduction of up to 19%.

Regarding mortar produced with insertion of recycled aggregates, Chen et al. [8], presented the study about the incorporation of fine recycled aggregates to replace natural sand in the mortars mixed. The authors used waste from construction rubbles after a recycling process, which basically consisted of brick and structural concrete waste. The results showed that with addition of fine recycled aggregates the strength of the mortar was reduced and its proportion of substitution governs the percentage of resistance reduction than the w/c ratio. This is totally different from the behavior of the recycled coarse aggregate used in concrete. The use of recycled sand in the mixes composition has been studied recently. As result of crushing leftover fresh structural concrete produced in a concrete dosing plant, the use of recycled sand to replace natural sand has attracted attention. It is common for quantities of concrete ordered in dosing plants to exceed the volume required necessary in the constructions resulting in leftovers of fresh concrete and these leftovers are discarded. A solution to treat the excess concrete is to promote its return to the dosing plant for the curing process for a few days and then crush it resulting in coarse and fine recycled aggregates.

Dapena et al. [9], presented studies on the substitution of recycled sand in the production of mortars, from different substitution proportions and the w/c ratio. The results obtained in mortars with insertion of up to 20% recycled sand caused a reduction of compression and flexural strengths. For higher replacement rates, the authors identified the flexural strengths values were similar to those obtained with 20% recycled sand, when 4% superplasticizer was used in the mixture. Another recycled material from construction and demolition that may have potential in the use of concrete and mortar production is ceramic brick waste. The powder obtained from crushing clay bricks can promote a more compact mixture and, consequently, improve the structure of the mortar and reduce the size and number of pores, resulting in a stronger and denser hardened paste [10]. In other words, the finer the particle size of the recycled brick waste, the denser the microstructure of the paste matrix and the greater the compressive strength of the pastes.

2.2 Self-compacting concrete and Sustainability

According to Gomes and Barros [11], self-compacting concrete (SCC) was developed in the 1980s, in Japan, by Professor Hajime Okamura, due to the need for savings and less execution time. Currently, SCC has multiple advantages, in addition to shorter execution times, labor savings, and durability.

Despite a relatively new practice, an interesting point in self-compacting concrete (SCC) technology has grown in recent years among builders and in the construction industry in several countries [12]. This interest is due to the several advantages provided by the use of self-compacting concrete, as, for example, according to Gomes and Barros [11], SCC is easy to use in concrete parts with a high reinforcement rate, that is, difficult to access. Besides reducing labor effort during the concreting phase, which shortens the construction period. And mainly, considering a healthy work environment and environment preservation, this technology results in a considerable reduction in the levels of acoustic noise due to the non-use of vibration equipment, as well as the reduction in the use of secondary raw materials.

SCC has particular characteristics that guarantee a lower porosity index than conventional concrete due to a greater addition of fine material in the mixture, which may have greater durability and mechanical resistance [13]. Recently, several studies have been developed on CAA with the addition or substitution of fine natural aggregates with fine recycled residues, of a mineral nature or from the manufacture of products, which are usually discarded, with some examples being mentioned, such as fly ash and bark ash. rice [14], recycled rubber powder waste [15], [16], marble and granite powder [17], [18], of plastics, as polymeric waste recycled from refrigerators [19]. With respect to construction and demolition waste, there is still little work on the subject. Venkateswara Rao et al. [13], proposed the study of the durability of the CAA with the addition of fine recycled aggregates, from crushed limestone residues, replacing the natural fine aggregates. The results obtained from the CAA samples with control of the a/c ratio and incorporation of silica active showed a considerable reduction in the permeability to the chloride ion due to the lower porosity index when compared to conventional vibrated concrete samples. This reduction in porosity is directly related to the better packaging of particles within the microstructure. Omrane et al. [20] evaluated the results of the experimental analysis on the mechanical, rheological and durability properties of the CAA produced with fine aggregates and recycled coarse, from crushed concrete and with natural polozane replacing cement. The samples with 50% substitution of coarse and fine aggregates and with addition between 15% and 20% of polozane, allowed to obtain the rheological properties within the necessary limits required for self-compacting concrete.

Other researchers concluded that the incorporation of masonry wastes, with a density of 2.63 g/cm^3 and an average size of 24.08 μm, as a partial replacement for cement, affects the compressive strength, reducing it as the waste increases [3]. They concluded that this reduction may be caused by the effect of dilution and low reactivity of the waste because there is less formation of hydration products as the cement is replaced, and the waste does not have high reactivity with water, resulting in decreased strength. Regarding the increased strength between the ages of 180 and 360 days, the study indicates that it may be a consequence of the pozzolanic reaction, and in the replacements of 12.5%, 25%, and 37.5% cement, reaches concrete with performances equal to or greater than the reference.

Jerônimo et al. [21], in their studies on the incorporation of ceramic waste in SCC, concluded that the cement replacement, in 20%, 30%, and 40% contributes to reducing porosity. Regarding the compressive strength, Jerônimo et al. [21] obtained a specific result of greater strength at 7 days of curing with 20% replacement. However, the other replacements showed values lower than the base mix design at this same age. In the study by Jerônimo et al. [21], at 28 and 90 days, the strength gain in relation to the reference mix design varied, respectively, from 0% to 4% and 6 to 11%, which implies a greater pozzolanic effect over time.

Sahmaran *et.al.* (2006) evaluated the effectiveness of various mineral additives and chemical additives in the production of self-compacting mortar. In the work, they used four mineral additives (fly ash, brick powder, limestone powder, and kaolinite), three superplasticizers and two viscosity modifying additives. The results showed that fly ash and limestone powder significantly increased the workability of SCM samples. The same occurred with the use of polycarboxylate superplasticizers. The use of mineral additives reduced mechanical resistance in comparison with the reference samples [22].

Several other studies on SCM have been developed recently. The influence on the mechanical properties and durability SCM produced with proportional replacement of cement by pumice as a mineral additive [23]. Study of the effects of superplasticizer and silica fume on the fresh and mechanical properties of self-compacting mortars [24]. Lozano-Lunar et al. [25] evaluated the replacement of conventional fine aggregate (natural sand) with granite sludge as an alternative for SCM production.

A study using blast furnace slag was prepared and used as an additive for self-compacting mortar. Blast furnace slag was crushed and ground to nano particle size [26]. Mechanical properties increased and physical properties, such as total water absorption and porosity, decreased as the percentage of nano dust was increased. Still in the scope of replacing cement in the SCM mixtures, Matos et al. [27] used casting sand from calcined residues and observed that there was an increase in mechanical strength of about 14% in relation to samples containing limestone. Brick residues from construction and demolition as partial replacement of natural aggregates or after crushing, as fines for partial replacement of cement, represent an important socio-environmental alternative.

The use of crushed brick powder as a cement replacement material in SCM production was analyzed in Si-Ahmed and Kenai [28]. The results showed that in up to 15% substitution of cement with crushed brick powder, it has little influence on the rheological parameters of the self-compacting mortar and the compressive strength increased in the long term. It is important to note that studies of the behavior of SCM with incorporation of recycled fine aggregates for construction and demolition are largely scarce and there is a strong demand for research, since they constitute low-cost recycling materials and sustainable alternative to conventional aggregates in the manufacture of self-compacting mortar by reducing the consumption of raw materials.

2.3 Equating the packaging of EMMA® particles for the production of concrete

The compressible packaging model (CPM) appears as a dosing tool that allows the selection and formulation of the concrete constituents, which increases the compactness of the granular mixture and decreases the risk of segregation, as shown in Figure 1 [11]. These models are analytical models that calculate the overall packing density of a mixture based on the geometry of the combined particle groups.

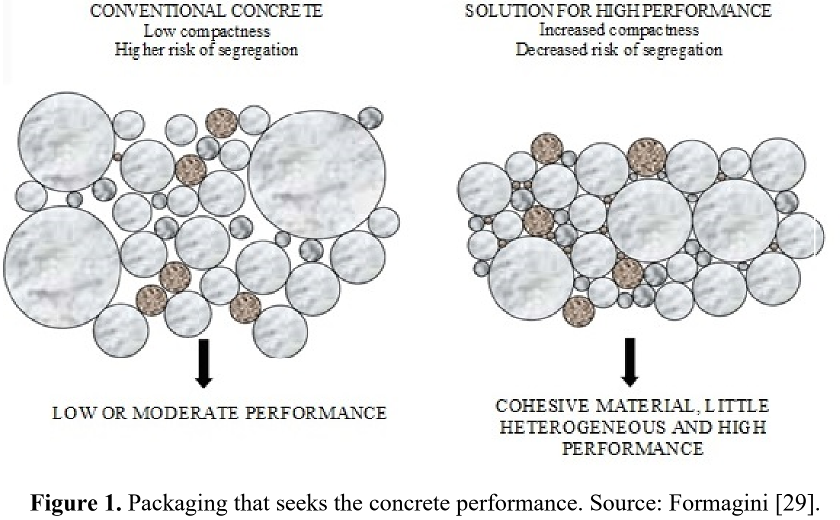

Figure 1. Packaging that seeks the concrete performance. Source: Formagini [29].

EMMA® (*Elkem Materials Mixture Analyzer*) is a software for evaluation of particle-packing, including the production of self-flowing concrete to achieve a suitable workability. Due to the limitation of conventional methods of estimating compacted unit mass for high-fine concrete, the company Elkem developed and made available this computational tool, which calculates and presents the particle size distribution of a mixture of components, in order to optimize particle packaging.

The use of the EMMA® is effective in obtaining the granular skeleton of the SCM, thus avoiding the experimental realization of several mix designs to achieve the proper characteristics of the SCC. According to Castro and Pandolfelli [30], as classics, there is the model proposed by Furnas, which considers particles individually, and the model proposed by Andreassen, which considers particles as continuous and infinitely small distributions and for this reason does not represent real situations with fidelity. Therefore, a new model was developed (Alfred Model), presenting an improvement of the previous models [30]. Alfred's model comes close to Andreassen's model when the diameter of the smallest particle in the mixture tends to zero. For this reason, Alfred's model is also known as a modified Andreassen model, and its mathematical formulation is presented in Equation 1:

$$CPFT = 100 \cdot \left(\frac{D_P^q - D_S^q}{D_L^q - D_S^q} \right) \tag{1}$$

where CPFT: percentage of particles with a diameter less than DP [%];

DP: diameter of the particle;

DS: diameter of the smallest particle;

DL: diameter of the largest particle;

q: distribution coefficient.

The model modified Andreassen, correlates a particle size distribution factor “q”, and limits the maximum and minimum particle sizes. Through computer simulations, it was found that values less than or equal to 0.37 for the distribution coefficient favor the maximum packaging of the particles, while values greater than 0.37 imply residual porosity. Also, for a mixture to have a good flow capacity, the value of the distribution coefficient must be less than 0.30 [31].

In the present work, a distribution coefficient q = 0.28 and a maximum diameter of 4800 micrometers were used, in order to optimize the amount of fines present in the SCM. The laser granulometric curves of cement, metakaolin, brick and ceramic, granulometric curves of sand and specific gravities materials were inserted in EMMA® *software*.

Other researchers also used EMMA® program to particle size distributions and achieve a suitable workability to concrete. In the study, the q-values for shotcreting and dry-gunning mixes are 0,27 and 0,22, respectively [32].

3. METHODOLOGY

3.1 Characterization of materials

CP V-ARI cement, used in this experiment, has a finer grinding of Portland clinker, thus adding a material with a favorable granulometry to obtain SCC. To simplify the waste nomenclature in this research, the ground brick waste was called RT (Brick Waste) and the ceramic waste was RP (Ceramic Waste).

In this case, the specific gravity, specific surface, and laser granulometry of the cement were evaluated according to current regulations. Granulometry, specific gravity, unit mass, and water absorption tests were also carried out for the sand, according to current regulations.

The additive used in the SCC is a polycarboxylate superplasticizer.

It was decided to add metakaolin to increase the percentage of fines, improving the mixture cohesion. The tests performed were specific gravity and laser granulometry. The high specific surface area improves rheological aspects by optimizing the granulometric distribution of the paste, contributing to water retention, increased cohesion, reduced exudation, and segregation [33].

The superplasticizer was also used to avoid excessive water consumption.

Finally, as the main objective is the analysis of the percentage replacement of cement by ceramic materials, it was necessary to carry out specific gravity tests for powder materials and granulometry by laser granulometer (Model MasterSizer Micro, Measuring range: 0,3 a 300 μm.), in this case the powder materials are cement, metakaolin, brick and ceramic.

3.2 Dosing and mixing method

To perform SCM, the concept of paste by the method of Gomes and Barros [11] was used, in which a w/c ratio is chosen according to the strength expected to be achieved for the concrete, and a proportion of SP and the amount of fines according to the amount of cement used.

The method of Gomes and Barros [11] has as principle the optimization of the paste and the granular skeleton separately, and the model suggests that the viscosity and fluidity of the paste lead to the concrete flow behavior. According to Gomes and Barros [11], the model is developed in three stages, obtaining the composition of the paste, determining the proportion of the mixture of the aggregates and selecting the paste contents.

According to Gomes and Barros [11], the composition of the paste is defined by the amount of cement and the relationships of the other components of the paste as a function of the cement mass. The paste volume is obtained by Equation 2:

$$V_P = \frac{C}{\rho_c} + \frac{P_a}{\rho_a} + \frac{P_{cs}}{\rho_{cs}} + \frac{P_{mtc}}{\rho_{mtc}} + \frac{P_{spl}}{\rho_{sp}} - \frac{P_{asp}}{\rho_a} \quad (2)$$

Where: C: cement mass [g];
ρc: specific gravity of cement [g/cm^3];
Pa = (w/c) · C: water mass [g];
ρa: specific gravity of water [g/cm^3];
Pcs = (cs/c) · C: mass of silicon carbide [g];
ρcs: specific gravity of silicon carbide [g/cm^3];
Pmtc = (mtc/c) · C: metakaolin mass [g];
ρmtc: specific gravity of metakaolin [g/cm^3];
Pspl = [(sp/c) · C] ÷ [Tsp / 100]: mass of liquid superplasticizer [g];
Tsp: solid content of the superplasticizer;
ρsp: specific gravity of the superplasticizer [g/cm^3];
Pasp = [(sp/c) · C]·[(100 / Tsp) - 1]: mass of water contained in the superplasticizer [g].

Then, the composition of the granular skeleton must be defined. Granular skeleton means the association of large and small aggregates that make up the concrete structure. As an adaptation and simplification of the method by Gomes and Barros [11], the coarse aggregates were disregarded of the dosing procedures so that it was possible to produce SCM. Also, according to the author, the volume of fine aggregates in relation to the total mortar volume should preferably be not less than 40% and not more than 50%.

After defining the w/c and SP/c ratios according to the desired fluidity and viscosity properties, the cement mass is calculated for the volume of one cubic meter of mortar, according to Equation 3 [11].

$$C = \frac{V_P}{\frac{1}{\rho_C} + \frac{(a/c)}{\rho_a} + \frac{(cs/c)}{\rho_{cs}} + \frac{(mtc/c)}{\rho_{mic}} + \frac{(sp/c)\cdot\left(\frac{100}{T_{sp}}\right)}{\rho_{sp}} - \frac{(sp/c)\cdot\left[\left(\frac{100}{T_{sP}}\right)-1\right]}{\rho_a}} \quad (3)$$

Where VP is the volume of the paste previously determined.

The mixing process was carried out as proposed [34]. The materials used and the mixing process are shown in Table 1. The mixer used is in accordance with [34].

Table 1. SCM mixing process developed in this article

	Addition
1 minute	Cement, metakaolin, sand, and ground brick (or ceramic)
1 minute	80% of the total volume of water
5 minutes	20% of the total volume of water + superplasticizer
2 minutes	Rest in mortar
1 minute	Mix again in the mortar

3.3 Mortar properties

3.3.1 Properties in the hardened state

According to the standards [35] and [36], the axial compressive strength and flexural tensile strength tests were performed. Four cylindrical specimens (CP) were molded, 5 cm in diameter, and 10 cm high for the compressive test, and 3 prismatic CPs, 4 cm wide, 4 cm high, and 16 cm long for the flexural.

The flexural tensile test is subjected to a force until rupture according to Equation 4:

$$Rf = \left(\frac{1,5 * Ft * L}{40^3} \right) \tag{4}$$

Where:

Rf: flexural tensile strength [MPa];

Ft: load applied at the center of the CP [N];

L = 100 mm: distance between supports [mm].

To reduce the volume of mixing water, the ADITIBRAS® ADI-SUPER H25 superplasticizer was used, which, according to the manufacturer, had a solids content of 25%. In the Flowchart shown in Figure 2, the characterization path after the mixing of the materials is observed, both in the pasty and in the hardened state.

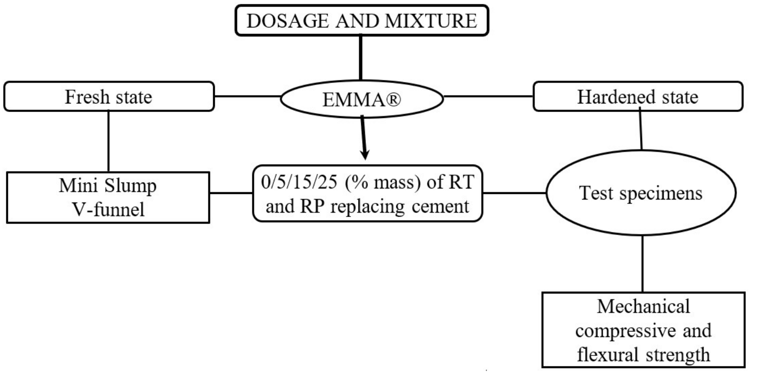

Figure 2. Flowchart on how the dosing and mixing process was carried out, both fresh and hardened.

4 EXPERIMENTAL RESULTS AND DISCUSSION

The results of the characterization tests for cement, metakaolin, sand, RT, and RP can be seen in Table 2.

Table 2. Characterization of the materials.

Material	Specific gravity (g/cm^3)	Unit Mass (g/cm^3)	Absorption (%)	Specific Surface (cm^2/g)	d50 (µm)	dmax (µm)
Cement	3.10	-	-	6.35	15.44	-
Metakaolin	2.56	-	-	-	12.40	113.20
Sand	2.57	1.45	0.37	-	983.09	-
RT	2.67	-	-	-	150.84	-
RP	2.55	-	-	-	272.45	-

Figure 3 shows the granulometric curves of the materials (cement, metakaolin, flooring (ceramic), brick, and sand) used in the mix design.

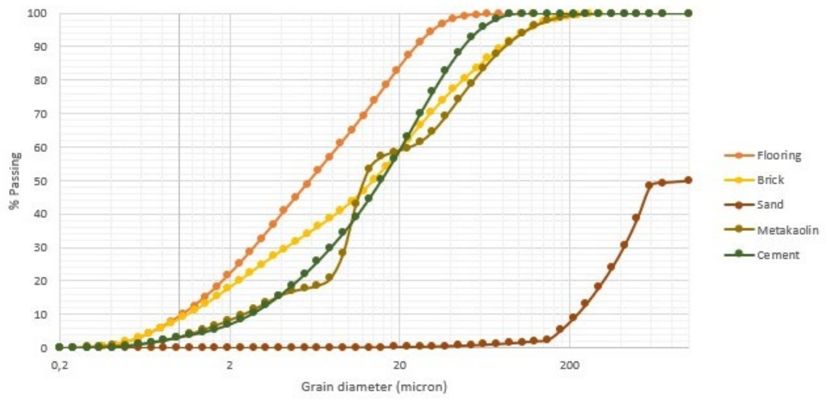

Figure 3. Granulometric curve of the materials used in the mix design.

After inserting the granulometric curves and specific gravities, the mean granulometry D50 of the materials is obtained using the EMMA®, as shown in Table 2. The EMMA® software calculates and displays the particle size distribution of a concrete mix.

Some simulations within EMMA® were carried out for the concrete mix, varying the percentages of the materials. The *software* generates two curves: the mix composition (blue) and the ideal one (red). It is understood that the more coincident the curves are, the greater the level of packaging of the particles and, therefore, the greater the compactness and the lower the porosity of the mixture. The base mix design (TB) curves, Figure 4 (a), and the percentages of 5%, 15%, and 25% replacement of cement by ground brick in Figure 4 (b), (c) and (d) were presented, respectively. These curves demonstrate the best packaging of the particles for the dry components, according to the granulometry, proportion and density of the materials

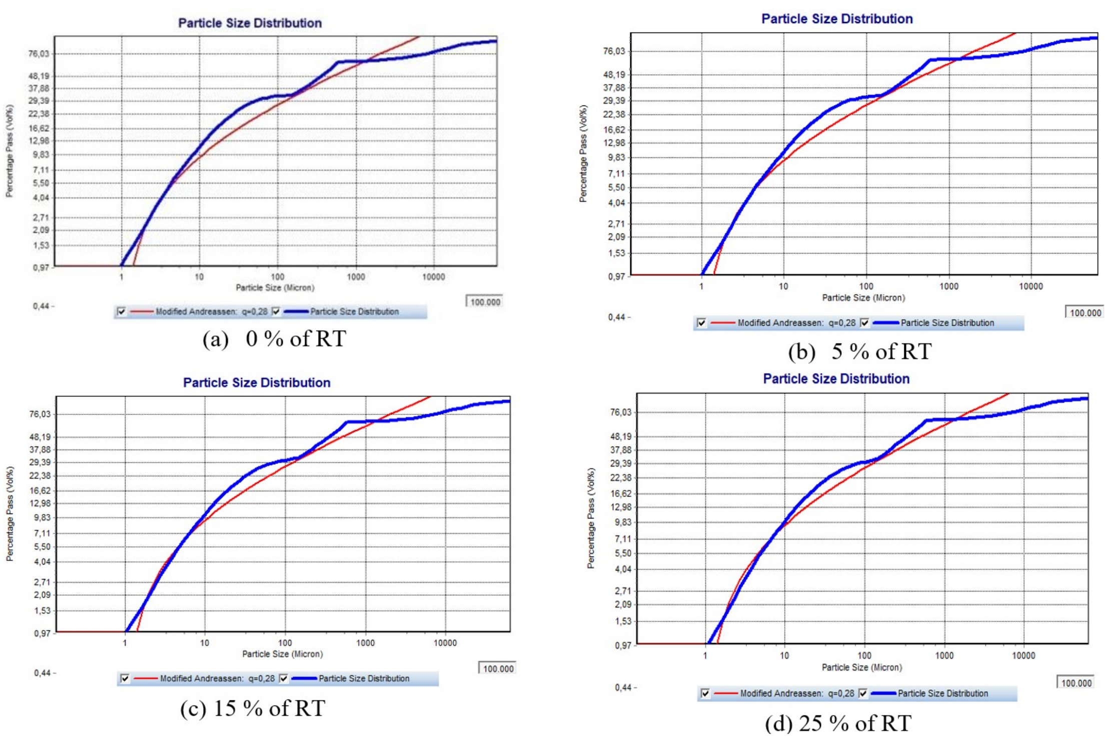

(a) 0 % of RT
(b) 5 % of RT
(c) 15 % of RT
(d) 25 % of RT

Figure 4. Packing curves of the particles obtained by the EMMA® software.

As with ground brick, percentage replacements of cement for ceramic waste of 5% to 30% were used, and also, after the analysis, replacements of 5%, 15%, and 25% were chosen, as seen in Figure 5 (a), (b), and (c).

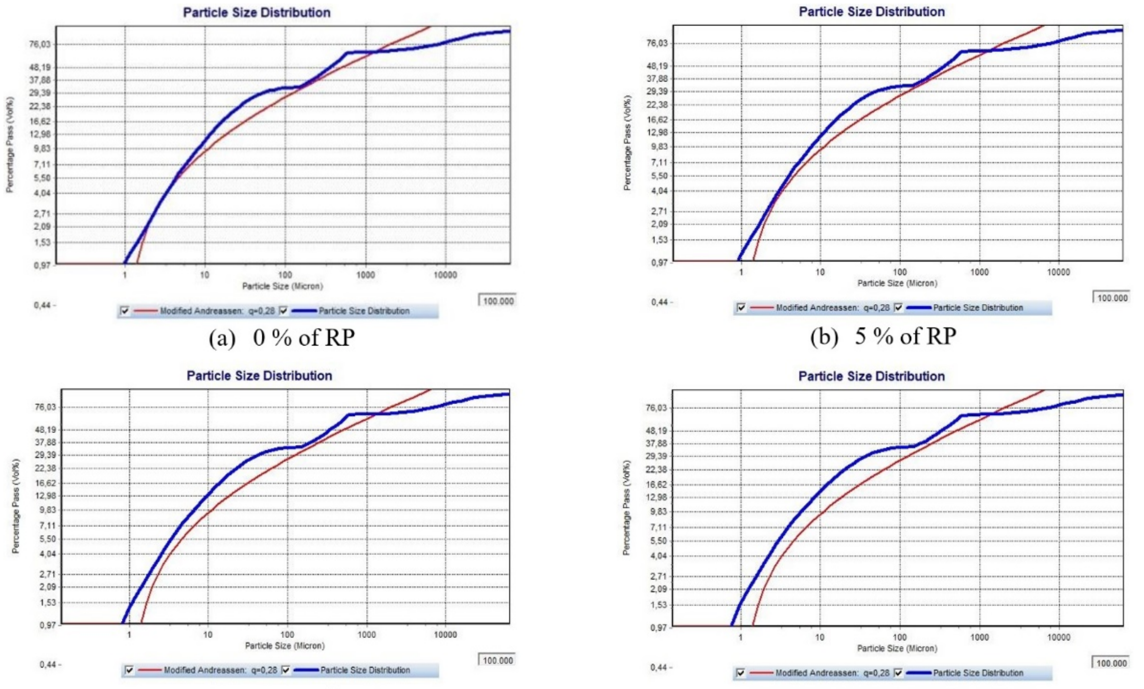

(a) 0 % of RP (b) 5 % of RP (c) 15 % of RP (d) 25 % of RP

Figure 5. Packing curves of the particles obtained by the EMMA® software.

The percentage replacements of cement for the waste of 5% to 30% were studied, and the best replacements were of 5%, 15%, 25% of cement for both waste. Looking at Figures 4 and 5, it is possible to observe that, although there is an approximation with the optimal curve (Modified Andreassen) in the range of 10 to 100 µm, there is a gap in the ranges of 100 to 325 µm and 1 to 10 µm. In the graphs of Figure 4 - RT (Brick Waste) is observed for particles size from 10 to 100 µm, the passing percentage is very close to the red curve in the average of 2.7% and 1.05% respectively for any percentage studied. Making the same analysis for Figure 5 - RP (Ceramic Waste) the difference is in the order of 5.7% and 8.22% respectively. It is also observed that the shapes of the curves are similar for both materials and the different proportions. This similarity may indicate that the percentages used were small to be observed by this method. EMMA® was also used to obtain the base trace, thus decreasing the number of experimental tests to find the optimal trace. The same analysis was carried out for the base trace for the particles size from 10 to 100 µm, the percentage and the difference of passing percentage between the red and blue curves were 2.7% and 5.67% respectively.

4.1 Dosing and Mixing

The base mix design and mix designs with the addition of brick (RT) and ceramic (RP) are shown in Table 3.

Table 3. Mix designs in % of SCC with the addition of RT and RP.

Mix design (%)	Cement	Metakaolin	RT	RP	Sand	SP	w/c
0	1	5	0	0	2	0.80	0.40
5	1	5	5	5	2	0.80	0.40
15	1	5	15	15	2	0.80	0.40
25	1	5	25	25	2	0.80	0.40

The mix design, Table 4, and the percentages of 0%, 5%, 15%, and 25% replacement of cement by RT e RP were presented, respectively. After preparing the SCM, tests were carried out in the fresh test to measure the fluidity and viscosity and compare them with the characteristic range of a self-compacting mortar. The results can be seen in Table 4.

Table 4. Results of fresh experiments with the addition of ground brick (RT) and ceramic waste (RP).

Mix designs fi(%)	Mini-slump (mm) SCM range 200 – 280 mm		V-funnel (s) SCM range 5 – 10 s	
	RT	RP	RT	RP
0	275	275	7.72	7.72
5	255	270	7.7	5.65
15	275	280	5.63	5
25	280	280	5.52	5.16

It is concluded that all mortars are SCM since they are within the limits established by Gomes and Barros [11], both concerning the mean diameter and the flow time. There is also a decreasing result in the v-funnel test, characterizing an increase in the capacity to fill shapes and containers. It is also possible to notice an increasing result in the mini-slump test, which characterizes an increase in fluidity. The results of v-funnel and mini-slump test for RT and RP substitutions did not change significantly between themselves. The percentages of 15% and 25% were more fluid than those of 0% and 5%, that is, the more RT and RP material the more fluid is the mortar.

Figure 6 shows the result of the mini-slump test, and it is not possible to observe the phenomenon of exudation, defined as a phenomenon that results in the appearance of water on the concrete surface after it is released and densified and before the setting occurs. This phenomenon can occur due to several factors, such as for example, the increase in the water/cement ratio or the presence of pozzolanic material.

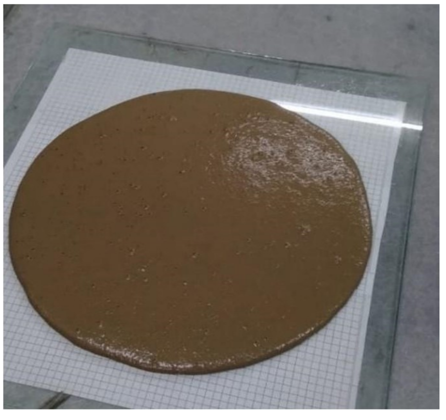

Figure 6. Mini Slump experiment.

Table 5 presents the results of the tests of compressive strength and flexural tensile strength using the two types of waste (RP and RT).

Table 5. Mean of the test results of mechanical compressive strength and flexural strength in MPa.

Mix design (%)	Compressive Strength (MPa)		Flexural Strength (MPa)	
	RT	RP	RT	RP
0	44.95	44.95	8.74	8.74
5	40.68	30.5	7.58	7.16
15	37.35	27.74	8.12	7.13
25	43.8	40.47	8.66	7.15

It is observed in the results of both tests in the hardened state that the 25% replacement of cement by ground brick does not bring significant changes in the strength values of the mortars. Concerning the base mix design, a decrease of 2.56% in the compressive strength and 0.91% in the flexural tensile is noted.

The strength results in all tested ceramic waste replacements caused lower compressive and tensile values than the base mix design. The greatest decrease in compressive strength is a mix design with 5% replacement, 38.29% in relation to the base. Comparing the flexural tensile strengths, there is the greatest decrease in the mix design with 15% replacement, with an 18.42% change. Like this work [3], a reduction in strength was also found with the partial replacement of cement by brick waste with a mean particle size of 24.08 μm smaller than that used in this work. The d50 or average diameter of RT and RP are 150.84 μm and 272.45 μm, respectively, the Figure 4 and 5 showed that mixtures containing RT had better results, in other words, the mixture curve (blue) approaches the optimal curve generated by EMMA®.

Regarding the results of compressive strength for initial high-strength cement, the standard [37] provides for a minimum limit of 34 MPa. In this case, the 5% and 15% with RP replaced mix designs do not have satisfactory strength results, with means of 30.50 MPa and 27.74 MPa, respectively, both below the standard. All percentages containing RT are satisfactory for the results of compressive strength.

This difference in compressive strength and flexural strength observed in both the brick and ceramic waste has also been observed in other publications. Other researchers have studied the percentage replacement of Portland CPII cement by ground ceramic block waste, in 10%, 20%, 30%, 40%, and 50%, and concluded that there is a decrease in the compressive strength with the increase in the waste. However, it was realized that this difference between the strengths decreases after the age of 56 days; that is, more days of curing favor the increase of strength [38]. However, despite this decrease in difference in relation to the base in older ages, in the study of [38], there was no mix design that exceeded the values obtained by the base mix design; and the 50% replacement, regardless of age, only resulted in decreased strength.

5 CONCLUSION

The objective of this study was to prove the viability of the replacement of cement in SCM by ceramic waste and brick waste. For this research, the self-compacting concrete dosing method (SCC) was carried out, which is known to be sound based on the lowest void ratio as an ideal packaging proposal. For this, it used the EMMA® software (Elkem Materials Mix Analyzer), which calculates and presents the best granulometric distribution of a concrete mixture. And so, some simulations using EMMA® were performed in order to obtain a material with better physical and mechanical performance. Incorporations of RT and RP were performed to replace cement of 0, 5, 15 and 25% by weight. In the fresh state, all incorporated mix designs of construction waste have self-compacting characteristics. The increase in the percentages of the brick waste causes an increase in fluidity and slightly increasing the results of the mini-slump test up to the limit value of 280mm to 25% RT. The increase in the ceramic waste causes an increase in the filling capacity, decreasing the results of the v-funnel. The results found in the hardened state for ceramic waste mix designs with 5% and 15% replacement, do not have a satisfactory result of compressive strength provided by the standard [37]. The incorporation of the two waste, mainly in the 25% cement replacement, does not bring significant losses to the mechanical strength and can contribute to lesser manufacture of cement and an efficient destination of the construction waste. It is concluded that the waste used brick and ceramic waste can be added in replacement to the cement in SCM without loss of properties in the fresh and hardened state.

It is suggested the leaching test to analyze the transfer capacity of organic and inorganic substances present in the waste. This is a method used to diagnose how much of this material will be transferred to the natural environment.

ACKNOWLEDGEMENTS

The authors would like to thank ADITIBRÁS for supplying the superplasticizer admixture.

REFERENCES

[1] H. Okamura and M. Ouchi, "Self-compacting concrete," *J. Adv. Concr. Technol.*, vol. 1, no. 1, pp. 5–15, 2003.

[2] A. López, J. M. Tobes, G. Giaccio, and R. Zerbino, "Advantages of mortar-based design for coloured self-compacting concrete," *Cement Concr. Compos.*, vol. 31, no. 10, pp. 754–761, 2009, http://dx.doi.org/10.1016/j.cemconcomp.2009.07.005.

[3] Y. F. Silva, D. A. Lange, and S. Delvasto, "Effect of incorporation of masonry residue on the properties of self-compacting concretes," *Constr. Build. Mater.*, vol. 196, pp. 277–283, 2019, http://dx.doi.org/10.1016/j.conbuildmat.2018.11.132.

[4] A. Nagalli, *Gerenciamento de Resíduos Sólidos na Construção Civil, no. 11.* São Paulo: Oficina de Textos, 2014.

[5] M. Bravo, J. Brito, J. Pontes, and L. Evangelista, "Durability performance of concrete with recycled aggregates from construction and demolition waste plants," *Constr. Build. Mater.*, vol. 77, pp. 357–369, Feb 2015, http://dx.doi.org/10.1016/j.conbuildmat.2014.12.103.

[6] M. Bravo, J. Brito, L. Evangelista, and J. Pacheco, "Durability and shrinkage of concrete with CDW as recycled aggregates: benefits from superplasticizer's incorporation and influence of CDW composition," *Constr. Build. Mater.*, vol. 168, pp. 818–830, 2018, http://dx.doi.org/10.1016/j.conbuildmat.2018.02.176.

[7] L. Butler, J. S. West, and S. L. Tighe, "Effect of recycled concrete coarse aggregate from multiple sources on the hardened properties of concrete with equivalent compressive strength," *Constr. Build. Mater.*, vol. 47, pp. 1292–1301, 2013, http://dx.doi.org/10.1016/j.conbuildmat.2013.05.074.

[8] H. J. Chen, T. Yen, and K. H. Chen, "Use of building rubbles as recycled aggregates," *Cement Concr. Res.*, vol. 33, no. 1, pp. 125–132, 2003, http://dx.doi.org/10.1016/S0008-8846(02)00938-9.

[9] E. Dapena, P. Alaejos, A. Lobet, and D. Pérez, "Effect of recycled sand content on characteristics of mortars and concretes," *J. Mater. Civ. Eng.*, vol. 23, no. 4, pp. 414–422, 2011, http://dx.doi.org/10.1061/(ASCE)MT.1943-5533.0000183.

[10] L. Zhu and Z. Zhu, "Reuse of clay brick waste in mortar and concrete," *Adv. Mater. Sci. Eng.*, vol. 2020, pp. 1–11, 2020, http://dx.doi.org/10.1155/2020/6326178.

[11] P. C. Gomes and A. Barros, *Métodos de Dosagem de Concreto Autoadensável*. São Paulo: PINI, 2009.

[12] S. Nunes, H. Figueiras, P. Milheiro Oliveira, J. S. Coutinho, and J. Figueiras, "A methodology to assess robustness of SCC mixtures," *Cement Concr. Res.*, vol. 36, no. 12, pp. 2115–2122, Dec 2006, http://dx.doi.org/10.1016/j.cemconres.2006.10.003.

[13] S. Venkateswara Rao, M. V. Seshagiri Rao, D. Ramaseshu, and P. Rathish Kumar, "Durability performance of self-compacting concrete," *Mag. Concr. Res.*, vol. 64, no. 11, pp. 1005–1013, Nov 2012, http://dx.doi.org/10.1680/macr.11.00165.

[14] G. Sua-Iam and N. Makul, "Utilization of limestone powder to improve the properties of self-compacting concrete incorporating high volumes of untreated rice husk ash as fine aggregate," *Constr. Build. Mater.*, vol. 38, pp. 455–464, 2013, http://dx.doi.org/10.1016/j.conbuildmat.2012.08.016.

[15] W. H. Yung, L. C. Yung, and L. H. Hua, "A study of the durability properties of waste tire rubber applied to self-compacting concrete," *Constr. Build. Mater.*, vol. 41, pp. 665–672, 2013, http://dx.doi.org/10.1016/j.conbuildmat.2012.11.019.

[16] N. Li et al., "Properties of self-compacting concrete (SCC) with recycled tire rubber aggregate: a comprehensive study," *J. Clean. Prod.*, vol. 236, 117707, 2019, http://dx.doi.org/10.1016/j.jclepro.2019.117707.

[17] D. M. Sadek, M. M. El-Attar, and H. A. Ali, "Reusing of marble and granite powders in self-compacting concrete for sustainable development," *J. Clean. Prod.*, vol. 121, pp. 19–32, 2016, http://dx.doi.org/10.1016/j.jclepro.2016.02.044.

[18] A. Boukhelkhal, L. Azzouz, B. Benabed, and A. Belaïdi, "Strength and durability of low-impact environmental self-compacting concrete incorporating waste marble powder," *Build. Mater. Struct.*, vol. 4, pp. 31–41, 2018. http://dx.doi.org/10.5281/zenodo.1134146.

[19] L. R. R. Silva et al., "Polymeric waste from recycling refrigerators as an aggregate for self-compacting concrete," *Sustain.*, vol. 12, no. 20, pp. 8731, 2020, http://dx.doi.org/10.3390/su12208731.

[20] M. Omrane, S. Kenai, E. H. Kadri, and A. Aït-Mokhtar, "Performance and durability of self compacting concrete using recycled concrete aggregates and natural pozzolan," *J. Clean. Prod.*, vol. 165, pp. 415–430, 2017., http://dx.doi.org/10.1016/j.jclepro.2017.07.139.

[21] V. L. Jerônimo, G. R. Meira, and L. C. P. da Silva Fo., "Performance of self-compacting concretes with wastes from heavy ceramic industry against corrosion by chlorides," *Constr. Build. Mater.*, vol. 169, pp. 900–910, 2018, http://dx.doi.org/10.1016/j.conbuildmat.2018.03.034.

[22] M. Şahmaran, H. A. Christianto, and I. Ö. Yaman, "The effect of chemical admixtures and mineral additives on the properties of self-compacting mortars," *Cement Concr. Compos.*, vol. 28, no. 5, pp. 432–440, 2006, http://dx.doi.org/10.1016/j.cemconcomp.2005.12.003.

[23] M. Karataş, A. Benli, and A. Ergin, "Influence of ground pumice powder on the mechanical properties and durability of self-compacting mortars," *Constr. Build. Mater.*, vol. 150, pp. 467–479, 2017, http://dx.doi.org/10.1016/j.conbuildmat.2017.05.220.

[24] A. O. Smirnov, L. M. Dobshits, and S. N. Anisimov, "Effect of superplasticizer and silica fume on the properties of self-compacting mortars," *IOP Conf. Ser. Mater. Sci. Eng.*, vol. 896, no. 1, 2020, http://dx.doi.org/10.1088/1757-899X/896/1/012095.

[25] A. Lozano-Lunar, I. Dubchenko, S. Bashynskyi, A. Rodero, J. M. Fernández, and J. R. Jiménez, "Performance of self-compacting mortars with granite sludge as aggregate," *Constr. Build. Mater.*, vol. 251, pp. 118998, 2020, http://dx.doi.org/10.1016/j.conbuildmat.2020.118998.

[26] A. A. Atiyah, S. A. Salih, and A. S. Kadhim, "Properties of self-compacting mortar containing nano blast furnace slag," *IOP Conf. Ser. Mater. Sci. Eng.*, vol. 737, no. 1, 2020, http://dx.doi.org/10.1088/1757-899X/737/1/012054.

[27] P. R. Matos, R. Pilar, L. H. Bromerchenkel, R. A. Schankoski, P. J. P. Gleize, and J. Brito, "Self-compacting mortars produced with fine fraction of calcined waste foundry sand (WFS) as alternative filler: fresh-state, hydration and hardened-state properties," *J. Clean. Prod.*, vol. 252, pp. 119871, 2020, http://dx.doi.org/10.1016/j.jclepro.2019.119871.

[28] M. Si-Ahmed and S. Kenai, "Behavior of self-compacting mortars based on waste brick powder," *Curr. Mater. Sci.*, vol. 13, no. 1, pp. 39–44, 2020, http://dx.doi.org/10.2174/2666145413666200219091459.

[29] S. Formagini, "Dosagem científica e caracterização mecânica de concretos de altíssimo desempenho," Ph.D. dissertation, COPPE, Univ. Fed. Rio de Janeiro, Rio de Janeiro, 2005.

[30] A. L. Castro and V. C. Pandolfelli, "Revisão: conceitos de dispersão e empacotamento de partículas para a produção de concretos especiais aplicados na construção civil," *Ceramica*, vol. 55, no. 333, pp. 18–32, 2009, http://dx.doi.org/10.1590/S0366-69132009000100003.

[31] A. L. Castro, J. B. L. Liborio, and V. C. Pandolfeg, "Review article: rheology of high performance concretes applied in building site," *Ceramica*, vol. 57, no. 341, pp. 63–75, 2011, http://dx.doi.org/10.1590/s0366-69132011000100009.

[32] H. Peng and B. Myhre, "No-cement refractory shotcrete and gunning mixes," *TechTrends*, vol. 9, pp. 1–5, 2017.

[33] E. A. Medina, "Pozolanicidade do metacaulim em sistemas binários com cimento Portland e hidróxido de cálcio," M.S. thesis, Esc. Politéc., Univ. São Paulo, São Paulo, 2011.

[34] A. Tuaum, S. Shitote, and W. Oyawa, "Experimental study of self-compacting mortar incorporating recycled glass aggregate," *Buildings*, vol. 8, no. 2, pp. 15, Jan 2018, http://dx.doi.org/10.3390/buildings8020015.

[35] Associação Brasileira de Normas Técnicas, *Cimento Portland - Determinação da Resistência à Compressão,* NBR 7215, 1996, pp. 8.

[36] Associação Brasileira de Normas Técnicas, *Argamassa para Assentamento e Revestimento - Determinação da Resistência à Tração na Flexão e Compressão,* NBR 13279, 2005, pp. 3–4.

[37] Associação Brasileira de Normas Técnicas, *Cimento Portland – Requisitos,* NBR 16697, 2018, pp. 1–7.

[38] F. Carvalho et al., "Influência da substituição de cimento Portland por resíduo moído de blocos cerâmicos na resistência mecânica do concreto auto-adensável," in *An. 53 Congr. Bras. Concr., vol. 1*, pp. 1–10, 2011, http://dx.doi.org/10.13140/RG.2.1.2114.6724.

Author contributions: FRSV: conceptualization, methodological design, data collection and treatment, analysis/ interpretation; PCG: analysis/ interpretation, literature survey, critical review, others; MGAR: literature survey, critical review, others; MLNMM: literature survey, critical review, others; VCS: conceptualization, methodological design, supervision, analysis / interpretation, writing, critical review.

Editors: Fernando Pelisser, Guilherme Aris Parsekian.

IBRACON Structures and Materials Journal
Revista IBRACON de Estruturas e Materiais
ISSN 1983-4195 ismj.org

ORIGINAL ARTICLE

M-N interaction curves for rectangular concrete-filled steel tube columns subjected to uniaxial bending moments

Curvas de interação M-N para pilares mistos preenchidos de seção retangular sujeitos a flexão composta reta

Matheus Fernandes[a]
Silvana De Nardin[a]
Fernando Menezes de Almeida Filho[a]

[a]Universidade Federal de São Carlos – UFSCar, Programa de Pós-graduação em Engenharia Civil, São Carlos, SP, Brasil

Received 11 March 2021
Accepted 26 May 2021

Abstract: In this paper, a computational code was developed to obtain M-N interaction curves for rectangular concrete-filled steel tube columns considering the strain compatibility in the cross-section. Considering the composite section subjected to uniaxial bending moments, expressions were developed to determine normal force, moment resistance, neutral axis depth and components resistance of cross-section. Such expressions were implemented in a computational tool developed to the authors and that allows to obtain the M-N pairs of strength. The steel and concrete ultimate strains were defined with the aid of the Brazilian standard for reinforced concrete structures ABNT NBR 6118. The obtained results were compared to simplified curves defined according to the theoretical models of ABNT NBR 8800, ABNT NBR 16239, EN 1994-1-1 and literature data. The proposed model showed good agreement with literature results and had good precision to estimate the ultimate moment values. To further understand the resistance of composite columns under uniaxial bending moments, parametric study was performed to evaluate the influence of the compressive strength of concrete, yielding strength of steel and steel area ratio on M-N interaction curves. The results indicate that the yielding strength of steel and the steel area ratio were the variables that most influenced the values of composite columns resistance (normal force and bending moment).

Keywords: concrete-filled steel tube column, uniaxial bending moment, M-N interaction curve.

Resumo: Neste trabalho é proposto um processo computacional para obtenção de curvas de interação M-N para pilares mistos preenchidos de seção retangular, por meio da compatibilidade de deformações na seção transversal. Considerando flexão composta reta, foram desenvolvidas expressões que relacionam esforço normal, momento resistente, profundidade da linha neutra e resistência dos componentes da seção transversal. Tais expressões foram implementadas em uma ferramenta computacional que possibilita a definição dos pares resistentes M-N. As deformações específicas últimas de compressão do concreto e de tração no aço foram definidas com auxílio da norma brasileira para estruturas de concreto armado ABNT NBR 6118. Para verificação do processo elaborado, os resultados obtidos foram confrontados com curvas simplificadas traçadas de acordo com os modelos da ABNT NBR 8800, ABNT NBR 16239 e EN 1994-1-1 e com resultados da literatura. O modelo proposto apresentou boa concordância com resultados da literatura e estimou, com boa precisão, os momentos resistentes últimos. Por meio de um estudo paramétrico foi avaliada a influência da resistência à compressão do concreto, resistência ao escoamento do aço e taxa de aço nas curvas de interação M-N. Os resultados mostraram que a resistência ao escoamento do aço e a taxa de aço foram as variáveis que mais influenciaram nos valores resistentes (força normal e momento fletor).

Palavras-chave: pilar misto preenchido, flexão composta reta, curva de interação M-N.

How to cite: M. Fernandes, S. De Nardin, and F. M. Almeida Filho, "M-N interaction curves for rectangular concrete-filled steel tube columns subjected to uniaxial bending moments," *Rev. IBRACON Estrut. Mater.*, vol. 15, no. 1, e15108, 2022, https://doi.org/10.1590/S1983-41952022000100008

Corresponding author: Matheus Fernandes. E-mail: matheustkful@gmail.com
Financial support: None.
Conflict of interest: Nothing to declare.

1 INTRODUCTION

The concrete-filled steel tube columns have been widely used for construction in several countries due to their high resistant capacity, unnecessary of formwork and reinforcing bars and simplified construction process, resulting in saving and high execution speed. Such characteristics highlight this type of column in relation to both the steel and reinforced concrete columns. In this type of column, the steel tube is filled by concrete, assuming two main shapes: rectangular and circular. Both in the rectangular and circular sections there are great constructive advantages, reducing expenses related to the concreting process. From a structural point of view, the concrete-filled steel tube columns allow a better use of the concrete, due to the confinement effect provided by the steel profile. Such an effect is more significant in the circular concrete-filled steel tube columns [1].

Several numerical and experimental studies have evaluated the influence of parameters on the capacity of concrete-filled steel tube columns. Therefore, it is important to understand the structural behavior of such an element under a specific request, which allows a better use of the element. Uniaxial bending moment in concrete-filled steel tube columns has been extensively evaluated, several parameters such as the compressive strength of concrete, yielding strength of steel and eccentricities of axial force are widely evaluated in many studies. The first studies on rectangular concrete-filled steel tube columns subject to eccentric compression date from the 1960s [2], 1970s [3] e 1980s [4], [5]. Since then, many studies have investigated the influence of parameters such as eccentricity, slenderness, yielding strength of steel and compressive strength of concrete on the eccentric compression strength of the concrete-filled steel tube columns. About the eccentricities of normal force, a significant reduction in the ultimate force was observed with the increase in the eccentricity [6]–[9]. Experimental results showed that the reduction in ultimate force occurs due to the increase in flexural buckling [4], [10]; the effects of flexural buckling are even more significant when the element is subjected to uniaxial bending moment about the minor axis [4]. The increase in the compressive strength of concrete also has a direct influence on the eccentric compression strength; the greater the compressive strength of concrete the greater the resistant capacity of the column [11]–[14]. However, the use of high-strength concretes significantly reduces the ductility of the column [11], [14], while the use of concretes of strength below 50 MPa favors the ductility [15]. Like the effect caused by the variation in the compressive strength of concrete, the increase in the yielding strength of steel also increases the eccentric compression strength of the column [16]–[19]. For certain eccentricity values, regardless of the shape of the filled section, a small increase was observed in the eccentric compression strength [16]. For example, by varying the yield strength of steel from 488 to 690 MPa, increases of 27% and 30% were observed for ultimate values of force and moment, respectively [18]. The results showed that the increase in the eccentric compression strength of the rectangular concrete-filled steel tube column is more significant as there is a successive increase in the yielding strength of steel [17].

Standard codes as ABNT NBR 8800 [20], ABNT NBR 16239 [21] and EN 1994-1-1 [22] present simplified procedures for the design of composite columns under eccentric loads. Such simplifications may not accurately represent the properties of the components of composite section [23], but the use of that is very simple and practice [24]. The main simplification adopted is the linearization of the diagrams using straight lines. Although this is a procedure that greatly simplifies the design/verification process, it can be quite a distance from the real response. Studies based on experimental analyzes show that technical standards, in general, conservatively estimate the eccentric compression strength [25]–[27]. When comparing such simplified diagrams that consider a plastic stress distribution with results obtained by strain compatibility, the simplified results were shown to be non-conservative and with considerable error for rectangular concrete-filled steel tube columns with the use of high-strength steel [28]. Another important aspect is the Brazilian standard code [20] limits the compressive strength of concrete to 50 MPa. On the other hand, the Brazilian code for reinforced concrete elements [29] allows the use of concrete up to 90 MPa. Thus, in the present study, a software was developed to predict the M-N interaction curve of rectangular concrete-filled section considering the strain compatibility and concrete strength between 20 and 90 MPa. Moreover, the influence of compressive strength of concrete (f_c), yielding strength of steel tube (f_y) and steel ratio was investigated in this study. The influence of these parameters on the interaction curve shape and resistance of concrete-filled steel tube column under eccentric load were evaluated in the present study. In addition, the parabolic interaction diagrams were compared to design interaction diagrams of the Brazilian [20], [21] and European [22] standard codes and with literature responses [17], [18].

2 SIMPLIFIED M-N INTERACTION STRENGTH

The Brazilian standard code for steel and composite structures [20] presents two simplified models for verify the composite columns subjected to eccentric compression; both assume the plastic stress distribution. The Model I is based on the American standard code for steel structures [30] while the Model II is based on the European standard for composite structures [22]. The verification of M-N interaction strength using Model I is done using a simplified curve (Figure 1a) composed of two parts: line passing through points A and B; another passing through points B and C. Such a model provides for a 10% reduction in the design value of plastic resistance moment ($M_{pl,\,Rd}$) to obtain the design value of resistance moment (M_{Rd}). The M-N interaction model presented in the Brazilian standard code for steel and composite structures with use of tubular profiles [21] is like Model I [20]. However, points A and B of the M-N interaction diagram have the same value of resistance moment (Figure 1b).

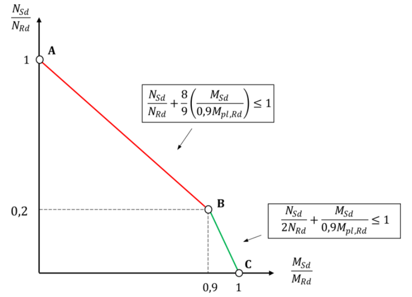

a) Model I for M-N interaction. Adapted from ABNT NBR 8800 [20].

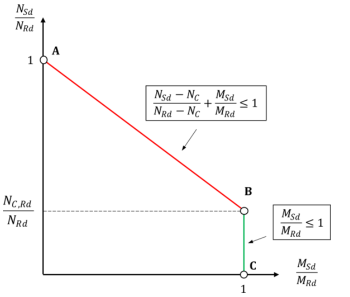

b) Model for M-N interaction. Adapted from ABNT NBR 16239 [21].

Figure 1. Models for M-N interaction: ABNT NBR 8800 [20] and ABNT NBR 16239 [21].

In addition, the Model I and takes into account the effects of flexural buckling using the parameter χ (Equation 1 and Equation 2) for resistance of composite column under compressive normal force (N_{Rd}). The M-N interaction model presented by ABNT NBR 16239 [21] also considers the effects of flexural buckling, but in a less conservative way (Parameter χ, Figure 1b).

$$\chi = 0,658^{\lambda_o{}^2},\ for\ \lambda_o \leq 1,5 \tag{1}$$

$$\chi = \frac{0,877}{\lambda_o^2},\ for\ \lambda_o > 1,5 \tag{2}$$

where λ_o = relative slenderness of composite column.

The Model II is similar to EN 1994-1-1 [22] model and the M-N interaction curve is represented by three parts (Figure 2).

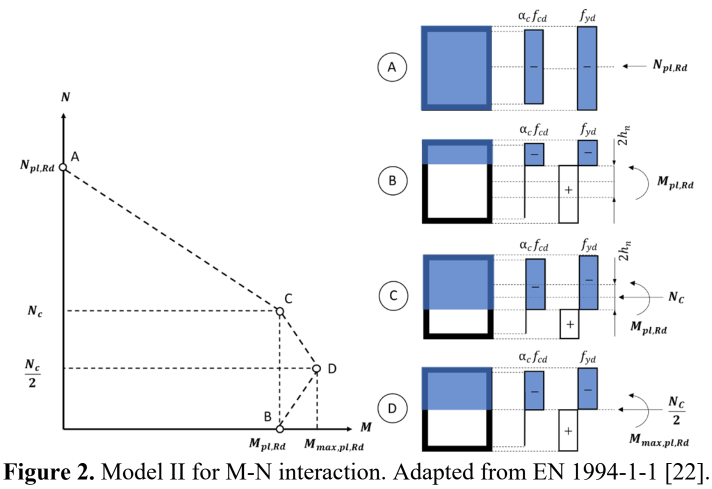

Figure 2. Model II for M-N interaction. Adapted from EN 1994-1-1 [22].

The α_c coefficient is considered equal to 0,85 by ABNT NBR 8800 [20]. The Brazilian standard [20] does not consider the effects of concrete confinement for filled rectangular sections; in the proposed model α_c coefficient is defined with the aid of Equation 6. The European standard [22] considers a specific formulation for filled circular sections, for better consideration of the concrete confinement effect. On the other hand, in filled rectangular sections, EN 1994-1-1 [22] considers α_c equal to 1. In the present study, the simplified curves of strength considering the two models (I and II) presented by Brazilian Standard code [20] and the curves of strength presented by ABNT NBR 16239 [21], are compared to parabolic curves obtained from the strain compatibility for rectangular concrete-filled steel tube column.

3 CONSTRUCTION OF AXIAL FORCE-MOMENT INTERACTION CURVES

Strain compatibility method assumes two main hypotheses: 1) plane sections remain plane; 2) steel-concrete full-composite action. Following the assumption of strain compatibility and linear strain distribution over the entire cross-section, the M-N pair of strength is defined from the variation of the neutral axis depth: a depth of neutral axis is arbitrated, and the M-N pair of strength is obtained for that, considering the composite section subjected to uniaxial bending moment. The process is analogous to the commonly used in reinforced concrete sections and it follows the steps: description of cross-section equilibrium using equilibrium equations, calculation of components strains in function of the neutral axis depth, considering the flexural buckling parameter. By shifting the neutral axis position consecutively, numerous combinations of axial force N and bending moment M can be generated and the full range of interaction diagrams from pure compression to pure bending can be traced by the software developed by the authors. The main steps are detailed in the next items.

3.1 Equilibrium equations of cross-section

The resulting forces in the composite section, regarding to the steel profile and concrete, are shown in Figure 3. Equation 3 and Equation 4 define the M-N pair of strength (Table 1), where x is the neutral axis depth.

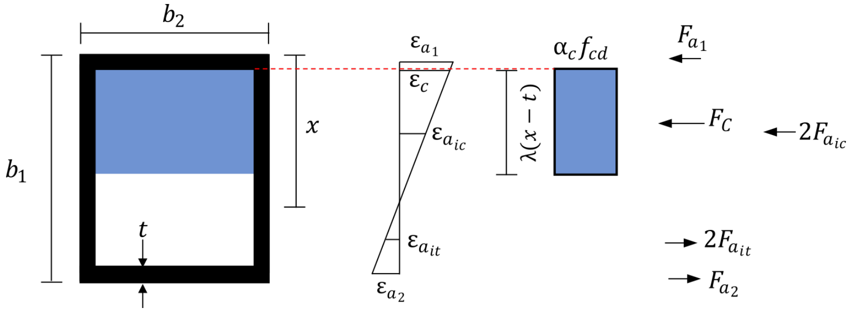

Figure 3. Resulting forces on components of rectangular composite cross-section.

Table 1. M-N pair of cross-section strength.

Plastic resistance to compression, $N_{pl,Rd}$	
$N_{pl,Rd} = \lambda(x-t)(b_2-2t)(-\alpha_c f_{cd}) - \sigma_{a_1} A_{a_1} + \sigma_{a_2} A_{a_2} - \sum_{i=1}^{n} 2\sigma_{a_{ic}} A_{a_{ic}} + \sum_{i=1}^{n} 2\sigma_{a_{it}} A_{a_{it}}$	(3)
Resistance moment, M_{Rd}	
$M_{Rd} = \lambda(x-t)(b_2-2t)\left(\frac{b_1}{2} - \frac{\lambda(x-t)}{2} - t\right)(-\alpha_c f_{cd}) - \sigma_{a_1} A_{a_1} y_{a1} + \sigma_{a_2} A_{a_2} y_{a_2} - \sum_{i=1}^{n} 2\sigma_{a_{ic}} A_{a_{ic}} y_{aic} + \sum_{i=1}^{n} 2\sigma_{a_{it}} A_{a_{it}} y_{ait}$	(4)

where σ_a = stress on portion of steel section (kN/cm^2); y_a = distance between the gravity center of a portion of steel and the gravity center of the cross-section (cm); A_a, A_{ai} = portion area of flanges of the steel profile and infinitesimal area of steel tube, respectively (cm^2); and f_{cd} = design value of compressive strength of concrete (kN/cm^2).

The coefficients λ and α_c are defined according to ABNT NBR 6118 [29] and shown in Equation 5 and Equation 6.

$$\lambda = 0,8 - \frac{f_c - 50}{400} \leq 0,8 \quad (5)$$

$$\alpha_c = 0,85\left[1 - \frac{f_c - 50}{200}\right] \leq 0,85 \quad (6)$$

where f_c = compressive strength of concrete (MPa).

If the normal force is not prevalent in the cross-section, as in concrete, plastic behavior was adopted, the proposed model may not adequately represent the real situation. Despite this, the simplified models of ABNT NBR 8800 [20] and EN 1994-1-1 [22] also consider plastic behavior of concrete. Such simplification is coherent, as in columns the axial force is generally high.

3.2 Strains in composite cross-section

Stresses acting on steel components (σ_i, Equation 7 and Equation 8) are defined from the strains. The linear elastic behavior and validity of Hooke's Law are considered for strains less than or equal to ε_{ydi} (Equation 7). For strains higher than ε_{ydi}, the stresses in the steel components are limited by the yielding strength of steel (f_{ydi}), as shown in Equation 8. The strains in cross-section (ε_i) are calculated according to the strain region: Region I, II and III (Figure 4), according to coefficient β_x (Equation 9).

$$\sigma_i = \varepsilon_i E_i,\ for\ \varepsilon_i \leq \varepsilon_{y_{di}} \quad (7)$$

$$\sigma_i = f_{yd_i},\ for\ \varepsilon_i > \varepsilon_{y_{di}} \quad (8)$$

$$\beta_x = \frac{x}{d_s} \quad (9)$$

where E_i = modulus of elasticity of steel component i (kN/cm²); d_s = effective depth of the cross-section (cm); and $\varepsilon_{y_{di}}$ = steel design yield strain of steel component i (dimensionless).

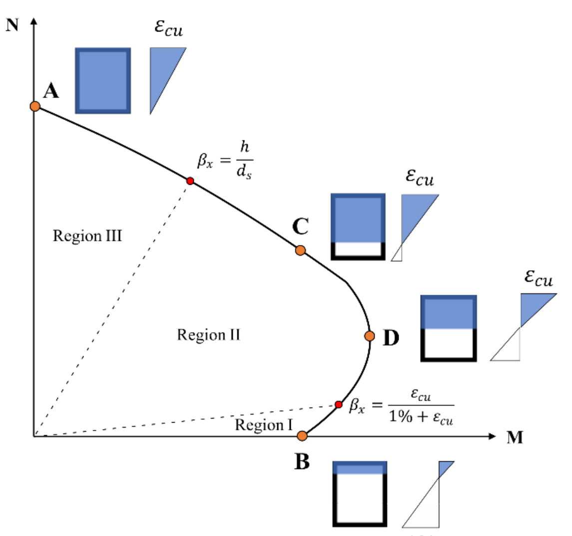

Figure 4. Strain limits for strain regions of composite cross-section.

The ultimate value of concrete compressive strain ε_{cu} (Table 2) is defined according to the recommendations of ABNT NBR 6118 [29] and depends on the compressive strength of concrete.

Table 2. Ultimate values-concrete compressive strains. Adapted from ABNT NBR 6118 [29].

Concrete strength classes	Concrete strain
C20-C50	$\varepsilon_{cu} = -0{,}35\%$; $\varepsilon_{c2} = -0{,}2\ \%$
C55-C90	$\varepsilon_{cu} = -\left(0{,}26\% + 3{,}5\% \left[\frac{90 - f_c}{100}\right]^4\right)$
	$\varepsilon_{c2} = -\left(0{,}2\% + 0{,}0085\% \left(f_c - 50\right)^{0{,}53}\right)$

The ultimate strain in steel (ε_{su}) was adopted equal to 0,01 for the most external tensile steel component [29]; this defines the effective depth (d_s). The strains in the composite section depend on each strain region type (Figure 4) and are calculated with the aid of Table 3. Strains are obtained considering a horizontal layer in the cross-section (layer i).

Table 3. Strains in cross-section according to strain region.

	Cross-section	Strain in the layer i
Region I	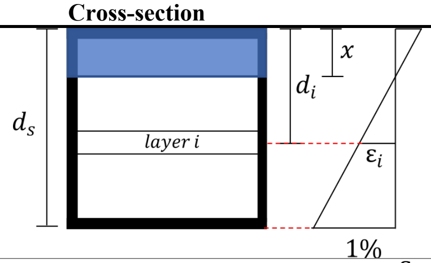	$\varepsilon_i = \frac{1\%\left(d_i - x\right)}{d_s - x}$
Region II	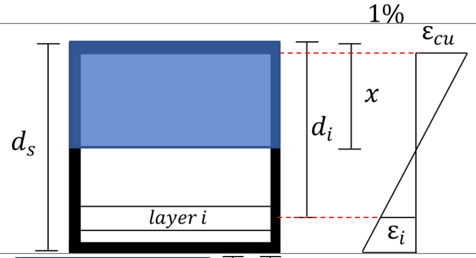	$\varepsilon_i = \frac{-\varepsilon_{cu}\left(d_i - x\right)}{x - t}$
Region III	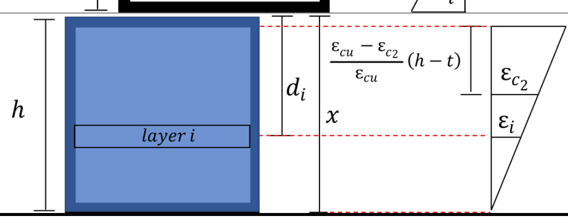	$\varepsilon_i = \frac{-\varepsilon_{c2}\left(x - d_i\right)}{x - t - \frac{\varepsilon_{cu} - \varepsilon_{c2}}{\varepsilon_{cu}}\left(h - t\right)}$

3.3 Factor reduction for buckling curve (χ)

The relevant buckling mode, considered by using the parameter χ, reduces the axial load capacity of the composite column. This can be observed in the curve that starts from point A2 (Figure 5). The reduction factor χ is depending on relative slenderness (λ_o). The M-N interaction curve of composite column and cross-section are parallel however the contour diagram of the first is smaller than the other. In present study, the flexural buckling was included on the axial load capacity using the parameter χ (Figure 5) and this same procedure was also proposed by Perea et al. [31].

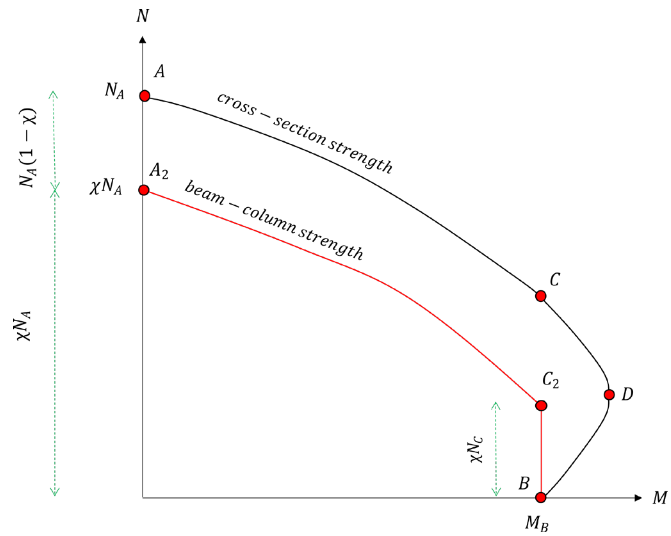

Figure 5. Reduction of plastic resistance to axial force due to flexural buckling.

Some authors present the possibility of reducing axial compressive resistance between points A and C [31], [32], and exclude the point D replacing of CDB portion by a straight-line connecting points C and B [31]. The point D on the interaction curve corresponds to the maximum moment resistance that can be achieved by the section. This is greater than M_B (uniaxial bending resistance) because the compressive axial force inhibits tensile cracking of the concrete, thus enhancing its flexural resistance. This simplification is also adopted by design curve of the Model I presented by Brazilian Standard Code [20]. Ziemian [33] proposes the reduction of the plastic resistance moment (M_B) by a coefficient equal to 0,9, like adopted by ANSI/AISC 360 [30].

In the proposed model, the reduction on plastic resistance to compression N_A was made considering the relevant buckling mode (parameter χ, Equation 1 and Equation 2) and the point D was maintained in the interaction curves. Although the consideration of point D can lead to unsafe results [34], such point was maintained so that the generated M-N interaction curve preserved its original contour resulting from the application of strain compatibility. Therefore, from these considerations, the resistance to axial force (N_{Rd}) of the rectangular concrete-filled steel tube columns, including the buckling effects in given by Equation 10, Table 4. The coefficient μ, which reduces the moment resistance, was adopted equal to 0,9 [33].

Table 4. M-N pair of strength including the reduction effects due to buckling mode.

Resistance to axial force, N_{Rd}	
$N_{Rd}=\left[\lambda(x-t)(b_2-2t)(-\alpha_c f_{cd})-\sigma_{a_1}A_{a_1}+\sigma_{a_2}A_{a_2}-\sum_{i=1}^{n}2\sigma_{a_{ic}}A_{a_{ic}}+\sum_{i=1}^{n}2\sigma_{a_{it}}A_{a_{it}}\right]\chi$	(10)
Resistance moment, M_{Rd}	
$M_{Rd}=\left[\lambda(x-t)(b_2-2t)\left(\frac{b_1}{2}-\frac{\lambda(x-t)}{2}-t\right)(-\alpha_c f_{cd})-\sigma_{a_1}A_{a_1}y_{a1}+\sigma_{a_2}A_{a_2}y_{a_2}-\sum_{i=1}^{n}2\sigma_{a_{ic}}A_{a_{ic}}y_{aic}+\sum_{i=1}^{n}2\sigma_{a_{it}}A_{a_{it}}y_{ait}\right]\mu$	(11)

3.4 Iterative process

Following the assumption of strain compatibility and linear strain distribution over the entire cross-section, the M-N pair of strength for each arbitrated depth can be obtained. A computational code was then developed in Visual Basic language that allow to obtain the M-N pairs of strength following the steps shown in Figure 6.

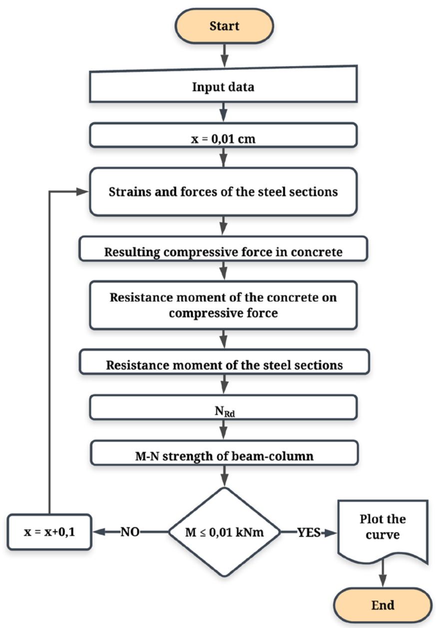

Figure 6. Iterative process of computational code.

In the verification of convergence, the computational code evaluates how close the moment resistance obtained by the equilibrium of bending moments is to point A of the interaction diagram M-N (pure compression). Is verified if the moment resistance, is less than 0,01 kN.m. If this is true, the interaction curve is plotted, because the M-N pair of strength obtained is close to Point A. Otherwise, the neutral axis is increased to by 0,1 cm and the process returns to third step (Figure 6).

The computational code was employed in a parametric study. Before that, a first analysis was done to evaluate the correlation of the results in comparison to those available in the literature. The influence of some parameters on the shape of M-N interaction diagrams was evaluates in the parametric study considering the parameters as: compressive strength of concrete, yielding strength of steel tube and the steel ratio (ratio between the area of steel tube and the concrete area in the composite section). In this study only rectangular concrete-filled steel tube columns without reinforcing bars were evaluated using the computational code. The second order effects were not taking account in the present analysis.

4 RESULTS AND DISCUSSIONS

This section presents the M-N interaction curves obtained for several rectangular concrete-filled steel tube columns. The results of M-N interaction curves were compared with simplified curves of standard codes [20]–[22] and with literature results [17], [18].

4.1 Comparison with literature responses

In this phase, the results of computational code were compared to literature results [17], [18]. In the comparative analysis with literature results, the coefficients of strength materials were adopted equal to 1,0. The simplified interaction diagrams correspond to the Brazilian Standard Codes [20], [21] and EN 1994-1-1 [22]. The simplified M- N interaction strength of the beam-column using recommendations of Brazilian Standard code [20] (Model I) interaction curve was called "Model I [20]". These results include the consideration of reduction factor χ for the relevant buckling mode given in terms of the slenderness column.

Model II [20] and Eurocode [22] correspond to the Brazilian code [20] and EN 1994-1-1 [22], respectively. The slenderness effect of the column (Figure 5) on the M-N interaction curves is not consider by these simplified curves that consider the cross-section strength [20], [22]. In this paper, the authors included the parameter χ to taking in account the slenderness effect of columns and modified the Model II [20] and Eurocode [22] curves. The new curves were called as "Modified Model II [20]" and "Modified EN 1994-1-1 [22]" respectively (Figure 7).

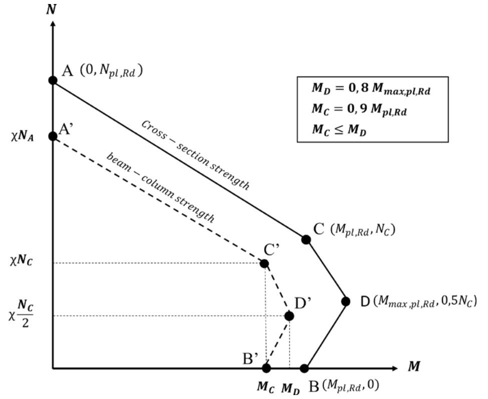

Figure 7. Modified interaction curves for Model II [20] and Eurocode [22].

The compressive resistance of the point A (Figure 7) was decreased by the slenderness reduction factor (χ) and moment values in the points B and D were also decreased considering the reductions of 0,9 or 0,8 (Figure 7). Although the Model II [20] and the Eurocode [22] are very similar, there are some differences in the partial safety factors. To the design compressive strength of concrete, the reductions are 85% and 100%, respectively from [20] and [22]. The partial safety factors for compressive strength of concrete are equal to 1,4 and 1,5, respectively for Brazilian code [20] and Eurocode [22]. The details of specimens are in Table 5.

Table 5. Validation of computational code: specimens' details of refs [17], [18].

Author	Specimen	H × B × t (mm)	f_y (MPa)	f_c (MPa)	L_e (mm)	λ_o	e (mm)	N_{exp} (kN)	M_{exp} (kNcm)
Du et al. [18]	D1	150×150×8,28	488,4	55,3	1180	0,33	0	2947	0
	D2						45	1672,5	8770
	D3						150	807,1	12970
	D4						1200	108,5	13220
Melo [17]	M1	150×150×3	250	40	1240	0,29	20	966	2445,9
	M2						30	858,3	3116,8
	M3						40	765,8	3716,0
Le: effective length									

The results of Du et al. [18] were compared to M-N curves of beam-column obtained by both proposed model and simplified interaction diagrams (Figure 8).

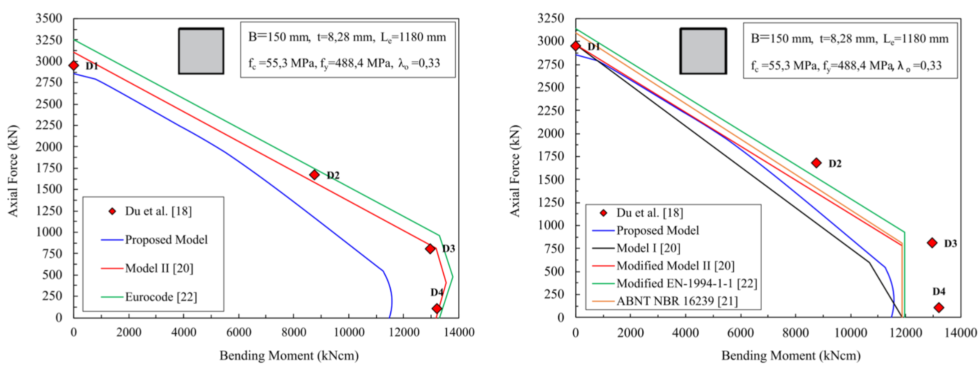

a) Proposed model *vs*. simplified M-N interaction curves (cross-section strength) *vs*. Du *et al.* [18]

b) Proposed model *vs*. simplified M-N interaction curves (beam-column strength) *vs*. Du *et al.* [18]

Figure 8. Comparison of parabolic and simplified M-N interaction curves with results of Du et al. [18].

The estimated values of eccentric compression strength, according to model, for results of Du et al. [18] are shown in Table 6.

Table 6. Estimated values of M-N pairs of strength vs. results of Du et al. [18].

Model	**D1**		**D2**		**D3**		**D4**	
	N (kN)	**M (kNm)**	**N (kN)**	**M (kNm)**	**N (kN)**	**M (kNm)**	**N (kN)**	**M (kNm)**
Du et al. [18]	2947	0	1672,5	87,7	807,1	129,7	108,5	132,2
Proposed model	2855,41 (- 3,1%)	0	1451,03 (- 13,2%)	76,05 (- 13,3%)	671,17 (- 16,8%)	107,61 (- 17%)	93,15 (- 14,1%)	115,48 (- 12,6%)
Model II [20]	3107,24 (+5,4%)	0	1628,8 (- 2,6%)	85,1 (-3%)	819,18 (+1,5%)	131,71 (+1,5%)	107,67 (- 0,8%)	132,82 (+0,5%)
Eurocode [22]	3251,03 (+10,3%)	0	1711,07 (+2,3%)	89,39 (+1,9%)	834,62 (+3,4%)	134,2 (+3,5%)	108,75 (+0,2%)	134,19 (+1,5%)
Model I [20]	2969,18 (+0,8%)	0	1365,34 (- 18,4%)	71,98 (- 17,9%)	645,05 (- 20,1%)	104,55 (- 19,4%)	91,9 (- 15,3%)	116,93 (- 11,6%)
Modified Model II [20]	2969,18 (+0,8%)	0	1505,33 (- 10%)	79,35 (- 9,5%)	733,11 (- 9,2%)	118,85 (- 8,4%)	93,36 (- 14%)	118,85 (- 10,1%)
Modified EN-1994-1-1 [22]	3136 (+6,4%)	0	1588,31 (- 5%)	83,73 (- 4,5%)	739,68 (- 8,4%)	119,93 (- 7,5%)	94,02 (- 13,3%)	119,93 (- 9,3%)
ABNT NBR 16239 [21]	3098,30 (+5,1%)	0	1539,70 (- 7,9%)	80,70 (- 7,9%)	733,11 (- 9,2%)	118,85 (- 8,4%)	93,36 (- 14%)	118,85 (- 10,1%)

The results of proposed model were conservative (blue curve, Figure 8a and Table 6) and the results of simplified M-N interaction curves were unsafe when considering the cross-section strength (Figure 8a and Table 6). The simplified M-N interaction curves overestimated the value of beam-column strength to compressive normal force (N_{Rd}) in relation to the proposed model (Figure 8b); this is due the simplified models [20]–[22] take in account the plastic stress distribution. The M-N interaction curve proposed by ABNT NBR 16239 [21], presented less conservative results in relation to the interaction models of ABNT NBR 8800 [20] (Model I and Modified Model II).

The accuracy of results of proposed model in relation to compressive normal force (N_{Rd}) considering recommendations of ABNT NBR 8800 [20] (Model I and Modified Model II) was not verified for results of literature (Figure 8). In the proposed model the plastic resistance of the steel components was not reached, and this occurred because in the strain compatibility method the stress acting on steel components were obtained considering linear elastic behavior. The strains in the steel components of Du et al. [18] were lower than the strains that limit the elastic region; therefore, the yielding strength of steel was not reached for proposed model.

The results of Melo [17] are compared (Figure 9) to the proposed model and simplified diagrams of ABNT NBR 8800 [20], ABNT NBR 16239 [21] and EN 1994-1-1 [22].

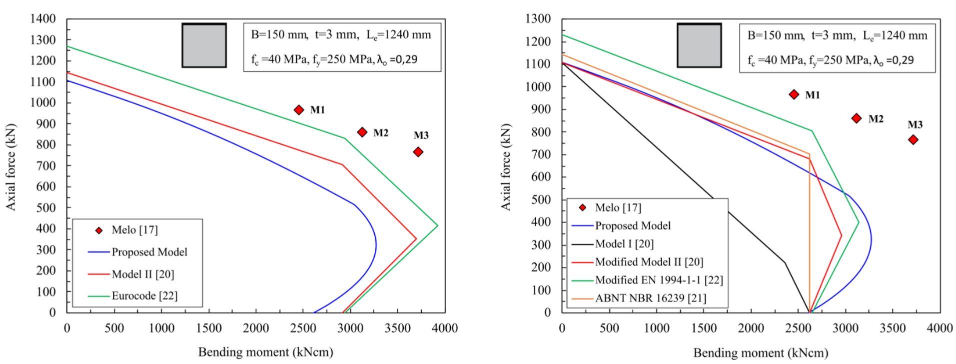

a) Proposed model *vs*. simplified M-N interaction curves (cross-section strength) *vs*. Melo [17]

b) Proposed model *vs*. simplified M-N interaction curves (beam-column strength) *vs*. Melo [17]

Figure 9. Comparison of parabolic and simplified M-N interaction curves with results of Melo [17].

The estimated values of M-N pairs of strength for results of Melo [17] are shown in Table 7.

Table 7. Estimated values of M-N pairs of strength vs. results of Melo [17].

Model	M1		M2		M3	
	N (kN)	M (kNm)	N (kN)	M (kNm)	N (kN)	M (kNm)
Melo [17]	966	24,46	858,3	31,17	765,8	37,16
Proposed model	763,56 (-21%)	19,45 (-20,5%)	663,48 (-22,7%)	24,05 (-22,8%)	575,56 (-24,8%)	27,91 (-24,9%)
Model II [20]	824,52 (-14,6%)	20,98 (-14,2%)	737,48 (-14,1%)	26,74 (-14,2%)	632,35 (-17,4%)	30,71 (-17,4%)
Eurocode [22]	917,43 (-5%)	23,29 (-4,8%)	815,33 (-5%)	29,63 (-4,9%)	677,68 (-11,5%)	32,91 (-11,4%)
Model I [20]	564,95 (-41,5%)	14,32 (-41,5%)	466,03 (-45,7%)	16,97 (-45,6%)	389,93 (-49,1%)	18,98 (-48,9%)
Modified Model II [20]	780,82 (-19,2%)	19,83 (-18,9%)	692,34 (-19,3%)	25,20 (-19,2%)	560,31 (-26,8%)	27,34 (-26,4%)
Modified EN-1994- 1- 1 [22]	868,98 (-10%)	22,11 (-9,6%)	745,36 (-13,2%)	27,17 (-12,8%)	594,73 (-22,3%)	29,02 (-21,9%)
ABNT NBR 16239 [21]	801,57 (-17,0%)	20,46 (-16,3%)	708,64 (-17,4%)	25,97 (-16,7%)	539,73 (-29,5%)	26,37 (-29,0%)

As plotted in Figure 9, a good agreement is achieved for pure bending between proposed model and the simplified M-N interaction curves when considering the beam-column strength. The results of the proposed model underestimated the resistance of all specimens [17] (Figure 9, Table 7). For beam-column strength (Figure 9b), the values of pure compressive normal force (N_{Rd}) were very close between the proposed model and the simplified curves of ABNT NBR 8800 [20]. On other hand, the value of modified EN 1994-1-1 [22] was higher than the other results (Table 7), since the European standard [22] considers 100% of the design value of compressive strength of concrete for rectangular concrete-filled steel tube columns. Additionally, the M-N interaction model proposed by ABNT NBR 16239 [21] proved to be less conservative in relation to ABNT NBR 8800 [20] (Model I and Modified Model II) for all responses in the literature [17], [18]. This is because ABNT NBR 16239 [21] considers the effects of flexural buckling in a less conservative way.

In this phase, the comparative analysis allows to observe the follow points:

- In some analyzes, the simplified models of standard codes [20], [22] allows to prevent only the cross-section strength not considering the stability reduction factor χ. This fact occurs mainly in EN 1994-1-1 [22].
- The proposed model allows to predict the M-N par of strength however the obtained values underestimated the literature responses [17], [18];
- The values of compressive normal force (N_{Rd}) obtained from proposed model were lower than that of simplified model proposed by EN 1994-1-1 [22];
- There is a strong correlation between the values of ultimate moment (M_{Rd}) resulted of proposed model and simplified models [20]–[22] when the stability factor χ (beam-column strength) was included in the interaction curves.
- The comparison between M-N pairs of strength obtained from several models including simplified models of standard codes and results of literature clearly shows the complexity of this type of analysis.

3.2 Parametric study

The parametric analysis comprised a total of three parameters: compressive strength of concrete, yielding strength of steel tube and steel ratio. Square cross-section having width of 150 mm and effective length (L_e) of 2000 mm were evaluated in this phase. When the influence of concrete strength was investigated the thickness of steel tube and the yielding strength were kept constant and equal to 3mm and 250 MPa, respectively. In this first analysis, the compressive strength of concrete varied from 20 MPa to 90 MPa in increments of 10 MPa. The yielding strength of steel was investigated considering the compressive strength of concrete equal to 20 MPa. The yielding strength of steel tube was varied from 250 MPa to 450 MPa, with increments of 50 MPa. The steel ratio was evaluated considering the thickness of steel tube equal to 4 mm, 5 mm, and 6 mm; resulting in steel ratios of 0,116, 0,178 and 0,181, respectively. Parabolic curves as well as dimensionless curves for several values of compressive strength of concrete are shown in Figure 10.

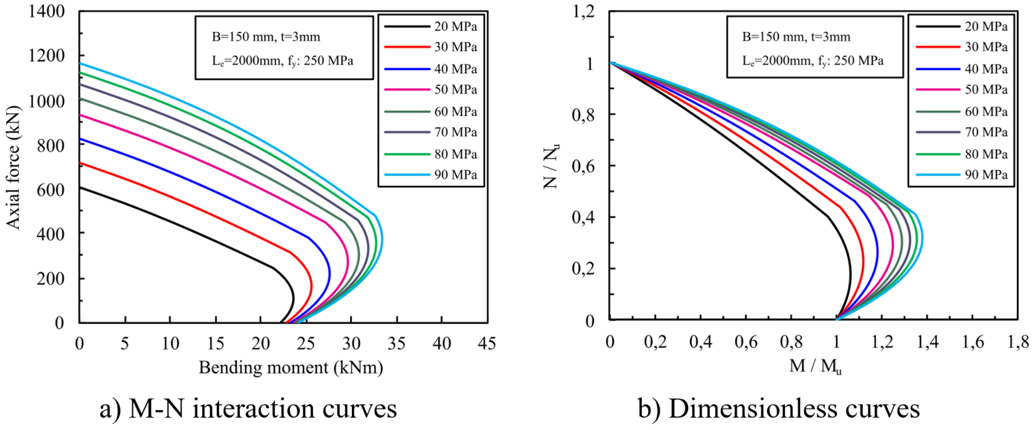

Figure 10. Effects of concrete strength on M-N interaction curves.

The shape of the M-N diagram is highly influenced by the compressive strength of concrete. Parabolic curves are parallel to each other for all values of compressive strength of concrete. However, the offset distance between parabolic curves is higher for concretes of usual strength (20-50 MPa, Figure 10a) and becomes significantly lower when the strength of concrete is higher than 50 MPa. The increase in the compressive strength of concrete results in a significant increase of compressive normal force (N_{Rd}). On the other hand, the values of ultimate moment (horizontal axis, Figure 10a) are less sensitive to this variation. Furthermore, the increases in the M-N pairs of strength are more expressive for concretes with strengths up to 50 MPa. This fact is due to the coefficients λ and α_c are function of concrete compressive strength and the use of high-strength concretes reduces the design strength (Equation 5 and Equation 6) increasing the relative slenderness value (Equation 1 and Equation 2). The coefficient α_c (Equation 6) applied to the design value of compressive strength of concrete in accordance to Brazilian standards [20], [29] assumes a maximum value of 0,85; in contrast, the European standard [22] adopts $\alpha_c = 1$ for rectangular concrete-filled sections. This difference in the coefficient that affects the compressive strength of concrete explains the divergences of results.

The values of moment resistance at the most external point of the dimensionless interaction curves (Figure 10) were 24,9% and 37,9% higher than the ultimate moment (Point B) for values of compressive strength of 90 MPa and 50 MPa, respectively. An increase of 8,4% was observed in moment resistance at the most external point of the curve when the concrete strength varied from 20 MPa to 30 MPa, both concrete from C20-C50 class. Among the high-strength concretes, the most significant increase was 3,4% and occurred when the compressive strength varied from 60 MPa to 70 MPa. Comparing the lower and the higher values of compressive strength of concrete (C20 to C90) were observed increases of 262,9% and 41,5% in values of axial load capacity and bending moment capacity, respectively, at the most external point of the curve.

The values of the M-N pairs of strength are shown in Table 8. Comparing results of the lower and the higher values of compressive strength of concrete the axial load capacity at Point A was 92,1% higher while the bending moment capacity had an increase of only 8,9% (Point B). Therefore, an increase of compressive strength of concrete are more efficient to increase the axial load capacity and a less significant effect is observed on the values of bending moment capacity.

Table 8. Influence of concrete strength on M-N pair of strength.

Concrete (MPa)	**Point A**	**Point B**	**Point D**	
	N (kN)	**M (kNm)**	**N (kN)**	**M (kNm)**
C20	606,47	22,25	105,67	23,62
C30 (+50%)	716,69 (+18,2%)	22,91 (+2,9%)	163,7 (+54,9%)	25,62 (+8,4%)
C40 (+100%)	825,34 (+36,1%)	23,38 (+5,1%)	217,39 (+105,5%)	27,62 (+16,9%)
C50 (+150%)	932,64 (+53,8%)	23,72 (+6,6%)	272,19 (+157,6%)	29,63 (+25,4%)
C60 (+200%)	1006,68 (+66%)	23,93 (+7,5%)	304,6 (+188,2%)	30,85 (+30,6%)
C70 (+250%)	1070,19 (+76,4%)	24,07 (+8,2%)	330,86 (+213,1%)	31,89 (+35%)
C80 (+300%)	1123,42 (+85,2%)	24,18 (+8,6%)	356,98 (+237,8%)	32,75 (+38,6%)
C90 (+350%)	1165,05 (+92,1%)	24,23 (+8,9%)	383,56 (+262,9%)	33,42 (+41,5%)

In contrast to the observed for the variation of concrete strength, the interaction curves remain parallel for all values evaluated of yielding strength of steel (Figure 11a). For higher values of yielding strength, the moment resistance at Point D was closer to the ultimate moment. For the lowest value of yielding strength of steel (250 MPa) the value of moment resistance at point D was 6,2% higher than the value of ultimate moment (Figure 11b).

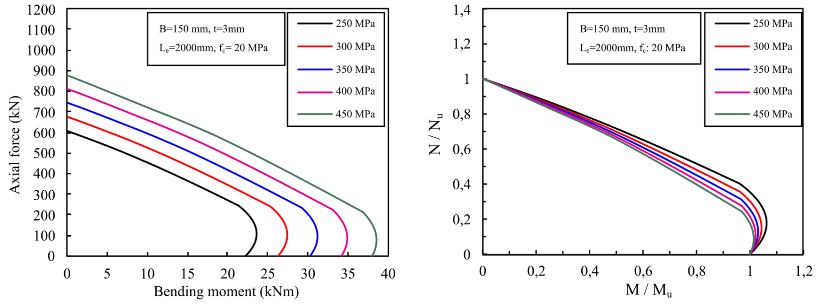

a) M-N interaction curves b) Dimensionless curves

Figure 11. Effect of yielding strength of steel on M-N interaction curves.

From the M-N pairs in the Table 9, an increase of 80% in the yielding strength results in increases of 44,6% and 71% in the axial load capacity (Point A) and pure bending moment (point B) respectively. In beam-column case (point D), it was observed an increase of 63,1% in the value of resistance moment and a reduction of 26,7% in the value of the resistance to compressive normal force when the yielding strength was increased to 450 MPa.

Table 9. Influence of yielding strength of steel on M-N pair of strength.

Yielding strength of steel (MPa)	Point A	Point B	Point D	
	N (kN)	M (kNm)	N (kN)	M (kNm)
250	606,46	22,24	106,82	23,63
300 (+20%)	675,71 (+11,4%)	26,31 (+18,3%)	102,08 (-4,4%)	27,44 (+16,1%)
350 (+40%)	743,83 (22,6%)	30,29 (+36,2%)	96,11 (-10%)	31,21 (+32,1%)
400 (+60%)	810,83 (+33,7%)	34,20 (53,8%)	85,26 (-20,2%)	34,91 (+47,7%)
450 (+80%)	876,73 (+44,6%)	38,03 (+71%)	78,32 (-26,7%)	38,55 (+63,1%)

The variation in the steel ratio significantly increased the M-N pairs of strength (Figure 12a). The increase in the steel ratio resulted in a similar effect of the yielding strength of steel: parallel curves and lower values of steel ratio resulted in more significant difference between the values of moment resistance (M_B) and ultimate moment (M_D, Figure 12b).

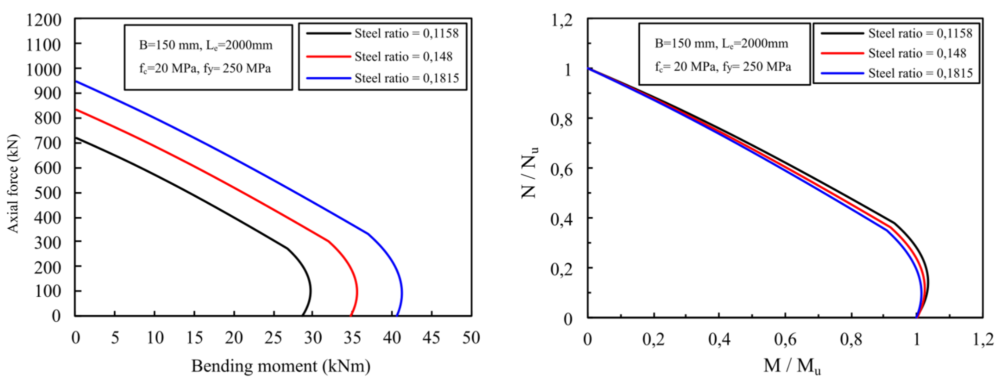

a) M-N interaction curves b) Dimensionless curves

Figure 12. Effect of steel ratio on M-N interaction curves.

When de steel ratio was increased in 50% (0,12 to 0,18, Table 10) occurred increase of 39,1% and decrease of 8,1% in the M-N pair of strength at Point D. Also, this increase in the steel ratio resulted in increase of 31,3% in axial load capacity to concentric compression (Point A, Table 10).

Table 10. Influence of steel ratio on M-N pair of strength.

Steel ratio	Point A	Point B	Point D	
	N (kN)	M (kNm)	N (kN)	M (kNm)
0,12	722,46	28,62	101,65	29,67
0,15 (+25%)	836,63 (+15,8%)	34,74 (+21,4%)	99,40 (-2,2%)	35,55 (+19,8%)
0,18 (+50%)	948,92 (+31,3%)	40,63 (+41,9%)	93,40 (-8,1%)	41,27 (+39,1%)

The variation in the compressive strength of concrete caused a significant effect on the axial load capacity (Figure 13a), the same has not observed on bending moment capacity (Figure 13b). There is a direct relationship between the compressive strength of concrete and the ultimate force on pure compression (Point A, Figure 13a): if the first is increased, the last also increase. However, the same effect showed not to be effective for increasing the ultimate moment capacity (Point B, Figure 13b). When the concrete strength exceeds 50 MPa, the difference between the ultimate values (normal force and moment) is reduced, also decreasing the influence of the compressive strength of concrete on the M- N pair of strength for high-strength concretes.

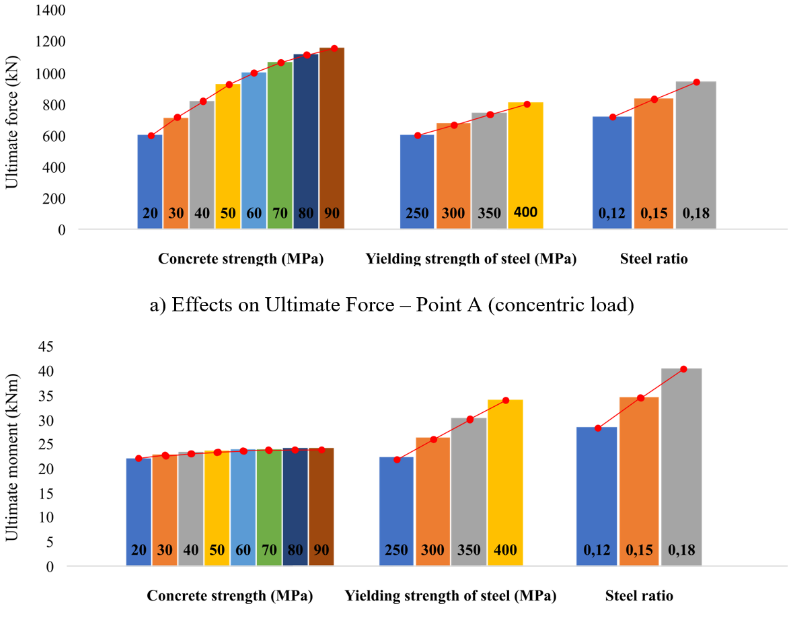

a) Effects on Ultimate Force – Point A (concentric load)

b) Effects on Ultimate Moment - Point B (pure bending)

Figure 13. Effect of variables on ultimate values of force and moment.

If the compressive strength of concrete or steel ratio have increases of 50% result on increases of 18,2% and 31,3% on the ultimate force for concentric load. Regarding to the values of ultimate moment (pure bending case), increases of 2,9% and 41,9% were observed respectively for strength of concrete and steel ratio. Similar effects were observed when the yielding strength of steel was increased in 40% (250 to 350 MPa): increase of 22,6% and 36,2% in the ultimate values of force and moment, respectively. Therefore, the results of parametric study allow to observe that the variables related to the steel profile (yield strength and steel ratio) had greater influence on the values of ultimate strength than the variation in the concrete strength.

Figure 14 shows the M-N interaction curves to consider the highest values of concrete strength and yielding strength of steel (90 MPa and 450 MPa, respectively) and thickness of the tube equal to 3 mm.

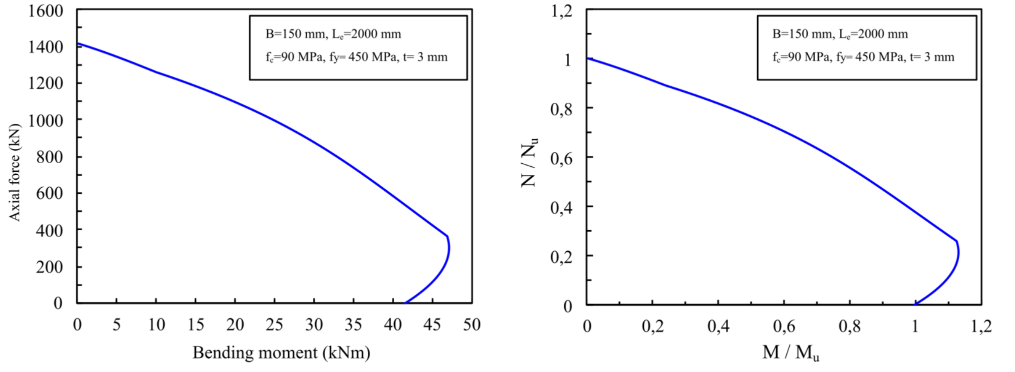

a) M-N interaction curve b) Dimensionless curve

Figure 14. Behavior of the M-N interaction curves for the highest values of concrete strength and yielding strength of steel.

Table 11 shows the M-N pairs of strength for Points A, B and D of the obtained M-N interaction curve.

Table 11. M-N pairs of strength for the highest values of concrete strength and yielding strength of steel.

Point A	Point B	Point D	
N (kN)	M (kNm)	N (kN)	M (kNm)
1417,4	41,5	300,8	47,07

The use of the highest strength values for steel and concrete resulted in the highest value of ultimate force on pure compression of the parametric study (Point A, Figure 14a and Table 11). Additionally, it was observed that the value of moment resistance at vertex D was 13,4% higher than the value of moment resistance at Point B (Figure 14b and Table 11). For all the analysis carried out, vertex D was more distant from Point B when there was an association of the lowest yielding strength of steel (250 MPa) and concrete C90 (Figure 11b).

5 CONCLUSIONS

This study presented a method for obtaining M-N interaction curves for rectangular concrete-filled steel tube columns. For this, was considered the strain compatibility method and a computational code was developed for rectangular concrete-filled subjected to uniaxial bending moments. The results of proposed method were coherent if compared to results of the literature [17], [18]. In comparison with literature results, the proposed model underestimated the M-N pairs of strength. On the other hand, in the comparison with Brazilian Standard Code [20] was observed an excellent correlation for compressive normal force (N_{Rd}) and moment strength M_{Rd} for both interaction models (I and II) when considering the beam-column strength. Additionally, in comparison with the simplified model of ABNT NBR 16239 [21], a good correlation was observed for moment strength M_{Rd}. The worst results were observed in the comparison of the proposed model with values of EN 1994-1-1 [22], especially for values of N_{Rd}. The proposed model presented regions in the M-N interaction curves that sometimes underestimated, sometimes overestimated the simplified curves of the standard code [20]–[22].

The influence of the compressive strength of concrete, yielding strength of steel and steel ratio on the eccentric compression strength was evaluated in a parametric study. Among the variables evaluated, those related to steel (yielding strength of steel and the steel ratio) contributed more significantly to the increase in the ultimate values of force and moment.

REFERENCES

[1] T. Fujimoto, A. Mukai, I. Nishiyama, and K. Sakino, "Behavior of eccentrically loaded concrete-filled steel tubular columns," *J. Struct. Eng.*, vol. 130, no. 2, pp. 203–212, 2004.

[2] P. Neogi, H. Sen, and J. Chapman, "Concrete-filled tubular steel columns under eccentric loading," *Struct. Eng.*, vol. 47, no. 5, pp. 187–195, 1969.

[3] R. Bridge, "Concrete filled steel tubular columns," *Civ. Eng. Trans.*, vol. 18, no. 2, pp. 127–133, 1976.

[4] H. Shakir-Khalil and J. Zeghiche, "Experimental behaviour of concrete-filled rolled rectangular hollow-section columns," *Struct. Eng.*, vol. 67, no. 19, pp. 346–353, 1989.

[5] M. Mouli, "*Behaviour of concrete-filled composite columns*," M.S. thesis, Univ. Manchester, Manchester, 1988.

[6] Q. Shan, J. Cai, X. Li, and J. Tan, "Analysis of concrete-filled square steel tube short columns under eccentric loading," *Math. Probl. Eng.*, vol. 2019, pp. 1–12, 2019.

[7] F. Yuan, H. Huang, and M. Chen, "Effect of stiffeners on the eccentric compression behaviour of square concrete-filled steel tubular columns," *Thin-walled Struct.*, vol. 135, pp. 196–209, 2019.

[8] D. Liu, "Behaviour of eccentrically loaded high-strength rectangular concrete-filled steel tubular columns," *J. Construct. Steel Res.*, vol. 62, no. 8, pp. 839–846, 2006.

[9], M. Kadhim, "Numerical modelling of concrete-filled stainless steel slender columns loaded eccentrically," *World J. Eng.*, vol. 17, no. 5, pp. 697–707, 2020., http://dx.doi.org/10.1108/WJE-09-2019-0268.

[10] X. Qu, Z. Chen, and G. Sun, "Experimental study of rectangular CFST columns subjected to eccentric loading," *Thin-walled Struct.*, vol. 64, pp. 83–93, 2013.

[11] E. Bonaldo, "Composite columns with high strength concrete core," M.S. thesis, Fac. Civ. Eng., State Univ. Campinas, 2001. [in Portuguese].

[12] J. Cai, J. Pan, C. Lu, and X. Li, "Nonlinear analysis of circular concrete filled steel tube columns under eccentric loading," *Mag. Concr. Res.*, vol. 72, no. 6, pp. 292–303, 2020.

[13] B. Uy, Z. Tao, and L.-H. Han, "Behaviour of short and slender concrete-filled stainless steel tubular columns," *J. Construct. Steel Res.*, vol. 67, no. 3, pp. 360–378, 2011.

[14] W. Li, L.-H. Han, and T.-M. Chan, "Performance of concrete-filled steel tubes subjected to eccentric tension," *J. Struct. Eng.*, vol. 141, no. 12, pp. 04015049, 2015.

[15] D. Hernández-Figueirido, M. L. Romero, J. L. Bonet, and J. M. Montalvá, "Ultimate capacity of rectangular concrete-filled steel tubular columns under unequal load eccentricities," *J. Construct. Steel Res.*, vol. 68, no. 1, pp. 107–117, 2012.

[16] S. De Nardin, "Concrete filled steel columns: a study of combined bending and compression and beam-column connections," Ph.D. dissertation, Eng. Sch. São Carlos, Univ. São Paulo, São Carlos, 2003. [in Portuguese].

[17] R. A. Melo, "Numerical analysis of the square concrete filled steel tube composite columns and under eccentric loads," M.S. thesis, Civ. Eng. Dep., Fed. Univ. São Carlos, São Carlos, 2018. [in Portuguese].

[18] Y. Du, Z. Chen, Y.-B. Wang, and J. Y. Richard Liew, "Ultimate resistance behavior of rectangular concrete-filled tubular beam-columns made of high-strength steel," *J. Construct. Steel Res.*, vol. 133, pp. 418–433, 2017.

[19] G. Li, B. Chen, Z. Yang, and Y. Feng, "Experimental and numerical behaviour of eccentrically loaded high strength concrete filled high strength square steel tube stub columns," *Thin-walled Struct.*, vol. 127, pp. 483–499, 2018.

[20] Associação Brasileira de Normas Técnicas, *Design of Steel and Composite Structures for Buildings*, NBR 8800:2008, 2008. [in Portuguese].

[21] Associação Brasileira de Normas Técnicas, *Design of Steel and Composite Structures for Buildings Using Hollow Sections*, NBR 16239:2013, 2013. [in Portuguese].

[22] European Committee for Standardization, *Eurocode 4: Design of Concrete Structures – Part 1-1: General Rules and Rules for Buildings*, EN 1994-1-1, 2004.

[23] Y. Bong Kwon and I. Kyu Jeong, "Resistance of rectangular concrete-filled tubular (CFT) sections to the axial load and combined axial compression and bending," *Thin-walled Struct.*, vol. 79, pp. 178–186, 2014.

[24] W. T. Hsu, D. M. Lue, and C. Y. Chang, "An investigation into the strength of concrete-filled tubes," *Appl. Mech. Mater.*, vol. 284-287, pp. 1208–1214, 2013.

[25] H.-J. Lee, I.-R. Choi, and H.-G. Park, "Eccentric compression strength of rectangular concrete-filled tubular columns using high-strength steel thin plates," *J. Struct. Eng.*, vol. 143, no. 5, 04016228, 2017.

[26] C.-H. Lee, T. H.-K. Kang, S.-Y. Kim, and K. Kang, "Strain compatibility method for the design of short rectangular concrete-filled tube columns under eccentric axial loads," *Constr. Build. Mater.*, vol. 121, pp. 143–153, 2016.

[27] Z. Lai, A. H. Varma, and K. Zhang, "Noncompact and slender rectangular CFT members: experimental database, analysis, and design," *J. Construct. Steel Res.*, vol. 101, pp. 455–468, 2014.

[28] A. Behnam and M. D. Denavit, "Plastic stress distribution method for predicting interaction strength of steel-concrete composite cross sections," *J. Construct. Steel Res.*, vol. 170, 106092, 2020.

[29] Associação Brasileira de Normas Técnicas, *Design of Concrete Structures – Procedure*, NBR 6118:2014, 2008. [in Portuguese].

[30] American National Standards Institute, *Specification for Steel Structural Buildings*, ANSI/AISC 360:16, 2016.

[31] T. Perea, R. Leon, J. Hajjar, and M. Denavit, "Full-scale tests of slender concrete-filled tubes: interaction behavior," *J. Struct. Eng.*, vol. 140, no. 9, 04014054, 2014.

[32] H.-J. Hwang, *Prefabricated Steel-Reinforced Concrete Composite Column – New Trends in Structural Engineering.* London: IntechOpen, 2018.

[33] R. D. Ziemian, *Guide to Stability Design Criteria for Metal Structures*, 6th ed. Hoboken: John Wiley & Sons, 2010.

[34] M. Malite, "Composite steel-concrete structures: column design," *Met. Constr. Sao Paulo*, vol. 4, no. 16, pp. 4–8, 1994. [in Portuguese].

Author contributions: MF: conceptualization, writing, formal analysis, methodology; SDN and FMAF: conceptualization, supervision, writing, formal analysis, methodology.

Editors: Bernardo Horowitz, Guilherme Aris Parsekian.

IBRACON Structures and Materials Journal
Revista IBRACON de Estruturas e Materiais
ISSN 1983-4195 ismj.org

ORIGINAL ARTICLE

Structural optimization of concrete plane frames considering the static and dynamic wind effect

Otimização estrutural de pórticos planos de concreto considerando o efeito estático e dinâmico do vento

Emanuely Ugulino Cardoso[a]
Rene Quispe Rodríguez[b]
Lucas Queiroz Machado[c]
Felipe Faustino Kunz[d]
Patrick dos Santos e Santos[e]
Alana Paula da Costa Quispe[f]

[a]Universidade de Brasília – UnB, Faculdade de Tecnologia, Brasília, DF, Brasil
[b]Universidade Federal de Santa Maria – UFSM, Centro de Tecnologia, Departamento de Engenharia Mecânica, Santa Maria, RS, Brasil
[c]School of Engineering and Physical Sciences, Heriot-Watt University, Edinburgh, Scotland
[d]Universidade do Estado de Mato Grosso – UNEMAT, Departamento de Engenharia Civil, Tangará da Serra, MT, Brasil
[e]Universidade do Estado de Santa Catarina – UDESC, Centro de Ciências Tecnológicas, Departamento de Engenharia Mecânica, Joinville, SC, Brasil
[f]Universidade Federal de Santa Maria – UFSM, Centro de Tecnologia, Programa de Pós-graduação em Engenharia Civil – PPGEC, Santa Maria, RS, Brasil

Received 02 March 2021
Accepted 07 June 2021

Abstract: This study has as its main purpose the structural optimization of plane frames in concrete, having as the objective function the minimum total weight of the structure. For this purpose, external actions, considered within the optimization process, are intended to represent accurately all effects observed in a real situation. In such manner, loads are dependent on the cross-section obtained in each optimization step, as well as the static and dynamic effects of the wind are considered for a more realistic representation. The optimization method adopted is the Teaching-Learning Based Optimization (TLBO). Thus, all proper design constraints were considered in accordance with Brazilian standards for concrete structures. From the results obtained in both situations (static and dynamic effects), it is possible to notice the difference regarding external actions, in which higher loads were obtained in higher floors, using the simplified dynamic model proposed in standards. Regarding the analysis of the structure optimization, the weight was higher when the applied forces were the result of the dynamic wind model, in which the larger cross-sections were found at the bottom of the structure. Even though this may be a well-known issue, the present work shows a quantitative study in which both effects are discussed in detail, as well as it features a methodology, based on a novel optimization method and with a straightforward implementation, that could be adapted for the analysis of more complex structures.

Keywords: finite element method, teaching-learning-based optimization, structural weight, Brazilian standards.

Resumo: O presente estudo tem como objetivo principal a otimização estrutural de pórticos planos de concreto, tendo como função objetivo o mínimo peso total da estrutura. Para este fim, ações externas, consideradas dentro do processo de otimização, tratam de representar de forma precisa todos os efeitos presentes em uma situação real. Desta forma, os carregamentos são dependentes das áreas da seção transversal obtidas em cada passo da otimização, assim como os efeitos estáticos e dinâmicos do vento são considerados para uma representação mais realista. O método de otimização adotado é o método de otimização baseado em ensino-aprendizagem, ou *Teaching-Learning Based Optimization,* em inglês. Além do mais, todas as restrições para um projeto adequado são consideradas usando as normas brasileiras para estruturas de concreto. Dos resultados obtidos em ambas as situações (estática e dinâmica), é possível notar a diferença com respeito às ações externas, onde maiores carregamentos são obtidos em pisos mais altos, usando a modelo dinâmico simplificado proposto em normas. Com respeito à análise de otimização, o peso foi maior no caso

Corresponding author: Rene Quispe Rodríguez. E-mail: rene.rodriguez@ufsm.br
Financial support: None.
Conflict of interest: Nothing to declare.

dinâmico, onde maiores áreas transversais foram necessárias. Apesar deste fato ser conhecido, o presente trabalho mostra um estudo quantitativo onde ambos os efeitos são discutidos em detalhes, assim como é apresentada uma metodologia, baseada em um método de otimização original e de fácil implementação, que pode ser adaptada à análise de estruturas mais complexas.

Palavras-chave: método dos elementos finitos, otimização baseada em ensino-aprendizagem, peso estrutural, normas brasileiras.

How to cite: E. U. Cardoso, R. Q. Rodríguez, L. Q. Machado, F. F. Kunz, P. S. Santos, and A. P. C. Quispe, "Structural optimization of concrete plane frames considering the static and dynamic wind effect," *Rev. IBRACON Estrut. Mater.*, vol. 15, no. 1, e15109, 2022, https://doi.org/10.1590/S1983-41952022000100009

1 INTRODUCTION

High building construction trend is increasing over recent years, due to factors such as urban sprawl and high land costs, stimulating the construction of cost-effective structures and bracing systems, as these buildings are mainly affected by lateral loads induced by wind effects [1]. Tall and slender structures have, in general, low frequencies and small rates of damping and under the action of dynamic environmental forces, such as those generated by the wind, can present great amplitude of oscillation, causing problems related to the comfort of users, use in service and even safety and service life of the structure [2]. Structures can be defined as physical systems subject to external actions, capable of transmitting efforts, and these actions are called dynamics when they generate forces of inertia [3]. An accurate realistic analysis should include the dynamic response of effects of resonance, acceleration, damping and structural stiffness variation [4]. Furthermore, external actions can cause vibrations in the structures and affect the users' comfort, in which the slender buildings are more susceptible to these effects. Generally, structural designs consider the wind effect wind as static loads, calculated from the average speed, without considering the components of the fluctuation part that can induce vibrations in the structural system. Thus, for a more realistic and reliable analysis, the dynamic characteristics of the wind must be considered, in such a way that the fluctuation part is used in dynamic modeling, in which the largest transfer of wind energy in the structure is concentrated in regions with low frequencies [5]. Structural design needs to find optimal dimensions for the elements when subjected to different loads [6]. Thus, structural optimization seeks to assist in the engineering area the determination of structures that offer the best performance. Concrete structures have good characteristics of durability and resistance to compression, being a material with wide use. However, most practical optimization procedures for concrete structures are based on iterative procedures, which may guarantee structural safety, but may not result in optimal structures [7].

Tapajós et al. [8] investigated the wind effect and its dependence on the concrete structure sizing and its foundation. Their study considered 10, 20 and 30 -story buildings with and without the wind effect. Results indicated that even for a 10-story building, the wind effect played an important role in the general security of the edification. Regarding the optimization of structural systems. Kripka et al. [9] studied the optimum spacing for concrete reinforced columns in building structures, aiming to minimize the total global cost in terms of concrete, steel and formworks use. The authors modeled the system using beam elements supported by springs with rotational rigidity. The design variables considered were geometric parameters of both beams and columns, while the optimization process consisted in an iterative process with removal of the less stressed columns. The results obtained were like those already used in practical cases. Breda et al. [10] presented a numerical optimization process, using the commercial software MATLAB as the main computational tool, for the optimization of steel-concrete composite beams and steel deck systems. The study demonstrated that increasing the number of beams, while reducing its individual weight, results in smaller slab spans and, consequently, in a reduction of the overall weight and costs. Recently, Gomez et al. [7] studied the topology optimization of buildings under wind stochastic loads. In this study the wind was modeled as a filtered white noise, while the optimization was accounted with a gradient-based method. The optimization procedure demonstrated high efficiency for tall buildings.

The present work aims to analyze the performance of concrete frame structures, subjected to both permanent and variable loads. The main objective is to optimize this kind of structure, using a metaheuristic optimization method based on a teaching-learning framework, namely teaching-learning-based optimization method (TLBO). The objective function is to minimize the total weight of the structure by minimizing the cross-section (design variable) of its components, which characterize a parametric optimization. The constructive constraints were those required by the Brazilian normative NBR 6118:2014 [11] and are in terms of specific maximum displacements and stresses. The optimization process is applied to two different situations, considering both a static wind analysis and the simplified dynamic effect according to the Brazilian standard NBR 6123:1988 [12].

2 THEORETICAL BACKGROUND

2.1 Structural Optimization

The optimization process seeks to maximize or minimize a certain objective function, within a domain that contains the acceptable values of the variables that will be processed, in such a way that the imposed constraints are satisfied. The best solution to the problem is designated as the optimal solution. Structural optimization, in many cases, is related to the interest in reducing costs. A relatively direct way of doing so is to find the minimum cross sections areas, reducing the overall structural weight, and a consequence, decreasing the material costs. Thus, some constraints can be considered, such as stresses and displacements. The optimization problem of minimizing the total weight of the structure can be defined as [13]. Minimize the weight objective function *w*:

$$w = \sum_{e=1}^{N_m} \gamma_e L_e A_e \, , \tag{1}$$

subject to stress constraints σ and displacements δ:

$$\sigma^L \le \sigma_e \le \sigma^U \text{ and } \delta^L \le \delta_e \le \delta^U \, , \tag{2}$$

where w is the weight of the structure composed of N_m members; γ_e is the unit weight of the material of each member; L_e the length, A_e determines the cross section. The solution must meet the stress limits σ and displacement δ, where L is defined as the lower limit and U as the upper limit. To account for elements that have not met the constraints, a penalty function is used, in such a way that the weight of the structure will be multiplied by the penalty factor. If the stress and displacements are within the stipulated limits, it will not suffer a penalty; otherwise, the stress penalty ϕ_σ^e for each element can be defined as

$$\phi_\sigma^e = \left| \left(\sigma_e - \sigma^{L,U} \right) / \sigma^{L,U} \right|^L . \tag{3}$$

The total stress penalty ϕ_σ^k for the design of a k structure being the sum over all elements. The penalty for displacement can be obtained in the same way, hence, the value of the total penalty ψ^k for a structure, can be calculated by

$$\psi^k = \left(1 + \phi_\sigma^k + \phi_\delta^k \right)^r , \tag{4}$$

where r is a positive penalty exponent. The penalized value that determines the weight of the structure by multiplying is real weight with the penalty ψ^k . Thus, the weight of the analyzed project is increased, as the elements that did not meet the constraints are penalized. The procedure continues until the optimal structure is obtained.

2.2 Teaching-Learning Based Optimization (TLBO)

The TLBO is a meta-heuristic optimization method that follows the analogy of the participation of a teacher and students in a class. The method is subdivided into two different consecutive processes: the teacher phase, that simulates his influence onto students; and a student phase, which models collaborative learning among students [14]. The teacher is considered the most educated person, who shares his knowledge and his ability to influence the class average, because the greater the teacher's capacity, the greater the average achieved by the class. In the same way that the interaction between the students themselves also improves the individual performance of each student [15]. Relating the TLBO method to an optimal structure design, the following relationships can be established: (1) a class of students represents the size of the population to be analyzed; (2) the design variables are considered as the subjects offered to students; and (3) the grade is the result of the structure weight, and the teacher is considered as the best solution obtained. This process is carried out until the objective function is minimized according to the imposed constraints [16].

Definition of the problem and optimization parameters

First, the number of students (population size), the stopping criteria (maximum number of iterations), the number of subjects (design variables) and the limits of the design variables (stresses and displacements) are defined. The matrix that represents the class is filled up with randomly generated students, according to the population size and the number of project variables [16].

Teacher phase

The influence of the teacher is considered, verifying the improvement of the knowledge of the students, based on the information transmitted by the teacher. In the optimization process, the design vector relates a student's current knowledge in different disciplines. Thus, the student's learning during this interaction with the teacher is expressed as:

$$X_{new}^{k}(j) = X_{old}^{k}(j) \pm \Delta(j)\,,\;\; \Delta(j) = T_F * r\left|M(j) - T(j)\right|, \tag{5}$$

where $X^k(j)$ indicates the j-th design variable for the k-th design vector; T_F is the teaching factor; r is a random number uniformly distributed within the range of [0,1]; $M(j)$ is the class average; $T(j)$ is the teacher's status; and $\Delta(j)$ indicates the difference between the teacher and the class average for each design variable, and its sign must be selected so that the student always move towards the teacher. The T_F teaching factor is used to increase the size of the local search space around each student and can take the value of 1 or 2 [14]. A modification of the TLBO method was proposed by Camp and Farshchin [14]. The class average is calculated by a weighted average based on the student's grade (structure weight), to give more emphasis to the most qualified students, and is defined by:

$$M(j) = \sum_{k=1}^{np} \frac{X^k(j)}{F^k} \Big/ \sum_{k=1}^{np} \frac{1}{F^k}\,. \tag{6}$$

If the calculation shows that $X_{new}^{k}(j)$ is better than the previous $X_{old}^{k}(j)$, the new solution will be replaced by the current solution, otherwise the old solution will be maintained.

Learner phase

It analyzes the interaction between students in a class, to improve their knowledge and improve the performance of the class. A given solution interacts randomly with other solutions to obtain new information [15]. The procedure starts with a random choice of two students in the class, p and q $(p \neq q)$. Then, the aptitude of each student is analyzed, p being considered as the most qualified student, aiming to improve his individual performance [14]. Considering that F^p and F^q are the students' grades and represent, in structural optimization, the weight of the structure, the following criteria are analyzed to determine the new solution. If $F^p < F^q$:

$$X_{new}^{p}(j) = X_{old}^{p}(j) + r\left[X_{old}^{p}(j) - X^{q}(j)\right] \tag{7}$$

When student p is better than student q, he goes in the opposite direction. If $F^p > F^q$:

$$X_{new}^{p}(j) = X_{old}^{p}(j) + r\left[X^{q}(j) - X_{old}^{p}(j)\right] \tag{8}$$

However, when the student q shows better performance, the student p tends to approach q to become better. In Equation 18, r is a random number uniformly distributed within the range [0,1]. In either case, student p is trying to improve his performance, and his movement tends to go towards the best solution. The value of $X_{new}^{p}(j)$ is accepted if it provides a better value for the objective function. The process is maintained until the best solution is found, ending when the algorithm converges to an optimal solution or reaches the maximum number of iterations. Figure 1 shows the flowchart of the optimization method identifying the steps performed.

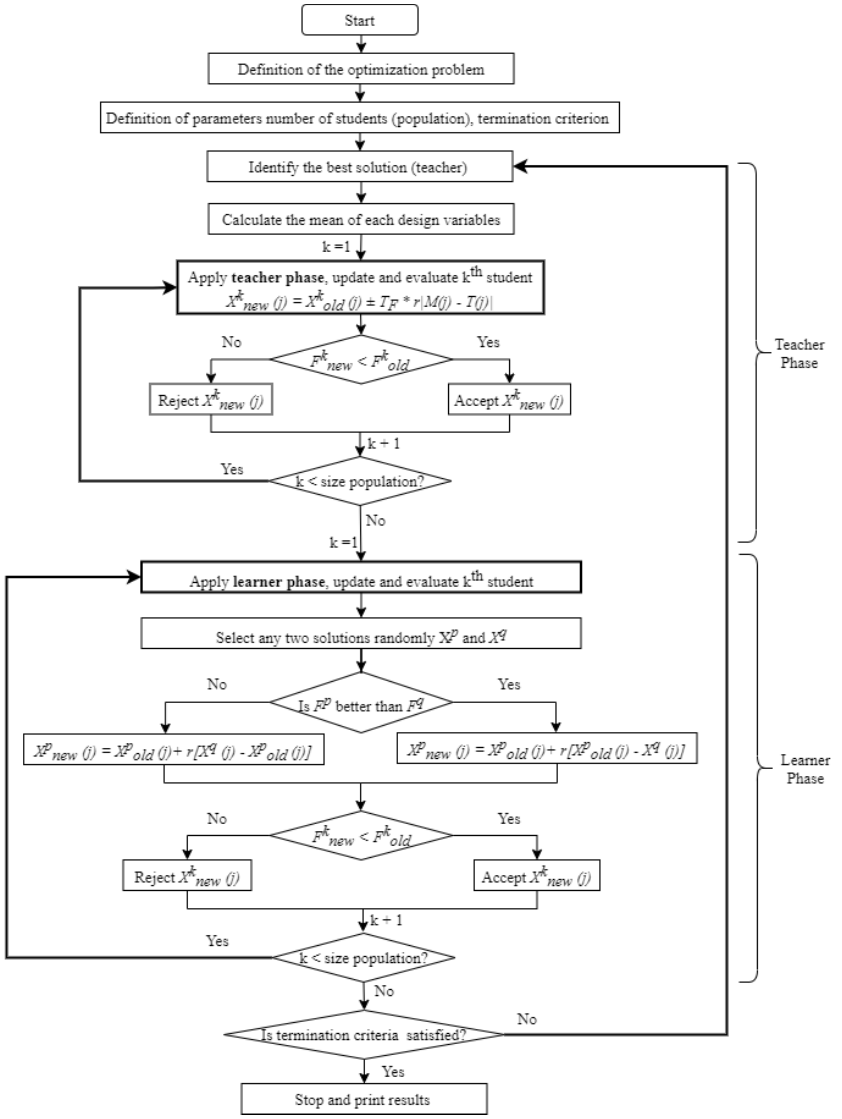

Figure 1. Flowchart for Teaching-Learning Based Optimization (TLBO), based on [20].

2.3 Methods for analyzing the influence of the wind

The structural wind effect occurs randomly on buildings, affecting, generally, all horizontal directions. In this manner, the most critical situation should be accounted for a proper structural design [16]. According to Chávez [17], the study of the wind effect in buildings should consider static and dynamic solicitations, both depending on the mean velocity and its fluctuations. These fluctuations are the gusts or turbulence that give rise to vibrations due to the various ways in which their force acts on the structure, producing a short-term random loading that makes direct stress analysis difficult. According to Islam et al. [18], the adequate control of the lateral deflection of buildings should allow the non-structural components to function correctly, avoid wear on the structure and the appearance of excessive deflection cracks, which, consequently, cause the loss of stiffness. When dimensioning a structural system, it must be rigid enough to avoid dynamic movements due to wind loads and any load redistribution to unplanned locations. The Brazilian standard NBR 6123:1988 [12], regulates the study of the effects of winds on structures and specifies the conditions required to consider the forces due to static and dynamic wind action, for the purpose a proper building design calculation.

Static wind analysis according to NBR 6123:1988 [12]

The Brazilian standard NBR 6123:1988 [12] presents a procedure for considering static loads due to the wind. The main aspects of the normative are presented for completeness, nonetheless, the reader can refer to the Brazilian standard for more details. The parameters considered for this simplification are the basic wind speed *(Vo)*, suitable for the place where the structure will be built; the factors *S1*, *S2* and *S3*, to be obtained the characteristic speed of the wind *(Vk)*, and with the characteristic speed. With this information it is possible to determine the dynamic pressure *(q)*, and finally, obtaining the forces, the pressure and shape coefficients [12].

The basic wind velocity *(Vo)*, obtained from the standard, is defined as the velocity of a 3 s gust, exceeded on average once in 50 years, 10 m above ground, in the field open and flat field. It is admitted that the basic wind can blow from any horizontal direction [12]. The topographic factor *(S1)* considers the topographic characteristics of the land on which the construction will take place. This coefficient is 1.0 for flat or slightly rugged locations, 0.9 for deep wind-protected valleys, and has a variation for slope-side buildings [19]. The factor *S2* considers the variation of the wind speed according to the roughness of the terrain, height, and dimensions of the construction. Thus, to perform the calculation of this factor one must determine the category to which the building belongs, as well as its class. The category is related to the roughness of the terrain, being established five categories, according to NBR 6123:1988 [12]. For the determination of the class that the building belongs to, one must consider the duration of the gust so that the wind encompasses the entire building, as well as the largest dimension. The Brazilian standard NBR 6123:1988 [12] establishes three classes. It is necessary to consider the category and class to determine the parameters used to calculate the factor *S2*. The statistical factor *(S3)* considers five groups for the required degree of security and the useful life of the building. From the values of *Vo*, *S1*, *S2* and *S3* it is possible to calculate the characteristic wind speed, in m/s, using the following expression:

$$V_k = V_o S1S2S3\,, \tag{9}$$

further obtaining the dynamic wind pressure, in N/m^2, as follows

$$q = 0.613 V_k{}^2\,. \tag{10}$$

Finally, the force due to the wind effect is calculated by multiplying the dynamic pressure by the area of influence and a pressure coefficient. This coefficient considers the building in external and internal parts, relating to the permeability, the shape of the building and the wind direction in the structure. The coefficients are described by means of tables and abacuses in NBR 6123:1988 [12] and if the difference between the external and internal pressure coefficients is positive, the total effective pressure will have the direction of the external overpressure, otherwise it will have the direction of an external suction [19].

Dynamic analysis by the simplified method of ABNT NBR 6123:1988 [12]

Dynamic actions cause vibrations in structures, which can not only damage them, but also cause fatigue in their materials, affect the comfort of users and the operation of equipment supported by them [3]. The effects generated by these actions on buildings are even more critical due to the structural characteristics themselves, such as the slenderness of the building. Wind speed fluctuations can cause flexible structures, especially in tall and slender constructions, to move in the direction of average speed, called the floating response. In constructions with a fundamental period of more than 1 s, particularly those that are weakly cushioned, a floating response in the direction of the average wind can be found. The total dynamic response is equal to the superposition of the average and floating responses [12]. Even if the models presented by the standard are called dynamic, the wind loading is considered only as static load. This method is applicable to structures supported exclusively at the base and height less than 150 m, considering only the first mode of vibration for calculating the floating response. In this case, the fundamental frequency of the building, the corresponding vibration mode, and the modal damping, are obtained approximately according to the height of the building and the characteristics of its structural system [17]. The design speed *(V'_p)* is calculated from the basic speed *Vo*, as

$$V'_p = 0.69 V_0 S1S3\,. \tag{11}$$

The dynamic pressure *q(z)*, from which forces are obtained, is a continuous function of height above ground and the first term of the expression corresponds to the mean response, while the second is the maximum amplitude of the floating response [12]. The dynamic pressure is expressed through Equation 12.

$$q(z) = q_0' b^2 \left[\left(\frac{z}{z_r} \right)^{2p} + \left(\frac{h}{z_r} \right)^{p} \left(\frac{z}{h} \right)^{\gamma} \frac{1+2\gamma}{1+\gamma+p} \xi \right] \quad (12)$$

The basic pressure, in N/m^2, can be determined according to Equation 13.

$$q_0' = 0.613 V_p'^{\,2} . \quad (13)$$

The coefficients b and p depend on the roughness of the terrain. The heights used in the calculation are determined as z_r, the reference height at 10 m, h the height of the building above the ground measured to the top and z the height above the ground in each coordinate. The values of the coefficients of the dynamic pressure are determined according to standards, and the coefficient γ determines the modal form and the dynamic amplification coefficient *(ξ)* can be obtained by means of abacuses and is in function of the dimensions of the building, the ratio critical damping *(ζ)* and frequency *(f)*. The force on the structure is the product of dynamic pressure, pressure coefficients and building size. According to Cerutti [20], the dynamic forces calculated here are obtained as dynamic-equivalent static loads, because they are determined by means of abacuses that simplify the calculations.

2.4 Concrete Structures

According to NBR 6118:2014 [11], simple concrete elements are defined as: structural elements made with concrete that does not have any type of armour or that has it in a quantity less than the minimum required for reinforced concrete [11]. In item 24 of this standard, to determine the limit values of the resistant stresses of calculation, we have for compression stress:

$$\sigma_{cRd} = 0.85 \frac{f_{ck}}{\gamma_c} , \quad (14)$$

where f_{ck} represents the compressive characteristic strength of concrete and γ_c is the weighting coefficient of concrete strength, for simple concrete cases one must adopt 1.68. For tensile stress, we have:

$$\sigma_{ctRd} = 0.85 \frac{f_{ctk,inf}}{\gamma_c} , \quad (15)$$

where $f_{ctk,inf}$ determines the concrete's resistance to direct traction and can be calculated using Equation 29 or 30; the value of γ_c is the same used for the compression calculation. The value for the resistance of concrete to direct traction varies according to the fck, being that, for group I concretes, that is, up to class C50 (f_{ck} up to 50 MPa):

$$f_{ctk,inf} = 0.7 * 0.3 f_{ck}^{\;2/3} , \quad (16)$$

and for group II concretes, that is, from C55 to class C90 (f_{ck} up to 90 MPa):

$$f_{ctk,inf} = 0.7 * 2.12 ln\left(1 + 0.11 f_{ck}\right) . \quad (17)$$

The modulus of elasticity of the concrete used in a structure can be calculated according to item 8.2.8 of NBR 6118:2014 [11]. In a basic concrete structure minimum limit values are prescribed, according to NBR 6118:2014 [11]. The objective of determining these limit dimensions is related to avoiding unacceptable performance and to having adequate conditions of execution [11]. As presented in item 13.2 of the standard, the cross section of the beams cannot be less than 12 cm wide, while for the columns the minimum dimension is 19 cm so that the cross-section area is also not less than 360 cm^2.

Loading on the slabs

According to Santos [21], the loading of the slab is transmitted to the beams, which are then applied to the columns. On the slabs, actions arising from the own weight, the weight of coatings and usage loads should be considered. Thus, to obtain these loads, the specific weights are multiplied by the respective thicknesses, as presented below.

$$g_{pp} = \gamma_c e_l \text{, and } g_{revest} = \gamma_{revest} e_{revest} , \tag{18}$$

where g_{pp} and g_{revest} represent the load of the slab's own weight and coating, respectively; γ_c and γ_{revest} determine the specific weight of the concrete and the coating material; e_l and e_{revest} are the thickness of the slab and the coating. In addition, the usage load should be calculated, according to NBR 6120:1980 [22], which expresses the calculation values for building structure loads. Usage loads are also defined as accidental loads and their effect may vary according to the number of floors that act on the analyzed element [23]. The proportion of reduction ratio for these loads are as follows: for 1 to 3 floors is 0%, for 4 floors is 20%, for 5 floors is 40% and for 6 or more is 60%. Then, the sum of all the loads applied to the slab is then multiplied by the area of influence that the slab has on a beam so that the linearly distributed load of the slab on the beam is determined.

Loading on the beams

The loads applied to the beams are distributed along their length, coming from the walls, slabs, and own weight. The beams can also receive concentrated loads from secondary beams that are supported [24]. Thus, the loads applied to the beams are calculated as:

$$g_{par} = \gamma_{tij} e_{tij} h_{par} \text{ and } g_{pp} = \gamma_c A_v , \tag{19}$$

where g_{par} and g_{pp} represent the load of walls and the own weight of the beams, respectively; γ_{tij} and γ_c are the specific weights of brick and concrete; e_{tij} is the thickness of the brick; h_{par} determines the height of the wall; Av is the cross-sectional area of the beam.

Loading on the columns

In the concrete structure, the columns have the function of receiving the loads from the beams and, in addition, it is necessary to consider the column's own weight [21]. The load generated by the weight of the column is obtained by:

$$g_{pp} = \gamma_c h A_p , \tag{20}$$

where g_{pp} represents the column load; γ_c the specific weight of the concrete; A_p is the cross-sectional area of the column.

3 RESULTS AND DISCUSSIONS

In this section three numerical examples are presented to show the applicability of the proposed optimization methodology. The first numerical example is related to the calculation of static wind forces. Then, the optimization method is tested with a well-known benchmark example obtained from literature. Finally, a practical case especially developed for this work is presented, with the objective of calculating the force caused by the static and dynamic effects of the wind, and performing the optimization of the cross sections, having the minimum weight as the objective function. The practical case proposes an analysis of a 2D structure, which represent a simplification of a 3D real structure. However, a more realistic analysis should include a full 3D formulation, which is not within the scope of the present work.

3.1 Static Effect of the Wind

The plane frame used for the analysis of the wind has a total height of 21.60 m, with the width of the facade in the X-direction equal to 32 m and in the Y-direction equal to 9 m. The building arrangement is composed from eight pavements. To assess the wind forces, the same values presented in Costa's [23] work were used, with the basic wind speed being 33 m/s, the coefficients *S1* and *S3* equal to 1.00, the drag coefficient for the X direction is 1.235 and the Y direction is 0.765. The value of the coefficient *S2* and the height of the floors are shown in Table 1.

Table 1. Data for the calculation of wind forces [23].

Floor	Height (m)	Factor *S2*	Floor	Height (m)	Factor *S2*
1º	2.70	0.720	5º	13.50	0.751
2º	5.40	0.720	6º	16.20	0.773
3º	8.10	0.720	7º	18.90	0.792
4º	10.80	0.724	8º	21.60	0.809

Each level of the slab is considered as a point for the application of wind forces, as these elements present greater rigidity. Thus, it was considered that the area of influence for each node is composed of half of the upper floor and half of the lower floor, except for the load applied on the first floor, in which the entire lower floor was considered. This methodology was also adopted for this work and the results are shown in Table 2.

The results obtained in both studies are similar, however, with small variations in wind forces when compared to the results of Costa [23], this fact could be explained by numerical truncation, for example.

Table 2. Comparison of results.

Floor	Wind forces (kN)			
	Direction X		Direction Y	
	Costa [23]	Present	Costa [23]	Present
1º	55.40	55.39	9.65	9.65
2º	36.93	36.93	6.43	6.43
3º	37.15	36.93	6.47	6.43
4º	38.75	37.34	6.75	6.50
5º	41.34	40.17	7.20	6.70
6º	43.62	42.56	7.60	7.42
7º	45.67	44.68	7.96	7.78
8º	23.32	23.31	4.07	4.06

3.2 Optimization Analysis

For testing the optimization method, a well-known benchmark example was evaluated. The geometry and boundary conditions are shown in Figure 2. Here, the TLBO was used as the optimization method, with the objective of finding the cross sections of the elements that result in the minimum weight of the structure. The analyzed frame shows forces concentrated in both directions and bending moments.

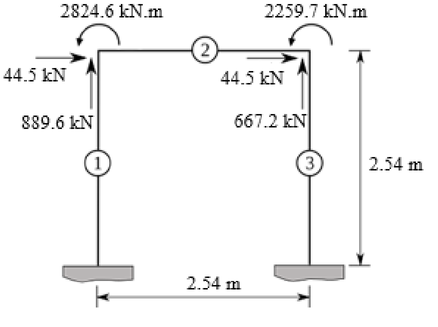

Figure 2. Plane frame optimization.

The analysis was carried out in three different cases, varying the displacement and stress constraints, according to the one presented in the work of Castro [6] and shown in Table 3. The sizing range for the areas A_i was from 0.65 to 967.74 cm^2, the modulus of elasticity E = 206.84x10^3 MPa, density ρ = 7833.41 kg/m^3, moment of inertia $I = 75\times A_i$ cm^4, and length of the neutral line $Y = I / (9\times A_i)$ cm. Khan et al. [25] and Castro [6] used continuous area variables in their analysis, and in the work carried out by Castro [6], the optimization method of genetic algorithms was used and in Khan's [25], an optimization algorithm based on constraints was developed.

Table 3. Data from the analyzed cases [6].

Case	Characteristics
I	Nodes restricted to displacement of ± 0.254 cm.
	All bars restricted to tension of ± 165.47 MPa.
II	Nodes restricted to displacement of ± 0.178 cm.
	All bars restricted to tension of ± 165.47 MPa.
III	Nodes restricted to displacement of ± 0.508 cm.

Here, discrete variables were used with discretization between the established area limits of 0.01 in^2. Results are presented in Table 4.

Table 4. Comparison of results.

Element	Cross section area (cm^2)								
	Case I			Case II			Case III		
	Khan et al. [25]	Castro [6]	Present	Khan et al. [25]	Castro [6]	Present	Khan et al. [25]	Castro [6]	Present
1	127.81	91.29	86.58	114.71	121.55	120.65	41.48	40.52	41.16
2	679.94	616.45	608.32	839.16	873.29	870.58	299.48	304.77	303.68
3	194.71	272.65	284.19	447.16	403.68	407.23	148.65	144.32	144.65
Weight (kg)	1994.22	1950.32	1947.76	2787.13	2782.13	2782.00	974.01	974.00	973.75

The results regarding the weight of the structure in the three cases analyzed were lower when using the TLBO as an optimization method, with the greatest variation occurring in case I, in which the present one studied obtained a reduction of 2.33% in relation to the weight found by Khan et al. [25]. The efficiency of the TLBO method for the optimization of frames, in which the results found in this study were lower when compared to those presented in the literature.

3.3 Study Case

In this work, a plane frame that simulates a simple building was analyzed, in which both the loads considered permanent in the structure and the variable loads were applied. For this example, it was considered a frame with 30 meters high, with 10 floors, and each floor has 3 meters in height. The facade is 10 meters long and the distance between the columns is 5 meters, as shown in Figure 3.

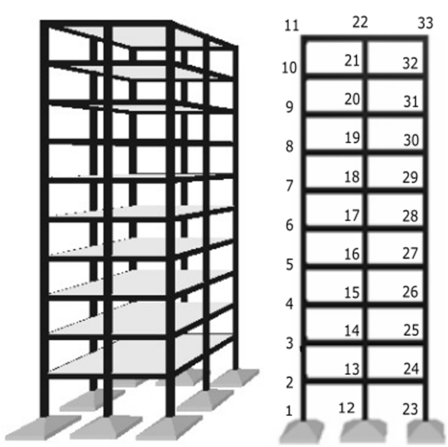

Figure 3. Case study frame.

For the structure of this frame, only the use of simple concrete was considered, with concrete fck equal to 50 MPa. The characteristics of the materials, according to NBR 6120:1980 [22], are: slab subfloor with specific weight of 21 kN/m^3 and 2.0 cm thick; ceramic coating 1.0 cm thick, having a specific weight of 18 kN/m^3; the slab 10 cm high by 5 meters long, where the specific weight of the concrete used was 24 kN/m^3; the building walls are 2.80 meters high, using a 9 cm thick perforated brick with a specific weight of 13 kN/m^3. For the utilization load, considered as a place for general use rooms and bathrooms, 2 kN/m^2 was adopted. To determine the low turbulence wind loads, the basic wind speed was 30 m/s, the topographic factor *S1* was 1.0, the probabilistic factor *S3* was 1.0 and the drag coefficient equal to 0.8. To determine the *S2* factor, the building belongs to category IV, in terms of the roughness of the land, and class B, in relation to its dimensions. The parameter for analyzing the wind effect are as follows: $p = 0.125$, $b = 0.85$, $F_r = 0.98$, for the static representation; while $\gamma = 1.2$, $\xi = 1.4$, $p = 0.23$, and $b = 0.71$, for the dynamic representation.

It is worth to point out that an initial linear dynamic analysis was accounted to obtain the first natural frequencies of the structure, being the first five frequencies: 0.81 Hz, 2.51 Hz, 4.38 Hz, 6.48 Hz and 8.86 Hz, respectively. The FEM commercial software Abaqus 2020 student edition was used to this end. The value of the first natural frequency (0.81 Hz) clearly does not attend the Brazilian normative NBR 6118:2014 [11], which requires a minimum value of 4.2 Hz for the first natural frequency, thus, a dynamic analysis is herewith justified.

Definition of structural optimization parameters

To carry out the analysis of the structure presented above, the NBR 6118:2014 [11] standard was used according to the class of concrete adopted (f_{ck} 50 MPa), the material's elasticity module and the calculation stress limits. To determine the modulus of elasticity it was adopted that the coarse aggregate to be used in the concrete will be the basalt, resulting in a value of 43.95 GPa. The ultimate stress in compression and traction were 25.3 MPa and 1.7 MPa, respectively. Regarding the limit displacement used in the structure calculation, it was considered *H/1700*, as presented in the item 13.3 of NBR 6118:2014 [11], where *H* is the total height of the building. Considering the analysis for the ultimate limit state of the structure, an equal weighting coefficient of 1.4 was used for the combination of permanent and variable actions.

Two groups of areas were defined for the optimization of the structure, one corresponding to the columns and the other to the beams. For the columns, a square section was used, with a minimum width of 19 cm and a maximum of 70 cm, resulting in a minimum area of 361 cm^2 and a maximum area of 4900 cm^2. As for the beams, it was adopted that the base would be fixed at 15 cm and the height could vary from 20 cm to 60 cm, with that the minimum area would be 300 cm^2 and the maximum 900 cm^2.

As established by Camp and Farshchin [14], for the optimization process to present good results convergence, a population of 75 students was adopted for this study, for the teacher factor (F_T) the value of 2 and for the exponent of the penalty (ε), the value of 2 was also adopted. At each iteration, 150 analyzes are performed, and the best result will be determined when 7500 analyzes are performed without changes, that is, 50 iterations, or until reaching the limit maximum of 200 iterations. To carry out the optimization study, the structure was divided into two main groups, one for beams and the other for columns. Each group was subdivided into three, in which the first went to the elements up to the 4th floor, the second group up to the 7th floor and the third group up to the 10th floor, both for beams and columns. In Table 5 the elements are identified in each group through the connection nodes. All elements that belong to the same group will have the same cross-sectional area.

Table 5. Division of the structure into groups.

Group	Type	Elements
1	Column	1:(1,2), 2:(2,3), 3:(3,4), 4:(4,5), 11:(12,13), 12:(13,14), 13:(14,15), 14:(15,16), 21:(23,24), 22:(24,25), 23:(25,26), 24:(26,27)
2		5:(5,6), 6:(6,7), 7:(7,8), 15:(16,17), 16:(17,18), 17:(18,19), 25:(27,28), 26:(28,29), 27:(29,30)
3		8:(8,9), 9:(9,10), 10:(10,11), 18:(19,20), 19:(20,21), 20:(21,22), 28:(30,31), 29:(31,32), 30:(32,33)
4	Beam	31:(2,13), 32:(3,14), 33:(4,15), 34:(5,16), 41:(13,24), 42:(14,25), 43:(15,26), 44:(16,27)
5		35:(6,17), 36:(7,18), 37:(8,19), 45:(17,28), 46:(18,29), 47:(19,30)
6		38:(9,20), 39:(10,21), 40:(11,22), 48:(20,31), 49:(21,32), 50:(22,33)

DISCUSSION

During the execution of the structural optimization some parameters are fixed, such as the characteristics of the material used in the structure, in this case the concrete, and the constraints of displacement and stress that were considered. The parameters that are of variable characteristics are the intervals adopted for the cross-sectional areas, whose purpose of optimization is to find the cross-sections values that minimize the structural weight and that meet the imposed constraints. Loads acting on the structure can be classified into external and internal loads. The external loads are determined by the action of the winds, so that their values do not vary during the optimization process, as they do not depend on the cross-sectional area of the elements. The area of influence used in the calculation of wind forces was considered according to the methodology presented in the example in section 3.1. Thus, Table 6 presents the values obtained for wind forces considering the static model and the simplified dynamic model. Internal loads are determined considering the cross-sectional area of the elements, i.e., these loads vary during the optimization process and, therefore, do not have fixed values. The internal loads are determined by the concrete structure itself, through the loads of slabs.

The forces in the static model were superior to the forces calculated by the simplified model on the first floors, whereas on the last floors the values were already closer, and, on the last two floors, the forces of the simplified model have already become greater. This same relationship occurred in a work developed by Almeida and Vidoto [26], who stressed the importance of performing this dynamic analysis so that these major forces are evaluated and considered during the design project.

Table 6. Forces caused by the wind.

Floor	Static model (kN)	Simplified dynamic model (kN)
1º	10.20	3.50
2º	8.09	3.67
3º	8.95	4.92
4º	9.62	6.12
5º	10.17	7.32
6º	10.64	8.51
7º	11.06	9.69
8º	11.44	10.89
9º	11.78	12.08
10º	6.05	6.64

The wind forces in the static model do not vary much from one floor to the next, as the dependence on height is only determined by the factor *S2*. Thus, even if the height increases, the strength value undergoes small changes. In the case of the simplified dynamic, the height establishes a direct relationship for the determination of the dynamic pressure and, with this, with each floor the forces present greater variations in relation to the previous one.

The results obtained, from the structural optimization, of the cross sections of the column and beam elements as well as the weight of the structure, are presented in Table 7, considering that in the first case, no forces were applied due to the wind in the structure and in the in other cases, the forces applied were according to the type of wind analysis that was considered, whether static or dynamic. According to the results presented in Table 7, when the analyzed structure was optimized without considering the loads caused by the action of the wind, the structural elements of both columns and beams presented the areas of minimum cross sections, as in this case there was only consideration of loads related to the calculation of the concrete structure itself. In the other two cases in which the wind forces were considered, the values of the areas of the structural elements underwent significant variations, as these forces are considered to have a relevant influence on the behavior of the structure.

Table 7. Cross sections and structure weight.

Group	Analysis without wind forces		Analysis with static wind		Analysis with dynamic wind	
	Dimensions (cm)	Area (cm^2)	Dimensions (cm)	Area (cm^2)	Dimensions (cm)	Area (cm^2)
1	19 x 19	361	50 x 50	2500	66 x 66	4356
2	19 x 19	361	39 x 39	1521	36 x 36	1296
3	19 x 19	361	28 x 28	784	25 x 25	625
4	15 x 20	300	15 x 52	780	15 x 60	885
5	15 x 20	300	15 x 48	720	15 x 40	600
6	15 x 20	300	15 x 46	690	15 x 42	630
Weight (kg)	14997.600		54176.400		67435.920	
Nº iterations	55		87		79	
Nº analyzes	8435		13299		12083	

When comparing only the weight, the structure showed an increase, compared to the analysis without considering the wind forces, of approximately 261.23% and 349.64%, for the analysis with static wind and dynamic wind, respectively. When analyzing the weight of the structure in the two cases in which the wind forces were considered, the highest value was found in the analysis with the dynamic wind, but it is observed that this difference in weight was due to the fact of the groups 1 and 4 the columns and the beams up to the fourth floor have larger sections, as the other groups have smaller sections than in the static analysis. As the wind forces in the dynamic analysis were smaller, the sections reduced in size, however, on the last floors these forces were higher and with that the structure presented larger sections at the base so that it would be more resistant to the efforts caused by the wind forces in the upper part of the frame. Thus, the higher the structure, the greater the need to verify its behavior regarding the dynamic characteristics of wind forces and not just the static effect. Figure 4 shows, for the three cases analyzed, the convergence process of the objective function and the optimized structure with the cross-sectional areas in proportion. According to Figure 4, the convergence of the TLBO method occurs with few iterations, with the greatest reduction at the beginning of optimization occurred in the case in which the dynamic wind was considered. Although more iterations are performed than the amount presented, in iteration 40 there has already been convergence to the final value. The cross-sectional areas presented in Table 7 can be observed in proportion in Figure 4 through the illustrations of the structure in each case.

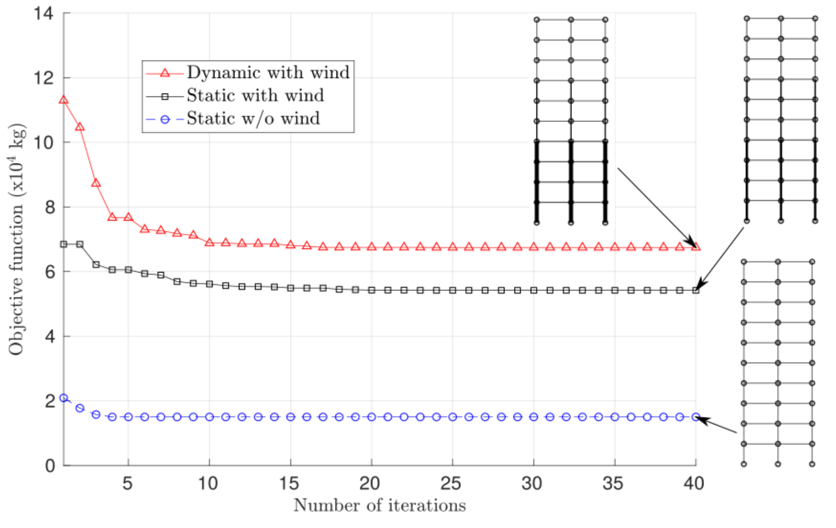

Figure 4. Convergence process for the three cases analyzed.

4 CONCLUSIONS

The main objectives of this paper were to analyze the influence of wind action on a building, considering both the static and simplified dynamic model loads of NBR 6123:1988 [12], as well as to perform the optimization of the structural weight of a building through a 2D model. Both objectives were also analyzed together, through the application of the practical case. From this paper, the following conclusions were obtained:

- Regarding the wind action, the static model presented for most of the points of application of forces a higher value than the simplified dynamic model, however the forces generated by the dynamic model were higher than the static model in the last floors, because in this model there is consideration of the height of the floor and the higher it is, the greater the influence of the wind, a parameter that is not considered in the static model.
- From the cases analyzed in the structural optimization it was obtained that the simplified dynamic model was the one that presented the greatest weight, whose cross-sectional areas were larger than the static model only in the structural elements of the lower part of the structure, because as the wind forces of the dynamic model were higher in the last floors the efforts generated in the lower region were greater.
- According to the convergence process for the cases analyzed in the optimization, the TLBO method that was used showed fast convergence, because with few iterations the final value was already obtained.
- The methodology herewith presented can simplify real structures analysis to a 2D frame optimization model, which can be useful as a first design result. In the case of more realistic building cases, it is necessary to expand the

methodology and perform the modelling to analyze a 3D structure, implying into the consideration of 3D frame elements, for example.

- For this paper, the wind action loads were considered only in relation to two models of the NBR 6123:1988 [12] standard, because one of the objectives of the paper was to verify the application of the methods recommended by the standard. However, if the objective is related to the analysis of the wind action in situations with a high degree of similarity with the real wind, it is necessary to consider the non-deterministic nature of the winds, with which one can apply, e.g., the Synthetic Wind Method that uses Monte Carlo simulation to determine the loads.
- Through the proposed methodology it is possible to determine an optimized structure through the weight objective function and considering the constraints of displacements and stresses. A possible expansion of the modelling carried out would be to consider the effect of the soil-structure interaction, so that the pressure that the structure causes in the soil can be analyzed and how this interaction influences the optimization.

REFERENCES

[1] Z. A. Siddiqi, R. Hameed, and U. Akmal, "Comparison of different bracing systems for tall buildings," *Pak. J. Engg. Appl. Sci*, vol. 14, pp. 17–26, Jan 2004.

[2] R. A. Souza, “Controle passivo/ativo das oscilações de estruturas esbeltas por meio de dispositivos fluido-dinâmicos,” M.S. thesis, Fed. Univ. Rio de Janeiro, Rio de Janeiro, 2003.

[3] H. L. Soriano, *Introdução à Dinâmica das Estruturas.* Rio de Janeiro: Elsevier, 2014.

[4] P. Mendis, T. Ngo, N. Haritos, and A. Hira, "Wind loading on tall building," *Eletronic J. Struct. Eng.*, vol. 7, pp. 41–54, 2007.

[5] A. Barile, L. S. Bastos, and J. G. S. Silva, "Human comfort assessment of buildings subjected to nondeterministic wind dynamic loadings," *Rev. IBRACON Estrut. Mater.*, vol. 13, no. 4, pp. 1–13, 2020, http://dx.doi.org/10.1590/S1983-41952020000400002.

[6] L. C. L. B. Castro, “Algoritmo genético para otimização de estruturas reticuladas,” M.S. thesis, Univ. Brasília, Brasília, 2003.

[7] F. Gomez, B. F. Spencer Jr., and J. Carrion, "Topology optimization of buildings subjected to stochastic wind loads," *Probab. Eng. Mech.*, vol. 64, 103127, 2021.

[8] L. S. Tapajós, J. A. T. Ferreira, A. F. Lima No., M. R. Teixeira, and M. P. Ferreira, "Effect of wind in the design of reinforced concrete buildings," *Rev. IBRACON Estrut. Mater.*, vol. 9, no. 6, pp. 883–910, 2016.

[9] M. Kripka, J. T. Boscardin, and S. D. Casteli, "Topology optimization of reinforced concrete plane frames”, Rev," *Sul-americana Eng. Estrutural*, vol. 13, no. 2, pp. 45–53, 2016.

[10] B. D. Breda, T. C. Pietralonga, and E. C. Alves, "Optimization of the structural system with composite beam and composite slab using Genetic Algorithm," *Rev. IBRACON Estrut. Mater.*, vol. 13, no. 6, e13602, 2020.

[11] Associação Brasileira de Normas Técnicas. *Projeto de Estruturas de Concreto - Procedimento*, NBR 6118, 2014.

[12] Associação Brasileira de Normas Técnicas. *Forças Devidas ao Vento em Edificacações*, NBR 6123, 1988.

[13] C. V. Camp, "Design of space trusses using big bang-big crunch optimization," *J. Struct. Eng.*, vol. 133, pp. 999–1008, 2007, http://dx.doi.org/10.1061/(ASCE)0733-9445(2007)133:7(999).

[14] C. V. Camp and M. Farshchin, "Design of space trusses using modified teaching-learning based optimization," *Eng. Struct.*, vol. 62-63, pp. 87–97, 2014, http://dx.doi.org/10.1016/j.engstruct.2014.01.020.

[15] R. V. Rao, V. J. Savsani, and D. P. Vakharia, "Teaching-learning-based optimization: a novel method for constrained mechanical design optimization problems," *Comput. Aided Des.*, vol. 43, no. 3, pp. 303–315, 2011, http://dx.doi.org/10.1016/j.cad.2010.12.015.

[16] V. Toğan, "Design of planar steel frames using teaching-learning based optimization," *Eng. Struct.*, vol. 34, pp. 225–232, Jan 2012, http://dx.doi.org/10.1016/j.engstruct.2011.08.035.

[17] E. S. Chávez, “Análise estrutural de edifício alto submetido às pressões flutuantes induzidas pela ação do vento,” M.S. thesis, Fed. Univ. Minas Gerais, Belo Horizonte, 2006.

[18] M. Islam, A. Siddique, and A. Murshed, “Sustainable development in drift control of tall buildings due to wind load: critical analyses of the structural systems,” in *Inter. Conf. Civ. Eng. Sustain. Dev.*, 2012, pp. 1-7.

[19] C. Slongo, “Análise dinâmica de uma torre metálica de telecomunicações utilizando o método do vento sintético,” M.S. thesis, Fed. Univ. Paraná, Curitiba, 2016.

[20] R. M. B. Cerutti, “Estudo comparativo de métodos para análise aerodinâmica de estruturas submetidas ao vento turbulento,” M.S. thesis, Fed. Univ. Rio de Janeiro, Rio de Janeiro, 2017.

[21] P. R. Santos, “Análise e cálculo de elementos estruturais em concreto armado de um edifício residencial,” M.S. thesis, Fed. Univ. Santa Catarina, Florianópolis, 2014.

[22] Associação Brasileira de Normas Técnicas, *Cargas para o Cálculo de Estruturas de Edificações*, NBR 6120, 1980.

[23] J. P. D. Costa, *A Influência do Efeito de Vento na Análise Estrutural de Edifícios.* Belo Horizonte: Univ. Fed. Minas Gerais, 2013.

[24] P. S. S. Bastos, *Fundamentos do Concreto Armado.* Bauru: Univ. Est. Paul., 2019.

[25] M. R. Khan, K. D. Willmert, and W. A. Thornton, "An optimality criterion method for large-scale structures," *AIAA J.*, vol. 17, pp. 753–761, May 1979, http://dx.doi.org/10.2514/3.61214.

[26] D. C. Almeida and T. A. H. Vidoto, "Análise comparativa dos métodos estático e dinâmicos da ação do vento em edifícios esbeltos de concreto armado segundo a NBR 6123/1988," M.S. thesis, Fed. Technol. Univ. Paraná, Curitiba, 2013. [Online]. Available: http://repositorio.roca.utfpr.edu.br/jspui/handle/1/2130

Author contributions: EUC: conceptualization, investigation, methodology, validation. RQR: conceptualization, formal analysis, investigation, methodology, supervision. LQM: supervision, writing-review & editing. FFK: conceptualization, investigation. PSS: conceptualization, investigation. APCQ: conceptualization, writing-review & editing.

Editors: Leandro Mouta Trautwein, Guilherme Aris Parsekian

Rev. IBRACON Estrut. Mater., vol. 15, no. 1, e15110, 2022

IBRACON Structures and Materials Journal
Revista IBRACON de Estruturas e Materiais
ISSN 1983-4195 ismj.org

ORIGINAL ARTICLE

Seismic reliability assessment of a non-seismic reinforced concrete framed structure designed according to ABNT NBR 6118:2014

Avaliação da confiabilidade sísmica de um pórtico de concreto armado não sismo-resistente dimensionado de acordo com a ABNT NBR 6118:2014

Eduardo Marques Vieira Pereira[a]
Gustavo Henrique Ferreira Cavalcante[a]
Isabela Durci Rodrigues[b]
Luiz Carlos Marcos Vieira Júnior[a]
Gustavo Henrique Siqueira[a]

[a]Universidade Estadual de Campinas – UNICAMP, Faculdade de Engenharia Civil, Arquitetura e Urbanismo, Departamento de Estruturas, Campinas, SP, Brasil

[b]Universidade de São Paulo – USP, Escola de Engenharia de São Carlos, Departamento de Estruturas, São Carlos, SP, Brasil

Received 18 March 2021
Accepted 26 June 2021

Abstract: Due to the paucity of studies regarding the seismic assessment of buildings in Brazil, this study aims to present and discuss a seismic reliability assessment of a reinforced concrete framed structure designed according to the Brazilian standard ABNT NBR 6118:2014 without the consideration of the seismic design requirements of ABNT NBR 15421:2006. Herein, fragility functions are generated through probabilistic seismic demand analysis, and integrated with hazard curves for Northeastern Brazil to generate regional failure probability maps for three limit-states: Immediate Occupancy (IO), Life Safety (LS), and Collapse Prevention (CP). The results indicated that the building performance is adequate for IO; however, for LS and CP, an unacceptable performance is observed.

Keywords: reinforced concrete, earthquakes, fragility functions, reliability.

Resumo: Diante da escassez de estudos sobre a avaliação sísmica de edificações brasileiras, esse estudo tem como objetivo apresentar e discutir a avaliação da confiabilidade sísmica de um pórtico de concreto armado dimensionado de acordo com a ABNT NBR 6118:2014 sem a consideração do dimensionamento sísmico prescrito pela ABNT NBR 15421:2006. Neste trabalho, funções de fragilidade são geradas através de análises probabilísticas de demanda sísmica e integradas com curvas de ameaça sísmica da região Nordeste do Brasil para gerar mapas regionais de probabilidade de falha para três estados limites: Ocupação Imediata (IO), Segurança à Vida (LS) e Prevenção ao Colapso (CP). Os resultados indicam que o desempenho da edificação é adequado para IO, mas para LS e CP, um desempenho inaceitável é observado.

Palavras-chave: concreto armado, sismos, funções de fragilidade, confiabilidade.

How to cite: E. M. V. Pereira, G. H. F. Cavalcante, I. D. Rodrigues, L. C. M. Vieira Júnior, and G. H. Siqueira, "Seismic reliability assessment of a non-seismic reinforced concrete framed structure designed according to ABNT NBR 6118:2014," *Rev. IBRACON Estrut. Mater.*, vol. 15, no. 1, e15110, 2022, https://doi.org/10.1590/S1983-41952022000100010

Corresponding author: Eduardo Marques Vieira Pereira. E-mail: eduardo.marquesvp@gmail.com
Financial support: Coordenação de Aperfeiçoamento de Pessoal de Nível Superior - Brasil (CAPES) - Finance Code 001; São Paulo Research Foundation (FAPESP) - Finance Code 2018/23304-9.
Conflict of interest: Nothing to declare.

1 INTRODUCTION

Brazil is located in a stable mid-plate South America region. The country, however, presents a considerable history of small-to-moderate earthquakes (Berrocal et al. [1], Assumpção et al. [2]). According to [2], in Brazil, moment magnitude (M) 5.0 events occur on average every five years, whereas M6.0 events are expected on average every 50 years. Since seismic risk is a combination of seismic hazard, exposure and structures' vulnerability, and although strong earthquakes are not expected or less frequent, if buildings are not properly detailed and designed to withstand seismic loads, high losses due to small-to-moderate events may be expected. For instance, Nievas et al. [3] present an extensive database of events worldwide with M from 4.0 to 5.5 for which damage and/or casualties have been reported. It also has to be highlighted damaging events that have occurred in Brazil, e.g., the João Câmara earthquake in Rio Grande do Norte state and the Itacarambi earthquake in Minas Gerais state ([2], Takeya et al. [4]); the latter causing the first reported fatal victim due to earthquakes in Brazil.

However, the first earthquake-resistant structural design code for buildings in Brazil, ABNT NBR 15421:2006 [5], was published only in 2006. However, modern ductile design principles, such as capacity-based design and special detailing rules (see Fardis [6]), were not included in the code. Before 2006, seismic loads have been traditionally considered only in special structures such as nuclear power plants (Santos and Lima [7]). A survey conducted by Miranda et al. [8] indicates that, even after ABNT NBR 15421:2006, seismic design may not have been properly considered by engineers for several reasons such as the lack of studies showing its importance. Moreover, the inconsistencies in the provisioned design acceleration map zones outlined by recent preliminary maps and some researchers ([2], Lopes and Nunes [9], Dourado [10], Petersen et al. [11], Nóbrega et al. [12]), as well as the possibility of induced earthquake events (Barros et al. [13], Silva et al. [14]), indicate that buildings in some regions may experience ground motions intensities higher than they were designed for.

Despite the possibility of potentially damaging earthquakes in Brazil, studies regarding the seismic assessment of the buildings in the country are still scarce. Structural seismic performance, as well as the adequacy of code provisions, can be assessed by means of reliability analyses using fragility functions (FF) and hazard curves. The former depicts the conditional probability that a structure will exceed a limit-state for various levels of ground shaking represented by an intensity measure (IM) (Siqueira et al. [15]), whereas the latter depicts the mean annual frequency of exceedance of the IM levels for the structure's site (McGuire [16]); both concepts are present in the performance-based earthquake engineering context and can be used to assess the failure probability of a structure during its lifetime (Krawinkler [17]).

Fragility functions can be empirical-based or analytical-based. The empirical-based FF can be derived using past earthquake survey damage reports, whereas the analytical-based FF are obtained through numerical analyses, especially for low seismic activity regions [15], e.g., Brazil, where field data of earthquakes is insufficient. Hazard curves are derived through probabilistic seismic hazard analysis (PSHA) of a specific region or site [16]. While there are a few PSHA studies for Brazil ([2], [10], [11], Souza et al. [18], Almeida et al. [19], Borges et al. [20], Alves [21], Nóbrega et al. [22]), studies focusing on fragility functions are currently lacking, as can be observed in the database presented in Silva et al. [23], although several were conducted worldwide (Ramamoorthy et al. [24], Ellingwood et al. [25], Ramamoorthy et al. [26], Kappos and Panagopoulos [27], Rajeev and Tesfamariam [28], Jeon et al. [29], Amirsaradi et al [30]).

This study aims to develop fragility functions for a reinforced concrete (RC) framed structure designed according to the Brazilian code ABNT NBR 6118:2014 [31] but with no earthquake resistant design, and perform its reliability assessment. Non-linear dynamic analyses using ground motion records are performed on finite element models of the RC structure to estimate the seismic demand. Fragility functions are then generated, and the failure probability for three limit states in a 50-year period is assessed by their convolution with seismic hazard curves for Northeastern Brazil. The results provide insight on the adequacy of the analyzed building in different locations through a regional failure probability map.

2 RELIABILITY ANALYSIS AND FRAGILITY FUNCTIONS METHODOLOGY

Within the framework of the performance-based earthquake engineering, structural performance can be defined as the probability that the seismic demand (D) on a structural system exceeds its structural capacity (C) (Cornell et al. [32]), which can also be stated in terms of fragility functions for several levels of ground motions intensity measure (IM). Both D and C inherently follow a distribution function due to uncertainties in ground motions characteristics (i.e., record-to-record variability), in material properties, geometry, construction quality, and modelling issues [26]; and, therefore, a probabilistic approach is required. Under the common assumption that the demand, the capacity, and the fragility function follow lognormal distributions, the structural fragility of a system can be computed in a closed-form expression as follows (Equation 1):

$$P[D \geq C \mid IM] = \Phi\left[\frac{\ln\left(\frac{S_D}{S_C}\right)}{\sqrt{\sigma_{D|IM}^2 + \sigma_C^2 + \sigma_M^2}}\right] \tag{1}$$

Where Φ is the standard normal cumulative distribution function; S_D and $\sigma_{D|IM}$ are the median and logarithmic dispersion of the seismic demand, respectively; S_C and σ_C are the capacity's median and dispersion, respectively; and σ_M represents the uncertainty in modelling the structural, e.g., non-simulated collapse modes. Note that the dispersion σ may also be referred as β in the literature, but herein we adopted σ to avoid confusion with the reliability index symbol (discussed later in this section).

The probabilistic parameters of the demand (S_D and $\sigma_{D|IM}$) are obtained by means of a cloud analysis (Jalayer et al. [33]), which consists in performing non-linear dynamic analyses using unscaled ground motion records on numerical models of the structure. Each model is generated considering materials and system's properties as random variables, whose values are sampled from their distribution using Latin Hypercube Sampling (McKay et al. [34]), and is randomly paired with each ground motion, as performed by Celik and Ellingwood [35]. The adopted random variables are indicated in Table 1: concrete strength (f_c), yield strength of longitudinal reinforcement (f_y), yield strength of transverse reinforcement (f_{yw}), modulus of elasticity of reinforcement (E_s), and damping ratio (ζ). The values in Table 1 should not be confused with the parameters used in design that consider characteristic values of materials strength and/or adopt code-prescribed values.

Table 1. Random variables adopted.

Determination	Distribution	Mean	Coefficient of variation	Reference
f_c (MPa)	Normal	33.01	0.15	Nogueira [36]
f_y (MPa)	Normal	576.00	0.08	Nogueira [36]
f_{yw} (MPa)	Normal	690.93	0.08	Nogueira [36]
E_s (GPa)	Normal	201.00	0.033	Mirza and MacGregor[37]
ζ	Log-normal	0.042	0.76	Healey et al. [38]

The maximum structural demand and the intensity measure of each simulation are related through a linear regression in the logarithmic space to determine the Probabilistic Seismic Demand Model (PSDM); that is, S_D and $\sigma_{D|IM}$. Based on [32], the relation between S_D and IM is assumed to follow the power law in Equation 2, which can be restated in the logarithmic space through Equation 3. The coefficients *a* and *b* are obtained directly from the linear regression, whereas $\sigma_{D|IM}$ is obtained by Equation 4, where N is the number of simulations and di is the maximum demand on the structure.

$$S_D = a\left(IM\right)^b \tag{2}$$

$$\ln\left(S_D\right) = \ln\left(a\right) + b \cdot \ln\left(IM\right) \tag{3}$$

$$\sigma_{D|IM} = \sqrt{\frac{\sum\left(\ln(d_i) - (\ln\left(a\left(IM\right)^b\right)\right)^2}{N-2}} \tag{4}$$

Herein, the spectral acceleration fixed at the 1s period, Sa(T = 1s), is adopted as the intensity measure (IM). It is chosen because there are large scale seismic hazard studies for South America using this IM [11], from which we can obtain the hazard curves. Moreover, the authors evaluated other two IM available from the hazard curves by [11]: peak ground acceleration and spectral acceleration fixed at the 0.2s period; both performed poorer than the adopted IM considering the proficiency and the sufficiency criteria described in Padgett et al. [39] and in Du et al. [40], thereby were excluded.

Ground motion records are applied in both orthogonal horizontal directions of the numerical model, therefore the geometric mean of the two orthogonal components is used as IM (Baker and Cornell [41]). The demand on the structure is measured by the inter-story drift ratio (IDR) observed during analysis among all floors, since it is well related to structural damage and have also been adopted by several researchers and design standards ([24], [25], Whittaker et al. [42]). IDR is defined by the relative displacements between floors divided by the floor height; the maximum IDR value observed among all floors in the analysis represents the seismic demand.

The structural capacity (C) can be defined as the maximum response that a structure can withstand without reaching a limit state (Wen et al. [43]). Three limit states are considered: Immediate Occupancy (IO), Life Safety (LS) and Collapse Prevention (CP). These limit states are qualitatively described in terms of building performance and functionality by ASCE/SEI 41-17 [44] (Table 2), in which the damage pattern observed depicts consequences that are readily identifiable in post-earthquake situations, and are meaningful to society. In addition, they have been widely adopted by researchers; thus, their use herein facilitates further comparisons with other works [35]. Other limit states related to structural and nonstructural damage, repairment measures and down-time can be found elsewhere ([24], FEMA P-58-1 [45], HAZUS MH-R1 [46]).

Table 2. Qualitative description of the limit states.

Limit state	Description
Immediate Occupancy (IO)	No permanent drift. Structure substantially retains its original strength and stiffness. Equipment and contents are generally secure but might not operate due to mechanical failure or lack of utilities. Some cracking of facades, partitions, and ceilings. Elevators can be restarted. Fire protection operable. Continued occupancy likely.
Life Safety (LS)	Some residual strength and stiffness left in all stories. Gravity-load-bearing elements function. Building might not be economical to repair. Falling hazards, such as parapets, mitigated, but many architectural, mechanical, and electrical systems are damaged. Continued occupancy might not be likely before repair.
Collapse Prevention (CP)	Small residual stiffness and strength to resist lateral loads, but gravity load-bearing columns function. Large permanent drifts. Some exits blocked. Extensive damage to nonstructural components. Infills and parapets failed or at incipient failure. Building is near collapse in aftershocks and should not continue to be occupied.

Values of S_C for IO, LS and CP are adopted as 0.5%, 1.0% and 2.0%, according to [24]. The same value of 0.3 is assumed for σ_C for all limit states, and also for σ_M, as suggested by [43]. One should note that adopting the same σ_C for all limit states is a simplification, since higher limit states present a greater uncertainty due to the complexity of structural behavior with the failure approximation (Tavares et al. [47]).

The fragility function and its lognormal parameters can then be determined from Equation 5 following a substitution of the linear regression parameters (see Equation 3). The values of θ and σ in Equations 6 and Equation 7 are the fragility functions' median and dispersion, respectively.

$$P[LS \mid IM] = \Phi\left[\frac{\ln(IM) - \dfrac{\ln(S_C) - ln(a)}{b}}{\dfrac{\sqrt{\sigma_{D|IM}^2 + \sigma_C^2 + \sigma_M^2}}{b}}\right] \tag{5}$$

$$\theta = \exp\left(\frac{\ln(S_C) - \ln(a)}{b}\right) \tag{6}$$

$$\sigma = \frac{\sqrt{\sigma_{D|IM}^2 + \sigma_C^2 + \sigma_M^2}}{b} \tag{7}$$

Once the fragility functions are defined, the mean annual frequency of exceedance of the limit state i (λ_i) is computed using the basic reliability theorem in Equation 8 (Melchers and Beck [48]), where $F_c(IM)$ is the fragility function and $f_d(IM)$ is the derivative of a hazard curve. The annual probability of failure (p_f) over a period of time t is determined according to Equation 9, and the Reliability Index (β) according to Equation 10. The obtained values of p_f and β can be compared to prescribed acceptance criteria found in literature or codes to check if the structural safety is adequate or not. A summary of the methodology is presented in Figure 1.

$$\lambda_i = \int_{IM} F_{C,i}\left(IM\right) f_d\left(IM\right) dIM \tag{8}$$

$$p_f = 1 - e^{-\lambda \cdot t} \tag{9}$$

$$\beta = -\Phi^{-1}\left(p_f\right) \tag{10}$$

The hazard curves developed by [11] are adopted herein, because they are publicly available for several geographic coordinates in South America, and ready for use in engineering applications, unlike the results of other hazard studies in Brazil. A class D soil is considered in this study; therefore, the accelerations must be amplified, because the reference soil in [11] is the limit between classes B and C. The soil amplification factors of ASCE/SEI 7-16 [49] are used for this, since the reference soil is the same. The hazard curves and the generated fragility functions paper are applied in Equation 8 to estimate the failure probability of the RC building at a regional scale in Northeastern Brazil, selected due to the relatively higher seismicity of this region. Maps of the estimated failure probability for the three limit states are generated to depict where the structure would experience unacceptable performance according to the criteria reported in the literature.

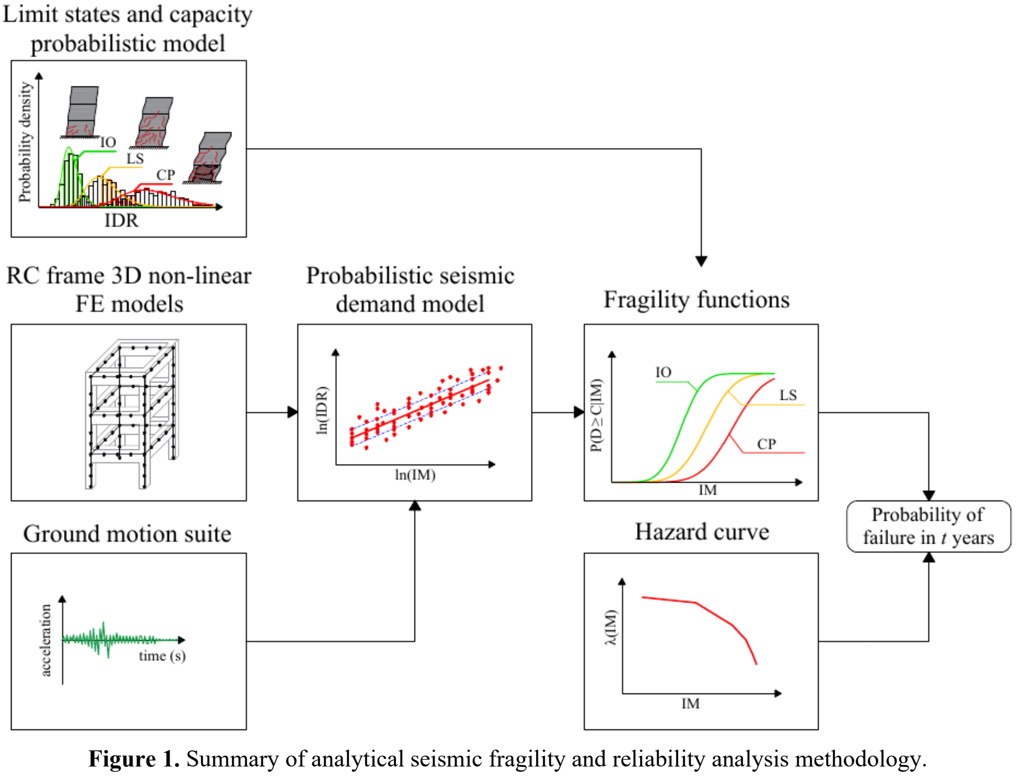

Figure 1. Summary of analytical seismic fragility and reliability analysis methodology.

Herein, the β values adopted by Priyadarshini et al. [50] are selected to evaluate the adequacy of the analyzed structure for each limit state (Table 3). These values are somewhat consistent and less conservative than the ones proposed by the Probabilistic Model Code [51] and ISO 2394 [52]. Regarding Collapse Prevention, they are more conservative than the one required by [49] (i.e., p_f of 1% in 50 years), but less conservative than other values used to generate seismic design maps in other countries (see Silva et al. [53]). Accordingly, the selected values represent a compromise between the less and more restrictive criteria found in the literature. The acceptable reliability depends on the consequences of failures and the cost of mitigating measures, as well as any other variables that somehow affect society, consequently the required reliability for hospitals or taller buildings, for example, should be more stringent. The values of p_f (t = 50 years) in Table 3 are used afterwards to verify if the expected seismic performance of the building described in the next section is adequate or not.

Table 3. Acceptance criteria in terms of annual failure probability (p_f) and reliability index (β) for each limit state.

Limit state	β (t = 1 year)	p_f (t = 1 year)	p_f (t = 50 year)
IO	2.5	0.0062	0.2666
LS	3.0	0.0013	0.0629
CP	4.0	$3.167 \cdot 10^5$	0.0016

2.1 Reinforced concrete building design

A symmetrical three-story three-bay 3D RC frame designed according to ABNT NBR 6118:2014 [31] is analyzed. A low-rise building is assessed because this typology is common in the Brazilian context (e.g., [14]), and tends to be more critical for seismic loads. Taller buildings have some inherent strength already provided by the wind load design, and are generally subjected to lower seismic loads due to the higher period of vibration. The elements' cross-section and the building's dimensions (Figure 2) are not necessarily representative of a specific building class in Brazil, since this definition would require an in-depth statistical study of several real buildings, which it is out of the scope of this paper; however, the adopted characteristics are enough to provide an overview of the expected seismic performance of low-rise frames. The number of bays has minor influence on the dynamic response of RC frames (Gkimprixis et al. [54]), hence three bays are assumed. Future studies should focus on other type of structures with different designs, and the consideration of masonry infills and soil-structure interaction.

The structure is for residential use, designed considering wind (30m/s basic speed) and out-of-plumbness as lateral loads, presents a C25 concrete class, and CA-50 and CA-60 steel reinforcement. No seismic provisions were considered, as it is the purpose of this work. Details concerning the elements' cross-section and the floor plan dimension are presented in Figure 2. All columns present 4Ø10.0mm as longitudinal reinforcement, equivalent to a 0.50% reinforcement ratio, and Ø5.0mm stirrups every 12 cm as transverse reinforcement. For beams, the longitudinal reinforcement ratio ranges from 0.42% to 1.28% depending on the beam and the section's position in the span, and the shear design resulted in the minimum shear reinforcement ratio required by the code.

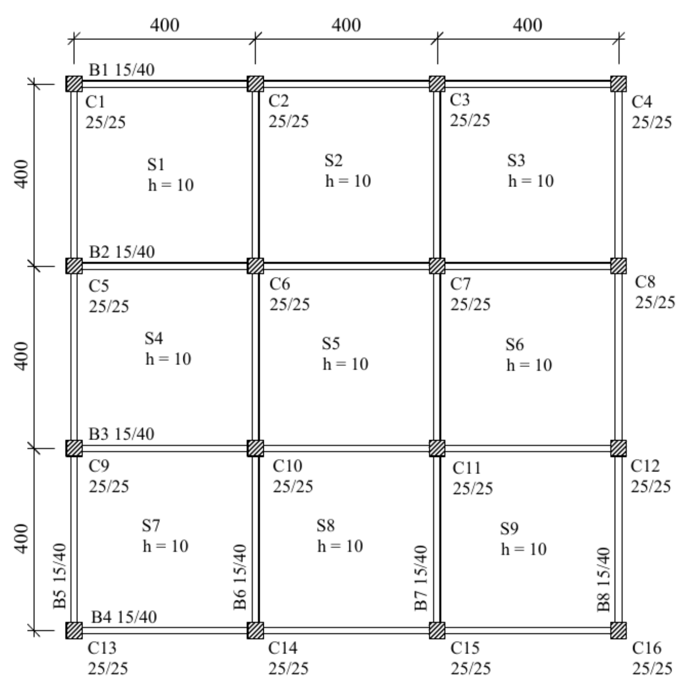

Figure 2. Designed floor plan, dimensions (in centimeters), and structural elements (not in scale).

2.2 Numerical model

Three-dimensional finite element models of the framed structure are generated in OpenSees (McKenna et al. [55]) (Figure 3). Reinforced concrete elements are modelled with displacement beam-column elements with spread plasticity and fiber sections; each beam and column with five and three finite elements, respectively. This modelling approach enables one to consider the confined concrete section core and unconfined concrete cover, as well as the longitudinal reinforcement, and the effect of physical non-linearities along the elements' length. Vertical loads are uniformly distributed along beams and calculated according to the tributary area considering the combination 1.1(D + 0.25L), as per [44], where D and L are the dead loads and live loads, respectively. Masses are lumped into column's nodes at floor level, and calculated according to the same combination. A modal analysis of the building's numerical model revealed a mean fundamental period of 0.60 seconds.

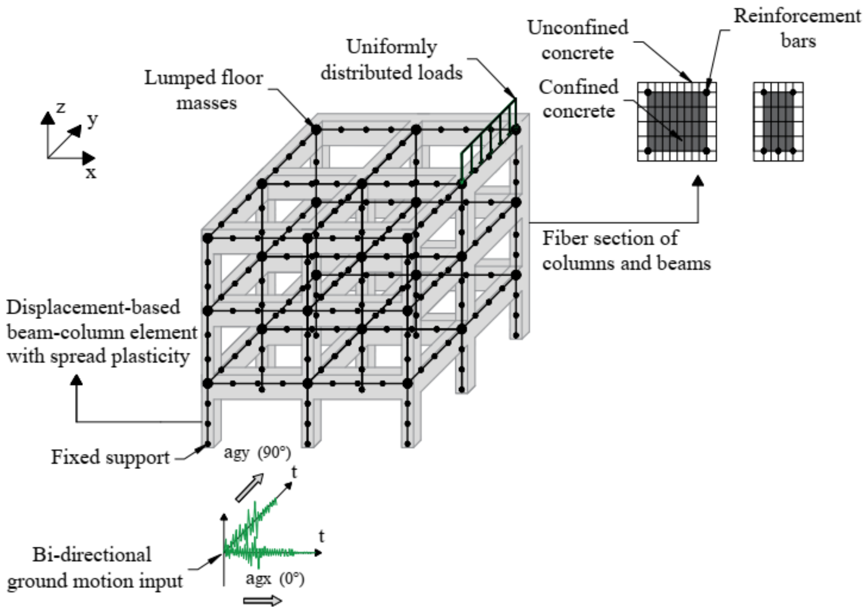

Figure 3. Summary of numerical model: elements, fiber cross-section, vertical loads, masses, and bi-directional ground motion input.

Confined and unconfined concrete constitutive law is defined according to Chang and Mander [56]. Steel material is modelled according to Giuffré-Menegetto-Pinto law with isotropic strain-hardening (Filippou et al. [57]), whose parameters are defined based on the mean values proposed by Carreño et al. [58] (Figure 4). The adequacy of the finite element model's response was verified by comparison with cyclic load experiments of simpler frames. Information on this can be found in Pereira [59].

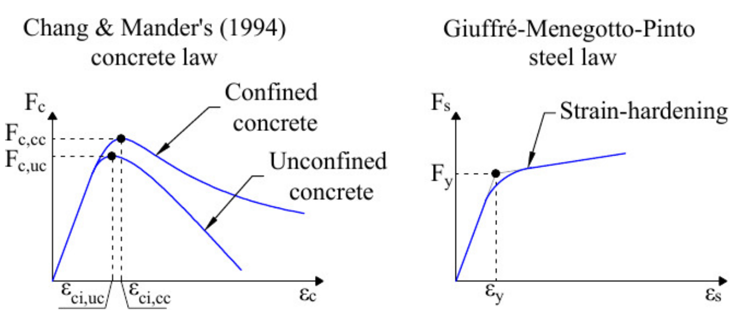

Figure 4. Generic representation of concrete and steel material law.

2.3 Ground motion records

The ground motion suite adopted to perform the dynamic analyses is the one used by Medina and Krawinkler [60], as it has been used by other researchers worldwide (Mehanny and El Howary [61]). The adopted suite consists of

80 recorded ground motion (GM) pairs from western United States earthquakes with two orthogonal components in the horizontal directions; it presents magnitude and closest distance to fault rupture (R) ranging from 5.5 to 7.0 and 13km to 60km, respectively, and it was recorded in Soil Class D. The GM suite is extracted from the PEER NGA-West2 database (Ancheta et al. [62]). The geometric mean of the two orthogonal components of all the individual records, along with the median and 10th and 90th percentile, are presented in Figure 5.

This suite is adopted because it presents some desirable attributes for this study. The lower distance limit avoids near-fault type events, whereas the upper limit minimizes the effect of different seismic attenuation between different regions, which is important since the records are not from Brazil. Also, the response spectrums ordinate ranges from more frequent to rarer expected accelerations in Brazil associated with different return periods such as 72, 475 and 2475 years, which is important to ensure the effectiveness of the linear regression [33]. It is also worth mentioning that the upper magnitude boundary is consistent with previous seismic hazard assessment studies performed for Brazil [11], [18]-[20].

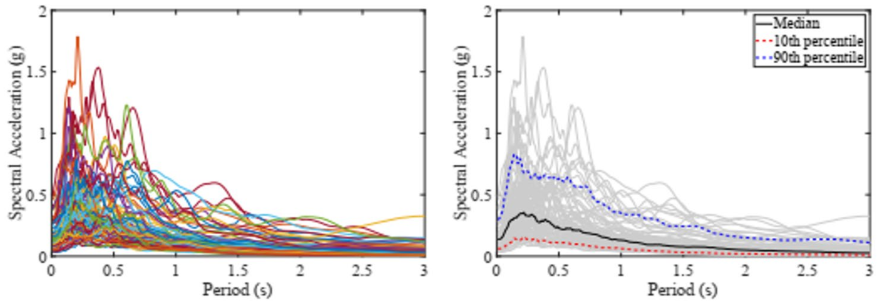

Figure 5. Response spectrum of all records (left) and median, 10th percentile, and 90th percentile of the ground motion suite spectral accelerations (right).

In addition, the adopted intensity measure attends the sufficiency criteria, as mentioned in Section 2. A sufficient IM helps to ensures an accurate estimate of the demand ([D|IM]), irrespective of the values of magnitude and distance of the adopted ground motion suite, and the validity of Equation 8 ([39], Luco and Cornell [63]); thus, the magnitude range of the GM suite does not strongly influence the results.

Ideally, the GM used in analyses should be recorded in tectonically similar regions (Bommer and Acevedo [64]); however, GM for stable continental regions such as Brazil are not widely available, thereby records from tectonically active regions worldwide, artificially-generated ones, or scaled records from stable regions are commonly adopted. Artificial records for Brazil are not readily available, to the best of our knowledge, and their development is out of the scope of this paper. Scaling of records from stable regions could result in excessive scale factors, and introduce some bias in the analysis that we intend to avoid. Hence, the natural records from tectonically active regions by [60] are adopted; nevertheless, we acknowledge that further discussion on the issue of ground motion selection is necessary.

3 RESULTS AND DISCUSSIONS

The probabilistic seismic demand model (PSDM) and the fragility function (FF) are presented in Figure 6. The median values (θ) of the FF for IO, LS and CP are 0.1214, 0.2005, and 0.3313, and the dispersion (σ) is 0.4648. These parameters are important to reproduce the fragility functions in future seismic risk or reliability studies.

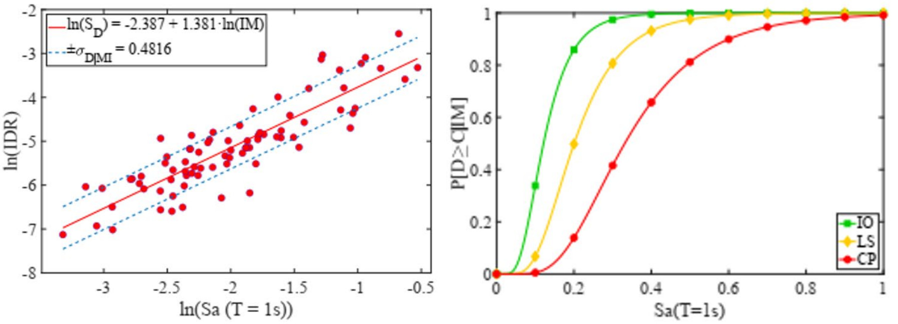

Figure 6. Probabilistic Seismic Demand Model (PSDM) (left) and fragility functions (right) of the analyzed RC structure.

The FF are integrated with the hazard curves developed by Petersen et al. [11] for Northeastern Brazil using Equation 8, and a failure probability map for each limit state is plotted for in Figure 7, where the orange and the blue colors shades refers to the regions where the structure would depict inadequate and adequate failure probability, respectively, according to the criteria described in Section 2. For the Immediate Occupancy limit state, Figure 7a indicates that the structure outperforms the acceptance criteria in the entire Northeastern region. Nevertheless, probabilities up to 25% are obtained; thereby in situations in which non-structural elements are important to building functionality (e.g., hospitals), one should be aware that this value is somewhat high and may represent a threat. The same is valid for Life Safety (Figure 7b), which there is a relatively small zone among the states of Paraíba (PB) and Rio Grande do Norte (RN) where an inadequate failure probability is observed, with values up to 12%, almost twice the acceptable value.

Regarding Collapse Prevention (Figure 7c), however, a large area with unacceptable failure probability is noticed, which implies that the building design is not enough to guarantee an adequate performance. A maximum probability of 6% in 50 years is observed, which is a considerable high value about 38 times the acceptable limit. An area in the southwest of the state of Bahia (BA) shall be highlighted, since it its located in Zone 0 of ABNT NBR 15421:2006 [5], i.e., seismic design is not required, but a large zone with unacceptable failure probability is observed, which indicates a possible region where seismic design should in fact be considered. Failure probability in this area reaches about 3% in 50 years. On the other hand, the upper zone of the studied region is consistent with the Zone 1 of the code, where seismic design is required.

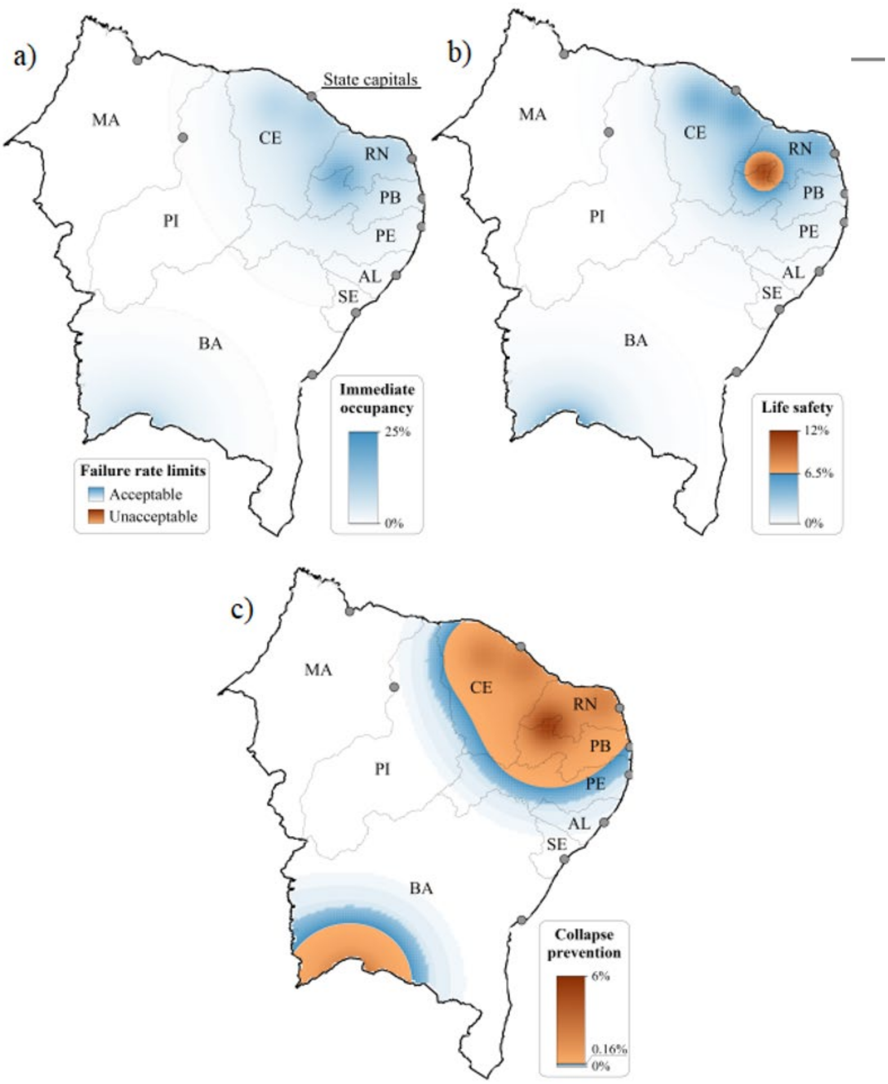

Figure 7. Failure probability maps considering a 50-year period: a) Immediate Occupancy; b) Life Safety; c) Collapse Prevention.

The maps in Figure 7 depicts the failure probability given the structure is built in those regions. A large part of Northeastern region, notwithstanding, comprises low population density cities, whose constructions are not-engineered houses, thus an engineered three-story building is unlikely. Despite that, two highly populated state capitals (Fortaleza in CE, and Natal in RN) are located within the unacceptable probability zone in Figure 7. For these cities, Collapse Prevention failure probability resulted even higher than 1% in 50 years which corresponds to the less conservative acceptance criteria of [49] mentioned in Section 2.

One should note that the maps were generated considering soil class D. Different soils amplify differently the ground accelerations, thereby the expected failure probability depends on the soil class of the building's site. The probabilities considering a soil class C are expected to be approximately half of those for soil class D, whereas for soil class B approximately five times smaller. For very soft soils (i.e., soil class E), the probabilities are expected to be on average two times higher. The fragility functions should obviously be different, since they were generated considering records from soil class D, but the largest influence should come from the hazard curves, so that the aforementioned estimates are enough to give an idea of what to expect. Regardless, the big picture would not change, and an unacceptable collapse probability would still be observed in a large area in the upper Northeastern, in spite of a much smaller area in the southwest of BA state, for all soil classes.

An issue outlined by the maps is the presence of a relatively higher seismicity among the states of Paraíba (PB) and Rio Grande do Norte (RN), responsible especially for the unacceptable performance for Life Safety (Figure 7b). Based on the available earthquake catalog, and other preliminary PSHA studies in Brazil, for example [2], we should point out that the relatively higher hazard in this particular zone seems inconsistent, and can be a consequence of the methodology adopted by [11]. In [11], the maps are generated using the smoothed seismicity-based seismic sources, which depends directly on the location of past earthquakes occurrence. The use of international catalogs (hence less precise values of magnitudes and epicenter location) likely influenced the generation of this zone. In [2], the maps are generated using the same methodology, but with a national catalog, combined with seismic sources defined based on expert judgment. The final map does not highlight this zone. Therefore, we believe that the failure probability in that region is overestimated. Despite that, the proposed accelerations values between both are similar for the rest of the upper Northeastern, thus similar failure probabilities would be expected. The point of this discussion is not to discredit the work by [11], but to highlight the importance and the need for more national PSHA studies in Brazil. In addition, one should be aware that the reference soil class of the both works are different, therefore any comparisons must be made following the application of soil amplification factors to correct the accelerations.

4 CONCLUSIONS

Brazil, although located in a seismically stable continental region, is prone to small-to-moderate earthquakes, strong enough to inflict structural and non-structural damage if buildings are not seismic designed. Reliability studies are essential to provide information regarding the performance of the structures under loads such as earthquakes, and if they meet the diverse needs of society, for instance, different limit states. In addition, important information on how to improve structural performance can be obtained.

However, studies focusing on the seismic reliability of the buildings designed according to Brazilian code provisions are still scarce. Herein, a three-story RC framed structure, designed according to ABNT NBR 6118:2014 but with no earthquake resistant design, is evaluated. Fragility functions were generated using non-linear dynamic analyses, and the failure probability of the structure was assessed considering different regions of Northeastern Brazil through combining the fragility with the hazard curves developed by Petersen et al. [11].

From the results it is possible to point out that the structure does not comply with Collapse Prevention structural requirements in several locations, and reaches considerable high values of failure probability. This result highlights the importance and the need for earthquake-resistant design in Brazil, since in a considerable area of Northeastern Brazil the collapse probability resulted unacceptable, including two state capital cities. Life Safety failure probability is inadequate in a much smaller area, whereas for Immediate Occupancy the building's performance is acceptable. The results also bring awareness about the need for more rigorous seismic provisions in zones where design requirements are minimum and/or non-existent, i.e., the Zone 0 of ABNT NBR 15421:2006.

Further research can provide more information for the improvement of acceleration design maps zoning, or demonstrate their adequacy, and provide information to improve seismic design provisions. The results in this paper should be improved as new PSHA for Brazil are developed.

ACKNOWLEDGEMENTS

This study was financed in part by the Coordenação de Aperfeiçoamento de Pessoal de Nível Superior - Brasil (CAPES) - Finance Code 001; and by the São Paulo Research Foundation (FAPESP) - Finance Code 2018/23304-9. The authors would also like to thank the company TQS Informática Ltda., and Prof. Dr. Petrus Nóbrega for providing the academic version of the software CAD/TQS V21 used to design the building in this paper.

REFERENCES

[1] J. Berrocal et al. *Sismicidade do Brasil*. São Paulo, Brazil: Esperança, 1984.

[2] M. S. Assumpção, M. Pirchiner, J. Dourado, and L. Barros "Terremotos no Brasil: preparando-se para eventos raros," *Boletim SBGf*, vol. 96, pp. 25–29, 2016. Accessed: May 2, 2021. [Online]. Available: https://sbgf.org.br/noticias/images/Boletim_96-2016.pdf

[3] C. I. Nievas, J. J. Bommer, H. Crowley, J. van Elk, M. Ntinalexis, and M. Sangirardi, "A database of damaging small-to-medium magnitude earthquakes," *J. Seismol.*, vol. 24, no. 2, pp. 263–292, 2020., http://dx.doi.org/10.1007/s10950-019-09897-0.

[4] M. Takeya, J. Ferreira, R. Pearce, M. Assumpção, J. Costa, and C. Sophia, "The 1986-1988 intraplate earthquake sequence near João Câmara, northeast Brazil—evolution of seismicity," *Tectonophysics*, vol. 167, no. 2-4, pp. 117–131, 1989., http://dx.doi.org/10.1016/0040-1951(89)90062-0.

[5] Associação Brasileira de Normas Técnicas, *Projeto de Estruturas Resistentes a Sismos – Procedimento,* ABNT NBR 15421, 2006.

[6] M. N. Fardis, "Capacity design: Early history," *Earthquake Eng. Struct. Dynam.*, vol. 47, no. 14, pp. 2887–2896, 2018., http://dx.doi.org/10.1002/eqe.3110.

[7] S. H. Santos and S. S. Lima "Subsídios para uma futura normalização brasileira para resistência anti-Sísmica das estruturas de concreto de edifícios," *IBRACON*, vol. 1, no. 1, pp. 47–62, 2005. Accessed: May 2, 2021. [Online]. Available: http://www.ibracon.org.br/publicacoes/revistas_ibracon/rev_estruturas/V1/RIEst_2004_0023-02br-v.01.pdf

[8] P. S. T. Miranda, H. S. A. Varum, and N. S. Vila-Pouca "Reflexões sobre o risco sísmico no Brasil," in *Proc. 11º Congresso Nacional de Sismologia e Engenharia Sísmica*, 2019. Accessed: May 2, 2021. [Online]. Available: https://repositorio-aberto.up.pt/bitstream/10216/133985/2/422679.pdf

[9] A. E. V. Lopes and L. C. Nunes, "Intensidades sísmicas de terremotos: formulação de cenário sísmico no Brasil," Revista USP, no. 91, pp. 90–103, 2011, https://doi.org/10.11606/issn.2316-9036.v0i91p90-103

[10] J. C. Dourado "Mapa de ameaça sísmica do Brasil," in *Proc. 47º Congresso Brasileiro de Geologia*, Set. 2014.

[11] M. D. Petersen et al., "Seismic hazard, risk, and design for South America," *Bull. Seismol. Soc. Am.*, vol. 108, no. 2, pp. 781–800, 2018. http://dx.doi.org/10.1785/0120170002.

[12] P. G. B. da Nóbrega, B. R. S. Souza, and M. L. C. Felipe "Sobre os mapas de perigo sísmico para o projeto de estruturas," in *Proc. 61º Congresso Brasileiro do Concreto*, Out. 2019. Accessed: May 2, 2021. [Online]. Available: https://www.researchgate.net/publication/336672092

[13] L. Barros, M. Assumpção, V. Ferreira, and L. Ribotta "Sismicidade induzida por reservatório: casos brasileiros," *Bull. Brazilian Geophys. Soc.*, vol. 96, pp. 16–21, 2016. Accessed: May 2, 2021. [Online]. Available: https://sbgf.org.br/noticias/images/Boletim_96-2016.pdf

[14] A. H. Silva, G. L. Pita, J. A. Inaudi, and L. C. Vieira Jr, "Induced earthquake damage assessment methodology for potential hydraulic fracturing sites: Application to Manaus, Brazil," *Earthq. Spectra*, vol. 37, no. 1, pp. 180–203, 2020., http://dx.doi.org/10.1177/8755293020944178.

[15] G. H. Siqueira, A. S. Sanda, P. Paultre, and J. E. Padgett, "Fragility curves for isolated bridges in eastern canada using experimental results," *Eng. Struct.*, vol. 74, no. 1, pp. 311–324, 2014., http://dx.doi.org/10.1016/j.engstruct.2014.04.053.

[16] R. K. McGuire, *Seismic Hazard and Risk Analysis.* Oakland, CA, USA: EERI, 2004.

[17] H. Krawinkler "Challenges and progress in performance-based earthquake engineering," in *Int. Seminar on Seismic Engineering for Tomorrow–In Honor of Professor Hiroshi Akiyama*, Nov., 1999.

[18] B. R. S. Souza, M. L. C. Felipe, P. G. B. da Nóbrega, and S. H. S. da Nóbrega "On the generation of hazard maps and response spectrum by the use of probabilistic seismic hazard analysis," in *Proc. 40º Ibero-Latin-American Congress of Computational Methods in Engineering*, 2019. [Online]. Available: https://www.researchgate.net/publication/337304762

[19] A. A. D. de Almeida, M. S. Assumpção, J. J. Bommer, S. Drouet, C. Riccomini, and C. L. Prates, "Probabilistic seismic hazard analysis for a nuclear power plant site in southeast Brazil," *J. Seismol.*, vol. 23, no. 1, pp. 1–23, 2019., http://dx.doi.org/10.1007/s10950-018-9755-8.

[20] R. G. Borges, M. S. Assumpção, M. C. F. de Almeida, and M. S. S. de Almeida, "Seismicity and seismic hazard in the continental margin of southeastern Brazil," *J. Seismol.*, vol. 24, pp. 1–20, 2020. http://dx.doi.org/10.1007/s10950-020-09941-4.

[21] F. Alves "Estudo de sismicidade do Brasil para revisão da ABNT NBR 15421," M.S. thesis, UFRJ, Rio de Janeiro, RJ, 2020. [Online]. Available: http://dissertacoes.poli.ufrj.br/dissertacoes/dissertpoli2885.pdf

[22] P. G. B. Nóbrega, B. R. S. Souza, and S. H. S. Nóbrega, "Towards improving the seismic hazard map and the response spectrum for the state of RN/Brazil," *IBRACON Struct. Mater. J.*, vol. 14, no. 3, pp. e14302-1–16, 2021., http://dx.doi.org/10.1590/S1983-41952021000300002.

[23] V. Silva et al., "Development of a global seismic risk model," *Earthq. Spectra*, vol. 36, no. 1, pp. 372–394, 2020., http://dx.doi.org/10.1177/8755293019899953.

[24] S. K. Ramamoorthy, P. Gardoni, and J. M. Bracci, "Probabilistic demand models and fragility curves for reinforced concrete frames," *J. Struct. Eng.*, vol. 132, no. 10, pp. 1563–1572, 2006., http://dx.doi.org/10.1061/(ASCE)0733-9445(2006)132:10(1563).

[25] B. R. Ellingwood, O. C. Celik, and K. Kinali, "Fragility assessment of building structural systems in mid-america," *Earthquake Eng. Struct. Dynam.*, vol. 36, no. 13, pp. 1935–1952, 2007., http://dx.doi.org/10.1002/eqe.693.

[26] S. K. Ramamoorthy, P. Gardoni, and J. M. Bracci, "Seismic fragility and confidence bounds for gravity load designed reinforced concrete frames of varying height," *J. Struct. Eng.*, vol. 134, no. 4, pp. 639–650, 2008., http://dx.doi.org/10.1061/(ASCE)0733-9445(2008)134:4(639).

[27] A. J. Kappos and G. Panagopoulos, "Fragility curves for reinforced concrete buildings in greece," *Struct. Infrastruct. Eng.*, vol. 6, no. 1-2, pp. 39–53, 2010., http://dx.doi.org/10.1080/15732470802663771.

[28] P. Rajeev and S. Tesfamariam, "Seismic fragilities of non-ductile reinforced concrete frames with consideration of soil structure interaction," *Soil. Dyn. Earthquake Eng.*, vol. 40, pp. 78–86, 2012. http://dx.doi.org/10.1016/j.soildyn.2012.04.008.

[29] J.-S. Jeon, L. N. Lowes, R. DesRoches, and I. Brilakis, "Fragility curves for non-ductile reinforced concrete frames that exhibit different component response mechanisms," *Eng. Struct.*, vol. 85, no. 15, pp. 127–143, 2015. http://dx.doi.org/10.1016/j.engstruct.2014.12.009.

[30] A. Amirsardari, E. Lumantarna, P. Rajeev, and H. M. Goldsworthy, "Seismic fragility assessment of non-ductile reinforced concrete buildings in Australia," *J. Earthquake Eng.*, 2020. http://dx.doi.org/10.1080/13632469.2020.1750508.

[31] Associação Brasileira de Normas Técnicas. *Projeto de estruturas de concreto – Procedimento*, ABNT NBR 6118, 2014.

[32] C. Cornell, F. Jalayer, R. Hamburger, and D. Foutch, "The probabilistic basis for the 2000 SAC/FEMA steel moment frame guidelines," *J. Struct. Eng.*, vol. 128, pp. 526–533, 2002. http://dx.doi.org/10.1061/(ASCE)0733-9445(2002)128:4(526).

[33] F. Jalayer, H. Ebrahimian, A. Miano, G. Manfredi, and H. Sezen, "Analytical fragility assessment using unscaled ground motion records," *Earthquake Eng. Struct. Dynam.*, vol. 46, no. 15, pp. 2639–2663, 2017., http://dx.doi.org/10.1002/eqe.2922.

[34] M. D. McKay, R. J. Beckman, and W. J. Conover, "Comparison of three methods for selecting values of input variables in the analysis of output from a computer code," *Technometrics*, vol. 21, no. 2, pp. 239–245, 1979., http://dx.doi.org/10.1080/00401706.1979.10489755.

[35] O. C. Celik and B. R. Ellingwood, "Seismic fragilities for non-ductile reinforced concrete frames–role of aleatoric and epistemic uncertainties," *Struct. Saf.*, vol. 32, no. 1, pp. 1–12, 2010., http://dx.doi.org/10.1016/j.strusafe.2009.04.003.

[36] C. G. Nogueira "Desenvolvimento de modelos mecânicos, de confiabilidade e de otimização para aplicação em estruturas de concreto armado," Ph.D. dissertation, USP, São Carlos, SP, Brazil, 2010. [Online]. Available: https://teses.usp.br/teses/disponiveis/18/18134/tde-29062010-113700/pt-br.php

[37] S. A. Mirza and J. G. MacGregor, "Variability of mechanical properties of reinforcing bars," *J. Struct. Div.*, vol. 105, no. 5, pp. 921–937, 1979. http://dx.doi.org/10.1061/JSDEAG.0005146.

[38] J. Healey, S. Wu, and M. Murga, *Seismic Safety Margins Research Program (Phase I). Project IV. Structural Building Response; Structural Building Response Review*, New York, USA: Ebasco Services, Inc., 1980. Acessed: May 2, 2021. [Online]. Available: https://www.osti.gov/servlets/purl/5627242

[39] J. E. Padgett, B. G. Nielson, and R. DesRoches, "Selection of optimal intensity measures in probabilistic seismic demand models of highway bridge portfolios," *Earthquake Eng. Struct. Dynam.*, vol. 37, no. 5, pp. 711–725, 2008., http://dx.doi.org/10.1002/eqe.782.

[40] A. Du, J. E. Padgett, and A. Shafieezadeh, "A posteriori optimal intensity measures for probabilistic seismic demand modeling," *Bull. Earthquake Eng.*, vol. 17, no. 2, pp. 681–706, 2019., http://dx.doi.org/10.1007/s10518-018-0484-8.

[41] J. W. Baker and C. A. Cornell, "Which spectral acceleration are you using," *Earthq. Spectra*, vol. 22, no. 2, pp. 293–312, 2006., http://dx.doi.org/10.1193/1.2191540.

[42] A. Whittaker, R. Hamburger, and M. Mahoney "Performance-based engineering of buildings and infrastructure for extreme loadings," in *Proc. AISC-SINY Symposium on Resisting Blast and Progressive Collapse*, New York, USA, 2003. [Online]. Available: https://atcouncil.org/pdfs/Whittaker2.pdf

[43] Y. Wen, B. R. Ellingwood, and J. M. Bracci, *Vulnerability Function Framework for Consequence-Based Engineering* (Report 04-04). Urbana, IL, USA: MAE Center, 2004. Accessed: May 2, 2021 [Online]. Available: http://mae.cee.illinois.edu/publications/reports/Report04-04.pdf

[44] American Society of Civil Engineers. *Seismic evaluation and retrofit of existing building*, ASCE/SEI 41-17, 2017.

[45] Federal Emergency Management Agency, *Seismic performance assessment of buildings,* FEMA P-58-1, 2012.

[46] Federal Emergency Management Agency, *Multi-hazard loss estimation methodology: Earthquake model*, HAZUS MH-R1, 2003. [Online]. Available: https://www.hsdl.org/?abstract&did=701264

[47] D. H. Tavares, J. E. Padgett, and P. Paultre, "Fragility curves of typical as-built highway bridges in eastern canada," *Eng. Struct.*, vol. 40, pp. 107–118, 2012., http://dx.doi.org/10.1016/j.engstruct.2012.02.019.

[48] R. E. Melchers and A. T. Beck *Structural Reliability Analysis and Prediction*, 3th ed., Hoboken, NJ, USA: John Wiley & Sons, 2018.

[49] American Society of Civil Engineers. *Minimum design loads and associated criteria for buildings and other structures*, ASCE/SEI 7-16, Reston, USA, 2016.

[50] M. Priyadarshini, P. R. Davis, D. C. H. Pragalath, and P. Sarkar "Seismic reliability assessment of typical soft-storey RC building in Manipur region," *Int. J. Sci. Eng. Res.*, vol. 4, no. 5, 2013. [Online]. Available: http://dspace.nitrkl.ac.in/dspace/bitstream/2080/2097/1/Seismic_71.pdf

[51] Joint Committee on Structural Safety. *Probabilistic Model Code, Part 1, Basis of Design*, JCSS-OSTL/DIA/VROU-10-11-2000, 2001.

[52] International Organization for Standardization. *General principles on reliability for structures*, ISO 2394, 2015.

[53] V. Silva, H. Crowley, and P. Bazzurro, "Exploring risk-targeted hazard maps for Europe," *Earthq. Spectra*, vol. 32, no. 2, pp. 1165–1186, 2016. http://dx.doi.org/10.1193/112514eqs198m.

[54] A. Gkimprixis, J. Douglas, E. Tubaldi, and D. Zonta "Development of fragility curves for use in seismic risk targeting," in *Proc. 16th European Conf. Earthquake Eng.*, Thessaloniki, Greece, 2018. Acessed: May 2, 2021. [Online] Available: https://www.researchgate.net/publication/332980845

[55] F. McKenna, M. H. Scott, and G. L. Fenves, "Nonlinear finite-element analysis software architecture using object composition," *J. Comput. Civ. Eng.*, vol. 24, no. 1, pp. 95–107, 2010., http://dx.doi.org/10.1061/(ASCE)CP.1943-5487.0000002.

[56] G. Chang and J. B. Mander, *Seismic Energy-Based Fatigue Damage Analysis of Bridge Columns: Part 1-Evaluation of Seismic Capacity* (Report NCEER-94-0006). Buffalo, NY, USA: NCEER, 1994. Acessed: May 2, 2021. [Online] Available: https://www.eng.buffalo.edu/mceer-reports/94/94-0006.pdf

[57] F. C. Filippou, V. V. Bertero, and E. P. Popov, *Effects of Bond Deterioration on Hysteretic Behavior of Reinforced Concrete Joints* (Report UCB/EERC-83/19). Berkeley, CA, USA: EERC, 1983. Acessed: May 2, 2021. [Online] Available: https://nehrpsearch.nist.gov/static/files/NSF/PB84192020.pdf

[58] R. Carreño, K. Lotfizadeh, J. Conte, and J. Restrepo, "Material model parameters for the giuffrè-menegotto-pinto uniaxial steel stress-strain model," *J. Struct. Eng.*, vol. 146, no. 2, pp. 04019205, 2020., http://dx.doi.org/10.1061/(ASCE)ST.1943-541X.0002505.

[59] E. M. V. Pereira "Estudo da fragilidade sísmica de pórticos de concreto armado com irregularidades estruturais," M.S. thesis, Unicamp, Campinas, SP, 2021. [Online]. Available: http://repositorio.unicamp.br/handle/REPOSIP/358300.

[60] R. A. Medina and H. Krawinkler, *Seismic Demands for Nondeteriorating Frame Structures and Their Dependence on Ground Motions* (Report 144). Stanford, CA, USA: Blume, 2004. [Online]. Available: https://stacks.stanford.edu/file/druid:jz144cw3119/TR144_Medina.pdf

[61] S. S. F. Mehanny and H. A. El Howary, "Assessment of RC moment frame buildings in moderate seismic zones: Evaluation of Egyptian seismic code implications and system configuration effects," *Eng. Struct.*, vol. 32, no. 8, pp. 2394–2406, 2010., http://dx.doi.org/10.1016/j.engstruct.2010.04.014.

[62] T. D. Ancheta et al., "NGA-West2 Database," *Earthq. Spectra*, vol. 30, no. 3, pp. 989–1005, 2014., http://dx.doi.org/10.1193/070913EQS197M.

[63] N. Luco and C. A. Cornell, "Structure-specific scalar intensity measures for near-source and ordinary earthquake ground motions," *Earthq. Spectra*, vol. 23, no. 2, pp. 357–392, 2007., http://dx.doi.org/10.1193/1.2723158.

[64] J. J. Bommer and A. B. Acevedo, "The use of real earthquake accelerograms as input to dynamic analysis," *J. Earthquake Eng.*, vol. 8, no. sup001, pp. 43–91, 2004, https://doi.org/10.1080/13632460409350521.

Author contributions: EMVP: conceptualization, formal analysis, funding acquisition, methodology, writing-original draft; GHFC, IDR: funding acquisition, methodology, writing-review & editing; LCMVJ, GHS: project administration, supervision, writing-review & editing.

Editors: Sergio Hampshire C. Santos, Guilherme Aris Parsekian.

IBRACON Structures and Materials Journal
Revista IBRACON de Estruturas e Materiais
ISSN 1983-4195 ismj.org

ORIGINAL ARTICLE

Numerical analysis of mechanical damage on concrete under high temperatures

Análise numérica do dano mecânico no concreto submetido a temperaturas elevadas

Lahis Souza de Assis[a]
Matheus Fernandes Dal Sasso[a]
Michèle Cristina Resende Farage[a]
Flávia de Souza Bastos[a]
Anne-Lise Beaucour[b]

[a]Universidade Federal de Juiz de Fora – UFJF, Juiz de Fora, MG, Brasil
[b]Université de Cergy-Pontoise – UCP, Cergy-Pontoise, France

Received 04 January 2021
Accepted 07 July 2021

Abstract: Concrete is a widespread material all over the world. Due to this material's heterogeneity and structural complexity, predicting the behavior of concrete structures under extreme environmental conditions is a very challenging task. High temperatures lead to microstructural changes which affect the macrostructural performance. In this context, computational tools that allow the simulation of structures may assist the analysis, by reproducing varied situations of thermal and mechanical loading and boundary conditions. In order to contribute to this scenario, this study proposes a numerical methodology to simulate the thermomechanical behavior of concrete under temperature gradients, through inverse analyses and a user subroutine implemented in Abaqus software. Thermal loading effects were considered as loading data for a damage model. Experimental data available in the literature was adopted for adjustment and validation purposes. The preliminary results presented herein encourage further improvements so as to allow realistic simulations of such an important aspect of concrete's behavior.

Keywords: damage, thermomechanical, concrete.

Resumo: O concreto é um material difundido e utilizado mundialmente. Devido à heterogeneidade e complexidade estrutural desse material, prever o comportamento de estruturas de concreto sob condições ambientais extremas é uma tarefa bastante difícil. Altas temperaturas provocam alterações microestruturais que afetam o desempenho macroestrutural. Nesse contexto, ferramentas computacionais que permitem a simulação de estruturas podem ser de grande ajuda, reproduzindo diversas situações de carregamento térmico e mecânico e condições de contorno. Visando contribuir com este cenário, este estudo propõe uma metodologia numérica para simular o comportamento termomecânico do concreto sob gradientes de temperatura, através de análises inversas e de uma subrotina de usuário implementada no *software* Abaqus. Os efeitos do carregamento térmico foram considerados como dados de carregamento para um modelo de dano. Dados experimentais disponíveis na literatura foram adotados para fins de ajuste e validação. Os resultados preliminares aqui apresentados encorajam melhorias adicionais, de modo a permitir simulações realistas de um aspecto tão importante do comportamento do concreto.

Palavras-chave: dano, termomecânico, concreto.

How to cite: L. S. Assis, M. F. Dal Sasso, M. C. R. Farage, F. S. Bastos, and A. L. Beaucour, "Numerical analysis of mechanical damage on concrete under high temperatures," *IBRACON Struct. Mater. J.*, vol. 15, no. 1, e15111, 2022, https://doi.org/10.1590/S1983-41952022000100011

Corresponding author: Lahis Souza de Assis. E-mail: lahis.assis@engenharia.ufjf.br
Financial support: CAPES, FAPEMIG, CNPq, UFJF and UCP.
Conflict of interest: Nothing to declare.

1 INTRODUCTION

According to ASTM (American Society of Tests and Materials), it is possible to define concrete as a composite material, which comprises a binding agent medium in which are incorporated different aggregates. According to Mehta and Monteiro [1], concrete is one of the most widely adopted construction materials, with world consumption of the order of 33 billion tons per year in 2016. In spite of this fact, the prediction of concrete behavior is rather complex, especially under extreme situations such as large displacements and high temperatures.

Exposure to high temperatures may be due to accidental reasons, such as fire situations, or to ordinary service conditions, which is the case of some components of nuclear power plants, blast furnaces and radioactive waste repositories. In either case, the knowledge of the effects of the temperature elevation on concrete's properties is paramount to an adequate executive or corrective design.

The evaluation of the behavior of concrete when subjected to high temperatures has increasingly aroused the interest of the scientific community. In this context, several constitutive models based on the continuum mechanics have been developed with this objective in mind. Mazars [2] proposed an isotropic damage model based on a single scalar variable in which the concrete has a damaged elastic behavior. In this model, the damage is directly associated with the existence of positive deformations. Thelandersson [3] described the thermomechanical response of concrete considering the thermal strain rate as a function of both rate of temperature change and the current state of stress. Damage is accounted by the change in elastic properties due to a temperature change. Simo and Ju [4] developed a cap plasticity model with an isotropic strain-based damage mechanism and proposed a viscoplastic extension for their model. Cervera et al. [5] implemented a rate-dependent isotropic damage model that incorporates stiffness degradation and stiffness recovery upon load reversals and strain-rate sensitivity in order to make a realistic seismic analysis. Pituba and Lacerda [6], on the other hand, admitted concrete as an initially isotropic medium that starts to present plastic deformations, bimodularity and damage-induced anisotropy.

In the field of experimental studies, Lima et al. [7] analyzed the damage caused by the increase in temperature in a reinforced concrete building. Arioz [8] studied the effects of high temperatures on the physical and mechanical properties of various concrete mixtures, determining weight losses and compressive strength after exposure. Arioz [8] concluded that weight losses and compressive strength are directly linked and that both decrease considerably with increasing temperature. Furthermore, in this study, the damage can be observed macroscopically on the concrete surface. Ehrenbring et al. [9] realized the inspection of a prefabricated hollow core slab of an industrial building, which was exposed to high temperatures due a fire in the underground of the same, estimating the loss of strength of the structural element and attesting the safety of the structure after the accident. Bailey and Toh [10] tested forty-eight horizontally unrestrained two-way spanning reinforced concrete slabs at ambient and elevated temperatures comparing the modes of failure observed in each case in order to provide a wealth of data, which can be used to further develop simple design methods. Souza et al. [11] presented the use of the factorial experimental design methodology with a star configuration for the study of the compressive strength of specimens heated in kilns. Dias et al. [12] studied the concrete subjected to high temperatures and concluded that in this situation the material undergoes significant deterioration as a reduction in the modulus of elasticity and resistance to compression, surface displacement and loss of durability.

As for the work involving numerical analysis, Ribeiro [13] developed a computer system for simulating the behavior of structural elements in a fire situation based on the Finite Element Method and obtained results similar to those observed in experimental tests. Subsequently, Padre et al. [14] used the created program, and developed an algorithm to check the resistance of reinforced concrete sections to oblique composite bending at ambient temperature and in fire situation. Izzuddin and Elghazouli [15] presented two analytical models, detailed and simplified, for the nonlinear analysis of axially restrained lightly reinforced concrete members under ambient and fire conditions with emphasis on the evaluation of steel reinforcement failures. Grassl and Pearce [16] used a meso-scale approach through a damage-plasticity model - considering concrete as a three phase material composed of aggregates, matrix and interfacial transition zones - to evaluate the transient thermal creep, concluding that this phenomenon results from the mismatch of thermal expansions of the meso-scale constituents. Ferreira [17] developed a numerical model for the simulation of reinforced concrete columns in a fire situation, also based on the Finite Element Method, in order to predict the structural behavior under high temperatures. Nguyen et al. [18] studied the thermal conductivity change of concrete when exposed to both mechanical and thermal loads through a numerical three-phase plane model using lattice discretization, where damage variable is accounted via crack opening. Rodovalho et al. [19] analyzed the mechanical resistance of concrete blocks subjected to compression and in a fire situation. Assis and Neto [20] evaluated the heat transfer in the cavity of the structural masonry blocks. Barbosa and Haach [21] analyzed the influence of fire in a room of a structural masonry building and checked the large reserve of resistant capacity of this type of construction, in addition to the great ability to redistribute efforts on the walls structural. Machado et al. [22] evaluated the stability of reinforced concrete panels under fire conditions, verifying the influence of the time of exposure to fire on the results obtained.

In turn, this work presents a numerical methodology consisting of simulating the material deterioration through the implementation of Mazars' [2] damage model in a finite element software. Experimental data available in the literature was adopted for data adjustment and numerical validation, and the results encourage further improvements so as to allow the reproduction of varied geometrical, loading and boundary conditions.

2 METHODOLOGY

2.1 Overview

This work employed a set of experimental data provided by Razafinjato [23] who studied the thermomechanical behavior of concretes of varied compositions.

According to Razafinjato [23], the experimental data were obtained from cylindrical specimens with a proportion of 40% of aggregates. These samples were molded covered with a damp cloth and stored in plastic bags for 90 days. Then the specimens were subjected to heating/cooling cycles, in a furnace, at a rate of 0.50K/min till temperatures of 573.15K, 723.15K, 873.15K and 1023.15K, maintained for two hours. After the heating/cooling cycles, at room temperature (293.15K), the specimens were taken to the press so that, from the uniaxial compression test, the residual concrete Young's modulus could be determined.

Figure 1 shows the resulting Young's modulus and temperature relation, for 293.15K, 573.15K, 723.15K and 873.15K – in which it is possible to observe the linear trend of the experimental results adjusted via the least-squares method. For the temperature of 1023.15K it was not possible to perform the uniaxial compression test due to the deterioration of the specimen. These points were used to calculate the objective function of the inverse iterative procedures that calculate mechanical properties and damage parameters, which will be presented in detail in the following sections.

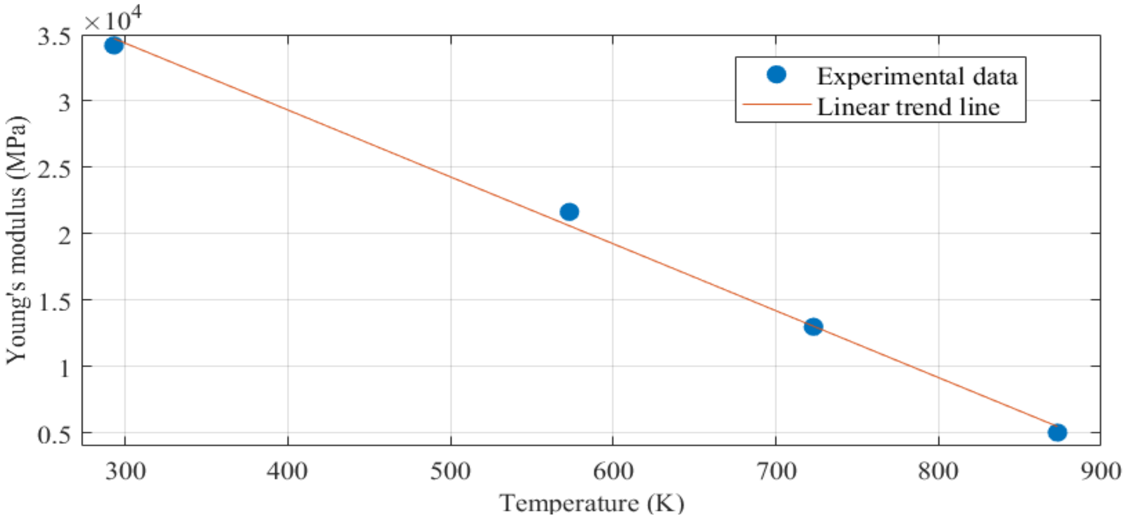

Figure 1. Relation between Young's modulus and temperature.

2.2 Numerical procedure

To evaluate the damage process in the concrete subjected to high temperatures the first step was to get, through the algorithm developed by Bonifácio [24], the geometric model of the cylindrical specimen of concrete. Then, it was developed a linear elastic analysis employing the Abaqus [25] finite element commercial program, to determine the unknown properties – Young's modulus of aggregate and Poisson's ratio of aggregate and mortar – for initial temperature, without damage, through a numerical adjustment. This process can be seen schematically in Figure 2.

Once evaluated the necessary property, the weakly coupled thermomechanical model was implemented in two steps. Firstly, the thermal model receives the values calculated in Flowchart 1 (Figure 2) and estimates the specimen temperature field. Then, the temperature field is applied as thermal loading and a damage model is adopted so as to evaluate the material's deterioration.

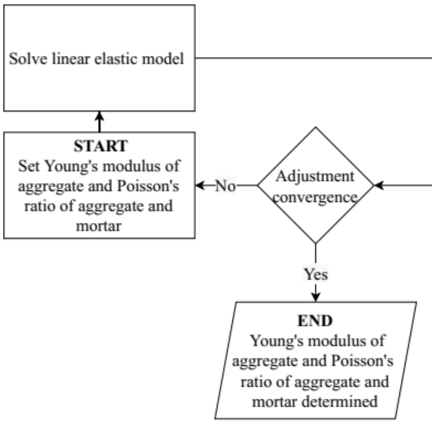

Figure 2. Flowchart 1: Linear elastic model – estimation of the unknown mechanical properties: Young's modulus of aggregate and Poisson's ratio of aggregate and mortar, for the initial temperature.

To evaluate the concrete deterioration process, opted to use the Mazars' [2] damage model, which is unavailable in the library of the Abaqus [25]. So, a UMAT subroutine [26] was implemented for the software to perform the analysis considering the desired model. However, Mazars' [2] parameters for the material were unknown and, therefore, it was necessary to use another numerical adjustment.

Finally, from the results of the damage model, it was possible to construct a damage curve as a function of temperature, from which we carried out the analysis of the behavior of the concrete under high thermal gradients.

We emphasize that the strategy used, which is summarized in a weak coupling, has the advantage of low computational cost. This process can be seen schematically in Figure 3.

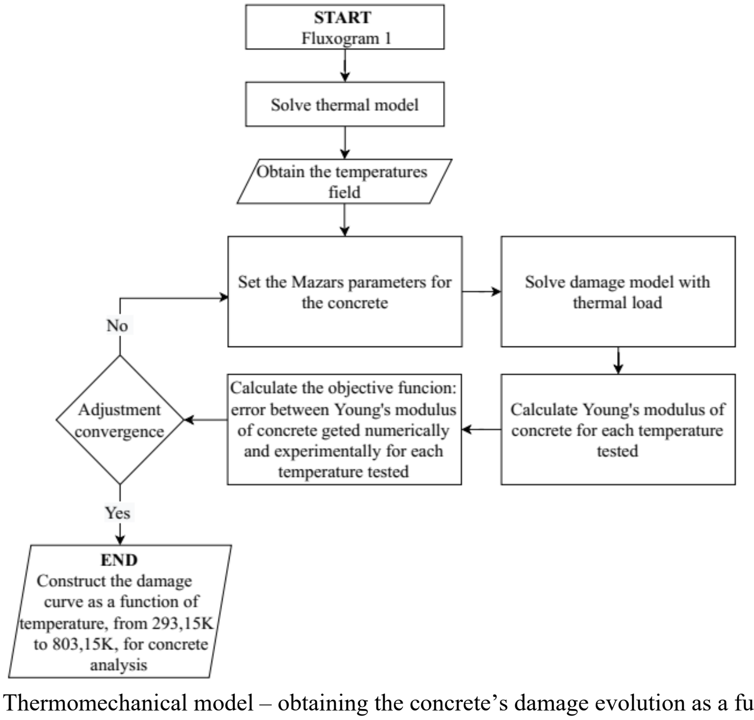

Figure 3. Flowchart 2: Thermomechanical model – obtaining the concrete's damage evolution as a function of temperature.

Both in the inverse problems employed to determine the unknown mechanical properties and in the necessary to find the parameters of the Mazars' [2] model, it was used experimental data from a thesis developed at the Cergy-Pontoise University [23], in France, and also functions of the package *optimize* from the *SciPy* library [27].

2.2.1 Governing equations

Regarding thermal models, in this study, the transfer of heat by conduction was considered, which is described by Equation 1. From the resolution of a thermal problem with this governing equation, it was possible to find the temperature field in the specimen section considered.

$$\rho c\frac{\partial T}{\partial t}-\nabla\cdot\left(\kappa\nabla T\right)=0\ , \tag{1}$$

where ρ is the density, c is the specific heat, T is the temperature, t is the time, κ is the thermal conductivity.

In relation to linear elastic model and to damage model Equation 2 was adopted, being that in the second case the Mazars' [2] damage model was considered.

$$B+\nabla\cdot\sigma=0\ , \tag{2}$$

where B are the body forces and σ is the normal stress.

About the Mazars' [2] damage model, it modifies the modulus of elasticity E of the intact material according the damage begins to develop, as can be seen in Equation 3,

$$E_d=\left(1-d\right)E\ , \tag{3}$$

where E_d is the Young's modulus of the damaged material and d is the damage variable, which is given by Equation 4.

$$d_{t,c}=1-\frac{e_{d0}\left(1-A_{t},_{c}\right)}{\tilde{e}}-\frac{A_{t},_{c}}{\exp\left(B_{t},_{c}\left(\tilde{e}-e_{d0}\right)\right)} \tag{4}$$

where t and c refer to traction and compression, respectively, e_{d0}, A_t, A_c, B_t and B_c are parameters of the Mazars' [2] model and $\tilde{e}$ is the equivalent deformation.

The damage variable d is given by a linear combination of d_t and d_c, involving weight functions α_t and α_c, according to Equation 5.

$$d=\alpha_t d_t+\alpha_c d_c. \tag{5}$$

2.2.2 Geometric model and mesh

So as to simulate the laboratory experiments developed by Razafinjato [23], it was necessary to reproduce the specimen geometry, by taking into account the adopted aggregate gradation and proportion. For reasons of symmetry, it was decided to consider 1/4 of the longitudinal section of a cylindrical specimen with 150mm in diameter and 300mm in height, composed of two phases: mortar and aggregate.

The center coordinate and the aggregates radius were generated using an algorithm developed by Bonifácio [24], in Python language, able to simulate the distribution of aggregate in a specimen, having as input data its dimensions, aggregates proportion and grading.

The model was discretized in 12175 linear elements, after convergence test. For the elastic model (Flowchart 1 – Figure 2) and in damage model (Flowchart 2 – Figure 3), elements of CPS4 type (4-node bilinear plane stress quadrilateral) and CPS3 type (3-node linear plane stress triangle) were employed. For the thermal model (Flowchart 2 – Figure 3), elements of the DC2D4 type (4-node linear heat transfer quadrilateral) and DC2D3 type (3-node linear heat transfer triangle) were adopted [25]. The adopted mesh is presented in Figure 4.

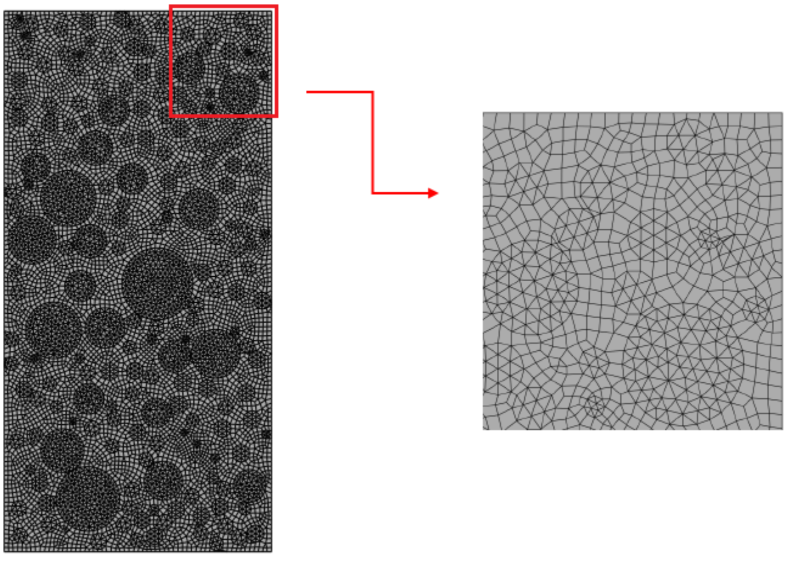

Figure 4. Mesh adopted to discretize the model.

2.2.3 Linear elastic model mesh

From mechanical properties, by Razafinjato [23], we had the Young's modulus of mortar and concrete. However, the Young's modulus of aggregate as well as the Poisson's ratio of the aggregate and the mortar were unknown and, to determine them, an inverse procedure was used.

The numerical procedure consisted of simulating a 1/4 of the longitudinal section of a cylindrical specimen with 150mm in diameter and 300mm in height, composed by two phases, mortar and aggregate, under increasing axial loading, through a displacement applied at the top of the sample as represented in Figure 5.

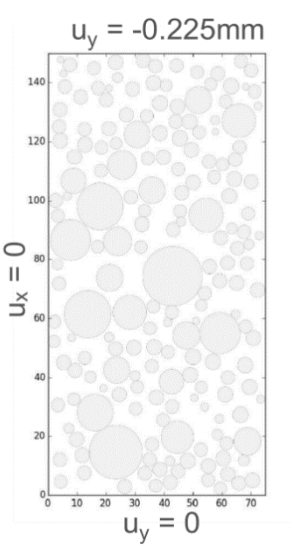

Figure 5. Synthetic specimen with loading and boundary conditions implemented in Abaqus [25].

Flowchart 1, in Figure 2 represents the applied inverse methodology, based on a trial and error procedure implemented in Python language, applying the differential_evolution function, from the *optimize* package of the *SciPy* library [27], assuming as objective function the error between the experimental Young's modulus and numerical. The latter was considered as the ratio between the vertical reactions in response to the applied displacement. Table 1 shows the obtained values.

Table 1. Materials mechanical properties.

Phase	Young's modulus (MPa)	Poisson's ratio
Aggregate	39486	0.201
Mortar	31000	0.129

2.2.4 Thermal model

A transient thermal analysis was performed via Abaqus [25], which adopts the Finite Element Method so as to evaluate the temperature field resulting from exposing a concrete specimen to thermal loading. The loading, initial and boundary conditions are indicated in Figure 6. It is emphasized that the initial and boundary conditions were chosen so to represent the experimental process developed by Razafinjato [23].

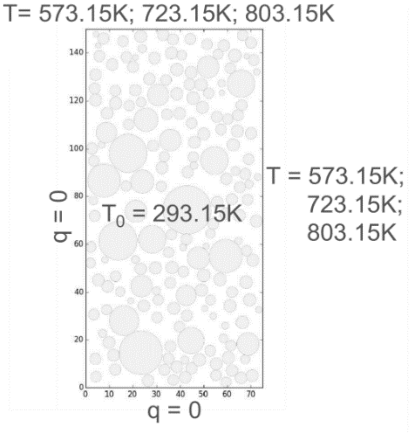

Figure 6. Synthetic specimen with loading and boundary conditions implemented in Abaqus [25].

Figure 7 shows the data provided by Razafinjato [23] for the thermal expansion coefficient of aggregate and mortar. The dashed lines are the simplified curves adopted herein. The curve is limited to 803.15K, since higher temperatures lead to strong non-linearities.

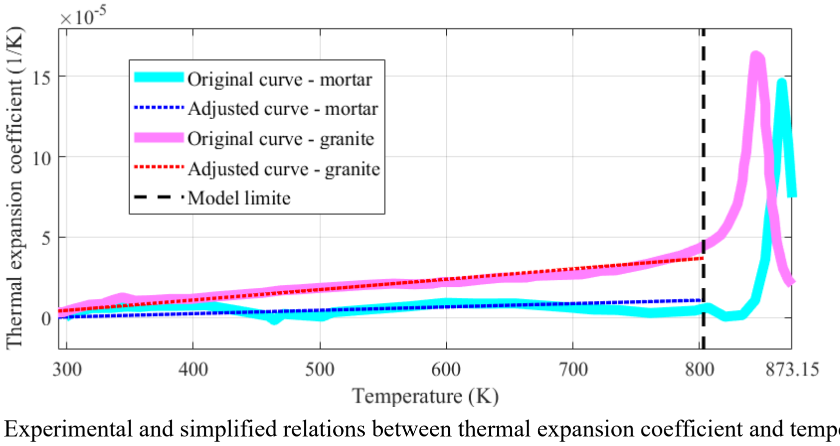

Figure 7. Experimental and simplified relations between thermal expansion coefficient and temperature.

Due to the lack of experimental data regarding the specific heat of the mortar, it was considered as an extrapolation of the concrete curve [23], as shown in Figure 8, and therefore it was assumed that the variation of this property in the mortar is proportional to the variation in the concrete. As a simplification, the specific heat of the granite was considered constant. The initial value for the specific heat of the mortar, the constant value for the specific heat of the granite and the thermal conductivity for both phases were provided by the Brazilian Standard NBR 15220-2: 2005 [28]. The density was adopted according to Razafinjato [23]. Table 2 presents a summary of the assumed properties of the materials.

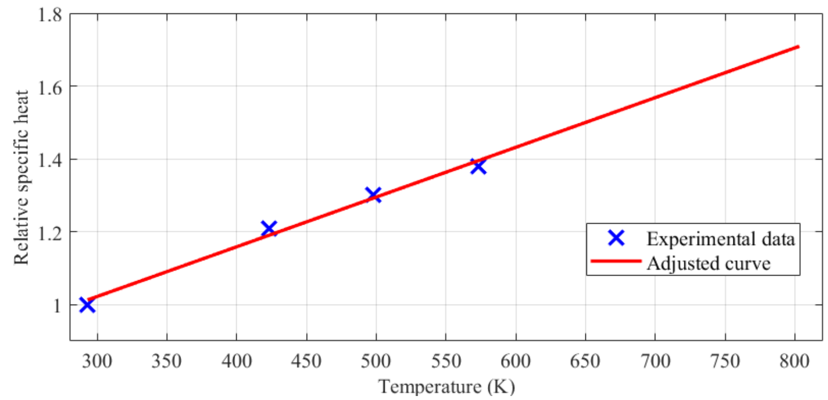

Figure 8. Relation between concrete relative specific heat and temperature.

Table 2. Materials thermal properties, T being the temperature considered.

Phase	Thermal conductivity (J/mmKmin)	Thermal expansion coefficient (1/K)	Specific heat (J/kgK)	Density (kg/mm³)
Aggregate	0.042 NBR 15220-2 [28]	$(0.065T - 15.02) \cdot 10^{-6}$	800 NBR 15220-2 [28]	$2.500 \cdot 10^{-6}$ Razafinjato [23]
Mortar	0.069 NBR 15220-2 [28]	$(0.021T - 6.00) \cdot 10^{-6}$	1.39T + 591.89	$2.252 \cdot 10^{-6}$ Razafinjato [23]

2.2.5 Damage model

Concrete deterioration was then quantified through the Mazars' [2] damage model, which is not available in the Abaqus [25] libraries. For this reason, the model was incorporated to the analysis via a user UMAT subroutine [26], schematically described in the Flowchart 3 shown in Figure 9. We emphasize that, in this work, it was considered that only the mortar and, consequently, the concrete, suffer damage. For the aggregate, the linear elastic behavior was adopted, without damage.

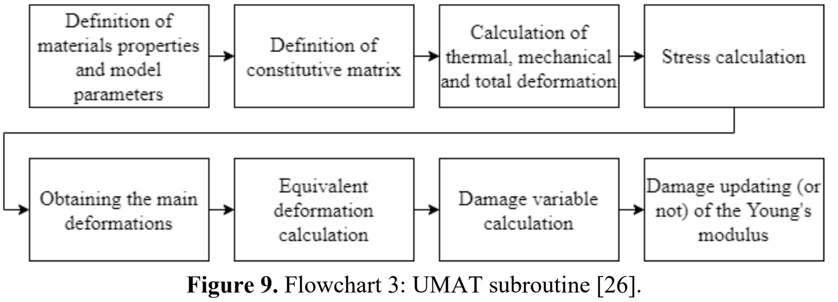

Figure 9. Flowchart 3: UMAT subroutine [26].

In Mazars' [2] damage model, the damage evolution law for traction and compression involves five parameters, A_c, B_c, A_t, B_t and e_{d0}, which were not available from experimental data.

Furthermore, in the proposed model, temperature variation is of the increasing monotonic type, that is, no cooling is considered. Thus, the level of compression identified in the concrete was low and, consequently, the estimated α_c values were lower than the α_t values. Thus, in Equation 5 it was adopted $\alpha_c = 0$, which reduced the parameters of interest to A_t, B_t and e_{d0}, in Equation 4.

These parameters were obtained from a second inverse problem using the function f_min of the package *optimize* from the *SciPy* library [27] in Python language, having as objective function the error between experimental and numerical mortar Young's modulus. This process can be seen in Flowchart 2 (Figure 3) and the obtained Mazars' [2] parameters may be seen in Table 3.

Table 3. Mazars' [2] parameters.

Parameter	Value
A_t	0.669
B_t	254.114
e_{d0}	$3.440 \cdot 10^{-4}$

3 RESULTS AND DISCUSSIONS

A thermal model was developed on the Abaqus [25] to evaluate the thermomechanical behavior of concrete through the Mazars' [2] damage model, obtaining the temperature field active in the entire section of the specimen. Figure 10 shows the uniform distribution of the initial temperature T_0 = 293.15K and the temperature range obtained for T = 573.15K, T = 723.15K and T = 803.15K. The mesh used in the problem was shown at the initial temperature so that it was possible to identify the problem geometry and hidden in the other temperature levels for better visualization of the results. The maximum temperature obtained in the section is found at the top and on the right side, which are the faces in contact with the thermal flow. Consequently, in the center of the specimen, the temperature was the minimum of the section.

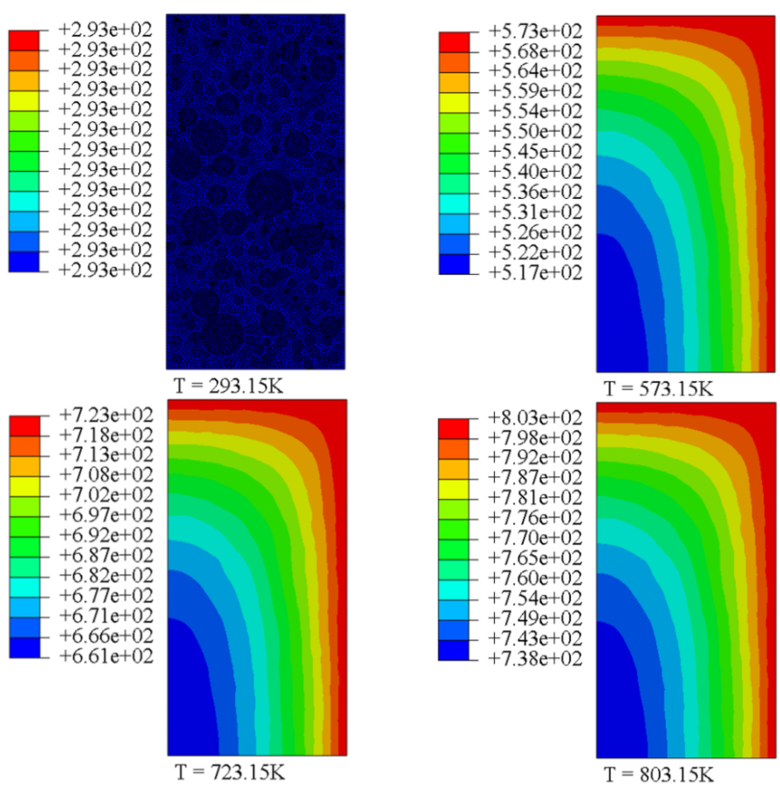

Figure 10. Temperature distribution for 293.15, 573.15, 723.15 and 803.15 K.

A damage model was implemented on the Abaqus [25] using the temperature field as imposed loading. As already explained, at this moment, a UMAT subroutine [26] was used for the model Mazars' [2] to be considered and to find its parameters an inverse problem was solved, from which the values of interest have been determined.

Figures 11 and 12 show, respectively, the damage and Young's modulus map for temperatures T_0 = 293.15K, T = 573.15K, T = 723.15K and T = 803.15K. The mesh used in the problem was shown at the initial temperature so that it was possible to identify the problem geometry and hidden in the other temperature levels for better visualization of the results. It is possible to identify that the greatest damages, and consequently, the smallest Young's modulus, are present in the areas of mortar that interconnect the aggregates.

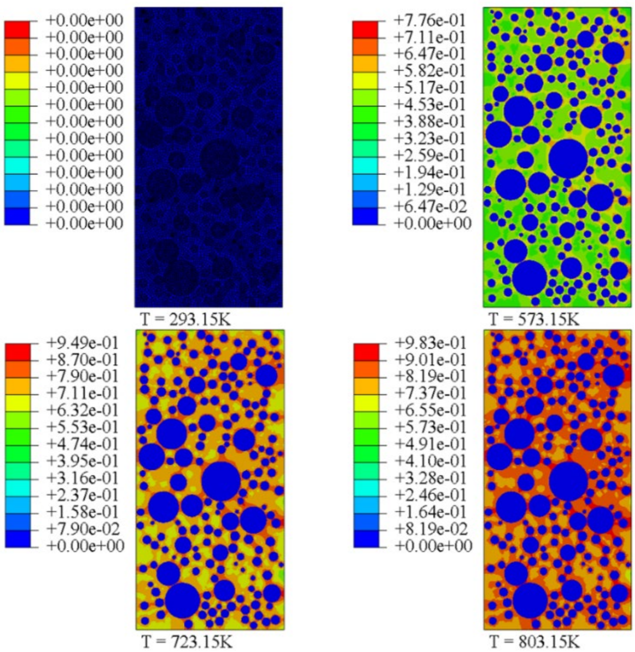

Figure 11. Damage map (adimensional) for 293.15, 573.15, 723.15 and 803.15 K.

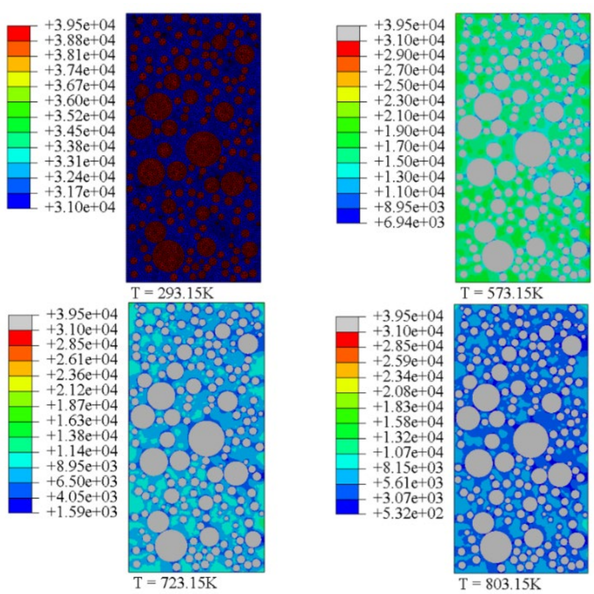

Figure 12. Young's module map, in MPa, for 293.15, 573.15, 723.15 and 803.15 K.

Figure 13 shows the mortar and concrete damage evolution. It is possible to observe that the beginning of the damage in the section occurs around 350K, reaching expressive values from 380K. In addition, it is observed that the final damage of the mortar is 0.84. As for concrete, there is a slightly lower value of 0.74, justified by the fact that the aggregate has null damage and, thus, contributes to the decrease in the homogenized Young's modulus being smaller. Therefore, at the final temperature of 803.15K Young's modulus of the aggregate, mortar, and concrete are equal to 39486MPa, 4920MPa, and 9000MPa respectively.

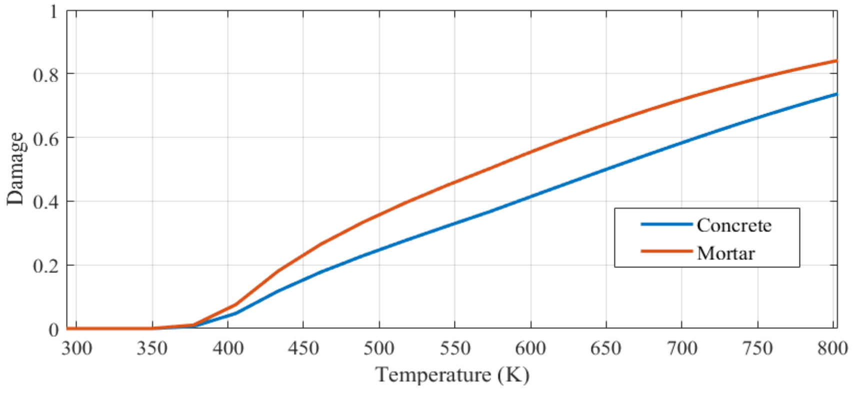

Figure 13. Relation between damage and temperature.

It is important to notice that since the aggregate does not present damage, its Young's modulus keeps constant, as shown in Table 1. In turn, the Young's modulus of mortar is estimated by considering the weighted average of this property in each element of the mesh belonging to this phase. Finally, the Young's modulus of concrete is obtained through the simulation of the uniaxial compression test assuming elastic behavior, as indicated in Figure 5, and by considering the previously estimated values for the mortar and the aggregate.

Figure 14 shows the evolution of Young's modulus obtained experimentally [23] and numerically - normalized from 0 to 1 - and the concrete damage variation with temperature. It is observed that the damage is inversely proportional to the Young's modulus. It is also verified that Young's modulus is reduced by half at 650K, the temperature under which the damage has a value of 0.5. In addition, the relative error between the numerical and experimental values of concrete Young's modulus under 293.15K, 573.15K, 723.15K and 803.15 K was approximately 0.03%.

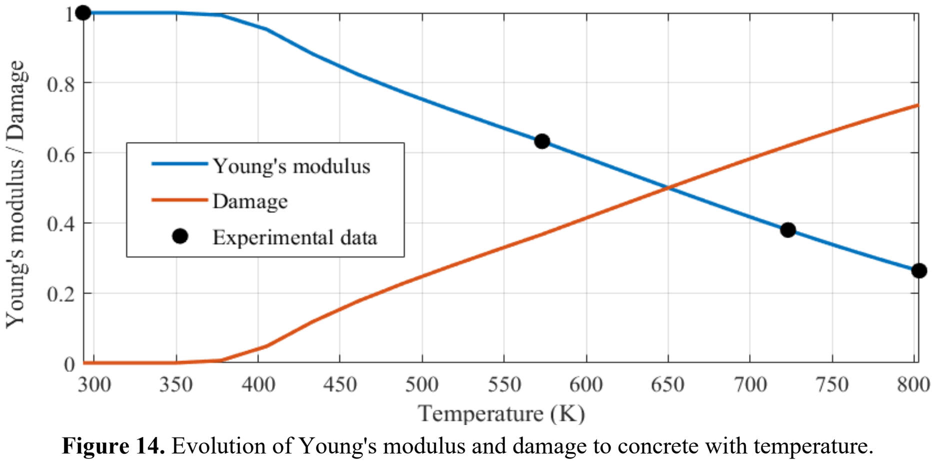

Figure 14. Evolution of Young's modulus and damage to concrete with temperature.

Then, considering the Mazars parameters and the mechanical properties obtained previously, the damage model was applied to other specimens in order to analyze the influence of aggregate grading on the damage evolution. In this sense, specimens were created with 40% of aggregates of fixed dimensions, of 4mm, 8mm, 16mm and 32mm to assess which diameter would result in the greatest damage. As a result, the graph in Figure 15 was obtained, showing that the larger the diameter of the aggregate, the greater the damage, although the difference is not so significant.

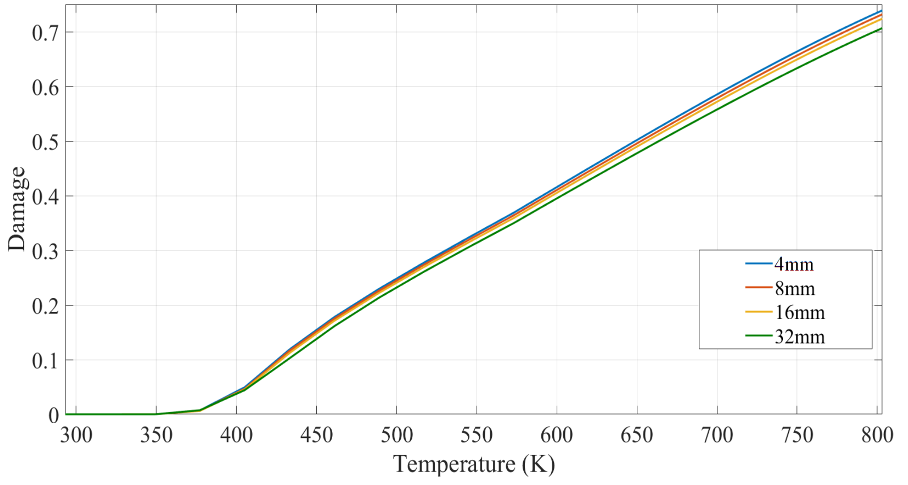

Figure 15. Damage x Temperature relation for concretes with different aggregates grading.

Specimens were also created with different proportions of aggregate, 40%, 30%, 20% and 10%, keeping the aggregate grading curve constant. As a result, the graph in Figure 16 was obtained, showing that the lower the percentage of aggregate, slower is the initial increase of the damage. Regarding the damage to higher temperatures, there are three simultaneous phenomena. The first concerns the damage to the mortar, which is directly proportional to the amount of aggregate. The second is about reducing the initial Young's modulus of concrete by reducing the relative volume of aggregate that has a Young's modulus greater than that of the mortar. The third, on the other hand, is related to the increase in the damaged portion of the model, by reducing the percentage of aggregates that represents the non-damaged portion of the model. These three phenomena, with opposite effects, mean that there is no well-defined pattern for the entire temperature domain, although at the final temperature of 803.15K the highest percentage of aggregates results in slightly higher damage.

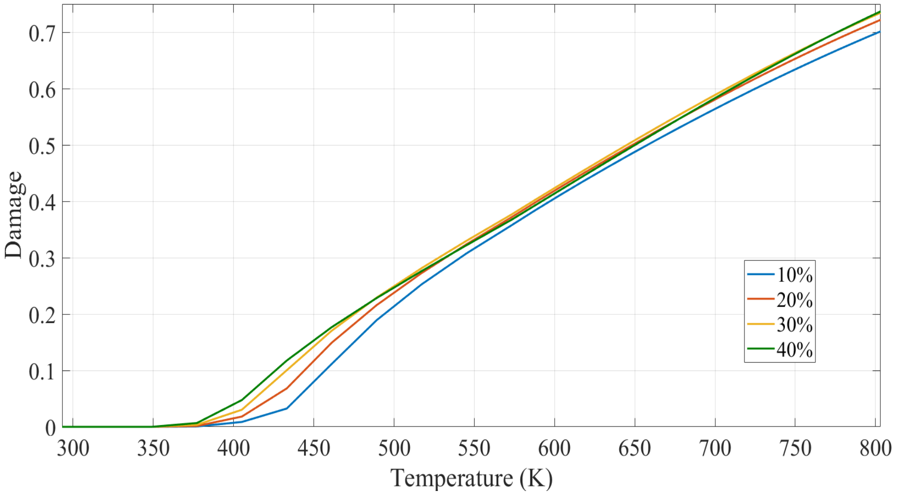

Figure 16. Damage x Temperature relation for concretes with different aggregates proportions.

4 CONCLUSIONS

The present work achieved the proposed objectives: the Mazars' [2] damage model was implemented in the Abaqus [25] software through the UMAT user subroutine, making it possible to observe how the increase in temperature influences the concrete damage and, consequently, in the material Young's modulus, obtaining results consistent with the theory.

Also, the proposed computational model was able to represent the results obtained experimentally by Razafinjato [23] with an error of the order of 0.03%, which is relatively small. Besides, the data available were referents to only four temperatures, while by the curve obtained numerically it was possible to evaluate Young's modulus at any point, between the maximum (803.15K) and minimum (293.15K) temperatures considered.

It is noteworthy the performance of the proposed model, which, with little experimental data, is able to contribute to the elucidation of the mechanism of damage generated in concrete subjected to high temperatures.

In this study, the Mazars' [2] model was implemented for a bidimensional domain. Thus, the implementation of a subroutine in which the model is considered in its tridimensional geometry, would be an improvement on the work done so far.

ACKNOWLEDGEMENTS

To the funding agencies - CAPES, FAPEMIG, and CNPq - for financial support. To the Federal University of Juiz de Fora, and the University of Cergy-Pontoise.

REFERENCES

[1] P. K. Mehta and P. J. M. Monteiro, *Concrete – Microstructure, Properties, and Materials*, 3th ed. Berkeley, USA: McGraw-Hill Education, 2006.

[2] J. Mazars "Application de la mécanique de l'endommagement au comportement non linéaire et à la rupture du béton de structure", Ph.D. dissertation, Univ. Pierre and Marie Curie, Paris, France, 1984.

[3] S. Thelandersson, "Modeling of combined thermal and mechanical action in concrete," *J. Eng. Mech.*, vol. 113, no. 6, pp. 893–906, 1987.

[4] J. C. Simo and J. W. Ju, "Strain and stress-based continuum damage models," *Int. J. Solids Struct.*, vol. 23, pp. 821–840, 1987.

[5] M. Cervera, J. Oliver, and O. Mazoli, "A rate-dependent isotropic damage model for the seismic analysis of concrete dams," *Earthquake Eng. Struct. Dynam.*, vol. 25, pp. 987–1010, 1996.

[6] J. J. C. Pituba and M. M. S. Lacerda, "Sobre o emprego de modelos simplificados de dano na análise de estruturas em concreto armado," *Ibracon Struct. Mater. J.*, vol. 5, no. 1, pp. 26–37, 2012.

[7] R. C. A. Lima, L. D. Kirchhof, C. A. Casonato, and L. C. P. Silva Filho "Efeito de altas temperaturas no concreto", *II Seminário de Patologias das Edificações*, Nov. 2004.

[8] O. Arioz, "Effects of elevated temperatures on properties of concrete," *Fire Saf. J.*, vol. 42, no. 8, pp. 516–522, 2007.

[9] Ehrenbring, H. Z., Ortolan, V., Bolina, F., Pacheco, F., Gil, A. M. and Tutikian, B. F., "Avaliação da resistência residual de lajes alveolares em concreto armado em uma edificação industrial após incêndio", *Matéria (Rio J.)*, vol. 22, no. 3, pp. 1-10, 2017.

[10] C. G. Bailey and W. S. Toh, "Small-scale concrete slab tests at ambient and elevated temperatures," *Eng. Struct.*, vol. 29, no. 10, pp. 2775–2791, 2007.

[11] L. D. P. Souza, G. A. Azerêdo, and F. A. Silva, "Comportamento do concreto sob altas temperaturas via planejamento experimental fatorial com configuração estrela," *Ambient. Constr.*, vol. 18, no. 1, pp. 237–344, 2018.

[12] Dias, A. R. O., Amâncio, F. A., Rafael, M. F. C. and Cabral, A. E. B., "Comportamento do concreto submetido a altas temperaturas", *Matéria (Rio J.)*, vol. 25, no. 2, pp. 1-14, 2020.

[13] J. C. L. Ribeiro "Desenvolvimento e aplicação de um sistema computacional via método dos elementos finitos do comportamento de estruturas de aço e mistas em situação de incêndio," Ph.D. dissertation, Federal Univ. Minas Gerais, Belo Horizonte, SC, Brazil, 2009.

[14] E. P. G. Padre, J. C. L. Ribeiro, R. C. S. S. Alvarenga, and R. C. Silva, "Algoritmo computacional para verificação de seções de concreto armado em situações de incêndio," *Ibracon Struct. Mater. J.*, vol. 12, no. 4, pp. 932–955, 2019.

[15] B. A. Izzuddin and A. Y. Elghazouli, "Failure of lightly reinforced concrete members under fire. I: Analytical modeling," *J. Struct. Eng.*, vol. 130, no. 1, pp. 3–17, 2004.

[16] P. Grassl and C. Pearce, "Mesoscale approach to modeling concrete subjected to thermomechanical loading," *J. Eng. Mech.*, vol. 136, no. 3, pp. 322–328, 2010.

[17] M. W. Ferreira "Estudo numérico dos efeitos estruturais da exposição de pilares em concreto armado a altas temperaturas", M.S. thesis, Federal Univ. Rio Grande do Sul, Porto Alegre, Brazil, 2019.

[18] T. D. Nguyen, D. T. Pham, and M. N. Vu, "Thermo-mechanically-induced thermal conductivity change and its effect on the behaviour of concrete," *Constr. Build. Mater.*, vol. 198, pp. 98–105, 2019.

[19] Rodovalho, F. S., Corrêa, M. R. S. and Neto, J. M., "Simulação termomecânica de prismas com blocos de concreto em situação de incêndio", *Matéria (Rio J.)*, vol. 25, no. 1, pp. 1-27, 2020.

[20] E. B. Assis and J. M. Neto "Analysis of heat transfer mechanisms on hollow concrete masonry units under standardized fire conditions", *XLI Ibero-Latin-American Congress on Computational Methods in Engineering*, 16-19 Nov. 2020.

[21] D. F. Barbosa and V. G. Haach "Estudo de caso de edifício de alvenaria estrutural em situação de incêndio por meio de simulação numérica", *XLI Ibero-Latin-American Congress on Computational Methods in Engineering*, 16-19 Nov. 2020.

[22] L. R. Machado, V. F. P. Dutra, and S. Maghous, "A limit analysis approach to the stability assessment of reinforced concrete panels in fire conditions," *Lat. Am. J. Solids Struct.*, vol. 17, no. 1, 2020.

[23] R. N. Razafinjato "Comportement des bétons à haute température: influence de la nature du granulat", Ph.D. Thesis, Univ. Cergy-Pontoise, Paris, France, 2015.

[24] A. L. Bonifácio "Estratégia computacional para avaliação de propriedades mecânicas de concreto de agregado leve", Ph.D. Thesis, Federal Univ. Juiz de Fora, Juiz de Fora, Brazil, 2017.

[25] Abaqus6.11., "Abaqus Documentation", http://130.149.89.49:2080/v6.11/index.html (July 16, 2020).

[26] Abaqus6.11., "Abaqus User Subroutines Reference Manual", http://193.136.142.5/v6.11/books/sub/default.htm?startat=ch02s01abu17.html (July 16, 2020).

[27] Python 3.8.5., "Python Documentation", https://docs.python.org/ptbr/3/tutorial/index.html (July 26, 2020).

[28] Associação Brasileira de Normas Técnicas, *Desempenho de edificações – Parte 2 – Método de cálculo da transmitância térmica, da capacidade térmica, do atraso térmico e do fator solar de elementos e componentes de edificações – NBR 15220-2*, 2005.

Author contributions: LSA and MFDS: formal analysis, methodology, validation, visualization, writing-original draft; MCRF: conceptualization, supervision, writing-review & editing; FSB: supervision, writing-review & editing; ALB: data curation.

Editors: Osvaldo Manzoli, Guilherme Aris Parsekian.

IBRACON Structures and Materials Journal
Revista IBRACON de Estruturas e Materiais
ISSN 1983-4195 ismj.org

ORIGINAL ARTICLE

Investigation of the adherence between clay blocks and grouts

Investigação da aderência entre blocos cerâmicos e grautes

Gustavo Sipp[a]
Guilherme Aris Parsekian[a]

[a]Universidade Federal de São Carlos - UFSCar, Departamento de Engenharia Civil, São Carlos, São Paulo, Brasil

Received 15 April 2021
Accepted 02 July 2021

Abstract: This study aims to evaluate the adherence between clay blocks and grouts. For this purpose, push-out and pull-out tests were performed to assess the adherence presented by different combinations of five types of clay blocks and two types of grouts. The results demonstrated that the geometry of the cells of the clay blocks has a preponderant role in their adherence with grout, as the extent of the contact area between grout and block depends on the geometry of the cell. The shrinkage of the grout can cause the formation of cracks at the interface between block and grout, reducing the adherence between the materials. The shrinkage formed inside each type of block can be estimated based on the testing procedure developed in this research and used in conjunction with the geometric characteristics of the cells of the blocks to estimate the maximum load in the push-out tests. The test procedure developed to estimate the percentage of contact area lost due to grouts shrinkage shows to be promising, since its results were used in the equation to estimate the bond strength between blocks and grouts and shown good correlation. However, more study must be done because there are other variables that can affect the results. These results show that it is possible to use different characteristics of blocks and grouts to increase the adherence between these materials and provide a better behavior for reinforced masonry structures. However, it looks like if block types with a grooved hollow cell are used, a bigger contact surface is produced, and a higher bond strength appears to be assured.

Keywords: Grout, clay block, adherence, push-out test, pull-out test.

Resumo: Este estudo tem como objetivo avaliar a aderência entre blocos cerâmicos e grautes. Para isso, foram realizados ensaios de *push-out* e *pull-out* para avaliar a aderência apresentada por diferentes combinações de cinco tipos de blocos cerâmicos e dois tipos de grautes. Os resultados demonstraram que a geometria da célula dos blocos cerâmicos tem papel preponderante em sua aderência com o graute, pois a extensão da área de contato entre graute e bloco depende da geometria da célula. A retração do graute pode causar a formação de fissuras na interface entre blocos e graute, reduzindo a aderência entre os materiais. A retração formada dentro de cada tipo de bloco pode ser estimada com base no procedimento de ensaio desenvolvido nesta pesquisa e usados em conjunto com as características geométricas das células dos blocos cerâmicos para estimar a carga máxima obtida nos ensaios de *push-out*. O ensaio desenvolvido para estimar a porcentagem de área de contato perdida devido a retração do graute mostra-se promissor, uma vez que seus resultados foram utilizados na equação para estimar a resistência de união entre blocos e rejuntes e apresentaram boa correlação. No entanto, mais estudos precisam ser feitos porque existem outras variáveis que podem afetar os resultados. Foi demonstrado que é possível utilizar diferentes características de blocos e grautes para aumentar a aderência entre esses materiais e proporcionar um melhor comportamento para estruturas de alvenaria armada. No entanto, conclui-se que se forem usados tipos de bloco com vazado ranhurado, uma superfície de contato maior é produzida e uma aderência parece ser garantida.

Palavras-chave: Graute, bloco cerâmico, aderência, ensaio de *push-out*, ensaio de *pull-out*.

How to cite: G. Sipp, and G. A. Parsekian, "Investigation of the adherence between clay blocks and grouts," *Rev. IBRACON Estrut. Mater.*, vol. 15, no. 1, e15112, 2022, https://doi.org/10.1590/S1983-41952022000100012

Corresponding author: Gustavo Sipp. E-mail: gsipp@hotmail.com
Financial support: This study was financed by the Associação Nacional da Indústria Cerâmica (ANICER) and by the Coordenação de Aperfeiçoamento de Pessoal de Nível Superior - Brasil (CAPES) - Finance Code 001.
Conflict of interest: Nothing to declare.

1 INTRODUCTION

In masonry structures, grout is often used to improve the mechanical properties of structural members. Grout can be used to fill the holes of the blocks, to enhance the compressive strength of the member, and in the case of reinforced masonry, grout serves as the connecting component between steel bars and blocks allowing tensile strength. The behavior of masonry structures is influenced by the physical and mechanical properties of the materials used in their construction and, also, by the characteristics of these materials in the contact interface. These characteristics have a fundamental role in the distribution of stresses and deformations among the various components that have contact surfaces. The shrinkage of the grout used to fill the blocks can also affect the contact surface influencing their bond capacity.

According to Kingsley et al. [1], due to the porous nature of the clay blocks, they tend to absorb water from the grout, the instant they come into contact. The magnitude of this absorption depends on the properties of block and grout. The result of the migration of water to the block will be the reduction of the water/cement ratio of the grout with a significant reduction in its volume (shrinkage). According to Soric and Tulin [2], to evaluate reinforced masonry two types of bond must be considered. The bond between reinforcement and grout, which is highly influenced by the interaction of the reinforcement transverse ribs with the grout and, the bond between grout and blocks, which is highly influenced by the adhesion developed in the contact interface. Ahmed and Feldman [3] and Kisin [4] found evidence of poor bond between concrete blocks and grout when performing 4-point flexural tests in reinforced masonry. The researchers' objective was to evaluate the behavior of walls using different techniques for lap splicing steel bars. The authors identified that walls on which the steel bars were lab spliced in contact (in the same block hollow cell), the mode of rupture was characterized by the pull-out of the reinforcement. However, for walls where the lapped bars were in adjacent cells of the blocks, the form of rupture was different, forming cracks at the interface between blocks and grouts. The load capacity of the walls with this second rupture mode was lower than that presented by the first one, indicating that a greater adherence between grout and blocks could improve the results.

Push-out tests were carried out by Izquierdo et al. [5] to assess the adherence between concrete and clay blocks to two types of grouts. As a result, the authors identified that the bond between grout and concrete blocks was adequate, as the rupture occurred due to cracking of the block. However, on the tests performed with clay blocks, the rupture mode presented by the specimens was the slippage of the grout, providing a significant reduction in the load capacity of the set. The roughness presented by the concrete blocks was 10 times greater than the roughness presented by the clay blocks. The bond strength identified by the authors for the clay blocks were 0.16 and 0.19 MPa, for the use of grout with 14 and 30 MPa of compressive strength, respectively. The authors identified an increase in the bond strength obtained for the clay blocks when the compressive strength of the filling material is greater.

Thamboo et al. [6] evaluated the influence of the surface roughness of concrete blocks on the bond strength with polymer cement mortars. According to the authors, blocks with smooth surfaces presented higher bond strength than blocks with rough surfaces. Pereira de Oliveira [7] reports a study to evaluate the effects of four different grout mixtures on the bond strength with one concrete block type. The mixtures had different levels of water/cement ratio (w/c) and specific area of the aggregates. The results shown that the increase in the w/c ratio decreased the bond strength of the grout/block interface. The increase in the specific area of the aggregate promoted an increase in the bond strength to a certain point and then it decreased. The author recommended to use the bond strength as a criterion to choose the grout for masonry, as well as its compressive strength. Pereira de Oliveira [8] investigated the influence of the bond strength of different grout mixtures on the compressive strength of masonry prisms. The author identified an increase in the compressive strength of prisms with an increase in the bond strength of the grout used. This shows the importance of evaluating this behavior in masonry, not only for reinforced masonry. The push-out test is also reported in Guarnieri et al. [9], to assess the influence of the compressive strength of clay blocks and its holes' geometric shapes on the bond strength with grout. The compressive strength of the grout was 30 MPa. The bond strength obtained was 1.73, 1.42, 2.93 and 2.64 MPa, for the blocks of 7, 10, 15 and 18 MPa of compressive strength, respectively. Results indicated that there is a tendency to increase the bond strength of the material as the compressive strength of the blocks increases. The predominant mode of rupture was the failure of the fired clay blocks, indicating that the bond strength of the set was superior to the blocks' mechanical capacity. Because the form of rupture identified in the tests was the cracking of the clay blocks, it makes sense to expect an increase on the bond strength for blocks with higher compressive strength, since they were the weak link on the test.

In addition to the push-out test, another technique that has been used to assess the adherence between the elements of reinforced masonry is the pull-out test. This test consists of connecting a steel bar in a masonry element, inside the holes of the blocks using grout. After curing the grout, a force is applied to pull-out the steel bar from the interior of the masonry, allowing to evaluate the adherence in the set. The maximum force in the test is divided by the cross-section area of the rebar, obtaining the maximum stress supported by the set. This stress is usually compared to the yield capacity of the steel. Usually, the pull-out test is used to verify the bond between the reinforcement and grout, however, Kisin [4] suggests that this test can also be used to measure the adherence of the rebar to the whole set, including the grout and the blocks that encases the grout. Izquierdo [10] states that the pull-out test evaluates the performance of the block/grout/reinforcement interfaces, as it exerts a force on all the materials in the set. Biggs [11] points out that the failure during the pull-out test will occur at the weakest connection within the set. This may be in the block/grout interface or in the grout/reinforcement interface. According to Biggs [11] there is three different forms of rupture on this test: 1) cracking of the block and its filling material; 2) cracking of the block and sliding of the filling material; and 3) rupture of the filling material around the reinforcement and slippage of the rebar.

Biggs [11] reports reinforcement bars pull-out tests in concrete block masonry, using fine-aggregate grout ("fine grout" according to ASTM C 476 [12]). The failure load for grout samples was higher than the yield strength load of the reinforcement. Soric and Tulim [13] carried out pull-out tests on masonry specimens built with concrete blocks and clay blocks. Reinforcement bars with 13 and 22 mm of diameter were used in the tests. The authors observed a similar behavior for specimens made with concrete and clay blocks when 13 mm bars were used. For specimens made with clay blocks and 22 mm bars, an increase in slip was observed at 25% of the yielding load, while for the specimens made with concrete units, they showed a slip at 50% of the yielding load. The diameter of the bar, the quality of the grout and the thickness of the masonry are decisive factors for reinforced masonry structures.

Izquierdo et al. [5] carried out pull-out tests to assess the adherence between clay and concrete blocks to the grouts, to complement the results obtained in the push-out tests. As in the push-out tests, the pull-out tests showed good adherence for the grouts when using concrete blocks, making it possible to reach loads higher than the reinforcement yielding capacity. On the other hand, for the tests performed with clay blocks, the slippage of the grout from the interior of the blocks was identified, causing the rupture of the set with loads below steel yielding capacity. The pull-out test allows to complement the results obtained in the push-out tests, with results closer to the behavior of actual masonry structures. The pull-out test allows to consider the influence of the imperfections of the vertical laying of the blocks between the courses, which create indents that can contribute to inhibit the slippage of the filling material and increase the adherence at the interface. This same effect can also be obtained by changing the geometry of the cells of the blocks. A mechanism to hinder the grout slippage can be created when protrusions or indents in the hollow cells of the blocks do not match in position at each laying course.

1.2 Objectives

This article aims to evaluate the adherence behavior between different types of fired clay blocks and grouts. Push-out and pull-out tests were performed to assess the adherence among different combinations of blocks and grouts. The hollow cells of the blocks have different geometric shapes, eventually incorporating protrusions and grooves inside the hollow in the contact face. From the results it was possible to assess the behavior of the block-grout interface and to conclude which is the best geometric shape for the block hollow. In addition, an equation was proposed to estimate the bond strength of each combination of block and grout, taken in to account the influence of the geometric shape of the cells of the blocks and the shrinkage of the grout.

2 MATERIALS AND METHODS

Five types of fired clay blocks and two types of grouts were tested. The grouts came from the same manufacturer in bags and were used without the addition of coarse aggregates, with nominal compressive strength of 15 MPa (G15) and 30 MPa (G30). The amount of water used was enough to promote a consistency of (250 $\pm$ 20 mm) in the slump test. The five types of blocks used in this research were manufactured by the same company. The dimensions of all the blocks were 140×390×190 mm, respectively, width, length, and height. The blocks differed mainly by their mechanical properties, geometries of the holes and the fact that some had a solid faceshell while others had a perforated faceshell.

Usually, the blocks have a smooth surface inside the holes. However, blocks with protrusions and grooves inside the hollow of the cells surface were produced for testing. To differentiate between the types of blocks, the blocks with a solid (massive) faceshell are called BM, while blocks with a perforated (voided) faceshell are called BV. These abbreviations are followed by a number that indicates the number of indentations present in one of the cells of the block. The different types of blocks used in this research and their nomenclature are shown in Figure 1.

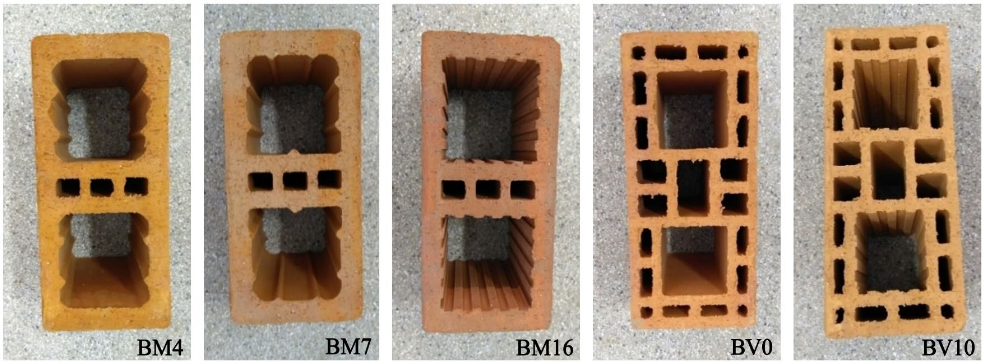

a) b) c) d) e)

Figure 1. Types of fired clay blocks.

As can be seen in Figure 1, block types BM4, BM7, and BM16 have solid (massive) faceshell. Block types BV0 and BV10 have a perforated (voided) faceshell. In block types BM16 and BV10, the internal surfaces of the cells are grooved to increase the contact area between block and grout. Block types BM4 and BM7 have few indentations in the internal surface of the cell. The block type BV0 is the only one that has smooth surfaces inside the hole. In block type BM7 the indentation in the web face will not match vertically when the block is laid into a running bond pattern, thus creating a kind of a vertical shear key between the grout and block.

2.1 First phase – Materials characterization

Physical and mechanical properties of all materials used in the research were determined. The main properties evaluated for the blocks were compressive strength and water absorption. These tests were carried out according to NBR 15270-2 [14] standard procedure, using 13 blocks for measuring compressive strength and six for the determination of water absorption of the blocks. The internal average roughness of each type of block was also measured, using the same equipment as described by Izquierdo [9]. For this test, 6 specimens of each type of block were cut from the faceshell of the blocks. More information can be seen in the Figure 2. Figure 2a shows the cut of a specimen. Figure 2b shows the places were specimens were cut in the blocks. Figure 2c shows the equipment used in the test.

a) b) c)

Figure 2. Scheme of roughness test.

The internal dimensions of the cells of the blocks were also measured to determine which type of block provided the largest contact area with grout, and what is the contribution of the indentations to increase the internal surface area of the cells. This geometric characteristic is especially important to understand the intensity of the shear stresses that block-grout interface can tolerate, especially in the push-out test. The main tests used to characterize the grout were compressive strength, tensile strength, elastic modulus, and water absorption. All these tests were performed with six cylindrical specimens (100 × 200 mm), following, respectively, the procedures presented in the NBR 5739 [15], NBR 7222 [16], NBR 8522 [17] and NBR 9778 [18] standard codes.

2.2 Second phase – Push-out test

The push-out test was used to determine the bond strength of the contact interface between each type of block and grout, to verify which properties of the materials analyzed in the first phase can affect the bond strength. The push-out specimen consisted of one single clay block with only one of the cells filled with grout. The grout was poured and compacted into the block cell until it protruded 30 mm out from the top of the block. The test consists of applying a force to remove the grout from the interior of the block. The specimen was positioned over a steel plate with a rectangular window cut. The dimensions of the window matched the overall dimension of the hollow cell of the block. The steel plate can support only the block, allowing the grout to move freely through the window. A displacement-controlled load was applied, at a 1 mm/minute rate, to the protruding grout surface to expel it from the interior of the block.

The bond strength and the contact area are obtained, respectively, with Equation 1 and Equation 2:

$$A.S. = \frac{Fmax.}{C.A.} \tag{1}$$

$$C.A. = P \times H \tag{2}$$

where $A.S.$ = bond strength (MPa); $Fmax.$ = maximum force during the push-out test (N); $C.A.$ = contact area between block and grout (mm^2); P = perimeter of the hole of the block; and H = height of the block.

The test procedure is illustrated in Figure 3. Figure 3a shows the compaction of the grout. Figure 3b shows the steel plate used to support the block. Figure 3c shows the set ready for test. The compaction of the grout began with the moistening of the interior of the blocks. Later, grout was added inside the block and 25 strokes were applied with a metal rod. After this step, more grout was added and, approximately 5 minutes later, another 25 strokes were applied to compact the grout. This same procedure was applied to all tests that use grout to fill the blocks.

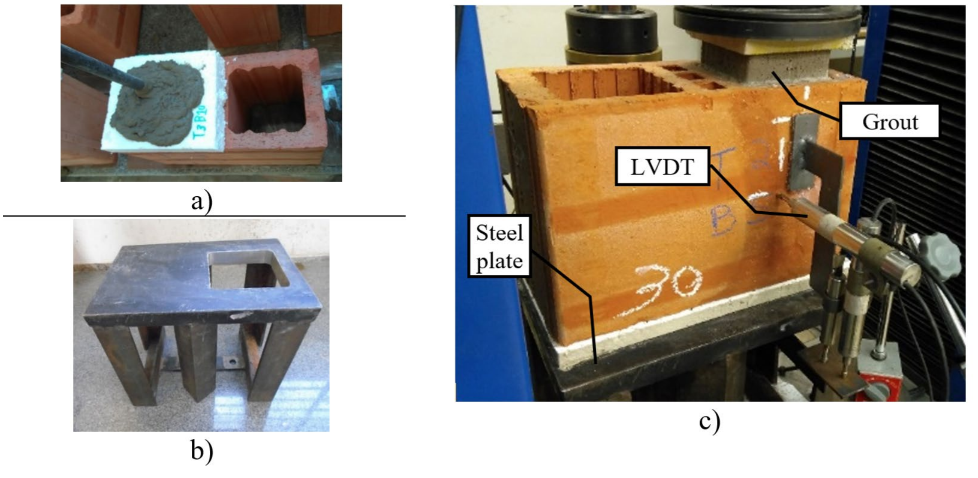

Figure 3. Scheme of push-out test.

For each combination of block and grout type, six specimens were tested. Considering five types of clay blocks and two types of grouts, a total of 60 specimens were tested. The slip of the grout was measured using displacement transducers placed at the block faceshell and connected to the bottom of the grout.

2.3 Third phase – Pull-out test

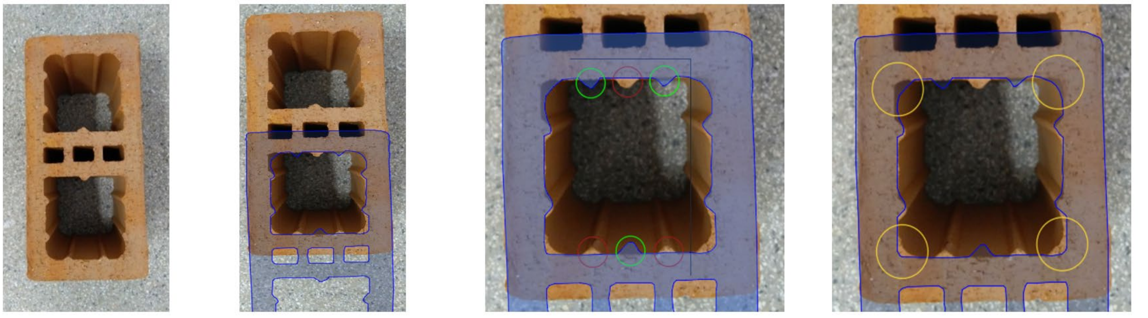

a) b) c) d)

Figure 4. Indentations on the internal surface of the cells (block type BM7).

For this test three types of blocks were used. The BM16 and BV10 types were chosen because they presented the highest bond strength values on the push-out test, among the solid and perforated faceshell blocks, respectively. Additionally, the BM7 type of block was also tested to verify if the presence of the shear keys showed in Figure 4 can contribute to improve adherence of the set, in comparison with the results obtained from push-out tests. Figure 5a shows how load was applied. Figure 5b illustrates the scheme assay used for pull-out test and a specimen used. The specimen used in this test was a wall with five-course high and 1.5 blocks wide with blocks laid in a running bond pattern. In the central hole of these walls, a steel bar was embedded in grout to perform the pull-out test after curing. The rebar used in all specimens have a diameter of 16 mm made from steel CA-50 by the manufacturer ArcelorMittal.

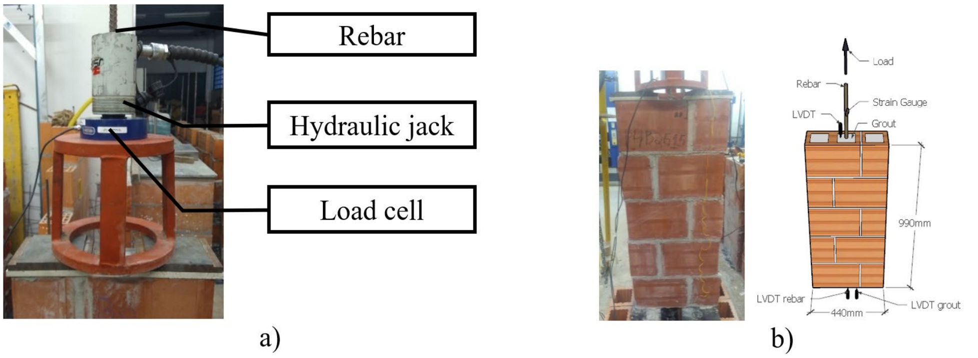

a) b)

Figure 5. Scheme assay of pull-out test.

The 16 mm bars were chosen because this is the largest diameter that can be used for block types BV0 and BV10, which have a hollow cross-sectional area of 70 cm^2. According to NBR 16868-1 [19], the reinforcement area cannot be greater than 8% of the grout area, considering the lap splice of the bars. The basic anchorage length for CA-50 16-mm reinforcement according to NBR 6118 [20] is 716 and 519 mm, respectively for grout G15 and G30, smaller than the height of the specimen. For each type of block six walls were built. In three of these walls, reinforcement was embedded in G15 grout, while in the other three walls the reinforcement was embedded in G30 grout. The two other (unreinforced) hollows of each one of the six walls were filled with G30 grout. As can be seen in Figure 5 a strain gauge was used to verify if the reinforcement bar achieves its yield capacity. Two LVDT were used to measure the slippage of the grout on the top and on the bottom of the specimen. Another LVDT was also used on the rebar on the bottom of the specimen to verify the slippage of the rebar. The load was applied on the rebar through a hydraulic jack with a capacity of 20 tf and the load was measured with the load cell with the same capacity.

2.4 Fourth phase – Investigations of the grouts' shrinkage

While the specimens earmarked for the push-out tests were curing, it was noticed that, in some cases, the grout showed signs of shrinkage inside the block. In these cases, a narrow gap appeared at the block-grout interface (Figure 6). Block types BM4 and BM7 presented similar behavior. There were light signals of gap formation in some places of the interface block/grout for the G15 grout and a little more accentuated signals with the G30 grout, outlining almost the entire block/grout interface. The BM16 type of block showed signs of gap formation at some small portions of the interface with the use of grout G15 and at slightly larger portions with grout G30. For the BV0 type of block, some signs of gap formation were observed in some spots of the interface with the G15 grout. For the G30 grout, signs of gap were observed also at some spots, perhaps a little larger than with the G15 grout. For block type BV10, very few signs were observed in small spots of some blocks with grout G15. For the grout G30 the signs seemed to be like the ones find for G15 grout. Thus, it became necessary to investigate the extent of the shrinkage of the two types of grouts and its impact on the bond with the different types of blocks. The shrinkage of the grout was assessed by monitoring the dimensional variation of grout prisms for 28 days as prescribed in NBR 15261 [19].

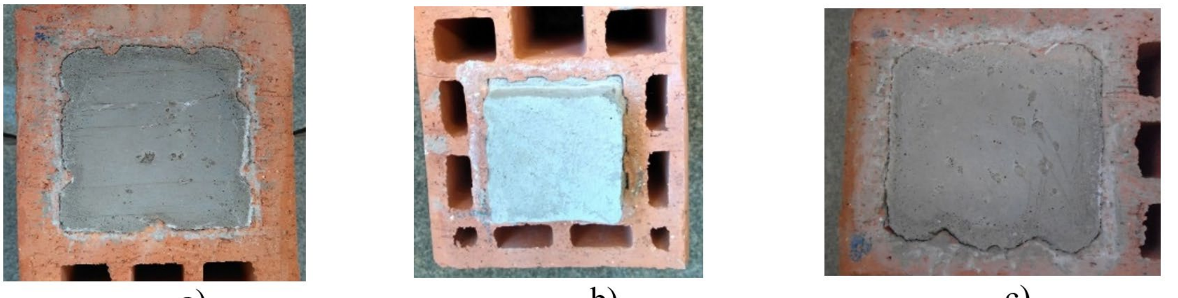

a) b) c)

Figure 6. Signs of shrinkage of the grout.

To assess the impact of the grout shrinkage on the interface between blocks and grouts, an alternative procedure was developed. Two blocks of each of the five types were assessed. Each block had one hole filled with grout G15 and other with grout G30. In total, ten blocks were assessed on this testing. After 28 days of grout curing, the blocks were cut in half of its height and the internal surfaces were photographed. The images were digitally incorporated into a CAD program allowing to measure the length of the cracks formed inside the grout and in the block-grout interface. These same images were also used to determine the length of the perimeter of the cell of each type of block used in the procedure. It is possible to calculate the percentage of cracks formed inside the grout or at the interface block/grout, dividing the length of cracks measured by the length of the perimeter of the cell of block.

The percentage of cracks formed at the interface block/grout can be considered as percentage of the contact area lost due to the shrinkage of the grout in certain type of block. This percentage will allow to evaluate which combination of block and grout forms the highest value of cracks and the higher reduction in the contact area due to shrinkage. In Figure 7 different images show the shrinkage in the different combinations of block and grout types: Figure 7a (BV0 and G15), Figure 7b (BV0 and G30), Figure 7c (BM16 and G15) and Figure 7d (BM16 and G30).

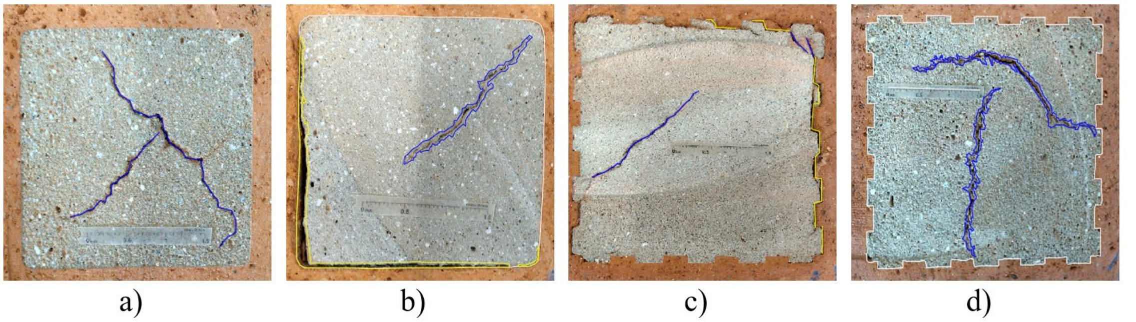

a) b) c) d)

Figure 7. Estimating the effects of shrinkage inside the specimens.

3 RESULTS AND DISCUSSION

3.1 First phase – Materials characterization

The geometric properties presented by the different types of clay blocks are shown in Table 1. Values between brackets are the coefficient of variation of the sample.

Table 1. Geometric characteristics of the blocks.

Type of block	Blocks' gross area (cm^2)	Blocks' net area (cm^2)	Characteristics of the holes of the blocks			
			Perimeter (cm)	Cross section (cm^2)	Smooth contact area (cm^2)	Total contact area (cm^2)
BM4	407 (1.2%)	201 (1.2%)	38.7 (0.6%)	91.8 (1.3%)	688 (1.2%)	725 (1.1%)
BM7	411 (0.4%)	209 (0.3%)	37.2 (0.3%)	89.2 (0.5%)	652 (0.6%)	699 (0.6%)
BM16	400 (0.8%)	197 (0.9%)	47.9 (0.2%)	91.5 (0.6%)	737 (0.7%)	899 (0.6%)
BV0	404 (0.5%)	180 (0.3%)	29.1 (0.3%)	52.9 (0.5%)	547 (0.5%)	547 (0.5%)
BV10	407 (0.3%)	184 (0.2%)	33.6 (0.2%)	51.6 (0.6%)	561 (0.4%)	638 (0.4%)

The smooth contact area of the blocks presents the contact area without considering the contribution of the indentations on the inside of the cells of the blocks. This contact area varies mainly due to the overall dimensions of the holes in each type of block. The total contact area considers the sum of the smooth area plus the area added by the indentations inside the holes of the blocks. Comparing the two contact areas shown in Table 1, contact area increases of 5, 7, 22, 0 and 14% resulted from the presence of the indentations, respectively for block types BM4, BM7, BM16, BV0, and BV10. The contact area of the block type BV0 did not show an increase in the total contact area, as it is the only one that has a cell with a smooth internal surface (without indentations). The largest contact area among the massive faceshell blocks was observed in BM16 while the largest contact area among the voided faceshell blocks was in BV10. Therefore, the two blocks with the most irregular (grooved) surfaces were those with the largest contact area. In addition to the geometric properties, water absorption, roughness and compressive strength of the clay blocks can influence the behavior of the adherence between blocks and grouts. The results of these properties can be seen in Table 2.

Table 2. Properties of the blocks.

Block Type	Water absorption (%)	Vertical roughness (μm)	Characteristic compressive strength (MPa)	Avg. compressive strength (MPa)*	Avg. compressive strength (MPa)**
BM4	12.2 (6.9%)	8.67 (26.6%)	20.48	27.8 (13.4%)	56.0 (13.4%)
BM7	13.2 (3.7%)	6.90 (25.1%)	16.82	19.7 (11.2%)	38.6 (11.2%)
BM16	11.2 (4.9%)	8.39 (37.7%)	16.76	18.9 (8.8%)	38.4 (8.8%)
BV0	12.8 (3.3%)	8.09 (28.4%)	13.31	17.2 (11.3%)	38.6 (11.3%)
BV10	13.9 (2.1%)	7.46 (37.6%)	12.12	13.4 (7.2%)	29.7 (7.2%)

(*) Compressive strength considering the gross area of the block. (**) Compressive strength Considering the net area of the block.

As can be seen in Table 2, the water absorption and roughness presented by the different types of blocks are not quite different and should not exert a significant influence on the bond between the materials. The characteristic compressive strength shown by voided faceshell blocks is lower than that presented by massive faceshell blocks. The characteristic compressive strength presented by blocks type BM7 and BM16 are similar, as are those presented by blocks BV0 and BV10, which makes easier the verification of the influence of geometry on the bond between blocks and grouts. However, for the case of average compressive strength in the net area, the block type BV0 presented a result considerably higher than the BV10, which could influence the result of the adherence. Among all types of blocks, the one with the highest resistance was the BM4 type, which has 56 MPa of compressive strength (net area). The block type BV10 has the lowest compressive strength values. Results of the grout characterization tests can be seen in Table 3. The water/grout (anhydrous) ratio used to obtain the desired consistency at this phase was approximately 0.13 and 0.16, respectively, for G15 and G30 type of grout. The modulus of elasticity presented by the two materials are similar because the grout used in this study had no coarse aggregate which would have increased the modulus for both types of grouts. The use of grout without the presence of coarse aggregates can facilitate the filling of the indentations of the cells of the blocks.

Table 3. Properties of the grouts.

Type of grout	Avg. Compressive strength (MPa)	Avg. Modulus of elasticity (GPa)	Avg. Tensile strength (MPa)
G15	20.3 (3.2%)	21.9 (2.3%)	2.2 (8.7%)
G30	33.6 (4.1%)	23.3 (1.8%)	3.7 (7.3%)

3.2 Second phase – Push-out test

The average maximum bond strength supported by each combination of block and grout type is presented in Table 4. The bond strength obtained with the use of 30 MPa grout was lower than that obtained with 15 MPa grout for all types of blocks. The bond strength in case of 30 MPa grout was lower by approximately 63% for block BM4, 82% for block BM7, 21% for block BM16, 44% for block BV0 and 1% for block BV10. This finding of lesser bond strength of the filling material with greater compressive strength differs from the findings of Izquierdo et al [5] and Biggs [11]. In a similar situation, they observed higher adherence values for the filling materials with higher compressive strength. The difference in the results obtained between the grouts G15 and G30, considering the same type of block, was smaller for the BM16 type of block, among the massive faceshell blocks and for BV10 among the voided faceshell blocks. These two types of blocks have the largest number of indentations inside the cells. This indicates that the presence of distinct geometries and a greater number of indentations contributes to a greater adherence between block and grout.

Among the massive and voided faceshell types of blocks, the geometric characteristics of the cells of the block types BM16 and BV10 provided the largest contact areas, respectively. The reduction in the bond strength observed for the block type BV10 with the use of 30 MPa grout was close to nil, perhaps due to the smaller orifice volume of this type of block as compared to BM16 block. The bond strengths of blocks BM7 and BM16 were different when the same type of grout was used. As these blocks displayed similar compressive strength, the distinct geometries of their cells and their distinct contact areas contributed to the difference in the results. The bond strength provided by BM16 was 24 and 83% higher than that provided by BM7, with the use of grouts G15 and G30, respectively. From the analysis of the bond results of these two types of blocks, the more irregular geometry of the cell of the blocks BM16, with higher number of protrusions, contributed to increase the adherence between the materials. This is even more evident with the results obtained with the grout G30 that caused a reduction in the adherence for all types of blocks.

Table 4. Results of the push-out test.

Type of block	Type of grout	Avg. maximum load (kN)	Avg. contact area (cm^2)	Avg. bond strength (MPa)	S. D. (MPa)	C. V. (%)
BM4	G15	72.9	725	1.01	0.27	26.5
	G30	26.6	724	0.37	0.23	61.3
BM7	G15	95.8	701	1.37	0.26	19.3
	G30	16.7	698	0.24	0.07	27.3
BM16	G15	161.0	899	1.80	0.17	9.2
	G30	128.8	899	1.43	0.19	13.3
BV0	G15	85.0	546	1.56	0.19	12.1
	G30	48.3	548	0.88	0.19	21.5
BV10	G15	96.6	637	1.52	0.04	2.5
	G30	96.5	638	1.51	0.18	11.7

Block types BV0 and BV10 also presented similar characteristic compressive strength and a very distinct geometry of the cells. However, despite the geometric differences between these types of blocks, the push-out test results were equivalents when 15 MPa grout was used. On the other hand, when G30 grout was used, the bond strength obtained with block BV10 was 42% higher than that obtained with BV0, which has a smooth internal surface. Thus, in the case of 30 MPa grout, the increase in the contact area provided by the BV10 type of block caused a significant increase in the bond strength, indicating the advantage of using a grooved geometry to improve the bond strength. The mode of rupture presented by the specimens on the push-out tests was in the greater part characterized by the failure of the block and sometimes also of the grout. Samples made with grout G15 were more likely to exhibit rupture of the block and grout. Samples made with grout G30 were more likely to exhibit rupture only of the block. The slippage of the grout was identified only for the combination of grout G30 with block types BM7 and BM4. The BM7 specimens after push-out test are shown in Figure 8a for the use of G15 grout and in Figure 8b for G30 grout. As can be seen, the use of grout G15 presented the rupture of the block and the use of grout G30 produced the slippage of the grout.

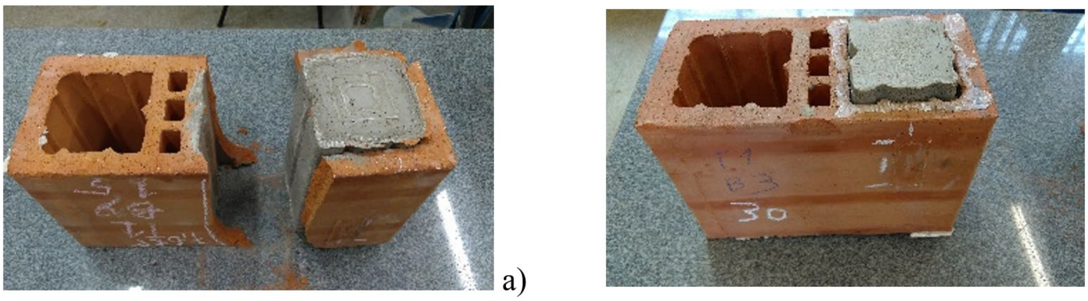

a) b)

Figure 8. BM7 specimens after push-out test.

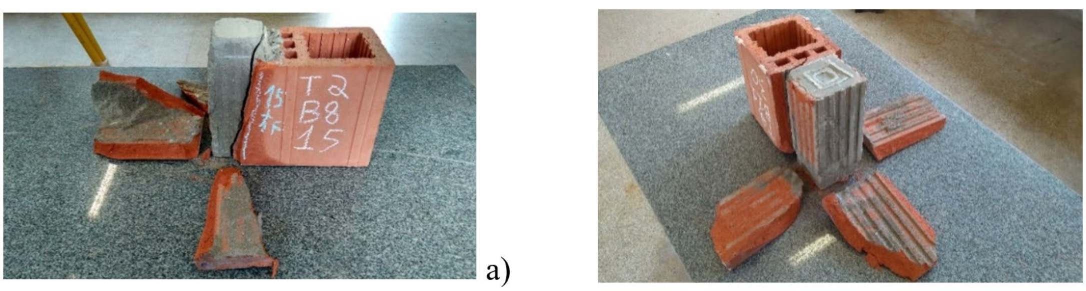

a) b)

Figure 9. BM16 specimens after push-out test.

The BM16 specimens after push-out test are shown in Figure 9a for the use of G15 grout and in Figure 9b for G30 grout. As can be seen, the use of grout G15 presented rupture of both block and grout, and the use of grout G30 produced the rupture of the block with little damage to the grout. The BM4 specimens after push-out test are shown in Figure 10a for the use of G15 grout and in Figure 10b for G30 grout. As can be seen the use of grout G15 produced rupture of the block and the use of grout G30 produced the slippage of the grout.

The BV0 specimens after push-out test are shown in Figure 11a for the use of G15 grout and in Figure 11b for G30 grout. As can be seen the use of grout G15 produced rupture of both block and gout, and the use of grout G30 produced the rupture of the block with little damage to the grout. The BV10 specimens after push-out test are shown in Figure 12a for the use of G15 grout and in Figure 12b for G30 grout. As can be seen the use of grout G15 produced rupture of both block and gout, and the use of grout G30 produced the rupture of the block with less damage to the grout. The influence of the block type on the push-out test may vary on account of the grout used. Thus, variance analysis of a single factor (the type of block) was performed for each type of grout, considering a 95% confidence level. The results showed that the type of block significantly influenced the results with both types of grouts. For G15, approximately 67% of the results of bond strength can be explained by the type of block. For the use of G30, approximately 90% of the bond strength results can be explained by the block type. Therefore, the type of block has a greater influence on the results of bond strength obtained with the 30 MPa grout.

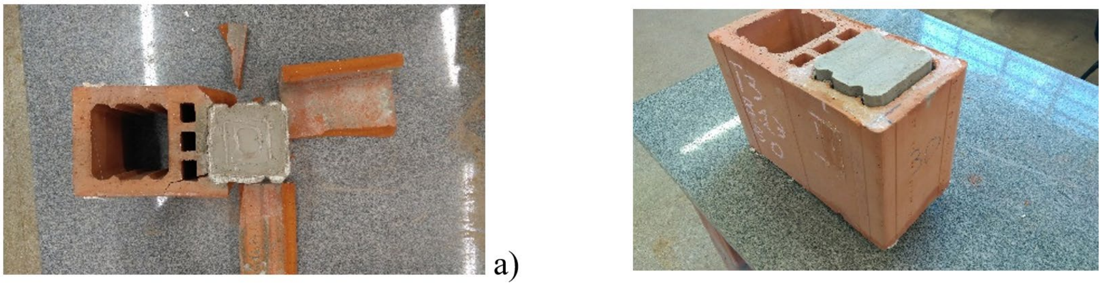

a) b)

Figure 10. BM4 specimens after push-out test.

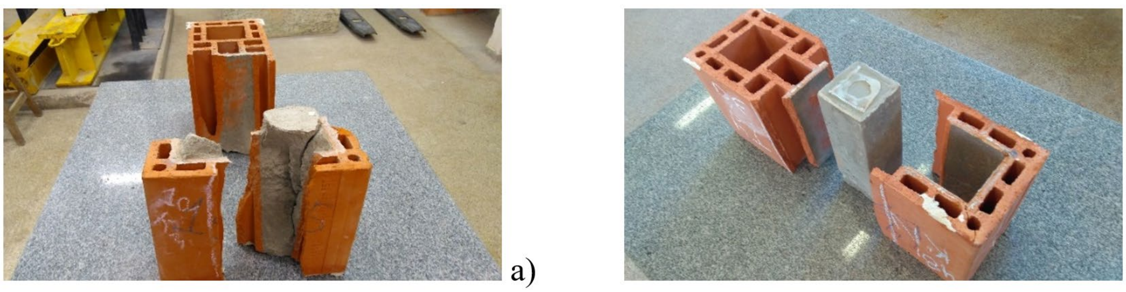

a) b)

Figure 11. BV0 specimens after push-out test.

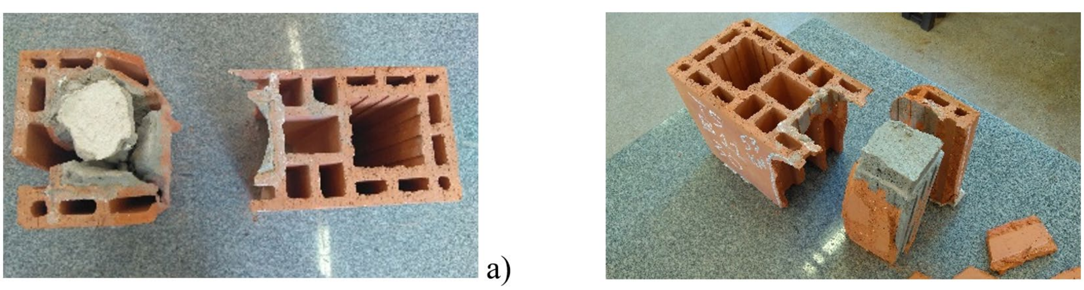

a) b)

Figure 12. BV10 specimens after push-out test.

To compare the bond strength provided by each type of block, the Tukey test was performed. The results of these tests are shown in Figure 13a and Figure 13b, respectively, for the use of grout G15 and G30. As can be seen in Figure 13, the red lines indicate that the results of these two types of blocks were significantly different from each other. The black lines indicate that the results were not significantly different. BM16 and BV10 were the only types of blocks that did not presented significant differences in the push-out results for both types of grouts. In Figure 12b there is a greater number of results indicating significant differences between blocks. Therefore, the bond strength was more influenced by the type of block for the use of grout G30.

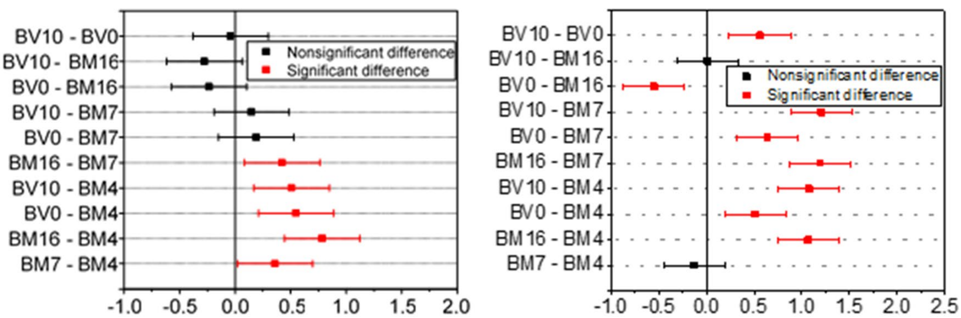

a) b)

Figure 13. Tukey test for the push-out results (mean comparison).

3.3 Third phase – Pull-out test

To complement the evaluation of the adherence, pull-out tests were carried out, for the block types BM7, BM16, and BV10. The mean ultimate stress obtained in the pull-out test for each one of these three types of blocks with both grout types are presented in Table 5. The compressive strength of mortar was tested according to NBR 13279 [21], with results equal to 11.6 MPa and 18.2 MPa, at 28 days. The first mortar was used with BV10, and the second with BM7 and BM16. The reinforcement tension properties were obtained by direct tension test, performed in three specimens according to the procedure described in NBR ISO 6892-1 [22]. The mean ultimate stress of the reinforcement was 689.1 MPa and the mean yield stress was 555.8 MPa. The mode of rupture observed did not show the slippage of the grout, but slippage of the rebar. This usually occurred after the rebar has reached its yield stress and some damage (cracks) to the walls has occurred. With blocks BM7 and BV10, and G15, the reinforcement bar reached 95% of its yield strength. All G30 and all BM16-specimens allowed the reinforcement to yield. All specimens not presented slippage of the grout. From these observations it is possible to admit that the three types of blocks can promote adequate bond strength with the grouts, with BM16 allowing a better bond.

Table 5. Pull-out results.

Type of block	Type of grout	Mean ultimate load (kN)	Mean ultimate stress (MPa)	S. D. (MPa)	C. V. (%)
BM7	G15*	121.9	610.0	64.2	10.5
	G30*	105.4	527.0 (**)	42.1	8.0
BM16	G15	123.8	619.0	32.6	5.3
	G30	114.4	572.1	39.6	6.9
BV10	G15	117.9	590.0	20.0	3.4
	G30	108.9	544.8 (**)	23.1	4.2

(*) One specimen was not considered because the bar slipped at a lower load. (**) Ultimate load smaller than the reinforcement yield strength

Table 5 shows that, for the same type of block, the highest values of tensile strength were obtained for the samples filled with G15 comparing to G30. This behavior occurred for the three types of blocks tested. This same behavior was also identified in the push-out tests, where the same type of block showed higher bond strength with G15 than with G30. The pull-out results with G15 as compared with G30 were approximately 14, 8 and 8% higher, respectively, for blocks BM7, BM16, and BV10. The difference obtained in the pull-out test for a block type when using G15 and G30 was smaller than the differences observed for the same block type on the push-out test. This reduced difference between the pull-out results may indicate that other factors than the bond strength between block and grout influenced the pull-out results. It is possible that the misalignment of the courses in a wall and the variation in the position of the indentations in BM7, between one course and the next, may have contributed to these results.

In the push-out test (second phase), the results obtained with block type BV10 were superior to those obtained with BM7, for both types of grouts. However, in the case of the pull-out tests the results obtained for BV10 and BM7 types of blocks became similar. This result reinforces the possibility of the existence of factors, other than the bond strength between the materials, that influences the pull-out results. It is likely that the distinct geometry of the block type BM7, which makes it possible to position the indentations between the blocks in one course different than that of the blocks in another course, may have contributed to the increased tension in the steel during the pull-out test. To check whether the type of block or type of grout had a significant influence on the mean ultimate load obtained in the pull-out test, analysis of variance (ANOVA) was performed taking two factors in consideration and a 95% confidence level. The results indicated that the type of block ($R^2 \cong 10\%$) does not have a significant influence on the stress observed in the pull-out test. However, the type of grout ($R^2 \cong 45\%$) can influence the results. The iteration between the types of blocks and grout ($R^2 \cong 4\%$), does not significantly influence the results.

3.4 Fourth phase – Grout Shrinkage

As the grout showed some signs of shrinkage in some specimens used in the push-out test, it was necessary to investigate this material's properties. The results of dimensional variation made with grout prisms indicate a greater shrinkage in grout G30 (0.96 mm/m) compared to grout G15 (0.66 mm/m), after 28 days of curing. The length reduction (shrinkage) observed for grout G15 was approximately 31% inferior to that observed for grout G30. These results were obtained according to the procedure described in NBR 15261 [23] code. The water/grout (anhydrous) ratio used to obtain the desired consistency at this phase was approximately 0.14 and 0.19, respectively, for G15 and G30. If shrinkage cracks are formed in the core of the grout, it can adversely affect its mechanical properties, and if cracks are formed in the interface between blocks and grout it can reduce the contact area between the materials, impairing their adherence. To evaluate the effects of the shrinkage inside the blocks, specimens were cut in half and the amount of cracks were measured. The percentage of the length of cracks formed, inside the grout or in the block-grout interface, in relation to the perimeter of the hole in each type of block are presented in Table 6. Based on the amount of cracks formed at interface block/grout it is possible to estimate the loss in the contact area between these materials, as can be seen in column 4 of Table 6.

Table 6. Percentual of cracks formed.

Block type	Grout type	Cracks in the grout	Cracks on the interface (Lost on the contact area)	Total cracks
BM4	G15	40.0%	9.0%	49.0%
	G30	8.8%	62.0%	70.8%
BM7	G15	36.3%	7.7%	44.0%
	G30	21.6%	37.8%	59.2%
BM16	G15	31.4%	0.0%	31.4%
	G30	12.4%	20.9%	33.2%
BV0	G15	41.6%	0.0%	41.6%
	G30	17.8%	42.2%	60.0%
BV10	G15	31.0%	0.0%	31.0%
	G30	46.1%	8.5%	54.6%

As can be seen in Table 6, for the same type of block, there was an increase in the percentage length of cracks formed at the block-grout interface and in total cracks, when using the grout with higher compressive strength (G30). In the case of the length of the cracks formed inside the grout, the opposite occurred, meaning that the grout with lower compressive strength (G15) presented a higher percentage of cracks, for the same type of block. The increase in the length of cracks formed at the block-grout interface for samples with 30 MPa grout may be one of the reasons for its lower performance in the push-out and pull-out tests. For both tests a better performance was observed with the use of grout 15 MPa. Kingsley et al [1] suggests that increasing the amount of water used in the mixture of grout will result in greater shrinkage. The results obtained in this research seems to agree with the authors observations, since the amount of cracks formed while using the grout G30 that consumed more water int mixture than G15, was greater. With the formation of a greater number of cracks at the interface between block and grout, the effective contact area between the materials was reduced. Thus, it is possible that the portion of material which was in contact resisting the load applied during the test was reduced, causing the lower results.

4 LOAD ESTIMATION IN THE PUSH-OUT TEST

This experimental program helped identify two factors that could affect the bond between clay blocks and grouts: the shrinkage of the filling material and the geometric shape of the cells of the blocks. These two factors produce changes in the real contact area presented by a particular type of block and grout. The contact area presented by a certain type of block can be larger or smaller, depending on the overall dimension of the cell and the presence of indentations inside the cells. The shrinkage of the grout can cause a reduction in the effective contact area between grout and block. Based on this information, it becomes possible to use coefficients that incorporate the changes caused in the contact area due the shrinkage of the grout and the geometry of the cells of the blocks, in the estimation of the maximum load supported by each type of block and grout during the push-out tests. To predict the maximum load resisted by each combination of block type and grout type, it is necessary to use a previously defined bond strength as a reference, and, to use two factors, namely:

- A geometric factor to represent the increase in the contact area promoted by the presence of indentations or grooves, inside of a cell (k1); and,
- The effects of the loss of contact area due to the shrinkage of the grout (k2).

The reference bond strength chosen for this estimate was provided by the combination of block type BV0 and grout type G15. This combination was chosen because this block type is the only one with a smooth surface inside the block's cell and this grout did not show any signs of shrinkage inside this block type. Two types of blocks that have the same length of cell-perimeter, may present different cross-sectional areas in the cell. These areas may be small if the number of indentations inside the cell are large. If the number of indentations inside the cell is small, the cross-section of the cell may be larger. Therefore, it is possible to estimate the influence of the presence of the indentations by comparing the cross-sectional area of a cell in a certain type of block with an assumed cross-sectional area, such as a square and smooth cross-section which has the same perimeter as the block that is being evaluated. Equation 3 and Equation 4 were used for calculating the fictitious contact area:

$$\mathrm{P} = \frac{C.A.}{H} \tag{3}$$

$$F.A. = \left(\frac{P}{4}\right)^2 \tag{4}$$

where P = perimeter of the block's cell (cm^2); $C.A.$ = contact area presented for this type of block (cm^2); H = nominal height of the block (19 cm); and $F.A.$ = fictitious cross-sectional area (cm^2), assumed to be a square with a smooth surface.

Based on the real and fictitious values of the cross-sectional area presented by the cell of each type of block, it is possible to calculate the geometric coefficient k1, using the Equation 5:

$$k1 = \frac{F.A.}{Cros.A.} \tag{5}$$

where $K1$ = geometric coefficient of the block's cell (dimensionless); $F.A.$ = fictitious cross-sectional area (cm^2); and $Cros.A.$ = real cross-sectional area of the cell (cm^2).

The coefficient k2 represents the value of the contact area lost by the shrinkage of the grout inside each type of block. This factor can be calculated using the Equation 6 and Equation 7 below:

$$R.C.A. = \left(A.\,C. - \frac{A.C. \times P.L.C}{100}\right) \tag{6}$$

$$k2 = \frac{A.C.R}{A.C.} \tag{7}$$

Where $R.C.A.$ = remaining contact area after shrinkage (cm^2); $A.C.$ = average contact area of the blocks used on the push-out test (cm^2); $P.L.C.$ = percentage value of loss of contact area due to shrinkage (%); and $K2$ = shrinkage coefficient (dimensionless).

The k1 factor represents the increase in the contact area of the blocks caused by the presence of indentations and grooves. However, the increase in the contact area can also be caused by the increase of the cell's overall dimensions.

Therefore, to consider this influence for estimating the load for each type of block and grout, the smooth contact area presented by each type of block must be considered. The smooth contact area was presented in Table 1. Now, with the use of the reference bond strength, the smooth contact area of each type of block and the factors k1 and k2, it is possible to estimate the maximum force necessary for each combination of block type and grout for the push-out test, using of the equation 8 below:

$$Q\ m\acute{a}x. = \frac{R.A.S. \times S.C.A \times k1 \times k2}{10} \tag{8}$$

Where $Q\,m\acute{a}x$ = maximum theoretical force estimated for each combination of block and grout (kN); R.A.S. = reference bond strength (MPa); $A.C.$ = average contact area of the blocks used on the push-out test (cm^2); S$.C.A.$ = smooth contact area of each type of block, ignoring the increments in the area caused by the indentations (cm^2); $K1$ = geometric coefficient of the block's cell (dimensionless); and $K2$ = shrinkage coefficient (dimensionless). The maximum theoretical forces obtained by using the Equation 8 are shown in Table 7.

Table 7. Maximum theoretical force.

Type of block	Type of grout	k1	k2	Smooth contact area (cm^2)	Bond strength (MPa)	Maximum theoretical force (kN)
BM4	G15	0.99	0.9	688	1.56	96.6
	G30	0.99	0.33	688	1.56	40.2
BM7	G15	0.96	0.92	652	1.56	89.7
	G30	0.95	0.59	652	1.56	59.9
BM16	G15	1.52	1	737	1.56	174.9
	G30	1.52	0.72	737	1.56	138.3
BV0	G15	0.97	1	547	1.56	83.1
	G30	0.98	0.58	547	1.56	48.4
BV10	G15	1.56	1	561	1.56	136.3
	G30	1.56	0.9	561	1.56	124.6

Figure 14 shows a graphical comparison of the theoretical and experimental results for each type of block and grout. As can be seen, there are some results in which the theoretical values are very close to the experimental ones. However, in other cases theoretical and experimental results differ considerably, as for the block type BM7 and grout G30. The large coefficient of variation observed in some of the push-out tests and the small number of samples used to determine the grout shrinkage percentage may have contributed to the larger differences. The correlation coefficient (R^2) between theoretical and experimental data was 0.86. Meaning that the theoretical results can represent 86% of the experimental ones. Which is a good degree of approximation. When separating the results for each type of grout, the correlation coefficient is equal to 0.77 for grout G15 and 0.87 for grout G30. Thus, the results indicate that it is possible to use the two coefficients mentioned here to estimate the maximum load obtained with each combination of block and grout on the push-out test. It will be necessary, however, to conduct more studies to improve this estimation and investigate another factor that can interfere in this behavior.

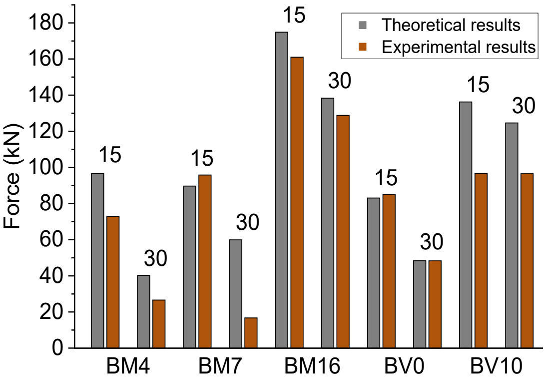

Figure 14. Comparison between theoretical and experimental results.

5 CONCLUSIONS

The objective of this article was to evaluate the adherence between five different types of fired clay blocks and two types of grouts. Push-out and pull-out tests were performed to assess the adherence among the different combinations of blocks and grouts.

There are many factors that can influence the performance of the adherence presented by the contact interface of blocks and grouts. One of these factors is the geometry of the cells of the blocks that can increase the bond strength by providing a higher contact area. This increase in the contact area can be reached by a grooved internal surface and a greater number of indentations inside the cells. Other factor that can influence the bond strength is the properties of the grout used. In the case of this research, the highest values of adherence were obtained while utilizing the grout G15 in relation to the grout G30, for the same type of block. Specimens constructed with G15 grout provided higher values of adherence in the Push-out and in the Pull-out tests. One of possible the explanations is the fact that the shrinkage presented by the grout G30 was higher than that presented by the grout G15, reducing the contact surface of block and grout.

The shrinkage of the grout and the geometry of the cell of the block can be used to estimate the bond strength between the clay blocks and grouts on the Push-out tests. The equation developed using factors k1 and k2 to compensate these factors shown to be effective to obtain theoretical results similar to the experimental ones, with good correlation. The test procedure developed to estimate the percentage of contact area lost due to grouts shrinkage shows to be promising, since its results were used in the equation to estimate the bond strength between blocks and grouts and shown good correlation. However, more study must be done because there are other variables that can affect the results. These results show that it is possible to use different characteristics of blocks and grouts to increase the adherence between these materials and provide a better behavior for reinforced masonry structures. However, it looks like if block types with a grooved hollow cell are used, a bigger contact surface is produced, and a higher bond strength appears to be assured.

ACKNOWLEDGEMENTS

This study was financed by the Associação Nacional da Indústria Cerâmica (ANICER) and by the Coordenação de Aperfeiçoamento de Pessoal de Nível Superior - Brasil (CAPES) - Finance Code 001.

REFERENCES

[1] G. R. Kingsley, L. G. Tulin, and J. L. Noland (1985). Parameters influencing the quality of grout in hollow clay masonry. In *7th Int. Brick and Block Masonry Conf. (IBMAC)*, Melbourne, Fev. 1985, pp. 1085-1091.

[2] Z. Soric and L. G. Tulin. Bond in reinforced concrete masonry. In: *4th North American Masonry Conf.*, Los Angeles, California, 1987, p. 47.1-47.16.

[3] K. Ahmed and L. R. Feldman. Evaluation of contact and noncontact lap splices in concrete block masonry construction, *Canadian J. Civil Eng.*, vol. 39, n. 515-525, 2012.

[4] A. Kisin (2014). "Evaluation of mitigative techniques for non-contact lap splices in concrete block construction," Ph.D. dissertation, Dept. Civil and Geological Eng., Univ. Saskatchewan, Saskatoon, Canada. 201 p.

[5] O. S. Izquierdo, M. R. S. Corrêa and I. I. Soto, Study of the block/grout interface in concrete and clay block masonry structures," *Rev. IBRACON Estrut. Mater.*, vol. 10, n. 4, pp. 924-936, Ago. 2017. http://dx.doi.org/10.1590/s1983-41952017000400009.

[6] J. A. Thamboo, M. Dhanasekar and C. Yan, "Flexural and shear bond characteristics of thin layer polymer cement mortared concrete masonry," *Construction and Building Mater.*, vol. 46, pp. 104-113, Set. 2013. http://dx.doi.org/10.1016/j.conbuildmat.2013.04.002.

[7] L. A. Pereira de Oliveira, "Resistência de aderência como parâmetro de compatibilidade entre o graute de enchimentos e as unidades da alvenaria estrutural," in *5th Inter. Seminar on Structural Masonry for Develop. Countries*, Florianópolis, SC, Brasil, 1994, pp. 214-227.

[8] L. A. Pereira de Oliveira, "The micro-concrete infill strength's influence on the compressive masonry strength," in *European Ready Mix Org. Congr. – ERMCO 98*, Lisboa, Portugal, 1998, pp. 691-700.

[9] L. Guarnieri, C. P. Bergmann and Filho, L. C. P. S. "Influência da aderência graute/bloco cerâmico estrutural na resistência mecânica do conjunto," in *XIII Congr. Inter. sobre Patologia e Reabilitação de Estruturas (13° CINPAR)*. Crato, CE, Brazil, 2017.

[10] O. S. Izquierdo, "Estudo da interface bloco/graute em elementos de alvenaria estrutural," Ph.D. dissertation, Univ. São Paulo, São Carlos, SP, Brasil, 2015. 322 p.

[11] D.T. Biggs, "Grouting masonry using Portland cement-lime mortars," in *Int. Building Lime Symp.*, Orlando, FL, USA, 2005 p. 2-15.

[12] American Society for Testing and Materials, *Standard Specification for Grout for Masonry*, ASTM C476, 2020.

[13] Z. Soric and L.G. Tulin, "Bond Stress/Deformation in Pull-Out Masonry Specimens," *J. Struct. Eng.*, vol. 115, no. 10, pp. 2588–2602, 1989., http://dx.doi.org/10.1061/ (ASCE)0733-9445(1989)115:10(2588).

[14] Associação Brasileira de Normas Técnicas, *Componentes cerâmicos - Blocos e tijolos para alvenaria Parte 2: Métodos de ensaios*, NBR 15270-2, 2017.

[15] Associação Brasileira de Normas Técnicas, *Concreto – ensaios de compressão de corpos de prova cilíndricos*, NBR 5739, 2018.

[16] Associação Brasileira de Normas Técnicas, *Concreto e argamassa — Determinação da resistência à tração por compressão diametral de corpos de prova cilíndricos*, NBR 7222, 2011.

[17] Associação Brasileira de Normas Técnicas, *Concreto – Determinação do módulo estático de elasticidade à compressão*, NBR 8522, 2008.

[18] Associação Brasileira de Normas Técnicas, *Argamassa e concreto endurecidos - Determinação da absorção de água, índice de vazios e massa específica*, NBR 9778, 2005.

[19] Associação Brasileira de Normas Técnicas, *Alvenaria estrutural – Parte 1: Projeto*, NBR 16868-1, 2020.

[20] Associação Brasileira de Normas Técnicas, *Projeto de estruturas de concreto – Procedimento*, NBR 6118, 2014.

[21] Associação Brasileira de Normas Técnicas, *Argamassa para assentamento e revestimento de paredes e tetos - Determinação da resistência à tração na flexão e à compressão*, NBR 13279, 2005.

[22] Associação Brasileira de Normas Técnicas, *Materiais metálicos — Ensaio de Tração Parte 1: Método de ensaio à temperatura ambiente*, NBR ISO 6892-1, 2013.

[23] Associação Brasileira de Normas Técnicas, *Argamassa para assentamento e revestimento de paredes e tetos - Determinação da variação dimensional (retratação ou expansão linear)*, NBR 15261, 2005.

Author contributions: GS: conceptualization, testing, formal analyses, writing; GAP: conceptualization, formal analyses, writing, funding acquisition, supervision.

Editors: Fernando S. Fonseca